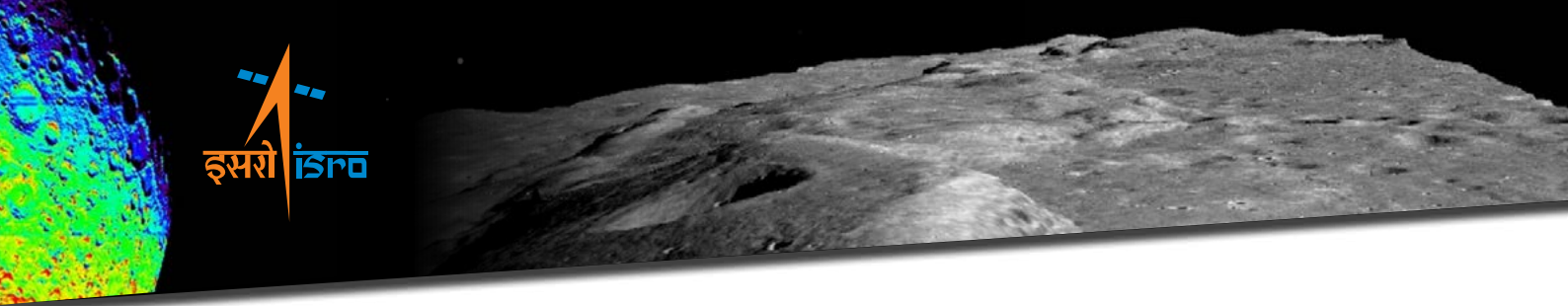


Science Results
from
CHANDRAYAAN 2
Mission



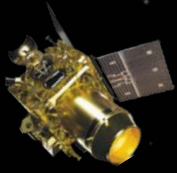


Science Results from CHANDRAYAAN 2 Mission

Version-1.0
August, 2021



INDIAN SPACE RESEARCH ORGANISATION
Bengaluru



Compiled and Edited by

Science Program Office

ISRO Headquarters

Antariksh Bhavan, New BEL Road

Bengaluru-560 231

Karnataka, India

Cover Page: Image of Lunar Surface (North Polar Region) captured by Terrain Mapping Camera-2 (TMC-2) of Chandrayaan 2 from an altitude of ~4375 km on 23rd August, 2019 @ 19:42 UT.

भारतीय अन्तरिक्ष अनुसंधान संगठन

अन्तरिक्ष विभाग

भारत सरकार

अन्तरिक्ष भवन

न्यू बी ई एल रोड, बेंगलूर - 560 231, भारत

दूरभाष : +91-80-2341 5241 / 2217 2333

फैक्स : +91-80-2341 5328



Indian Space Research Organisation

Department of Space

Government of India

Antariksh Bhavan

New BEL Road, Bangalore - 560 231, India

Telephone: +91-80-2341 5241 / 2217 2333

Fax : +91-80-2341 5328

e-mail : chairman@isro.gov.in

डॉ. कै. शिवन / Dr K. SIVAN
अध्यक्ष / Chairman

FOREWORD

Indian space programme originated with the fundamental research in space science. The scientific observations and findings of our planetary and space science missions are vast and diverse. India's first lunar mission Chandrayaan-1, flown in 2008, has opened up new scientific observations. The scientific observations, as well as the discovery class of findings therefrom have necessitated the second lunar mission from India, Chandrayaan-2, which was flown in 2019.

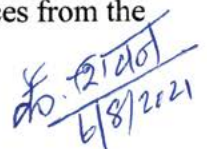


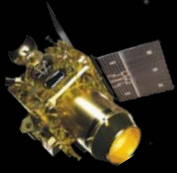
The Chandrayaan-2 mission aims at mapping of the volatiles including lunar water, mapping of the abundance of major rock forming elements, investigation of the lunar neutral exosphere and ion-environment, topography, morphology, studying the geo-tail dynamics when Moon passes through the geomagnetic tail, to name a few. The observations have been yielding intriguing scientific results, which are being published in peer-reviewed journals and presented in international meetings.

On the occasion of the completion of two years of Chandrayaan-2 in orbit, this collection of the major scientific results from the observations of Chandrayaan-2 attempts to cover the first-look of the Chandrayaan-2 data products which include the images, spectra and profiles obtained from the remote-sensing and in-situ observations. The Chandrayaan-2 Integrated Science Data is already released and different levels of data can be accessed through Indian Space Science Data Centre (ISSDC). The Space Science Programme Office, ISRO HQ, in association with the Principal Investigators of Chandrayaan-2, has brought out the documents on the major science results, as well as two compendia on the details of the science results and first-cut data products from the Chandrayaan-2 orbiter payloads.

I am sure that these documents provide inputs for valuable scientific information. I also hope that publication of these compendia will encourage the lunar scientific community as well as students and faculties of academia to investigate in depth and explore further sciences from the Chandrayaan-2 data.

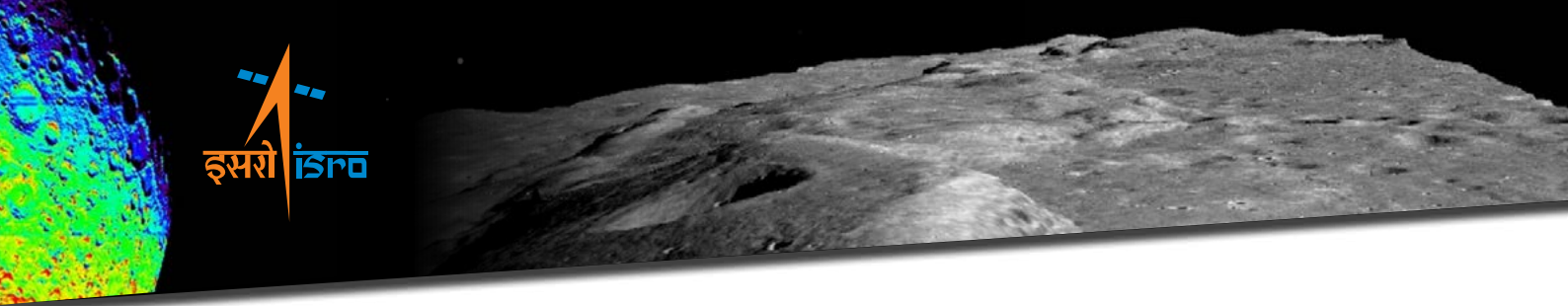
Dated: August 06, 2021


(कै. शिवन / K. Sivan)



CONTENTS

FOREWORD	IV
LIST OF FIGURES.	VI
LIST OF TABLES	XVI
LIST OF ABBREVIATIONS.	XVII
CHAPTER 1 Chandrayaan-2 Mission	1
CHAPTER 2 Chandrayaan-2 Orbiter Payloads	10
CHAPTER 3 Science Results from Chandrayaan-2 Large Area Soft X-ray Spectrometer (CLASS)	55
CHAPTER 4 Science Results from Solar X-ray Monitor (XSM)	64
CHAPTER 5 Science Results from CHandra's Atmospheric Composition Explorer-2 (CHACE-2)	74
CHAPTER 6 Science Results from Dual Frequency Synthetic Aperture Radar (DFSAR)	80
CHAPTER 7 Science Results from Imaging Infra-Red Spectrometer (IIRS)	94
CHAPTER 8 Science Results from Terrain Mapping Camera-2 (TMC-2)	103
CHAPTER 9 Science Results from Orbiter High Resolution Camera (OHRC)	122
CHAPTER 10 Science Results from Dual Frequency Radio Science (DFRS) Experiment	127



List of Figures

Figure 1.1:	Chandrayaan-2 mission profile.	3
Figure 1.2:	Chandrayaan-2 Spacecraft.. . . .	4
Figure 1.3:	Chandrayaan-2 Orbiter craft Payloads.	4
Figure 1.4:	Orbiter Season Definition.. . . .	7
Figure 1.5:	Payload Data Storage Streamline.	8
Figure 1.6:	Space and Ground Segment chain.	9
Figure 2.1:	CLASS Flight Instrument. The 16 X-ray detectors are arranged as four 'quads'. The door was closed enroute to the Moon and protected the X-ray detectors from radiation damage.	11
Figure 2.2:	Distribution of events in the energy space for the CLASS X-ray detector (SCD) for a beam of mono-energetic photons at 5.9 keV interacting at different regions of the device across the depth (Netra et al., 2021).. . . .	12
Figure 2.3:	⁵⁵ Fe on-board source spectrum observed in CLASS pre-flight and in-flight. The individual SCD spectra are co-added with a temperature dependent gain correction. The background increased in-flight due to the ambient particles in the orbit (Netra et al, 2021)..	13
Figure 2.4:	A photograph of the Chandrayaan-2 XSM instrument packages: (i) Sensor package that houses the detector, front-end electronics, and filter wheel mechanism. Mithun et al. [2021b].	16
Figure 2.5:	A photograph of the Chandrayaan-2 XSM instrument packages: (ii) Processing electronics package that houses the FPGA based data acquisition system, power electronics, and spacecraft interfaces. Mithun et al. [2021b].	16
Figure 2.6:	XSM spectra of mono-energetic X-ray beams at three energies. Note that for better clarity the spectra are normalized to different peak intensities. Best fit spectral response models are overplotted with solid lines, and the bottom panel shows the residuals in terms of sigma with error bars of size one sigma. Mithun et al. [2021b].	18
Figure 2.7:	Spectral response model parameters obtained from fitting mono-energetic spectra: FWHM (top left), the relative intensity of the escape peak (top right), and intensity of the tail component (bottom) are plotted as a function of energy. Statistical errors are smaller than the symbol size. The red solid lines show the best fit models, in the case of FWHM and intensity of the tail component, respectively, whereas for the escape peak intensity (top right), the line represents the result from Geant4 simulations. Figure taken from Mithun et al. [2021b].. . . .	18

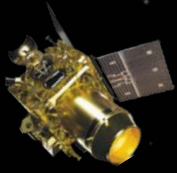


Figure 2.8: Top: Photograph showing the aperture of the XSM collimator. bottom: Transmission of the silver-coated (50 μm on both sides) collimator obtained as the ratio of X-ray gun spectrum recorded with a specially made collimator. The red solid line shows the expected transmission of the collimator. Figure taken from Mithun et al. [2021b]. 20

Figure 2.9: The visibility of the Sun with XSM over the year. 21

Figure 2.10: FM of the CHACE-2 instrument. 24

Figure 2.11: Typical mass spectrum of CHACE-2 in the Lunar orbit. 26

Figure 2.12: CHACE-2 local time coverage from September 2019 to April 2020, in LSE (Lunar Centric Solar Ecliptic) Coordinates coordinate system. 27

Figure 2.13: Selenographic Coverage during September 2019-April 2020. 27

Figure 2.14: DFSAR Electronics and Antenna Systems. 30

Figure 2.15: DFSAR configuration and imaging geometry. 30

Figure 2.16: Compact-Pol and Full-Pol. 31

Figure 2.17: Axial Ratio and Polarimetric characterization of DFSAR instrument. . . . 32

Figure 2.18: First DFSAR Acquisition in L-band. 33

Figure 2.19: Polarimetric calibration illustrated using histograms of Co-pol (HH/VV) and Cross-pol (HV/VH) phase differences. 34

Figure 2.20: Polarimetric signatures corresponding to opportunity point target, to assess the efficacy of polarimetric calibration. 34

Figure 2.21: Flow chart showing methodology involved in the processing of Ch-2 IIRS data. 36

Figure 2.22: Reflectance spectra of particulate lunar soil, rock and minerals measured in Earth-based laboratory (RELAB) in the spectral range $\sim 0.5\text{--}4.0\ \mu\text{m}$ comparable with the IIRS spectral range (Source: supporting on-line material by Pieters et al. (2009) published in Science). 37

Figure. 2.23: Isometric view of electro optical module and camera electronics of Terrain Mapping Camera (TMC-2). 41

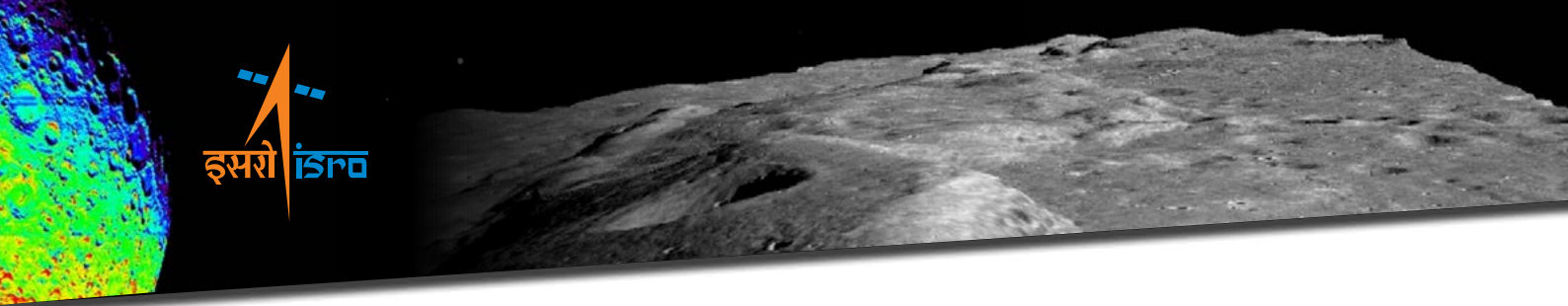


Figure 2.24: TMC-2 Principle of Operations. 42

Figure 2.25: Figure shows uniform region selected in a Nadir image of a Lunar pole taken by TMC-2 and comparison of achieved and expected SNR.. . . . 43

Figure 2.26: Figure shows the ROI in a crater having a sharp edge separating the illuminated and shadow region of the crater and MTF generated. 44

Figure 2.27: Figure showing the flow chart of methodology adopted for TMC-2 data analysis. 45

Figure 2.28: This shows the front view of the OHRC in lab. 47

Figure 2.29: The data analysis and interpretation for generalized problems using OHRC data.. . . . 48

Figure 2.30: Schematic for Radio Occultation (After Choudhary et al, 2019).. 49

Figure 2.31: Bending of waves due to the atmosphere of the celestial body.. . . . 50

Figure 2.32: Block diagram of different components of DFRS. 51

Figure 2.33: Flight model version of DFRS-10 and DFRS-20 at Chandrayaan-2 (After Choudhary et al, 2019).. 51

Figure 3.1(a): X-ray coverage of the Moon from pre-Chandrayaan-2 measurements (Ref: Weider et al, 2012).. 56

Figure 3.1(b): X-ray Fluorescence coverage with Chandrayaan-2 Large Area Soft X-ray Spectrometer 56

Figure 3.2: CLASS observations in the far side highland (R1) and a region in Mare Imbrium (R2) (Netra et al, 2021). 57

Figure 3.3: Elemental abundances of Mg and Al derived from R1 (Far side highlands) and R2 (In Mare Imbrium) compared to Apollo soil averages and Chang'e-3 insitu measurements (Netra et al, 2021). 58

Figure 3.4: (a) A track across the near side Mare at 12.5 Km spatial resolution. (b) Spectra from two adjacent pixels show discernible differences in composition. All major elements present are clearly detected. 58

Figure 3.5: Elemental maps of (a) Mg , (b) Al, (c) Si, (d) Ca (e) Ti and (f) Fe show compositional differences at the spatial resolution of 12.5 km , first of its kind. 59

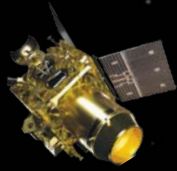


Figure 3.6: Al and Fe abundance (in weight %) shows the expected anti-correlation across the track. Small features such as freshly exposed crater (in the background LRO-WAC image) shows high Al value. 60

Figure 3.7: Lunar XRF spectrum from a region in Mare Imbrium modelled. There is a clear detection of Na XRF line. 61

Figure 3.8: Na detections with CLASS (only intervals where XSM spectrum is available is plotted). The weight % of Na in these areas are being derived (work in progress). 61

Figure 3.9: First detection of Cr and Mn through remote sensing with CLASS from a 250 km x 12.5 km pixel in Mare Nectaris (Narendranath et al, NASA_SSERVI and ELS 2021 proceedings 2021). 62

Figure 4.1: Panels a and b show the X-ray flux in the 1 – 15 keV energy range with a time cadence of 120 s, as measured by the XSM during two observing seasons. Different background shades represent activity levels on the Sun, with orange representing periods when NOAA active regions are present; pink representing periods of enhanced activity visible in both the XSM light curve as well as EUV/X-ray images but not classified as AR; and blue representing periods selected for the present study when no major activity was observed on the Sun. The microflares detected during the quiet periods are marked with red points, representing their peaks; and red vertical bars, representing their time. Vadawale et al. [2021a]. 65

Figure 4.2: Panel **a** shows temperature and EM for 86 of the 98 quiet Sun (QS) microflares observed by the XSM with blue star symbols. The error bars represent 1σ uncertainties. Magneta squares and red filled circles correspond to QS microflares observed by SphinX [Sylwester et al., 2019] and NuSTAR [Kuhar et al., 2018], respectively. Parameter space of active region (AR) events observed by RHESSI [Hannah et al., 2008] and SphinX [Gryciuk et al., 2017] are shown with orange and gray shades, respectively. The brown open circles represent the four AR microflares reported by NuSTAR [Wright et al., 2017, Glesener et al., 2017, Hannah et al., 2019, Cooper et al., 2020]. Dashed lines represent the isoflux curves corresponding to GOES/XRS 1 – 8 Å X-ray flux levels from A0.001 (10^{-11} Wm^{-2}) to B1 (10^{-7} Wm^{-2}). Panel **b** shows the frequency distribution of thermal energies of 63 microflares for which the measurements are available. The green dashed line corresponds to a power law index (α) of two shown for comparison. The dotted lines correspond to power laws reported from quiet Sun EUV observations by Krucker and Benz [1998] [KB98], Aschwanden et al. [2000] [A00], and Parnell and Jupp [2000] [PJ00] as shown in Figure 10 of Aschwanden et al. [2000]. Vadawale et al. [2021a]. 67

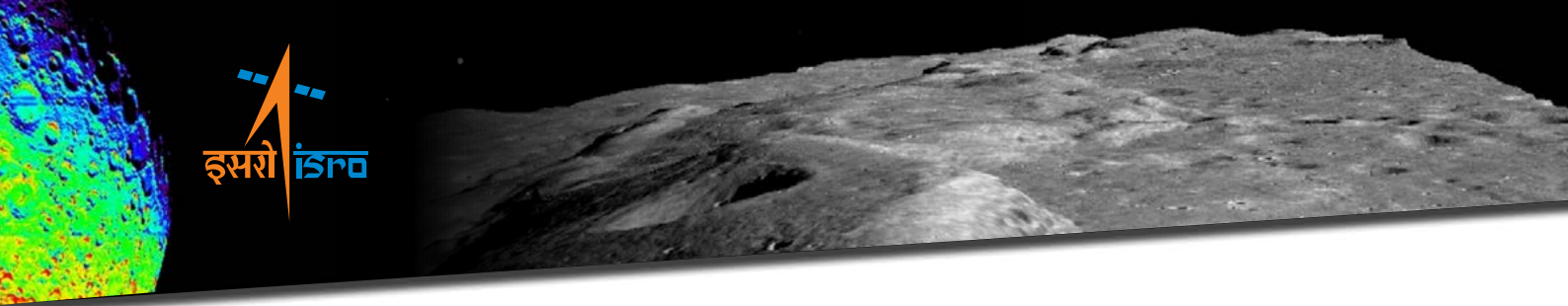


Figure 4.3: Soft X-ray spectra measured by the XSM for two representative days of quiet Sun observations are shown. Solid lines represent the best fit isothermal model and the residuals are shown in the bottom panel. Gray points correspond to non-solar background spectrum. Vadawale et al. [2021b]. 68

Figure 4.4: The five panels show the results of the spectral fitting, viz. Temperature (a), EM (b), as well as the absolute abundances of Mg (c), Al (d), and Si (e) in logarithmic scale with $A(H)=12$. The red, green and blue points represent the best fit parameters obtained from the spectra integrated over one day, multiple days (2–4 days), and each quiet period, respectively. The y-error bars represents 1σ uncertainty for each parameter, whereas the x-error bars represent the duration over which a given spectrum is integrated. XSM light curves for the entire duration are shown in gray in the background. For a quick comparison with the reported values of abundances for these elements, the corresponding panels (c-e) also show lines representing active region values reported by [Feldman, 1992] (navy blue), [Fludra and Schmelz, 1999] (orange), and [Schmelz et al., 2012] (purple). The range of photospheric abundances from various authors compiled in the CHIANTI database are shown as green bands. The right y- axis in panels c-e show the FIP bias values for the respective elements with respect to average photospheric abundances. Vadawale et al. [2021b]. 69

Figure 5.1: Typical variation of the amu 40 signal (Ar-40) in the Lunar dawn-dusk orbit, along with variation in the context parameters, including selenographic latitude, longitude, spacecraft speed, altitude, Roll angle as well as Solar Zenith Angle (SZA). 75

Figure 5.2: Argon-40 global distribution from CHACE-2 observations, showing both low- and mid-latitude variations. 75

Figure 5.3: Map of amu-44 partial pressures observed by CHACE-2 observations, showing both low- and mid-latitude variations. 76

Figure 5.4: Comparison of Neon signal observed when Moon is in the upstream region and the magnetotail regions. The black and blue lines correspond to observations in the upstream and within the magnetotail respectively. 77

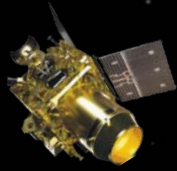


Figure 6.1: Raney ($m-\chi$) decomposed image of study area acquired by (a) CH-2 DFSAR S-band; (b) LRO Mini-RF S-band; (c) Average CPR values in the interior and exterior parts of various craters (one small and one large crater marked by red dotted circle) imaged by LRO-MiniRF (S-band) and CH-2 DFSAR (S-band). The triangle data points correspond to Mini-RF data and square data points correspond to DFSAR data. 81

Figure 6.2: Raney ($m-\chi$) decomposed image of study area acquired by (a) CH-2 DFSAR L band; (b) LRO-MiniRF S band; (c) corresponding optical image acquired by LRO Narrow Angle Camera image.. . . . 81

Figure 6.3: Average CPR values in the interior and exterior parts of various craters imaged by LRO-MiniRF (S-band) and CH-2 DFSAR (L-band). The triangle data points correspond to MiniRF data and square data points correspond to DFSAR data. 82

Figure 6.4: Boulder distribution studies using high-resolution data. Presence of large (cm to m scale) boulders on the inner wall of the secondary crater (on the floor of Manzinus crater) is identified from high resolution polarimetric decomposed image. 84

Figure 6.5: Inversion for Lunar Dielectric Constant and RMS height over Apollo-11 landing site. 86

Figure 6.6: Histogram showing distribution of Lunar Dielectric Constant and surface roughness parameters over Apollo-11 landing site 86

Figure 6.7: Inversion results (a) HH-pol backscatter image with multiple ROIs (b) Dielectric Constant (c) RMS Height (d) Correlation length (e) Statistics of DC (f) RMS Height over multiple ROIs over Non-polar anomalous Gardner Crater. 86

Figure 6.8: The novel integrated approach to unambiguously detect water ice, combining polarimetric parameters and model based Dielectric Constant and surface roughness properties derived from Full-Pol Chandrayaan-2 DFSAR data.. . . . 87

Figure 6.9: Map showing most probable locations (in cyan and blue colours) of regolith mixed water ice overlaid on CH-2 L-band CPR image within the interiors of secondary craters (mostly permanently shadowed regions) on the floor of Peary crater in Lunar North Pole. The SAR images are ortho-rectified and radiometrically terrain corrected using lunar DEM. The background image is a grey-scale DEM derived from NASA's LRO-LOLA data.. . . . 88

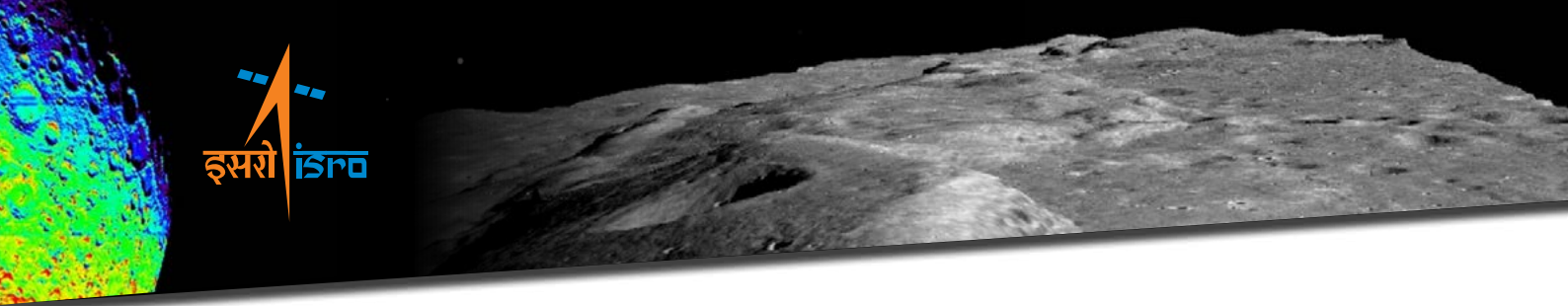


Figure 6.10: Distribution of probable water-ice bearing regions (in yellow and cyan colour) within a sampled crater (as shown in a box in Figure 6.9) overlaid on CPR, regolith dielectric constant and regolith roughness, derived from L-band full-polarimetric data. The cyan coloured regions are associated with low dielectric constant, low roughness and high CPR values and meet the criteria of water-ice bearing regolith, whereas yellow regions do not meet similar criteria and are categorised as no water ice.. 89

Figure 6.11: RMS Roughness and surface dielectric constant of two permanently shadowed regions (denoted as PSR-1 and PSR-2) and a sunlit portion within the Cabeus’s crater floor. Regions with low roughness, low to intermediate circular polarization ratio (CPR), and dielectric constant values within the ice-silicate mixture zone (3.15 to ~6) could possibly contain water ice patches mixed into the regolith. 90

Figure 6.12: Polarimetric characterization of various impact craters. 91

Figure 6.13: Left: L-band DFSAR HH polarization image of Tycho crater overlaid on an Arecibo P-band circular polarization ratio image for context. Right: Decomposition image of Tycho crater region followed by different geologic units showed in zoomed-in subsets. It can observed from these images that impact melts, floor and ejecta associated with Tycho crater appear ‘rough’ at L-band wavelength and are clearly separated from the background highlands region. 92

Figure 7.1: IIRS spectral data cube of a subset image acquired on August 23, 2019. The subset of the image has 169 cross-track samples, 73 lines and 251 spectral channels measuring from 810 to 5026 nm.. 94

Figure 7.2: Coloured rectangular boxes represent the Regions of Interest (ROIs) from where representative IIRS spectra have been obtained.. 95

Figure 7.3: Mean spectra of the ROIs shown in Figure 7.2 highlighting the presence of prominent 3000-nm hydration feature (black double-headed arrow). First ever detection of hydration in the spectral range of 2.7-3.2 μm at spatial resolution of ~80 m.. 96

Figure 7.4: **A.** 3000-nm Integrated Band Depth (IBD) map to highlight the variations in the strength of the hydration (OH/H₂O) feature as captured by Ch-2 IIRS data over the north polar region on the far side of the Moon; **B.** Band Center; **C.** Band Depth and **D.** Band Area map. 96

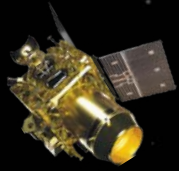


Figure 7.5: A. Ch-2 IIRS RGB-FCC. Coloured boxes indicate Regions of Interest (ROIs); B. IBD-Albedo-based FCC. ROIs are marked as 1-10; C. Mean spectral plot corresponding to the ROIs; D. Temperature map; E. ESPAT vis-à-vis H₂O content map of crater Aristarchus. 98

Figure 7.6: Thermally corrected lunar spectra for IIRS data strip-2 for bright anorthositic, mare and near polar highland surface. It shows significant lunar hydration feature varying with different surface composition types. 99

Figure 7.7: Total hydration maps for the thermally corrected Chandrayaan-2 IIRS strips analysed in the present study. The observed total water concentration is varying between near 0 to 800 ppm having strong control on mineralogy and latitudes. 100

Figure 8.1: (a) 3D perspective view of an oblique crater prepared by draping the TMC-2 orthoimage on DEM (b) Orthoimage. 104

Figure 8.2: (a) 3D perspective view of mass wasting in a crater prepared by draping the TMC-2 orthoimage on DEM (b) Orthoimage. 105

Figure 8.3: (a) 3D perspective view of lava-filled crater (arrow) and an effusive dome prepared by draping the TMC-2 orthoimage on DEM (b) Orthoimage.. . . 106

Figure 8.4: (a) 3D perspective view of a fresh young crater prepared by draping the TMC-2 orthoimage on DEM (b) Orthoimage. 107

Figure 8.5: (a) 3D perspective view of a young crater prepared by draping the TMC-2 orthoimage on DEM. (b) Orthoimage. 108

Figure 8.6: (a) 3D perspective view of rilles on a crater floor prepared by draping the TMC-2 orthoimage on DEM (b) Orthoimage. 109

Figure 8.7: (a) 3D perspective view of sinusoidal rilles prepared by draping the TMC-2 orthoimage on DEM (b) Orthoimage. 110

Figure 8.8: (a) 3D perspective view of a Lunar rille proximal to basin margin prepared by draping the TMC-2 orthoimage on DEM (b) Orthoimage. 111

Figure 8.9: (a) 3D perspective view of a Lunar volcanic dome (57.9300 W, 15.3000 N) mapped in the Marius hills region prepared by draping the TMC-2 orthoimage on DEM (b) Orthoimage (c) Topographic Map using DEM. . . 112

Figure 8.10: (a) 3D perspective view of a Lunar swirls prepared by draping the TMC-2 orthoimage on DEM (b) Orthoimage (c) Topographic Map using DEM. . . 113

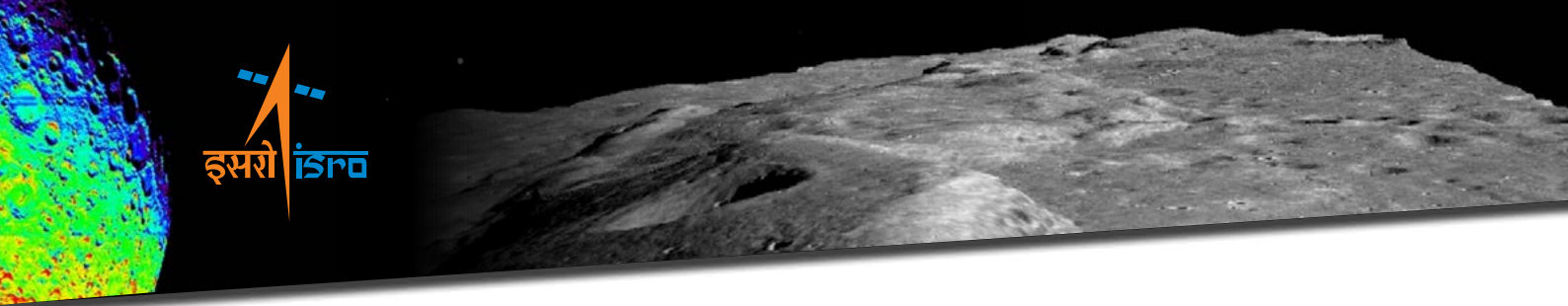


Figure 8.11: (a) 3D perspective view of Dorsa Geikie prepared by draping the TMC-2 orthoimage on DEM. Yellow arrows indicate direction of compressional stress perpendicular to the ridge (b) Orthoimage. 114

Figure 8.12: Figure showing the boulders (white arrows) in the TMC-2 Image acquired on 15 Oct. 2019 115

Figure 8.13: (a) and (b) shows a simple crater (0.326° S, 53.69° E) as seen in TMC-1 and TMC-2 images respectively. (c) and (d) show a simple crater (1.40° S , 53.52° E) in TMC-1 and TMC-2 images respectively. TMC-1 image is acquired at high sun elevation angle of 70.46° where as TMC-2 image acquired at low sun elevation angle of 15.03°. 116

Figure 8.14: Figure showing the plot of Lommel-Seeliger corrected RADF with respect to Phase angles. 117

Figure 8.15: (a) An elongated asymmetric crater and (b) Subsequent impact analysis showing distal and proximal ejecta. 118

Figure 8.16: Figure showing the schematic of a wrinkle ridge. 119

Figure 8.17: Figure showing the topographic cross-section of a wrinkle ridge Dorsa Geiki using TMC-2 DEM. 120

Figure 8.18: (a) Ortho image and (b) 3D perspective view of Dorsa Geikie prepared by draping the TMC-2 orthoimage on DEM. Yellow arrows indicate direction of compressional stress perpendicular to the ridge. 120

Figure 9.1: OHRC image of boulder field around a fresh crater near Boguslawsky E crater. The red circles represent the boulders bases and the lines represent the shadow length. 123

Figure 9.2: Map indicating the spatial distribution of boulders (yellow circles) around the crater. 124

Figure 9.3: Rose diagram showing the spatial distribution of boulders around the crater. 125

Figure 10.1: Time variation in calibrated frequency residual due to Lunar atmosphere on 04 October 2019 (orbit No. 0489). Left panel is showing variation in S-band signal (red curve) and Right panel is showing variations in X-band (multiplied with frequency ratio of S and X band). 128

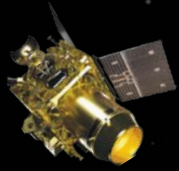


Figure 10.2: Altitude variation in calibrated frequency residual due to Lunar atmosphere. Left panel is showing variation in S-band signal (red curve) and Right panel is showing variations in X-band (multiplied with frequency ratio of S and X band).. 129

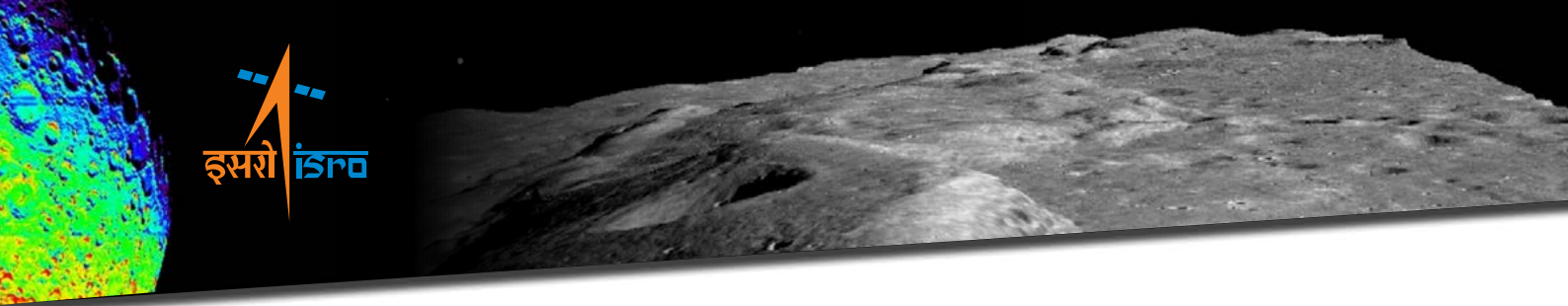
Figure 10.3: Time variation in calibrated frequency residual due to Lunar atmosphere on 27 January 2020 (orbit No. 1894). 129

Figure 10.4: Time variation in calibrated frequency residual due to Lunar atmosphere on 27th January 2020 (orbit No. 1897). 130

Figure 10.5: Time variation in calibrated frequency residual due to Lunar atmosphere on 01st February 2020 (orbit No. 1958). 130

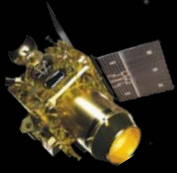
Figure 10.6: Time variation in calibrated frequency residual due to Lunar atmosphere on 01st February 2020 (orbit No. 1960). 131

Figure 10.7: Time variation in calibrated frequency residual due to Lunar atmosphere on 02nd February 2020 (orbit No. 1972). 131



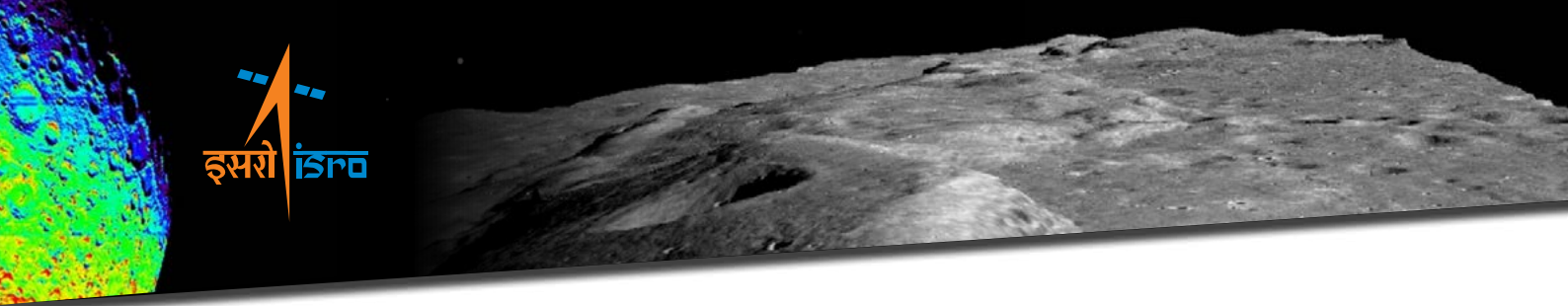
List of Tables

Table 1.2:	Typical Payload Operation plan	9
Table 2.1:	CLASS X-ray Fluorescence Experiment: A comparison with past experiments.	11
Table 2.2:	Specifications of XSM	15
Table 2.3:	Specifications of CHACE-2	24
Table 2.4:	Major Specifications of DFSAR.	29
Table 2.5:	Major specifications of IIRS.	35
Table 2.6:	Specifications of TMC-2 payload.	40
Table 2.7:	Table showing the details of TMC data products.	44
Table 2.8:	OHRC instrument major specifications.. . . .	46
Table 6.1:	Average CPR values in the interior and exterior parts of various craters imaged by LRO-MiniRF (S-band) and CH-2 DFSAR (L-band).. . . .	83

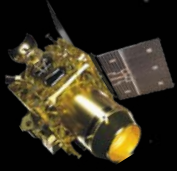


List of Abbreviations

AIEM	Advanced Integral Equation Method
ARF	Ancillary Response Function
ARs	Active Regions
CALDB	Calibration Database
CEM	Channel Electron Multiplier
CHACE-2	CHandra Atmospheric Composition Explorer 2
CLASS	Chandrayaan-2 Large Area Soft X-ray Spectrometer
CP	Compact Polarimetric
CPR	Circular Polarization Ratio
CSFD	Crater Size Frequency Distribution
DEMs	Digital Elevation Models
DFRS	Dual Frequency Radio Science
DFSAR	Dual Frequency Synthetic Aperture Radar
DGA	Dual Gimballed Antenna
DN	Digital Numbers
DPGS	Data Products Generation System
EMG	Electron Multiplier Gain
EMXO	Evacuated Miniaturized Crystal Oscillator
EPO	Earth Parking Orbit
ESPAT	Effective Single Particle Absorption Thickness
FC`	Faraday Cup
FIP	First Ionization Potential
FM	Flight Model
FP	Full-Polarimetry
FP	Full Pol
GSD	Ground Sampling Distance
IBD	Integrated Band Depth
IIRS	Imaging IR Spectrometer
ISSDC	Indian Space Science Data Centre
LACE	Lunar Atmospheric Composition Experiment
LACE	Lunar Atmospheric Composition Experiment
LCROSS	Lunar Crater Observation and Sensing Satellite



LRO	Lunar Reconnaissance Orbiter
LSE	Lunar Centric Solar Ecliptic
MTF	Modulation Transfer Function
NMS	Neutral Mass Spectrometer
OC	Orbiter Craft
OHRC	Orbiter High Resolution Camera
PDS	Planetary Data System
PPS	Payload Planning System
PRF	Pulse Repetition Frequency
PSRs	Permanently Shadowed Regions
QMS	Quadrupole Mass Spectrometer
QMA	Quadrupole Mass Analyzer
QMD	Quadrupole Mass Discrimination
ROI	Region of Interest
ROIs	Region of Interests
SBE	Surface Boundary Exosphere
SCD	Swept Charge Device
SERD	Single Bounce Eigenvalue Relative Difference
SLC	Single-Look Complex
SNR	Signal-to-noise ratio
SPA	South Pole Aitken
SRF	Spectral Re-Distribution Function
SSA	Single Scattering Albedo
SZA	Solar Zenith Angle
TDI	Time Delay Integration
TEC	Total Electron Content
TMC-2	Terrain Mapping Camera -2
VIS-NIR	Visible-Near-Infrared
XRF	X-ray Fluorescence
XSM	Solar X-ray Monitor
XSMDAS	XSM Data Analysis Software
XSPEC	X-ray spectral analysis software



CHAPTER 1

Chandrayaan-2 Mission

1.1 Introduction

Chandrayaan-2, is the second spacecraft in the Indian series of Lunar exploration satellites. It comprises of an Orbiter, Lander named Vikram and Rover named Pragyan to explore the unexplored South Polar region of the Moon.

It was launched on 22nd July 2019 from the Indian Space Port, Sriharikota by GSLV Mk-III. It was a highly complex mission, comprising of many new technological developments. The mission is designed to expand the lunar scientific knowledge through detailed study of topography, mineral identification and distribution, surface chemical composition, mapping, seismology, characterisation of top soil and compositional studies of the tenuous lunar atmosphere, leading to a new understanding of the origin and evolution of the Moon.

1.2 Objectives

1.2.1 Mission Objectives

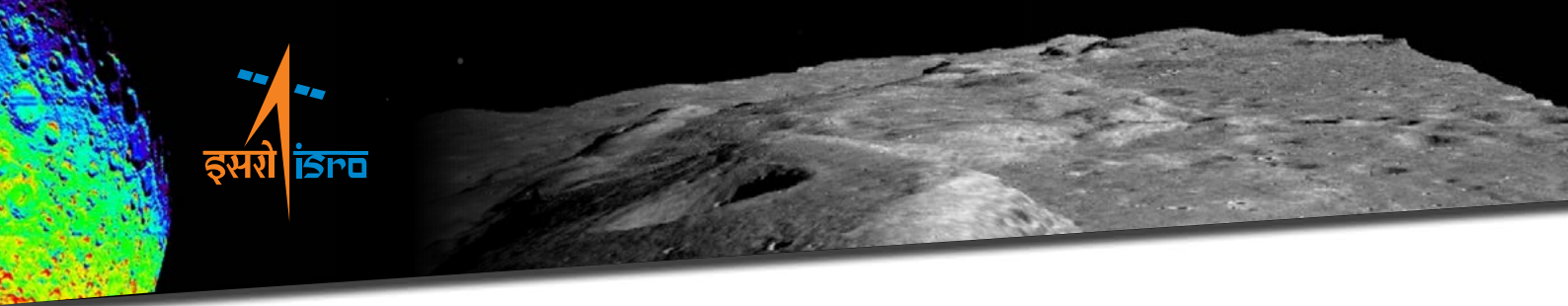
Mission objectives are as follows:

- Expanding the technologies inherited from Chandrayaan-1 spacecraft and “Develop and Demonstrate” newer technologies that will be useful for future planetary missions.
- To design, realize and deploy Lander-Vikram capable of soft landing on a specified lunar site and deploy a Rover to carry out in-situ analysis of elements.
- To carry payloads in the Orbiter-craft that will enhance the scientific objectives of Chandrayaan-1 with improved resolution.

A lunar landing site was selected in the lunar south pole region at about 70 deg Latitude.

1.2.2 Science Objectives

The scientific objective of the mission is to expand the lunar scientific knowledge through detailed study of topography, mineralogy, surface chemistry, regolith characterisation and exospheric molecules leading to a better understanding of the origin and evolution of the Moon.



1.3 Mission Description

1.3.1 Mission Overview

A highly complex mission with many time critical events, was divided into different phases as detailed below.

- **Earth-Centric Phase**

Chandrayaan-2, as a composite module (Lander stacked on the orbiter) with a mass of 3846 kg, was injected into an Earth Parking Orbit (EPO) of 170 km X 40,421 km on 22nd July 2019. After 5 successful orbit maneuvers, it was injected into the Lunar Transfer Trajectory on 14th Aug 2019.

- **Lunar-Transfer Phase**

After 6 days of cruise in the transfer trajectory it was inserted into a lunar orbit on 20th Aug 2019 with firing of thrusters on the orbiter.

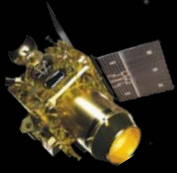
- **Moon-Centric Phase**

In this phase, 4 maneuvers were carried out to reach a lunar orbit of 100km X 100km. Further, the Orbiter and Lander modules were separated as two independent satellites at a pre-defined time on 2nd September 2019. Both remained in the same orbit for about one day. Later, a de-boost maneuver was performed to attain an interim orbit of 100 km x 30 km. Vikram remained in this orbit for ~4 days to verify and validate the performance of all sub-systems followed by a powered descent.

The Orbiter High Resolution Camera (provides the highest resolution of 0.3 m of any lunar mission to date) was used to image the landing site prior to landing (nearly 10 hours before) and the data were downloaded, analyzed and with the help of decision support system, hazards were identified and uplinked to the Vikram Lander, 4 hours prior to landing.

Vikram Lander descent was as planned and normal performance was observed up to an altitude of 2.1 km. Subsequently communication from lander to the ground stations was lost and the lander had a hard landing on the lunar surface.

The Orbiter, placed in its intended orbit around the Moon, will enrich our understanding of the Moon's evolution and mapping of minerals and water molecules in polar regions, using its eight advanced scientific instruments. The Orbiter camera with the highest resolution will provide high resolution images which will be immensely useful to the global scientific



community. The precise launch and optimised mission management has ensured a long life of almost seven years instead of the planned one year.

The mission profile is shown in the Figure 1.1 below:

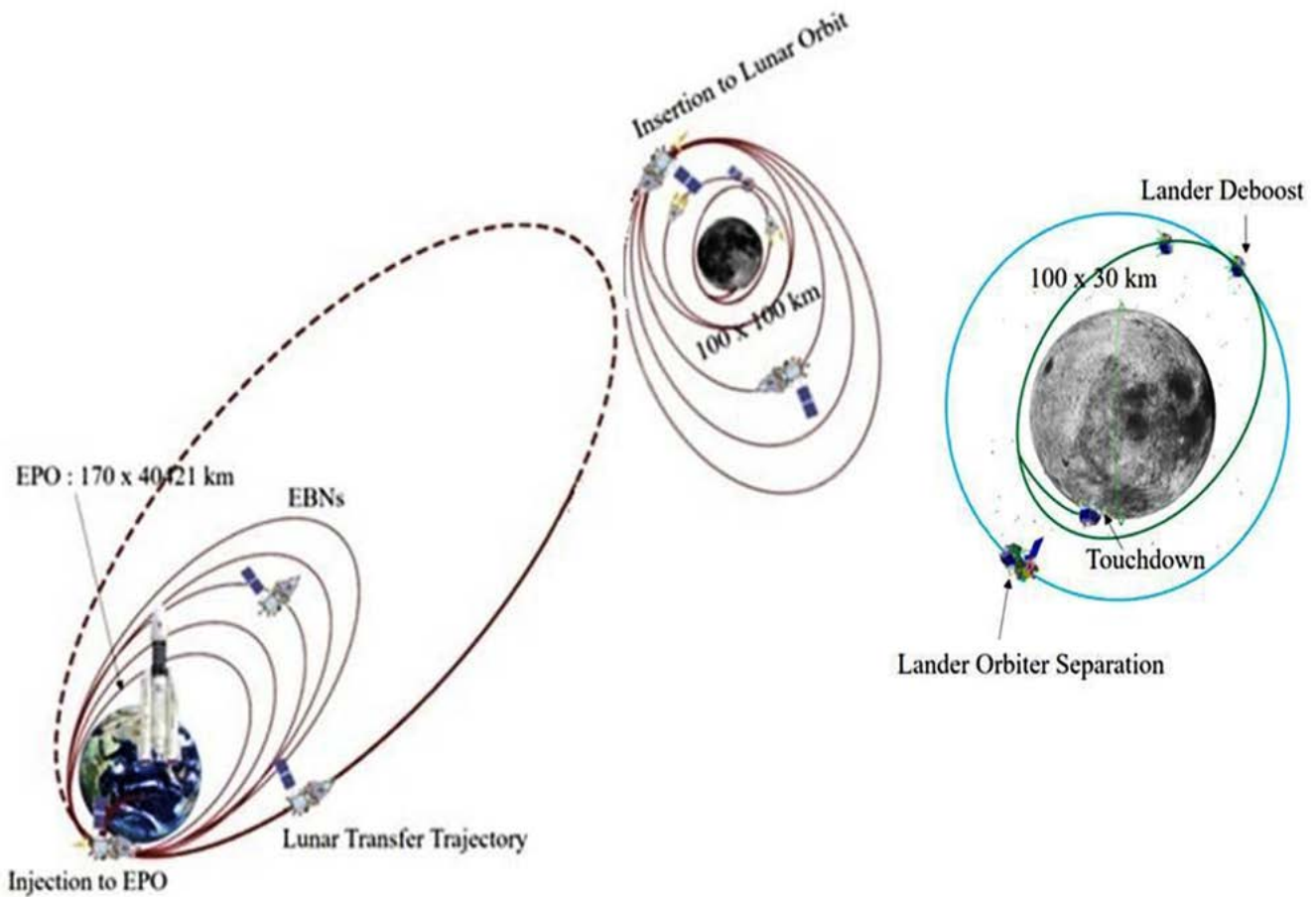


Figure 1.1: Chandrayaan-2 mission profile.

1.3.2 Spacecraft

Chandrayaan-2 spacecraft consists of an Orbiter Craft (OC) and a Vikram Lander, with a six wheeled Pragyan Rover accommodated inside Vikram. The Orbiter and Lander modules are interfaced mechanically by an inter module adapter.

The Chandrayaan-2 Orbiter is shown in [Figure 1.2](#)



Figure 1.2: Chandrayaan-2 Spacecraft.

Orbiter craft carried scientific payloads is shown in Figure 1.3.

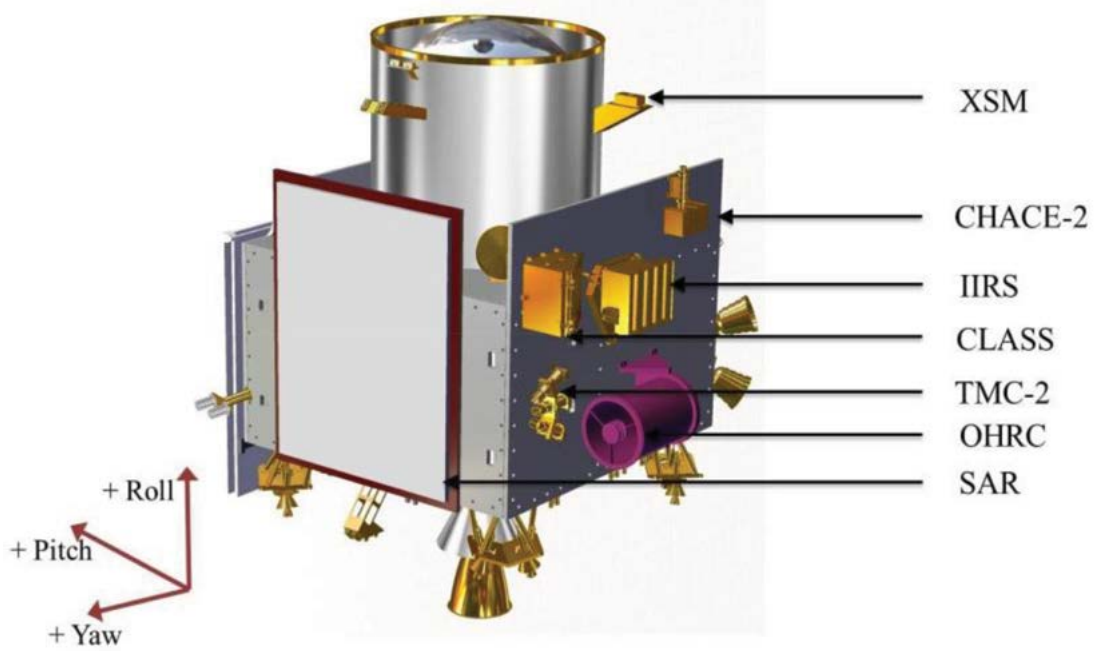
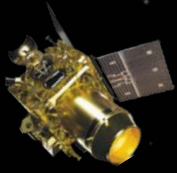


Figure 1.3: Chandrayaan-2 Orbiter craft Payloads.



1.3.3 Orbiter Payloads

There were eight scientific payloads hosted on the orbiter craft. Brief details about payloads are given below:

Chandrayaan-2 Large Area Soft X-ray Spectrometer (CLASS)

CLASS measures the Moon's X-ray Fluorescence (XRF) spectra to examine the presence of major elements such as Magnesium, Aluminium, Silicon, Calcium, Titanium, Iron, and Sodium. The XRF technique will detect these elements by measuring the characteristic X-rays they emit when excited by solar X-ray emission.

Solar X-ray Monitor (XSM)

XSM detects X-rays emitted by the Sun and its corona, measures its intensity, and supports the CLASS payload. It provides the solar X-ray spectrum in the energy range of 1-15 keV incident on the lunar surface. XSM provides high energy resolution and high-cadence measurements (full spectrum every second) as input for analysis of data from CLASS.

CHandra's Atmospheric Compositional Explorer 2 (CHACE 2)

CHACE 2 will expand upon the CHACE experiment on Chandrayaan-1. It is a Quadrupole Mass Spectrometer (QMA) capable of studies of the lunar neutral exosphere in the mass range of 1 to 300 amu with the mass resolution of ~0.5 amu. CHACE 2's primary objective is to carry out an in-situ study of the composition and distribution of the lunar neutral exosphere and its variability.

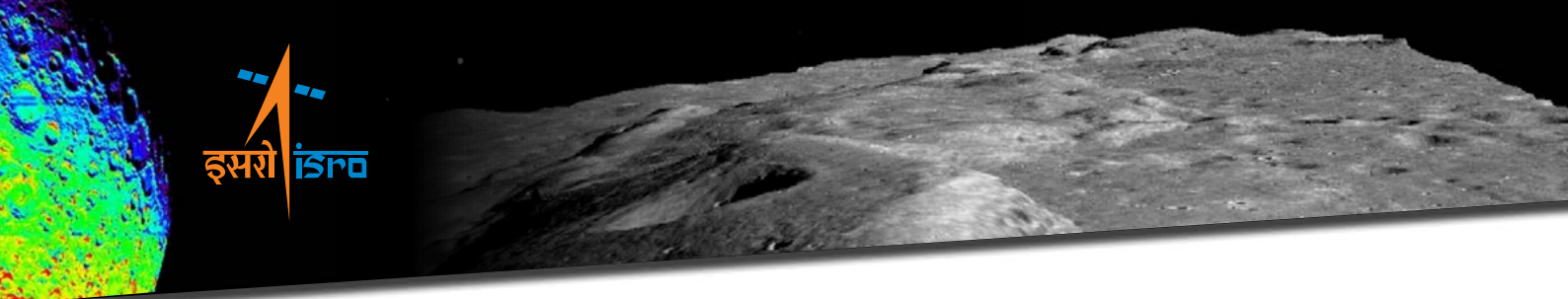
Dual Frequency Synthetic Aperture Radar (DFSAR)

The dual frequency (L and S) SAR will provide enhanced capabilities compared to Chandrayaan-1's S-band mini SAR in areas such as:

- L-band for greater depth of penetration (About 5m — twice that of S-band)
- Circular and full polarimetry — with a range of resolution options (2-75 m) and incident angles (9°-35°) — for understanding scattering properties of permanently shadowed regions

The main scientific objectives of this payload are:

- Quantitative estimation of water-ice in the polar regions
- High-resolution lunar mapping in the polar regions
- Estimation of regolith thickness and its distribution



Imaging Infra-Red Spectrometer (IIRS)

Imaging Infra-Red Spectrometer (IIRS) is a hyper-spectral optical imaging instrument. This instrument maps geomorphology and mineralogy of lunar surface. The mission is intended to cover the Moon surface. The prime objectives of IIRS are:

- Global mineralogical and volatile mapping of the Moon in the spectral range of $\sim 0.8-5.0 \mu\text{m}$ for the first time, at the high resolution of $\sim 20 \text{ nm}$
- Complete characterization of water/hydroxyl feature near $3.0 \mu\text{m}$ for the first time at high spatial ($\sim 80 \text{ m}$) and spectral ($\sim 20 \text{ nm}$) resolutions

IIRS will measure the solar radiation reflected off the Moon's surface in 256 contiguous spectral bands from a 100 km lunar orbit.

Terrain Mapping Camera (TMC 2)

TMC 2 is a miniature version of the Terrain Mapping Camera on Chandrayaan-1 mission. Its primary objective is to map the lunar surface in the panchromatic spectral band (0.5-0.8 microns) with a high spatial resolution of 5 m and a swath of 20 km from 100 km lunar polar orbit. The data collected by TMC 2 will give us clues about the Moon's evolution and help us prepare 3D maps of the lunar surface.

Orbiter High Resolution Camera (OHRC)

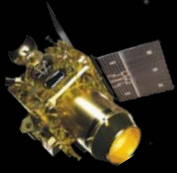
OHRC provides high-resolution images of the landing site which ensure the Lander's safe touchdown by detecting any craters or boulders, prior to separation. The images it captures, taken from two different look angles, serve dual purposes. First, these images are used to generate DEMs (Digital Elevation Models) of the landing site. Second, they are used for scientific research after its initial role in the landing phase. OHRC's images can capture the same area on the lunar surface from two different orbits. The coverage area in this case is of 12 km x 3 km with ground resolution of 0.32 m.

Dual Frequency Radio Science (DFRS) Experiment

To study the temporal evolution of electron density in the Lunar ionosphere. Two coherent signals at X (8496 MHz), and S (2240 MHz) band are transmitted simultaneously from satellite, and received at ground-based receivers.

2 Payload Operations

The Orbiter is in a 100km X 100km polar orbit around the Moon. The angle between sun's location, lunar region of study and the payload on the Orbiter (sun aspect angle) varies widely giving rise to extreme sun illumination conditions. Moreover, some are optical/IR payloads like TMC-2, IIRS and OHRC requiring certain illumination conditions for optimal operation of payload. Hence, payload operations are season based and classified as follows:



- **Dawn-Dusk Season:** Angle b/w sun and orbital plane is more than 30 deg. The primary payload (nominal) is the Dual Frequency SAR.
- **Noon-Midnight Season:** Angle b/w sun and orbital plane is less than 30 deg. The primary payload (nominal) is TMC 2 and IIRS.
- CLASS, CHACE 2 and XSM are all operated during all seasons.
- DFRS is operated whenever the constraints are met (i.e. S-band antenna looking at ground station and X-band antenna will be steered to the ground station). It is planned once a month. During DFRS operation, other payloads are not operated.
- OHRC operations are done based on feasibility and user requirements in campaign mode

The attitude followed is also different, based on the season to ensure maximum power generation. The spacecraft attitude followed during dawn-dusk season is called AD1 and attitude during noon-midnight season is AD2 (orbit reference frame attitude). While in AD2, yaw flip is needed to ensure sun on solar panel side and also provide better thermal environment. Thus twice a year, a yaw flip is required. The figure below summarizes the season-based payload operation:

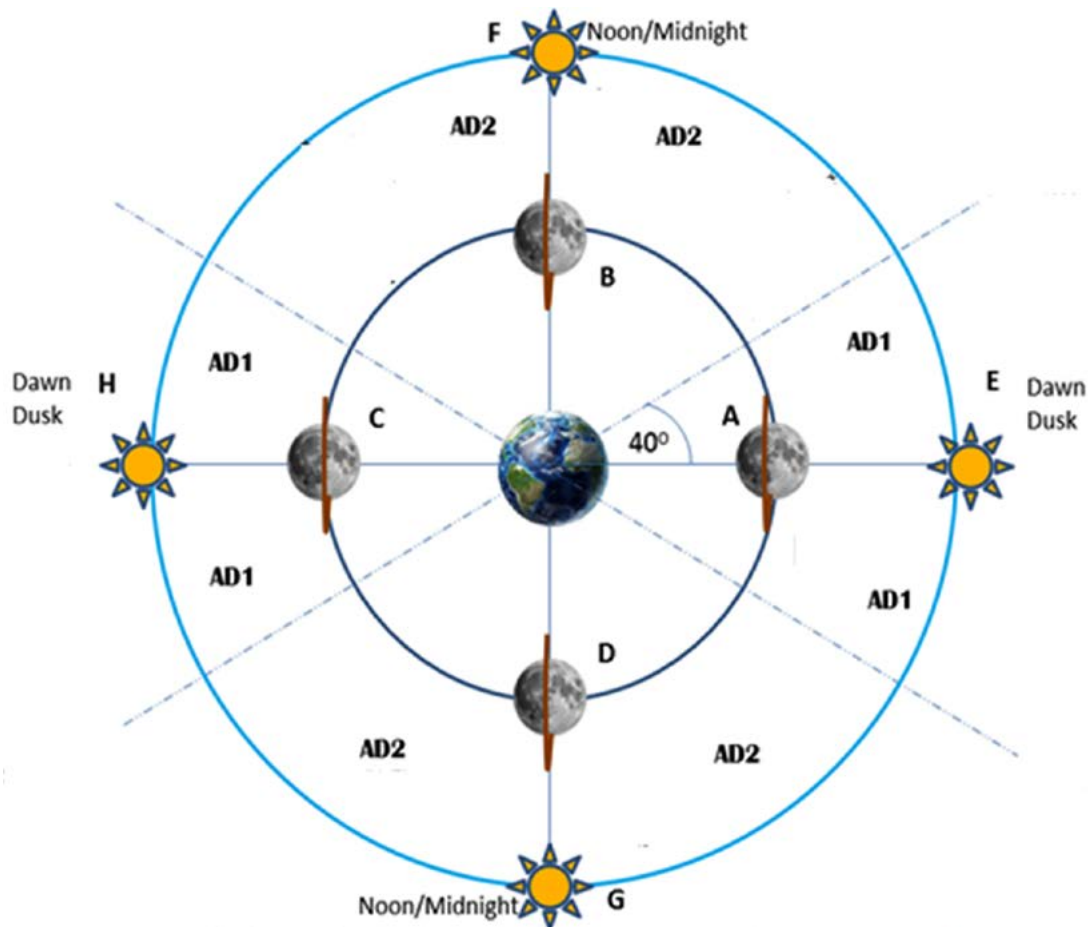
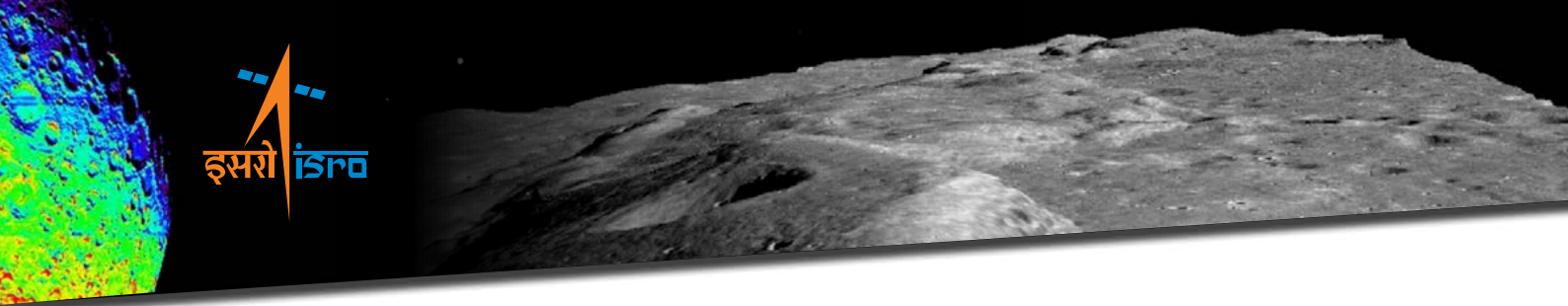


Figure 1.4: Orbiter Season Definition.



The nominal operations durations for different payloads are as follows:

- OHRC : 10 sec
- XSM : Continuously ON
- CLASS : During sunlit, continuously ON 10 days around full Moon.
- CHACE-2 : 130 min-260 min/twice a day 6 orbits apart
- SAR : 2 min
- TMC-2 : 10 min
- IIRS : 12 min(10 min of Imaging)
- DFRS : 6 min

The payload data is recorded onto onboard SSR of 40 Gb capacity which is partitioned into channels. The figure below shows the streamline of Payload data storage:

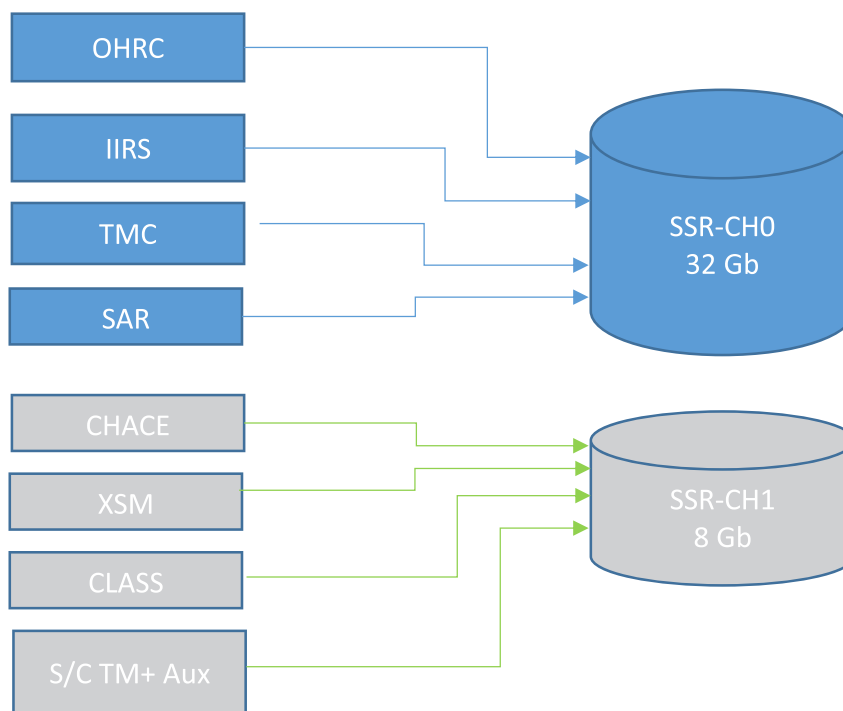


Figure 1.5: Payload Data Storage Streamline.

The data stored onboard is transmitted through X-band using DGA (Dual Gimballed Antenna) at a rate of 8.4 Mbps over IDSN stations and 4.2 Mbps over other stations network. The DGA is steered to the required position by onboard look vector generation algorithm based on the station index. The spacecraft is steered to the imaging attitude from the nominal attitude based on the requirement in each payload session. All payload operations and data download operations are automated and triggered onboard using macros and onboard-timer based commands. The user request handling, nominal payload operations planning and scheduling and translation of the plan to spacecraft commands and handled by the

Payload Planning System (PPS) software. The space and ground segment chain are shown below:

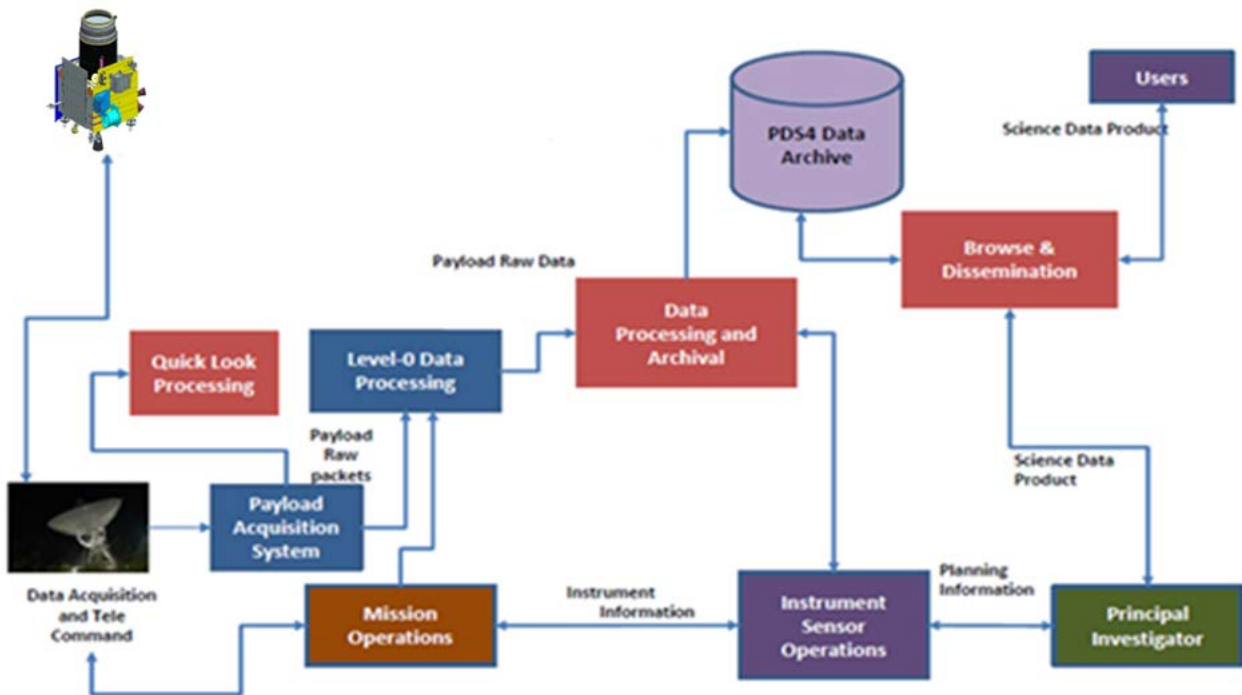


Figure 1.6 : Space and Ground Segment chain.

The typical operation plan during different scenarios is shown below:

Table 1.2: Typical Payload Operation plan

Plan	Attributes	Imaging payloads	Visibility Time / Playback(PB) Time	Imaging to PB ratio
Plan-A	NM + Edge-On+ Near Side SunLit	TMC+IIRS(10 mins) XSM+CLASS(10 mins) + CHACE(Continuous)	72 mins/ 60 mins	~ 1:6
Plan-B	NM + Edge-On+ Far Side SunLit	TMC+IIRS(10 mins) XSM+CLASS(20 mins) + CHACE(Continuous)	72 mins/ 65 mins	~1:6
Plan-C	NM + Face-On	TMC+IIRS(10 mins) XSM+CLASS(20 mins) + CHACE(Continuous) + SAR(3 mins Low Mode)	118 mins/80 mins	~1:6
Plan-D	DD + Face-On	XSM+Class(Continuous) SAR – L3 Mode(5mins) Or SAR-S3 mode(7 mins)	118mins/105 mins	~ 1:18 (SAR L3)
Plan-E	DD + Edge-On	XSM+Class(Continuous) SAR – L3 Mode(2.5 mins) Or SAR-S3 mode(3.5 mins)	72 mins/ 60 mins	~ 1:18 (SAR L3)

Chandrayaan-2 Orbiter Payloads

The Chandrayaan-2 Orbiter has eight scientific payloads to fulfill the scientific objectives. This chapter provides the description of these scientific payloads, science objectives and instrument specifications.

2.1 Chandrayaan-2 Large Area Soft X-ray Spectrometer (CLASS) Payload

Chandrayaan-2 Large Area Soft X-ray Spectrometer (CLASS) is an X-ray Fluorescence (XRF) experiment onboard the Chandrayaan-2 Orbiter. The primary objective of CLASS is mapping of the major refractory elements on the lunar surface. CLASS consists of sixteen Swept Charge Device (SCD) detectors, a variant of X-ray CCDs flown for the second time in space. The instrument is performing highly well in orbit since September 2019. CLASS operates continuously in the sunlit side of the orbit and has the largest coverage in X-rays ever done. During times of high solar activity, elemental maps of the highest spatial resolution are possible for some areas on the Moon.

X-ray fluorescence spectroscopy is based on identification of characteristic photons emitted from atoms in a material, excited by an external X-ray photon source. The photon line intensity is proportional to the number of those atoms or in other words, the abundance of the element from which they are emitted. This method is independent of the minerals that host the elements which enables a direct unambiguous detection of elements and their further quantification. The signal is also not affected by the lunar surface environment or by space weathering as in UV-Vis-NIR spectroscopy. For airless bodies like the Moon, XRF is triggered by the X-rays emitted by the solar corona that are incident on the lunar surface. XSM onboard Chandrayaan-2 orbiter provides a simultaneous measurement of the solar spectrum for deriving elemental abundance from CLASS data.

XRF experiments to the Moon in the past ([Table 2.1](#)) have suffered from limitations. CLASS is designed as a large area instrument, with low noise electronics, adequate radiation protection and requisite thermal environment demanded by the configuration.

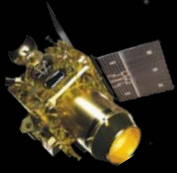


Table 2.1: CLASS X-ray Fluorescence Experiment: A comparison with past experiments

	Luna-10	Apollo 15&16	SMART-1 DCIXS	Kaguya XRS	Chang'e 1&2	Ch1-C1XS	Ch2-CLASS
Area	1.5 cm ²	75 cm ²	24 cm ²	100 cm ²	4 cm ²	24 cm ²	64 cm ²
Detector	GMC	GPC	SCD	X-ray CCD	Si-PIN	SCD	SCD
Detection reported	Mg,Al,Si	Mg,Al,Si	Mg,Al,Si, Ca,Ti,Fe	-	Mg,Al,Si, Ca,Ti,Fe	Na, Mg,Al,Si, Ca,Ti,Fe	Na, O, Mg, Al,Si,Ca,Ti,Cr, Mn, Fe
Best spatial resolution	-	100 km	42 km	20 km	73 x 200 km	25 km	12.5 km

2.1.1 CLASS Instrument

CLASS consists of 16 swept charge devices (SCDs) arranged as four ‘quads’ (Figure 2.1). It is a non-imaging spectrometer with gold coated copper collimators defining the field of view of each SCD as 7 deg X 7 deg Full Width at Half Maximum (FWHM). This translates to a 12.5 km X 12.5 km footprint at the 100 km altitude of the spacecraft. Aluminium door protected the devices from the high energy particle flux in the radiation belts en-route to the Moon. The door also housed radioactive isotopes with a Titanium foil for calibration onboard.

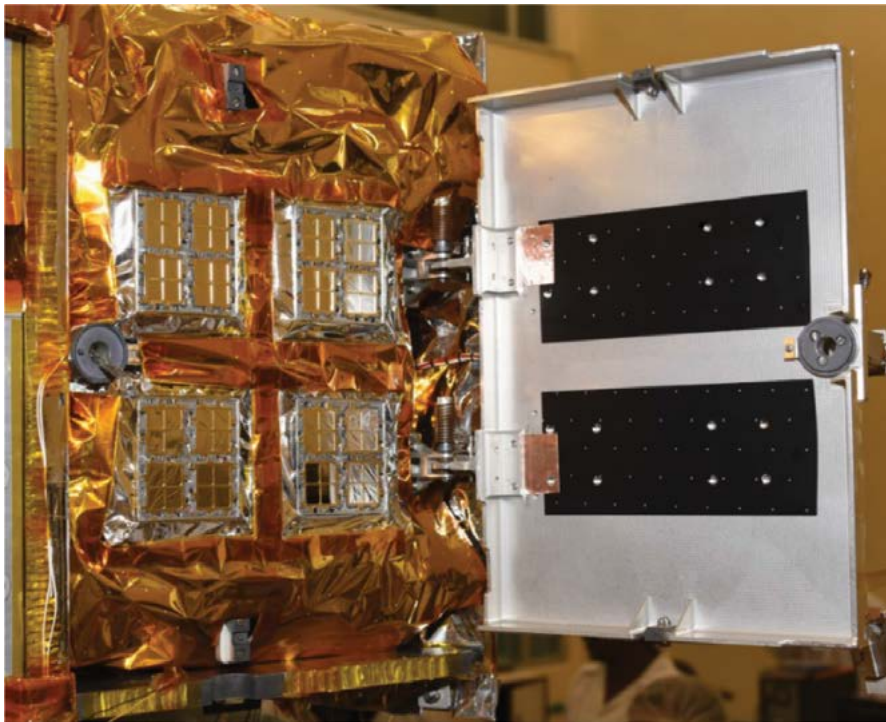
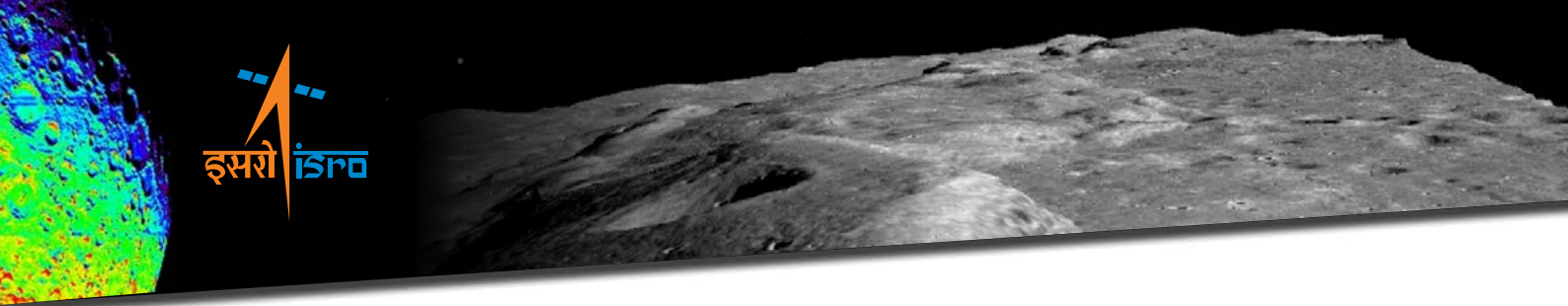


Figure 2.1: CLASS Flight Instrument. The 16 X-ray detectors are arranged as four ‘quads’. The door was closed enroute to the Moon and protected the X-ray detectors from radiation damage.



2.1.2 Calibration

In order to determine elemental abundances, the X-ray line flux of elements of interest from the lunar surface has to be accurately measured. The instrument was calibrated on ground using known XRF energy lines from lunar simulant JSC-1A at all the expected range of temperatures. Further the spectral re-distribution function (SRF) of the swept charge device was modeled based on previously constructed charge transport model for the SCD on Chandrayaan-1 C1XS (Athiray et al, 2015). [Figure 2.2](#) shows the distribution of events arising from different regions of the SCD for a mono-energetic beam of photons. The response of the instrument is expressed as a matrix R where each element R_{ij} is the probability that a photon of energy 'i' is registered in channel 'j'. The response matrix is used to de-convolve the incident spectrum from an observation. The effective area of CLASS is derived further with measurements of the collimator blocking fraction and Aluminum filter transmission.

CLASS is well calibrated and instrument response files compatible with standard X-ray spectral analysis software (XSPEC) is generated and disseminated along with the spectral data sets through the PRADAN portal at ISSDC.

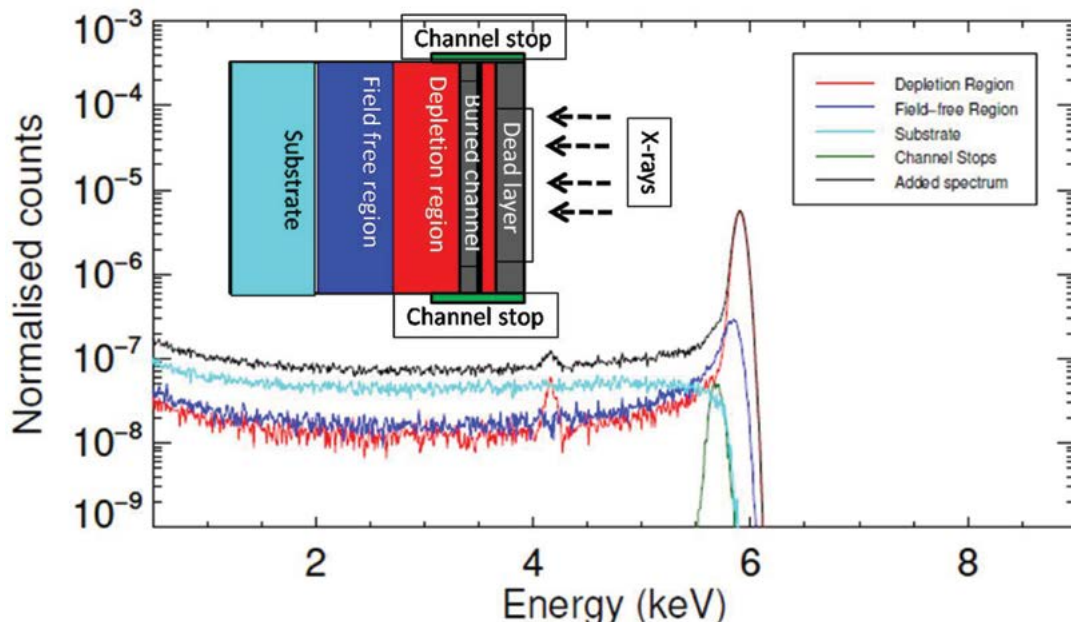
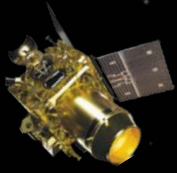


Figure 2.2: Distribution of events in the energy space for the CLASS X-ray detector (SCD) for a beam of mono-energetic photons at 5.9 keV interacting at different regions of the device across the depth (Netra et al., 2021).

2.1.3 Onboard Operations and Performance

CLASS is operating continuously since 11th September 2019. [Figure 2.3](#) shows a comparison of the spectra from the onboard radioactive source taken on ground and in-flight. The additional continuum especially



at higher energies arises from the particles in the lunar environment in-flight which is expected. At the beginning of the mission, the spectral performance of the instrument is almost identical to as obtained in the laboratory. Subsequently, the performance of CLASS is monitored and the spectral quality remains well within the requirements for scientific analysis. The temperatures encountered are less than -20°C across all seasons ensuring high quality spectra throughout.

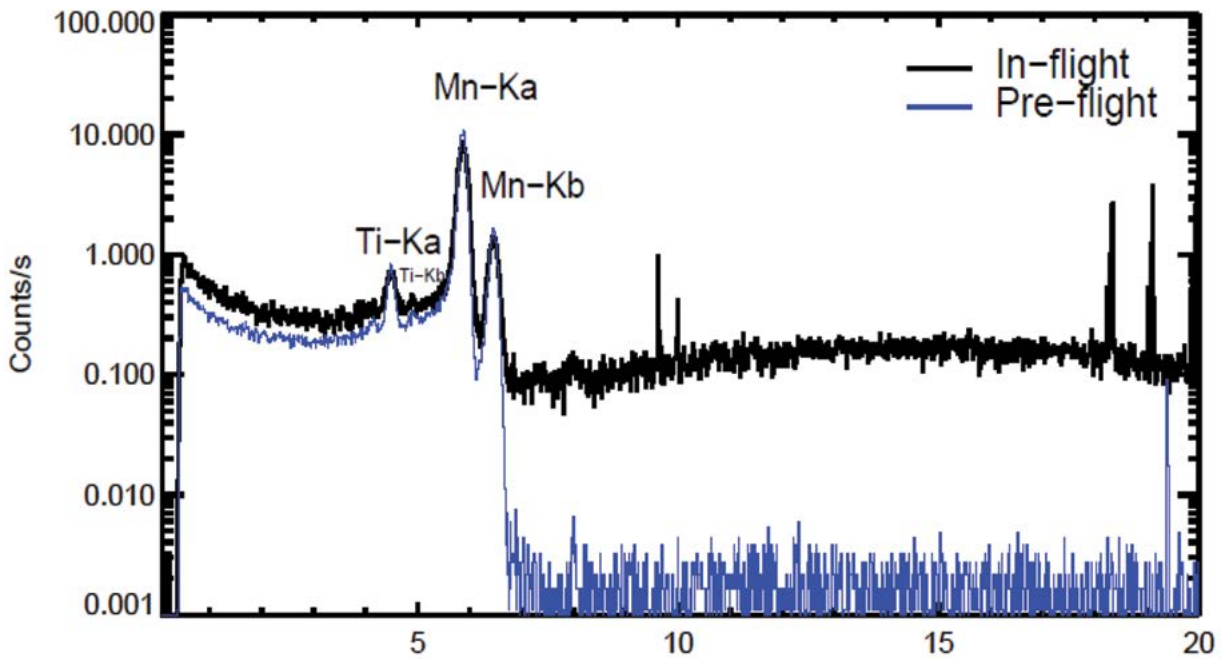


Figure 2.3: ^{55}Fe on-board source spectrum observed in CLASS pre-flight and in-flight. The individual SCD spectra are co-added with a temperature dependent gain correction. The background increased in-flight due to the ambient particles in the orbit (Netra et al, 2021).

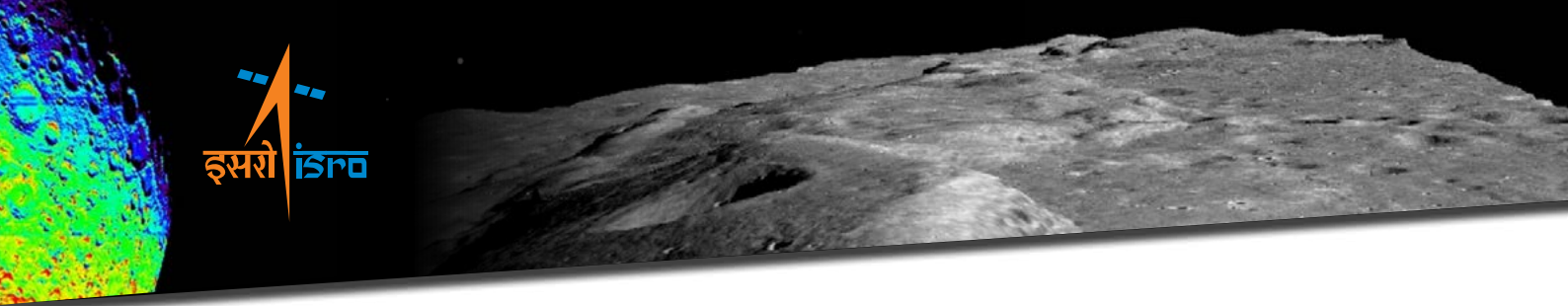
Onboard calibration was done using the radioactive sources that illuminate each of the 16 SCDs. The temperature was actively controlled during this to verify the spectral resolution and gain of all 16 SCDs as a function of temperature.

CLASS operates on the sunlit side of the orbit and in addition on the night side for six days centered around the full Moon to cover the entire geotail. Thus during Dawn- Dusk season, there is continuous operation while in Noon-Midnight CLASS operates half the time period of the orbit. During the geotail passes, in all seasons, CLASS operates continuously thus covering the night side of the orbit.

The spectral data from October 2019 to Jan 2020 is made available to the public through PRADAN portal at ISSDC (<https://pradan.issdc.gov.in/pradan>).

2.1.4 Analysis Methodology

The primary aim of CLASS is to derive elemental maps from the observed XRF spectra. The data is in the form of time tagged events from each of the 16 SCDs. Temperature dependent



correction is applied and co-added to a combined spectrum. A unique method refined from Chandrayaan-1 C1XS is applied to determine elemental abundances. This involves modeling the solar spectrum obtained during the same time. Chandrayaan-2 XSM L1 data is used for this purpose. The solar spectrum is modeled as a single temperature coronal plasma with variable coronal abundances. There are long periods especially in the Noon-Midnight season when Sun is not in the FOV of XSM. For those cases, the broad band flux ratios are used from GOES-16 X-ray Monitor to derive the solar spectral parameters.

The algorithm to derive elemental abundances was developed for CH1-C1XS (Athiray et al, 2013a, 2013b) and verified with laboratory experiments. This is implemented as a python based local model in XSPEC (standard X-ray spectral analysis package) which allows to fit the XRF spectra with a range in compositions and arrive at the best fit using a chi-square minimization. The lunar XRF model takes into account the geometry of observation and matrix effects and use the solar spectrum as input. It also includes a component scattered from the lunar surface which is calculated using the solar spectrum.

2.2 Solar X-ray Monitor (XSM)

The Solar X-ray Monitor (XSM) is an X-ray spectrometer on-board Chandrayaan-2 orbiter. It is essential to have simultaneous measurements of the incident X-rays from the Sun, provided by XSM, for the quantitative interpretation of the CLASS observations.

The XSM is operating in the lunar orbit from 12th September 2019. The XSM provides disk integrated solar spectra in the energy range of 1 – 15 keV with a spectral resolution of better than 180 eV at 5.9 keV, which is the best available so far among similar instruments that carried out such measurements. The XSM also offers the highest time cadence for such instruments: full spectrum every second and light curves in three energy bands every 100 ms. The unique design features of the XSM allows observations over a wide dynamic range of X-ray fluxes from the quiet Sun to X-class flares. Presently, the XSM is the only instrument operational providing soft X-ray spectral measurements of the Sun over a broad energy range.

2.2.1 XSM Instrument Description

Major specifications of the XSM instrument are given in [Table 2.2](#). [Figure 2.4](#) & [Figure 2.5](#) show the photograph of the XSM instrument which is configured as two packages: (i) a sensor package that houses the detector, front-end electronics, and a filter wheel mechanism; (ii) a processing electronics package that houses the FPGA based data acquisition system, power electronics, and spacecraft interfaces. The instrument is fix-mounted on the



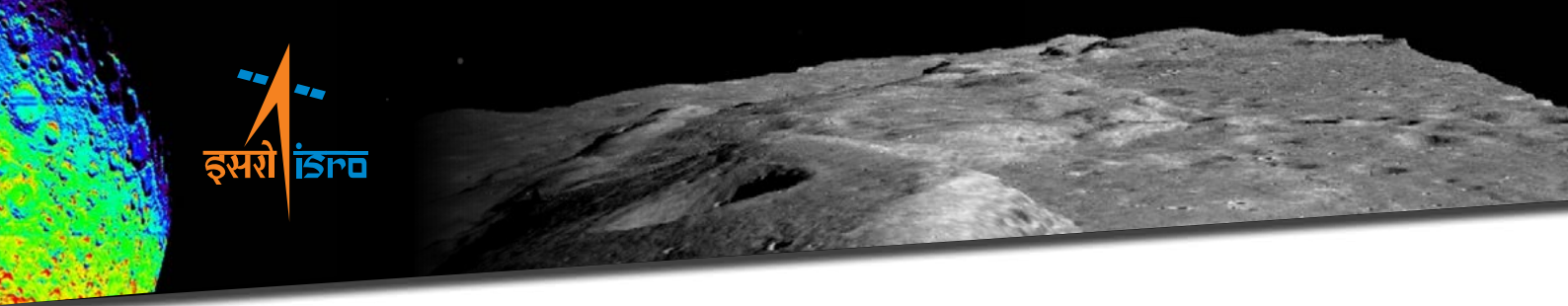
Chandrayaan-2 orbiter such that the spacecraft structures do not obstruct the instrument field of view (FOV).

The spectral performance of the detector, defined by the energy resolution, depends on its temperature. In order to achieve the targeted resolution of better than 180 eV, the SDD temperature needs to be maintained at $\sim -35^{\circ}\text{C}$. Since the ambient temperature during the lunar orbit is expected to vary over a wide range between -30°C to $+20^{\circ}\text{C}$, the XSM employs a closed-loop temperature control using the TEC, that is part of the detector module, to maintain the detector at -35°C .

It is well known that the solar X-ray intensities vary over several orders of magnitude between quiet and active phases of a solar cycle. Hence, the XSM includes a filter wheel mechanism mounted on the top cover of the sensor package.

Table 2.2: Specifications of XSM

Parameter	Specification
Energy Range	1 – 15 keV (up to \sim M5 class) 2 – 15 keV (above \sim M5 class)
Energy Resolution	< 180 eV @ 5.9 keV
Time cadence	1 second
Aperture area	0.367 mm ²
Field of view	± 40 degree
Filter wheel mechanism properties	
Positions	3 (Open, Be-filter, Cal)
Filter wheel movement modes	Automated and Manual
Be-filter thickness	250 μm
Automated Be-filter movement threshold	$80,000$ counts s^{-1} (\sim M5 class)
Calibration source	Fe-55 with Ti foil
Detector properties	
Type	Silicon Drift Detector (SDD)
Area	30 mm ²
Thickness	450 μm
Entrance Window	8 μm thick Be
Operating temperature	-35°C
Mass	1.35 kg
Power	6 W



As the spacecraft attitude configuration is dictated by the requirement of observation of the Moon by other instruments and other mission operation constraints, the Sun's position varies with respect to the bore-sight of the XSM. Hence, in order to maximize the duration of observation of the Sun, the XSM is designed with a large field of view of 40° half cone angle.

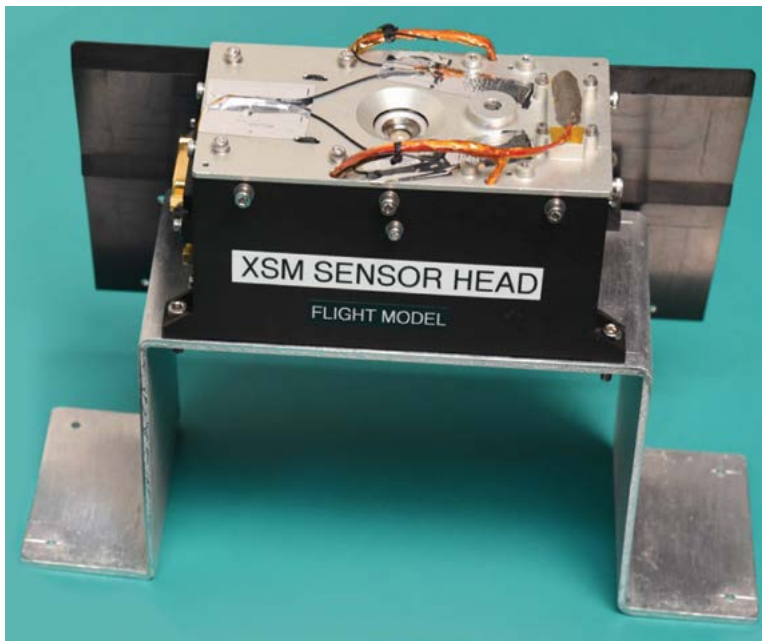


Figure 2.4: A photograph of the Chandrayaan-2 XSM instrument packages: (i) Sensor package that houses the detector, front-end electronics, and filter wheel mechanism. Mithun et al. [2021b].

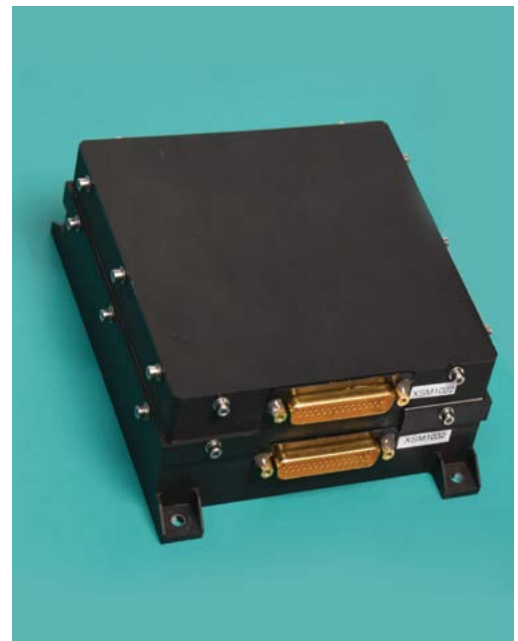
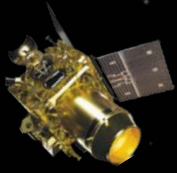


Figure 2.5: A photograph of the Chandrayaan-2 XSM instrument packages: (ii) Processing electronics package that houses the FPGA based data acquisition system, power electronics, and spacecraft interfaces. Mithun et al. [2021b].

2.2.2. Ground Calibration

Calibration primarily involves accurate determination of the response matrix. The XSM records the number of events detected (counts) every second in each ADC channel, also known as the Pulse Height Analysis (PHA) channel. Gain parameters determine the mapping of the PHA channel to the nominal energy of incident photons. As the gain usually varies with observing conditions, this mapping does not remain constant. To infer the incident photon spectrum from XSM observations, gain parameters for the conversion of PHA spectrum to PI spectrum, the redistribution matrix,



and the ancillary response function are determined during ground calibration. The spectral redistribution function for the SDD used in the XSM is modeled using observed mono-energetic line spectra, and the effective area as a function of energy and angle is computed from experimental data and appropriate detector module parameters.

Gain Calibration

The relation between the peak channel recorded by a spectrometer for mono-energetic lines and the incident photon energies provides the gain parameters. If this relation is linear, only two parameters are sufficient to describe it: gain and offset. These parameters are typically estimated by acquiring the spectra of sources with mono-energetic lines at known energies and obtaining the respective peak channel positions by fitting the observed spectra.

The spectral resolution, defined by the full width at half maximum (FWHM) of the Mn-K α line at 5.89 keV, is measured to be ≈ 175 eV. However, these measurements are restricted to only a narrow energy range of 4.5 – 6.5 keV compared to the 1 – 15 keV energy range of the XSM. Hence, in order to verify the linearity over the entire energy range and to model the response function, experiments were carried out with the XSM at the BL-03 [Modi et al., 2019] and BL-16 [Tiwari et al., 2013] X-ray beamlines of the Indus-2 synchrotron facility at the Raja Ramana Center for Advanced Technology (RRCAT), Indore, India.

Spectral Redistribution Function

The spectral redistribution function forms a major component of the response matrix of the detector system and is hence required to be determined accurately for inferring the incident photon spectrum from the observed spectrum.

In order to characterize the spectral response of the SDD, spectra of mono-energetic beams acquired with the XSM at the RRCAT facility were utilized. [Figure 2.6](#) shows three such XSM spectra for three different incident photon energies, and it can be seen that the spectra of mono-energetic lines show all the expected features.

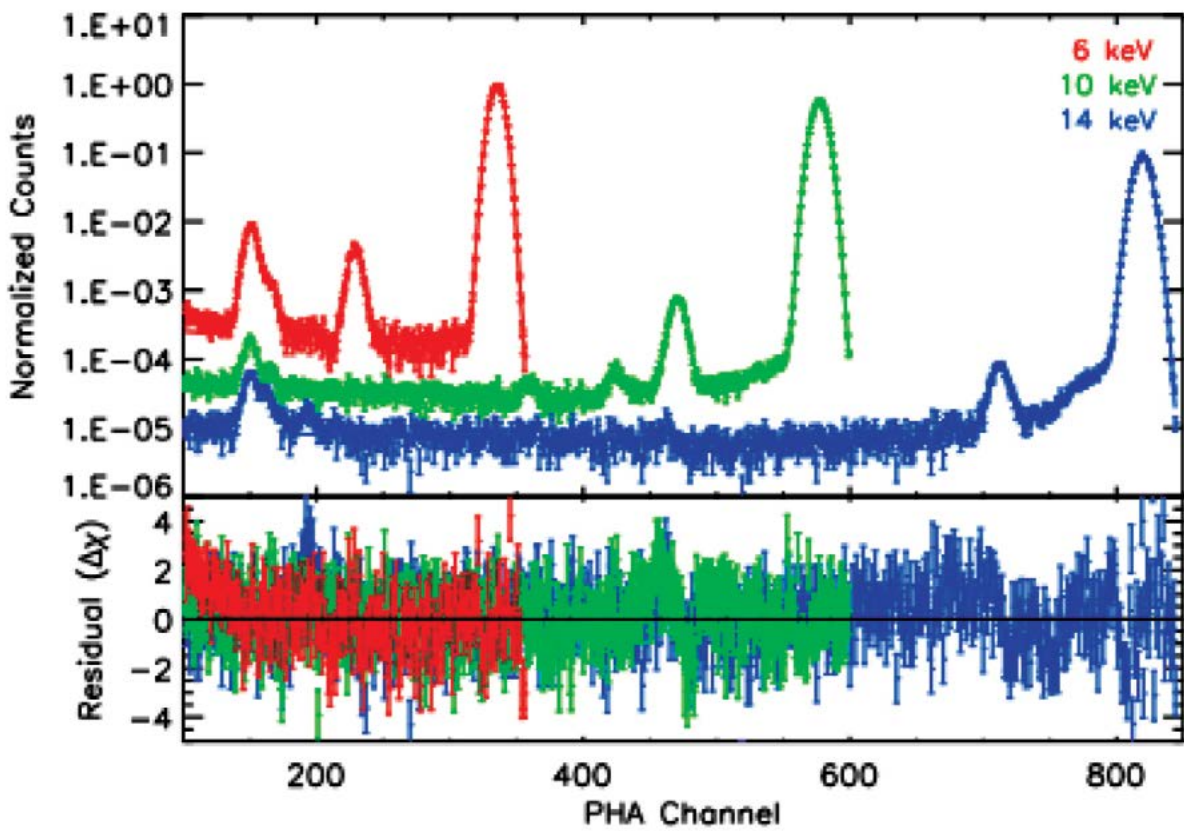


Figure 2.6: XSM spectra of mono-energetic X-ray beams at three energies. Note that for better clarity the spectra are normalized to different peak intensities. Best fit spectral response models are overplotted with solid lines, and the bottom panel shows the residuals in terms of sigma with error bars of size one sigma. Mithun et al. [2021b].

Spectra for three different incident photon energies, and it can be seen that the spectra of mono-energetic lines show all the expected features.

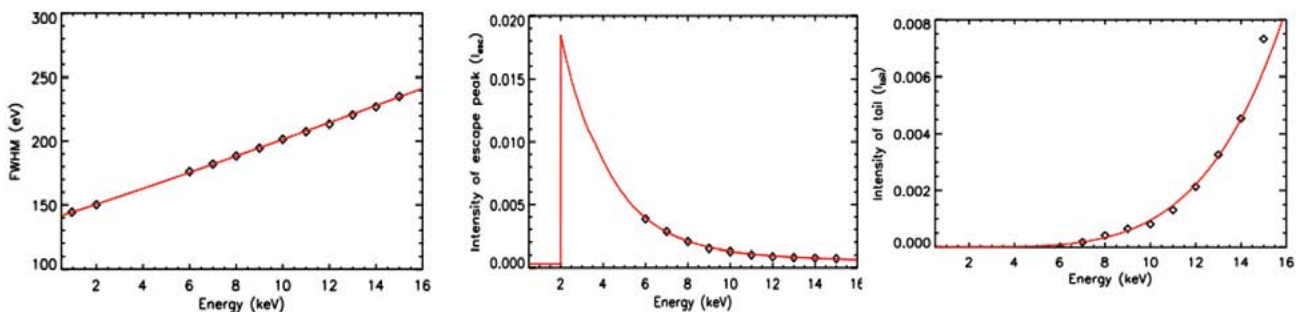
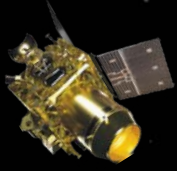


Figure 2.7: Spectral response model parameters obtained from fitting mono-energetic spectra: FWHM (top left), the relative intensity of the escape peak (top right), and intensity of the tail component (bottom) are plotted as a function of energy. Statistical errors are smaller than the symbol size. The red solid lines show the best fit models, in the case of FWHM and intensity of the tail component, respectively, whereas for the escape peak intensity (top right), the line represents the result from Geant4 simulations. Figure taken from Mithun et al. [2021b].



The observed spectra for all energies were fitted with the model. Best fit models are overplotted on the observed spectra shown in [Figure 2.6](#), and residuals plotted in the bottom panel of the figure show that the model describes the observed spectra very well.

In order to derive the spectral response of the instrument over the full energy range of 1 – 15 keV, the model parameters are required as a function of energy. [Figure 2.7](#) shows the three free parameters of the model plotted as a function of incident photon energy. The second panel shows the relative intensity of the escape peak as obtained from the spectral fits. As escape peaks are present only when incident photon energies are higher than the K-edge energy of Si, this parameter is not applicable for the monochromatic line at 1 keV. Taking different parameters into consideration, the observed mono-energetic spectral redistribution of the XSM detector has been modelled with an empirical function, which is then used to generate the redistribution matrix for the XSM.

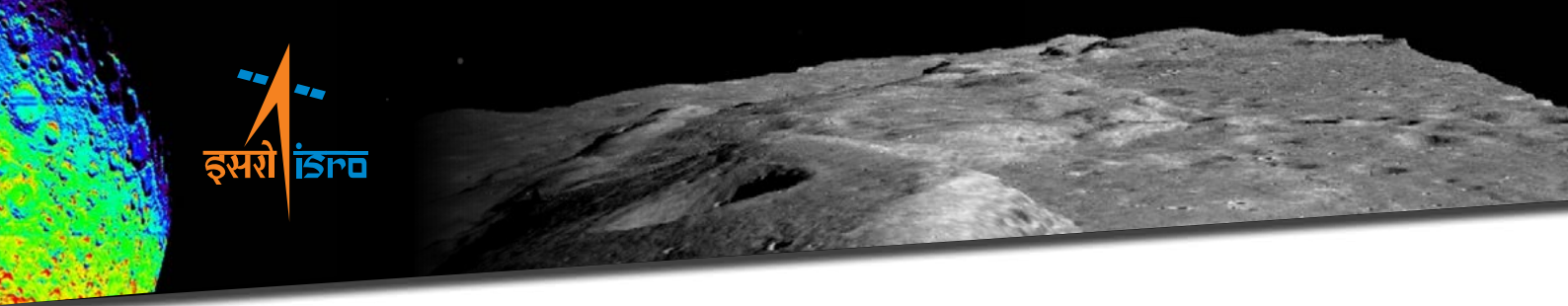
Ancillary Response Function

The ancillary response function (ARF) or the effective area of the XSM includes geometric area, collimator response, and detection efficiency and transmission of the entrance window as a function of energy. As the angle subtended by the Sun with respect to the axis of the XSM is expected to vary, the effective area needs to be estimated as a function of incidence angle.

The efficacy of the aluminum collimator, which is coated with 50 μm of silver on both sides, to block the X-rays from outside the FOV was also verified experimentally. Spectra without the collimator directly exposing the detector was also recorded, and from the ratio of both these spectra, the transmission of the collimator was obtained as a function of energy and is shown in the right panel of [Figure 2.8](#). This demonstrates that the collimator efficiently blocks X-rays over the energy range of the XSM as required.

2.2.3 XSM Observations and Analysis

During the nominal operation phase, the attitude of the Chandrayaan-2 spacecraft is such that the yaw direction always points to the Moon. The attitude of the spacecraft (other than yaw axis) is maintained according to the orbital seasons to optimize power generation. During the three months of D-D season surrounding the day when the orbital plane is perpendicular to the Moon- Sun vector, the spacecraft attitude is such that Sun is maintained in a yaw-roll plane. In this season, continuous observations of the Sun with



XSM are possible. In the N-M season covering three months around the day when the Sun vector lies in the orbital plane of the spacecraft, the spacecraft attitude follows the orbital reference frame, and the Sun does not remain within the FOV of XSM for the entire orbit. Nominally, the XSM is expected to operate at all times when the Sun is within the FOV of the instrument.

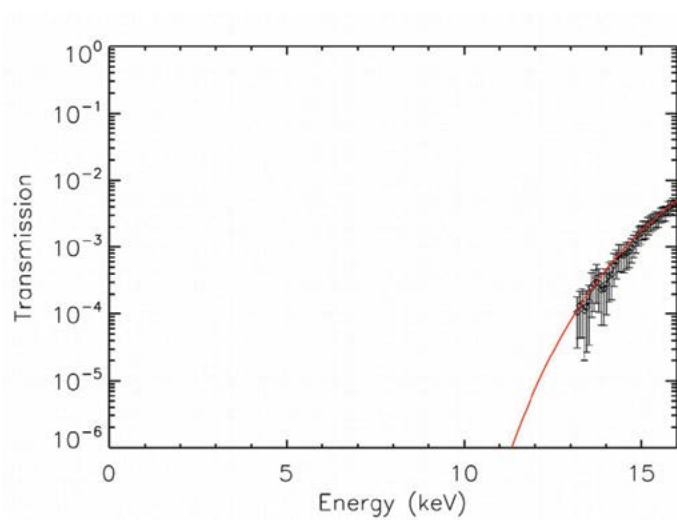
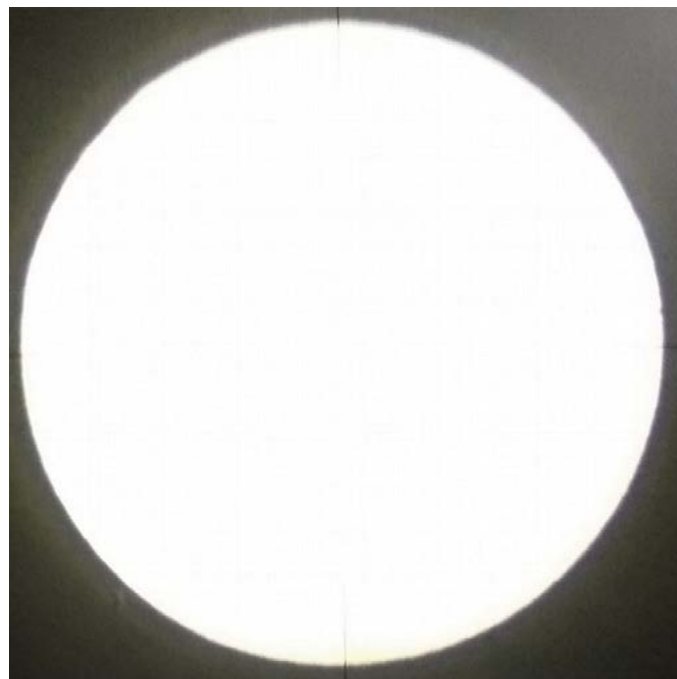


Figure 2.8: Top: Photograph showing the aperture of the XSM collimator. bottom: Transmission of the silver-coated ($50 \mu\text{m}$ on both sides) collimator obtained as the ratio of X-ray gun spectrum recorded with a specially made collimator. The red solid line shows the expected transmission of the collimator. Figure taken from Mithun et al. [2021b].

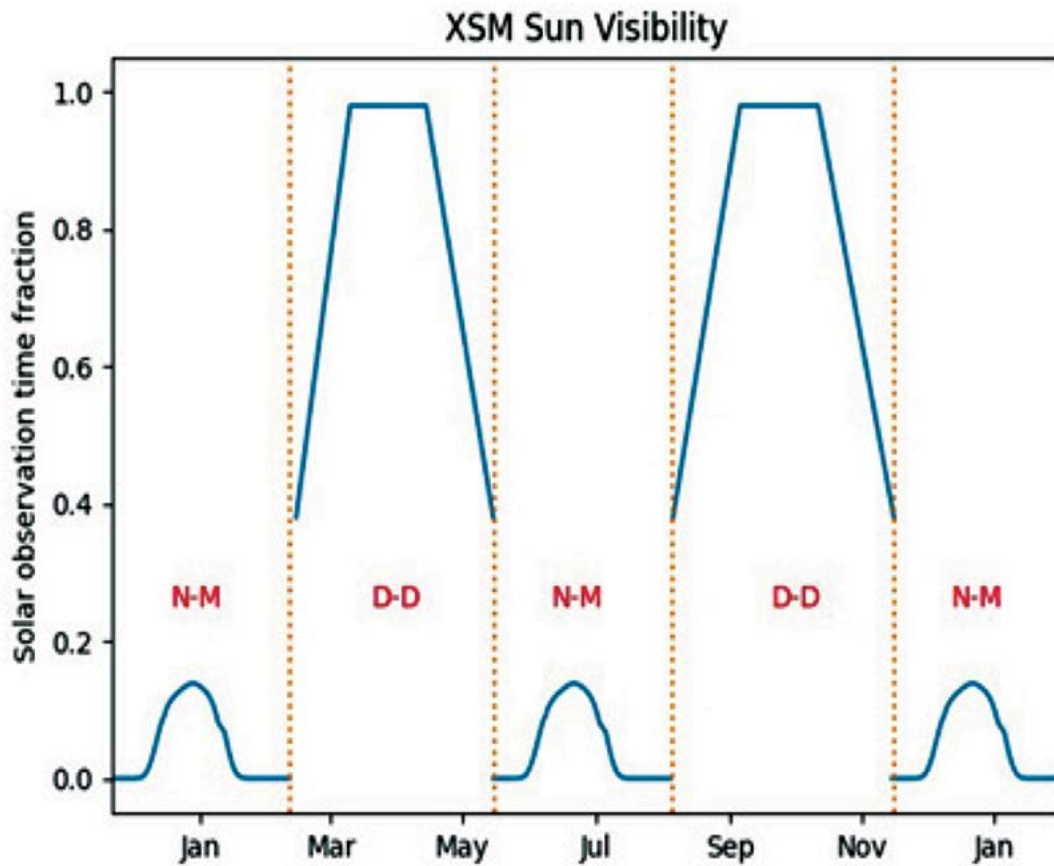
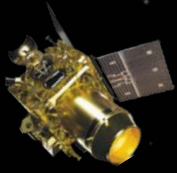
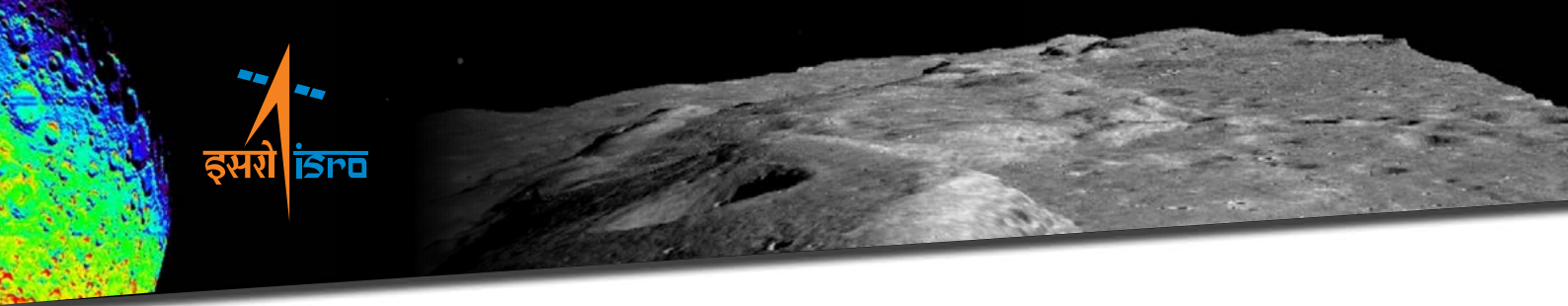


Figure 2.9: The visibility of the Sun with XSM over the year.

For the analysis of the XSM data, a user-level software named XSM Data Analysis Software (XSMDAS) and the required calibration database (CALDB) have been developed [Mithun et al., 2021a]. XSMDAS consists of individual modules to generate data products with a user-defined set of input parameters. All the data files of the XSM generated by XSMDAS are in FITS format. The raw data include the payload data frames, housekeeping information, and various observation geometry parameters. Using the XSMDAS modules light curves, spectra, and associated response matrices can be generated from the raw data with the required time or energy ranges and bins. The XSM data archive also contains standard calibrated products which are generated by the default processing at the POC. These include a time-series spectrum and total light curve for the full energy range, both with a time bin size of one second.

Spectra and response files generated by XSMDAS are directly usable with standard spectral analysis tools used in X-ray astronomy such as XSPEC [Arnaud, 1996] and ISIS [Houck and Denicola, 2000].



2.2.4 In-flight Performance and Calibration

After the launch of Chandrayaan-2, the XSM was first powered-on for a short duration in earth-bound orbit to verify its performance. Similar short observations were carried out in the lunar orbiting phase to investigate any effect of passage through the earth's radiation belt. Regular observations with the XSM started on 12 September 2019, and it has been operating almost continuously since then. The XSM acquires data even when the Sun is not within the FOV in order to obtain background measurements. The instrument is powered off occasionally for short periods during orbit maneuvers and other mission-critical operations.

The performance of the XSM has been evaluated during the six months of in-orbit operations with the on-board calibration source, background measurements, as well as solar observations. The stability of the energy resolution and gain using calibration source spectra are examined and compared the performance with the ground measurements, and using both background and solar observations, the sensitivity limit of the XSM is established. Further, with a careful analysis of the quiet Sun observations at different Sun angles, a refinement to the effective area was provided which was obtained from ground calibration.

2.3 CHandra's Atmospheric Compositional Explorer-2 (CHACE-2)

CHandra's Atmospheric Compositional Explorer-2 (CHACE-2), is a quadrupole mass spectrometer based payload in the orbiter segment of the Chandrayaan-2 mission. The scientific objective of this instrument is to study the neutral composition i.e. relative abundances of species of the tenuous lunar exosphere. Moon has a Surface Boundary Exosphere (SBE) which indicates that the local exosphere of the Moon contains direct information about the surface composition and any possible release of gases from the Lunar interior. While the Apollo series of missions by NASA (1969-1972) could measure the total surface pressure and a few atmospheric constituents (noble gases) on the night side of the Moon, there had been no measurement of the dayside lunar atmosphere (due to the saturation of the Lunar Atmospheric Composition Experiment (LACE) mass spectrometer carried in the Apollo-17 mission during lunar days). Later on, there were several studies, which provided the information on the presence of several species, and their column integrated densities mostly from spectroscopic observations [Cook et al., 2013].



2.3.1 CHACE-2 Instrument

The CHACE-2 is a quadrupole mass spectrometer based payload. [Figure 2.10](#) shows the flight model (FM) of the CHACE-2 instrument, and [Table-2.3](#) summarizes its important specifications. The CHACE-2 instrument consists of the sensor probe (cylindrical in shape) and the electronics. The sensor probe consists of a built-in electron impact ionizer along with a Bayard-Alpert collector to measure the total pressure; a set of four quadrupole rods and a detector assembly. The detector assembly consists of a Faraday Cup (FC) and a Channel Electron Multiplier (CEM).

In the ionizer section, the ambient neutrals are ionized by energetic electrons. The emission circuit of the ionizer consists of thoriated iridium dual filament system, which emits thermionic electrons when operated in vacuum. The emitted thermionic electrons are post-accelerated to a given energy (typically 70 eV) to ionize the neutrals. A part of the ambient neutrals gets positively ionized within a region in the ionizer called the source grid region. The ion optics potentials drag the ions formed in the ionizer through an orifice to the entry port of the quadrupole mass filter system. Another part of the ambient neutrals gets ionized outside the source grid; they are collected by the Bayard-Alpert gauge collector to constitute a line current, which is calibrated to read the total pressure.

The Quadrupole Mass Analyser (QMA) consists of a set of four conducting parallel cylindrical rods, arranged in equal angular separation of 90° . The pair of rods, which are diametrically opposite, are electrically shorted. Each pair of rods is applied with an RF (frequency ~ 2.3 MHz) potential with a superimposed DC potential. The positive ions, formed within the source grid, are attracted towards the entry aperture of the quadrupole rod system. While at the entry aperture all kinds of positively ionized species are present, only the species with a particular charge-to-mass-ratio will have stable trajectory and reach the detector. The other species, with different charge-to-mass-ratios have unstable trajectories and do not reach the detector. Thus the QMA functions like a mass filter. In CHACE-2, the pass band of the mass filter is sufficient to achieve unit mass resolution.

The detector assembly of CHACE-2 consists of a Faraday cup and a Channel Electron Multiplier (CEM) detector. By default, the path-stable ions impinge on the Faraday Cup detector to give rise to a detector current. While the Faraday cup detector has no internal gain the CEM detector has got a large gain and it can be biased with different voltages. The details of the CHACE-2 instrument and its laboratory calibration are given in Das et al. (2020).

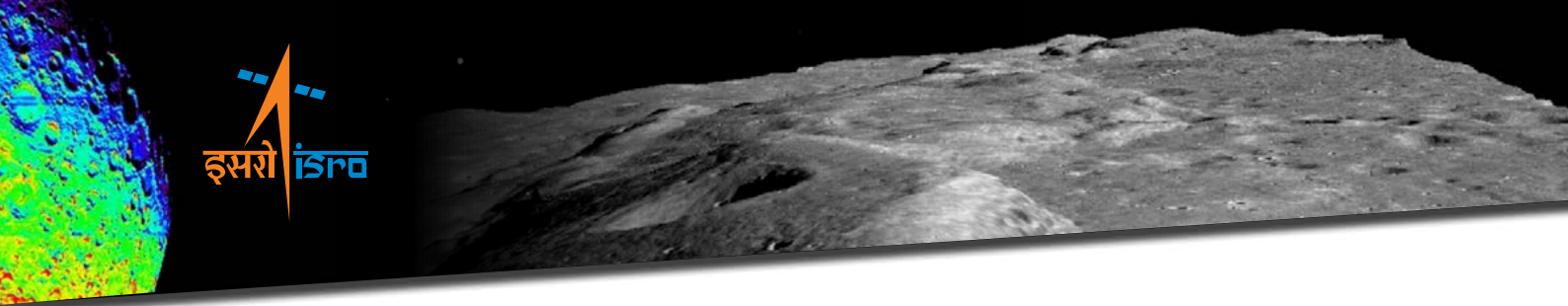
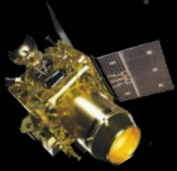


Figure 2.10: FM of the CHACE-2 instrument

Table-2.3: Specifications of CHACE-2

Parameter	Value
Mass range	1-300 amu (Programmable)
Mass Resolution	1 amu
Number of points per amu	9 (default), programmable
Mass filter type	Quadrupole
Detector	Beyard Alpert Gauge, Faraday Cup and Channel Electron Multiplier
Ionizer Electron energy	70 eV (default, Programmable)
Dynamic Range	10^{-4} to 10^{-14} Torr
Modes of operation	Mass Sweep, Trend



2.3.2 Calibration

The science data from CHACE-2 are the raw partial pressures (i.e. ion currents for different species with different mass-to-charge ratio, constituting a mass spectrum) and the total pressure. As the first step, the mass spectrum is subjected to two corrections, viz. 1) The Quadrupole Mass Discrimination (QMD) correction and Electron Multiplier Gain (EMG) correction. The effect of QMD and EMG are to compensate the discriminative behaviour of the QMA and the CEM detector respectively to the species with different mass-to-charge ratios. Until these corrections are carried out, the abundances of the species are incorrect.

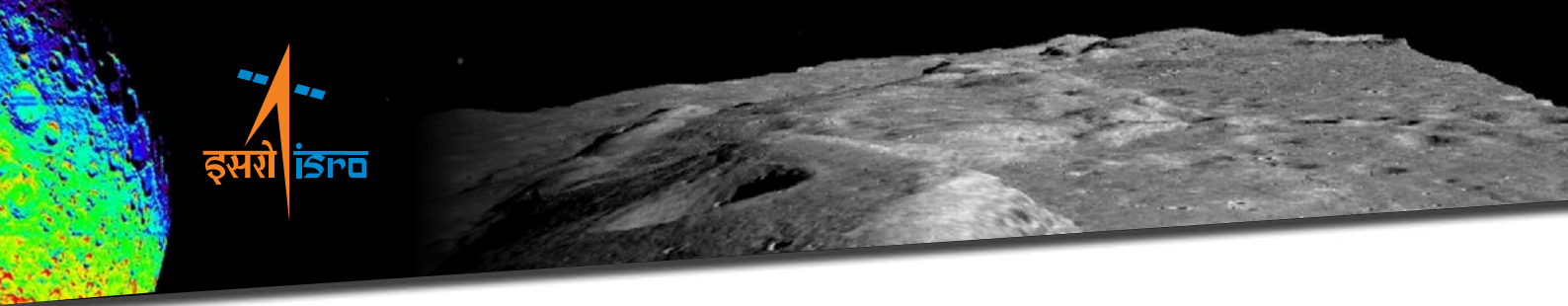
The corrected mass spectrum is now used to find out the dominant species. In turbo molecular pump based vacuum chambers, under residual gas environment, either water vapour or molecular Nitrogen are the dominant gases. This could be different for any other space environment. Once the dominant gas in the environment is identified, the total pressure reading by the B/A gauge, which is calibrated to read Nitrogen-equivalent pressure, is divided by the relative sensitivity factor of the dominant species. The relative (with respect to molecular Nitrogen) sensitivity factors of the gases are, in general, experimentally measured quantities with the help of absolute pressure sensors. Theoretically, it is the ratio of the electron ionization cross sections of the gas of interest to that of molecular Nitrogen.

Once the Nitrogen equivalent total pressure is corrected for the dominant gas, it is used for the normalization. The normalization constant (N) is calculated by dividing the corrected total pressure by the sum over the partial pressures for all the species detected in the mass range of operation.

In addition to the above steps, the correction for the sensor volume enhancement (Sridharan et al., 2015) and roll – angle correction need to be carried out. The roll angle data are provided in the operating parameter file.

Background Estimation

The background consists of species that are emanated due to degassing from the instrument as well as spacecraft modules. The mechanisms are thermal desorption, diffusion and decomposition [Schlappi et al., 2010]. This background needs to be carefully estimated from the observations and eliminated to obtain information on the actual lunar constituents. It should be noted that while deriving the absolute densities, the dissociation corrections also should be applied. For example, the signal at amu 20 is constituted both by the Neon-20 and doubly ionized Ar-40. Therefore, the user should also look into the Argon signal and estimate the fraction of Ar⁺⁺ that can be present, and subtract these from the observed amu-20 signal to arrive at the partial pressures of Neon-20.



2.3.3 Summary of Observations

The normal phase observations of CHACE-2 commenced on 04 September 2019. [Figure 2.11](#) shows a typical mass spectrum from CHACE-2.

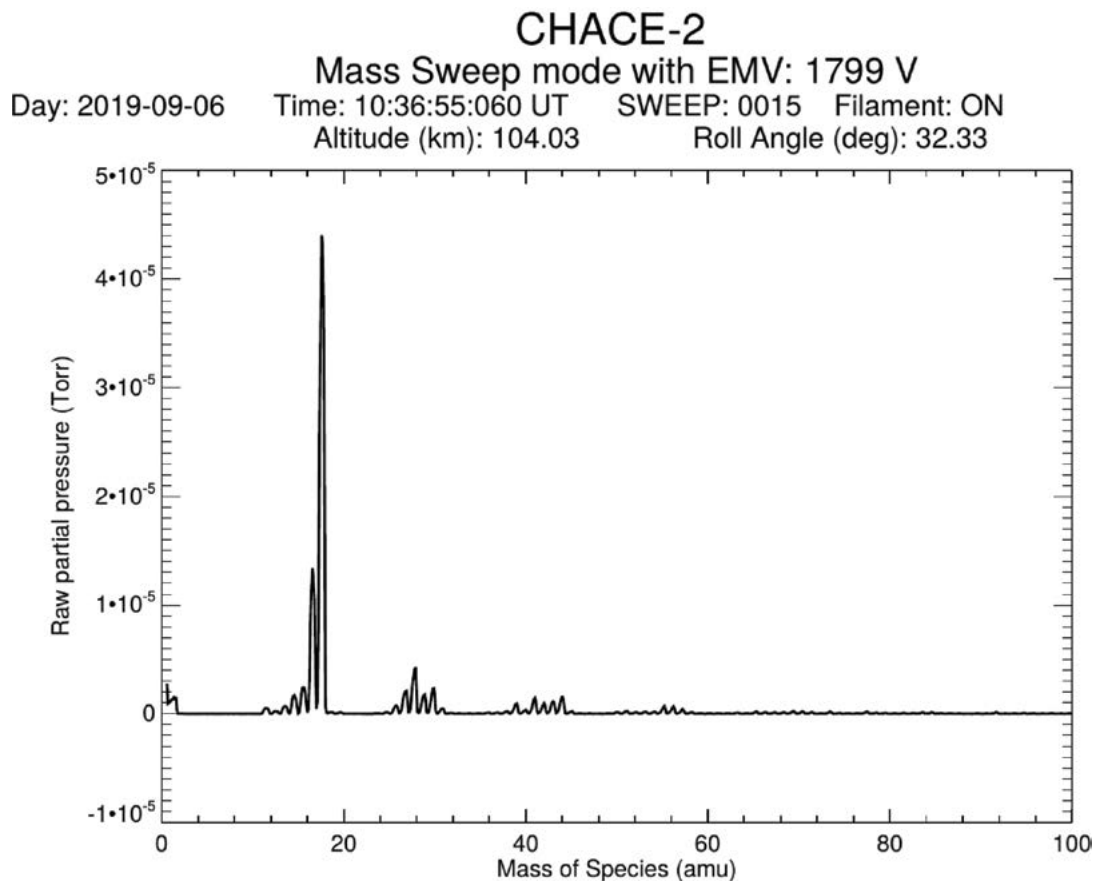


Figure 2.11: Typical mass spectrum of CHACE-2 in the Lunar orbit.

CHACE-2 has been regularly operated at Lunar orbit initially for 2 hours per operation (1 lunar orbit), and subsequently for 4 hours per operation (2 lunar orbits) during each Earth day. During the period from June 2020 to December 24, 2020 CHACE-2 data are obtained for 8 hours per Earth day for most of the days (two operations, each operation for 4 hours). Subsequently, CHACE-2 is being operated only once per Earth day, for 4 hours.

[Figure 2.12](#) summarizes the CHACE-2 local time coverage from September 2019 to April 2020, in LSE (Lunar Centric Solar Ecliptic) coordinate system where X-axis is along Moon-Sun line with positive x-axis points towards Sun, Z-axis is towards ecliptic north and y-axis completes right handed coordinate system. [Figure 2.13](#) summarizes its spatial coverage during the period September 2019-April 2020. It is to be noted that from March-April 2020, repeated observations in the same geometry are obtained and hence not shown in these figures.

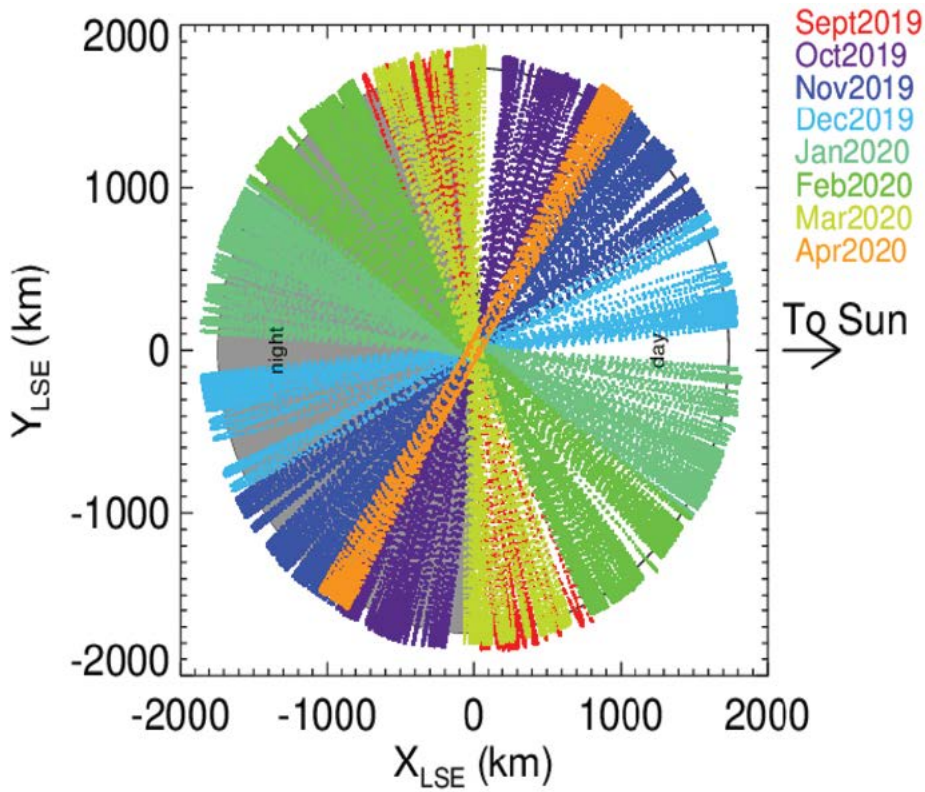
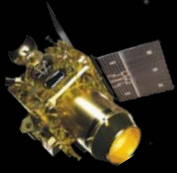


Figure 2.12: CHACE-2 local time coverage from September 2019 to April 2020, in LSE (Lunar Centric Solar Ecliptic) Coordinates coordinate system.

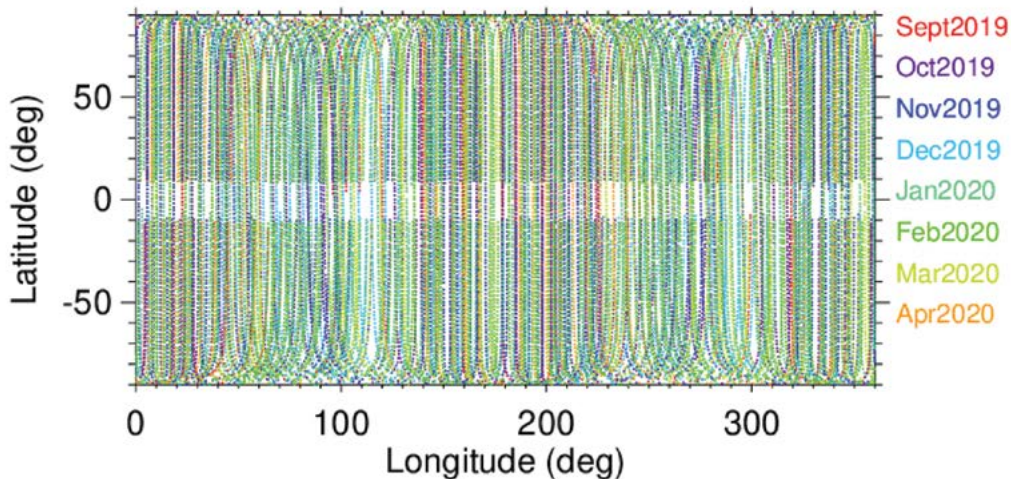
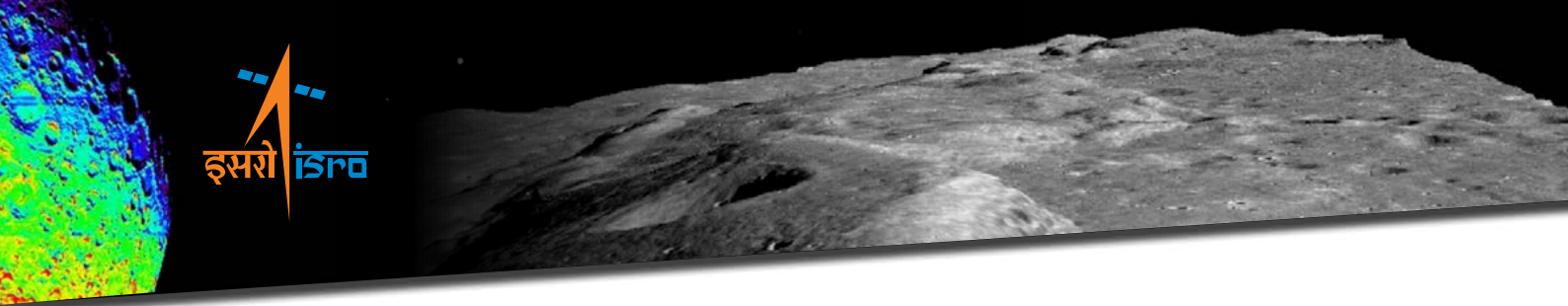


Figure 2.13: Selenographic Coverage during September 2019-April 2020.

2.4 Dual Frequency Synthetic Aperture Radar (DFSAR)

The Dual Frequency Synthetic Aperture Radar (DFSAR) on board Chandrayaan-2 Orbiter is a microwave imaging instrument in L- and S-band frequencies and the first fully-polarimetric



SAR to study the Moon. L-band frequency enables double the surface penetration capability with respect to what is obtained using S-band. The instrument is basically two SAR systems (for L & S bands) sharing a common antenna aperture with wide bandwidth. Various instrument features like high-efficiency transmitter, low-noise high-gain receiver, onboard range-compression (first for any ISRO SAR mission) have enabled a highly sensitive instrument with polarimetric capability. Its best resolution (2m in slant-range) is one order better than the previously flown SARs to the Moon.

The backscattered signals from the targets are coherently measured by the DFSAR in different polarizations to enable studies of physical and dielectric properties of the lunar surface/ shallow-subsurface. With these polarimetric measurements, the instrument primarily aims to unambiguously address the presence of water-ice in permanently shadowed regions (PSRs), characterizing the physical and dielectric properties of lunar surface, volcanic features, impact craters and their associated ejecta.

The key science objectives of the DFSAR instrument are:

1. Unambiguous detection and quantitative estimation of water-Ice in the lunar polar regions.
2. Dielectric constant and Surface roughness estimation over lunar surface.
3. High resolution lunar geological/ morphological mapping and polarimetric characterization, in polar and non-polar regions.

2.4.1 DFSAR Instrument

In order to meet the above science objectives within the mass, power, volume and data rate constraints of a planetary mission, many new technologies such as on-board range compression, miniaturized RF subsystems & dual frequency single aperture antenna were developed for this payload; major specifications are as given in Table-2.4. The developed dual frequency system, as shown in [Figure 2.14](#), has a total mass of 21 Kg and consumes 100 W raw bus power. The overall configuration and imaging geometry are illustrated in [Figure 2.15](#).

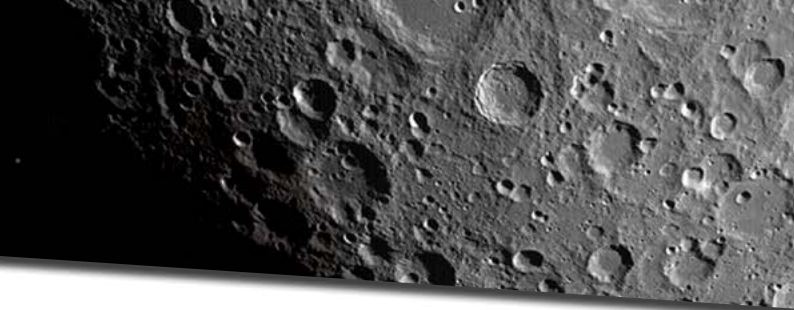
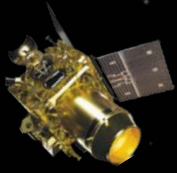


Table-2.4: Major Specifications of DFSAR

Parameters	L-Band	S-Band
Altitude	Nominal 100km	
Frequency	1.25GHz	2.5GHz
SAR Modes	Single / Dual/ Compact (CP) and Full-Polarimetry (FP)	
Range Swath	10km	
Incidence Angle	9.6° - 36.9°	
Resolution	2m – 75m	
Chirp Bandwidth	75MHz – 2MHz	
Antenna	Microstrip antenna, 1.4m x 1.1m	
Antenna Gain	22dBi	25dBi
Axial Ratio in Compact Pol	0.4dB	1.1dB
Transmit Pulse width	80 μ s - 25 μ s (CP), 50 μ s - 25 μ s (FP)	
SSPA Peak power	45W	40W
Max Duty cycle	24%	
Receiver Noise Figure	2.8dB	4.3dB
NESZ at swath end for 75m resolution and 30° incidence	-33.7dB (CP), -30dB (FP)	-26.2dB (CP), -22.5dB (FP)
Onboard Processing	Range compression and BAQ	
Data Rate	160Mbps	
Raw bus power	100W	

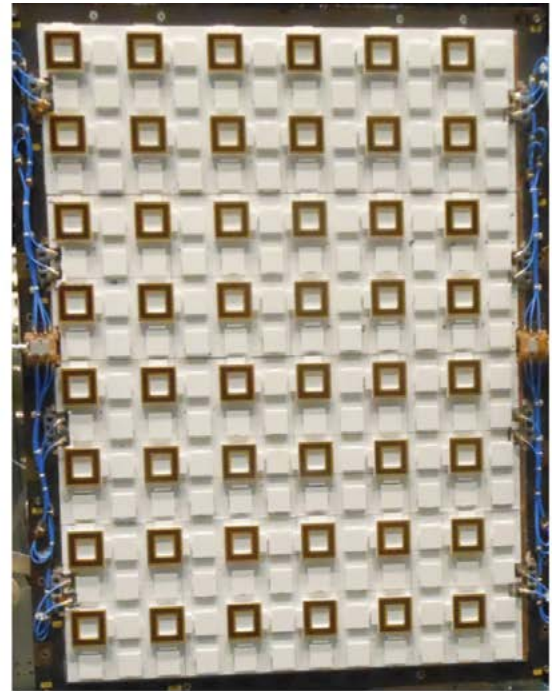
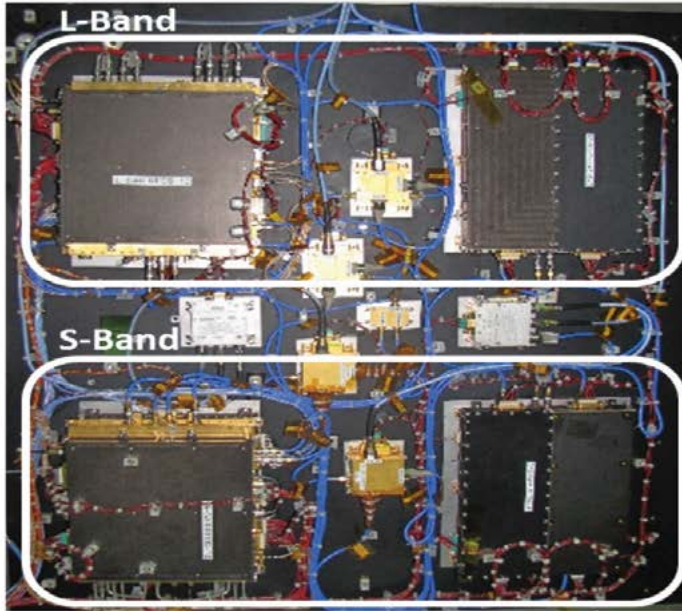


Figure 2.14: DFSAR Electronics and Antenna Systems.

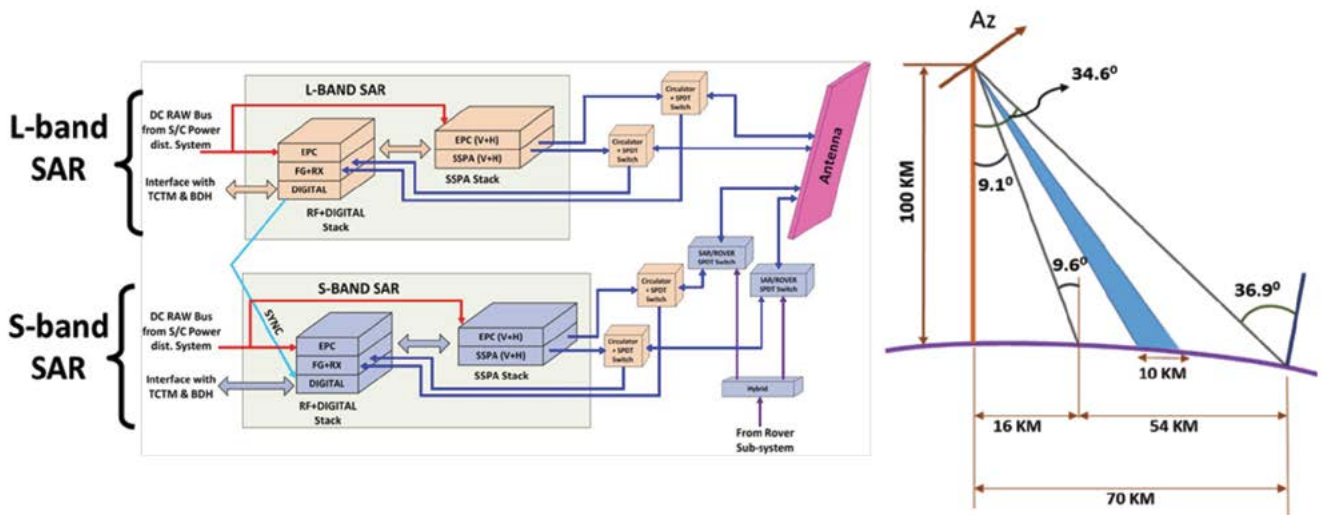


Figure 2.15: DFSAR configuration and imaging geometry.

2.4.2 DFSAR Polarimetric Configuration and Characterization

DFSAR payload is equipped with hybrid-polarimetry (transmit in circular polarization and receive in linear polarization) and full-polarimetry mode – a gold standard for polarimetric SARs.

A full polarimetric system transmits horizontally (H) and vertically (V) polarized waves alternatively at different pulse repetition frequency (PRF), and receives coherently at the same time on both channels H and V. However, various internal system information such as loss, phase & amplitude imbalance between H&V chains; the crosstalk between the chains during both the transmit and receive instances are required to deduce the “actual” target scattering matrix from the un-calibrated (measured) scattering matrix obtained using full-polarimetric SAR data.

In Hybrid or Compact-Pol mode, circular polarized transmission calls for the phase difference between H & V signals to be 90° and in Full Pol (FP) transmission the phase difference needs to be 0° , as illustrated in [Figure 2.16](#)

During radiated mode testing on the integrated payload SSPA phase coefficients for LHCP, RHCP and Full Pol transmission were derived. This was verified by measuring the axial ratio for each transmission using a rotatory probe at the receiving end, whose results are summarized in [Figure 2.17](#)

Similarly receive chain phase imbalance, transmit and receive crosstalk between H & V chains is measured for both L&S bands. End to end payload test was conducted using a physical delay line.

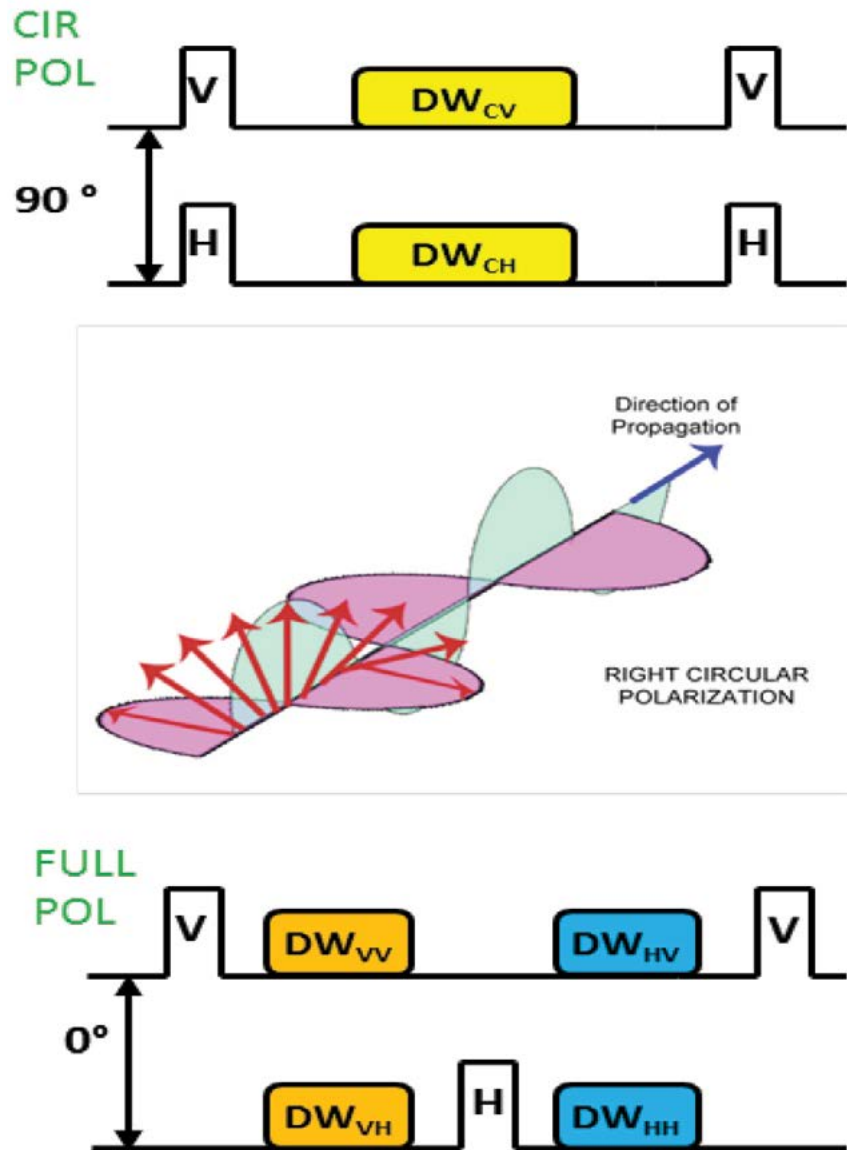


Figure 2.16 : Compact-Pol and Full-Pol.

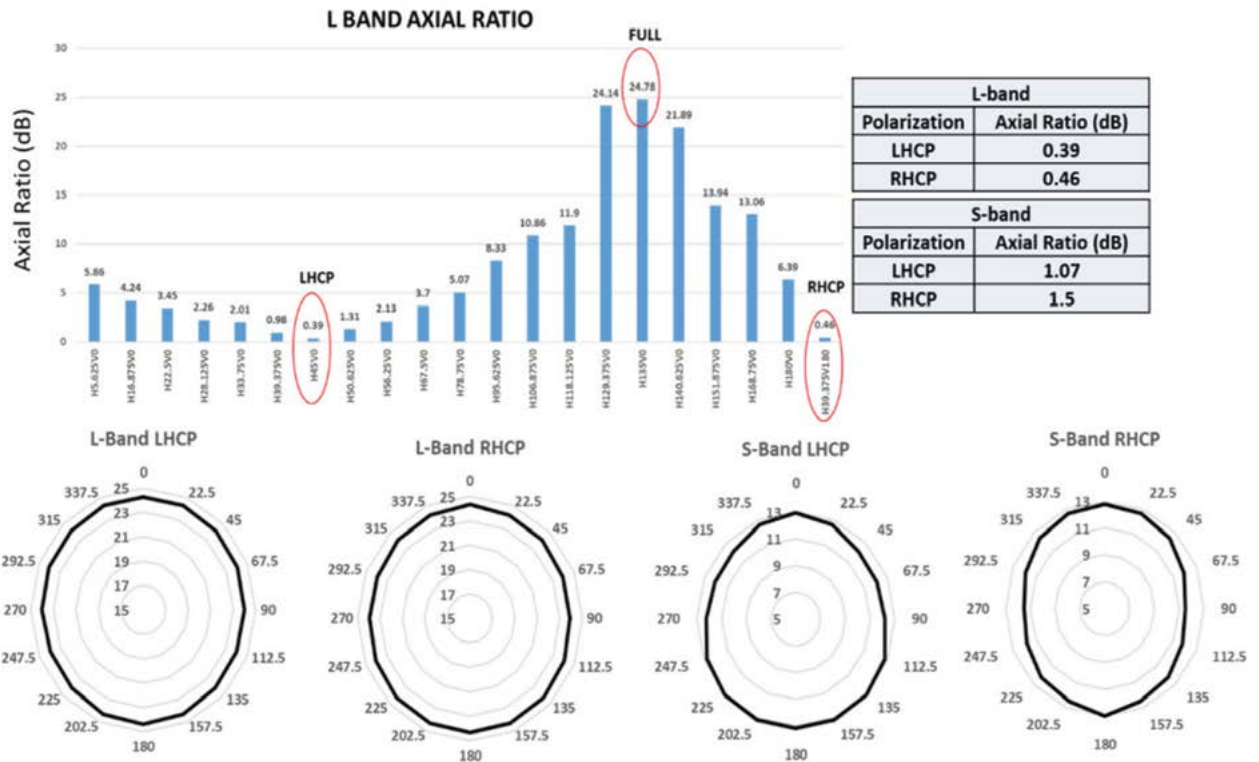


Figure 2.17: Axial Ratio and Polarimetric characterization of DFSAR instrument.

2.4.3 DFSAR Observation Strategy

DFSAR is the prime payload to be operated during dawn-dusk season of the Moon. This season comes twice a year, alternating with noon-midnight season, where imaging by optical sensors are the prime. Commissioning of the DFSAR was carried out in Sept, 2019, with the instrument operated in various modes, leading to validation/finalization of the operating settings. Several firsts were recorded during these operations, notably:

1. First full-polarimetric imaging of the Moon.
2. High resolution (4m ground-range resolution) SAR imaging of lunar surface. [Best SAR resolution till then was 30m by MiniRF of LRO]
3. L-band SAR imaging (standalone, as well as in synchronous mode with S-band); first acquisition on 4th Sept, 2019, with a sample image output shown in [Figure 2.18](#) .
4. Joint L & S-band “Receive-only” mode acquisition.
5. All the above modes were operated using “onboard range compression”, to reduce data-rate and maximize swath. This is the first ISRO SAR mission to have this feature.

Subsequently, systematic coverage of the polar-regions (85° to 90°, North and South) has been taken up, and is in progress during the designated seasons.

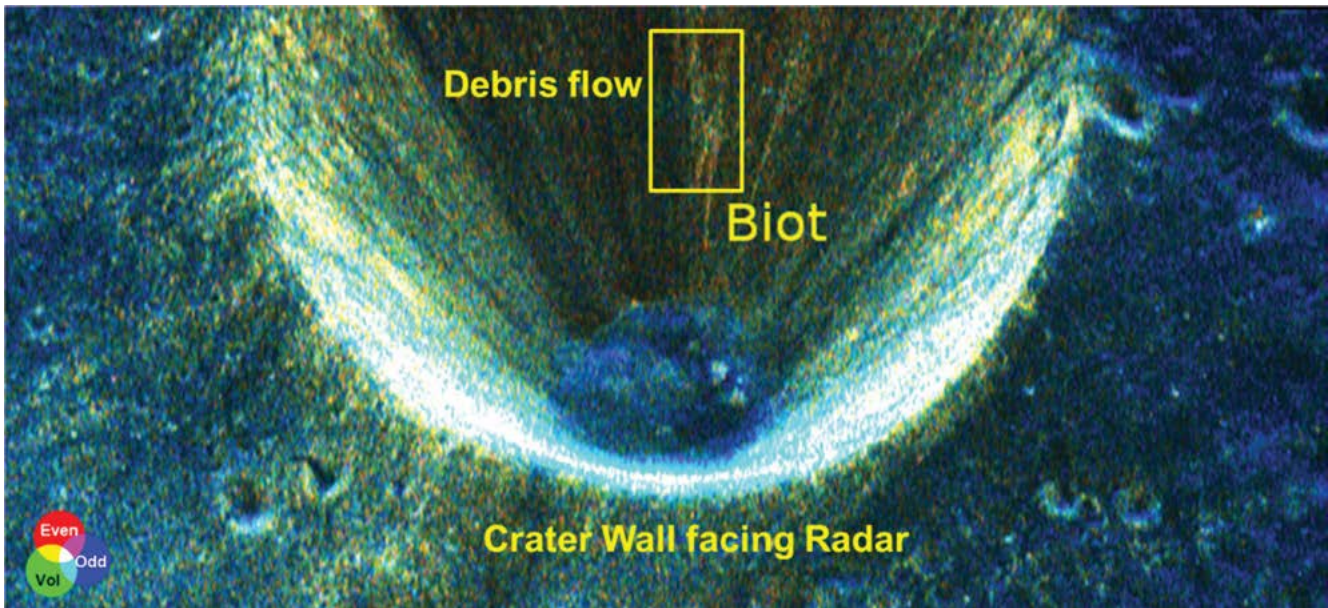
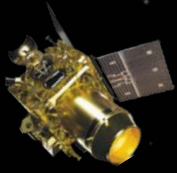


Figure 2.18 : First DFSAR Acquisition in L-band.

2.4.2 Data Processing and Calibration

Backscatter signal collected by SAR at each instant represents a coherent summation of returns from individual targets in the antenna field of view. This raw-data is down-linked for SAR processing on-ground. It is only after this processing that full-resolution of the SAR data is obtained. Following are the levels of the data-products generated and hosted on ISSDC:

Level-0A/0B: represent raw & range-compressed, respectively.

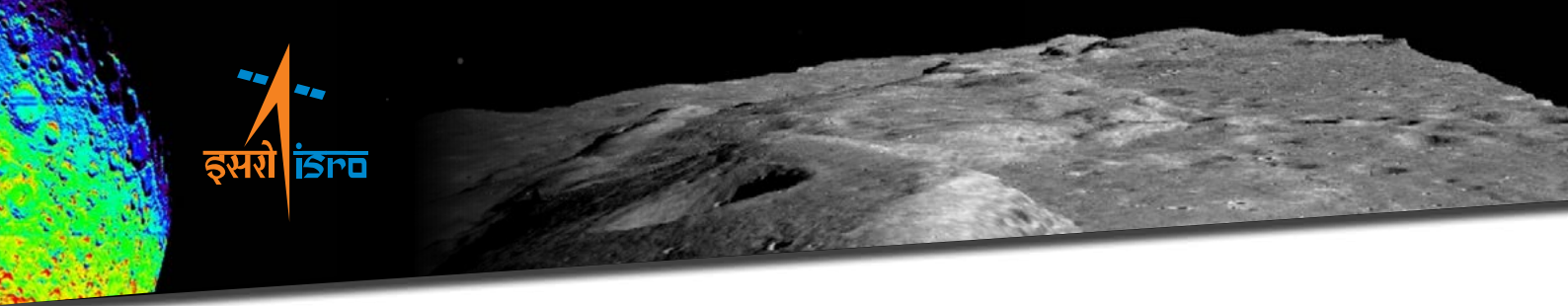
Level-1A: represents seleno-tagged single-look complex (SLC) data

Level-1B: represents seleno- tagged ground-range product

Level-2 : represents seleno-referenced product

As the DFSAR is a polarimetric system with capability of acquiring quad-pol and compact polarimetric (CP) data, radiometric and polarimetric calibration are critical for the derivation of lunar surface physical parameters.

Radiometric calibration provides the coefficients to map SAR data to their corresponding backscatter coefficients of targets. Due to the absence of any calibration targets on the Moon in L&S bands, the calibration is performed based on the radar-equation, using lab characterized system parameters. Radiometric accuracies were validated using LRO-MiniRF data and found to be better than 2dB.



Polarimetric characterization of a region of interest is heavily dependent on the quality of polarimetric calibration that establishes the inter-channel (HH/VV/HV/VH) phase-relationships. Calibration errors can affect polarimetry products thereby leading to misinterpretation of scattering/physical processes under study. The polarimetric corrections and validation of its efficacy have been illustrated in [Figures 2.19 and 2.20](#), respectively.

Polarimetric Calibration-Full Polarization (FP)

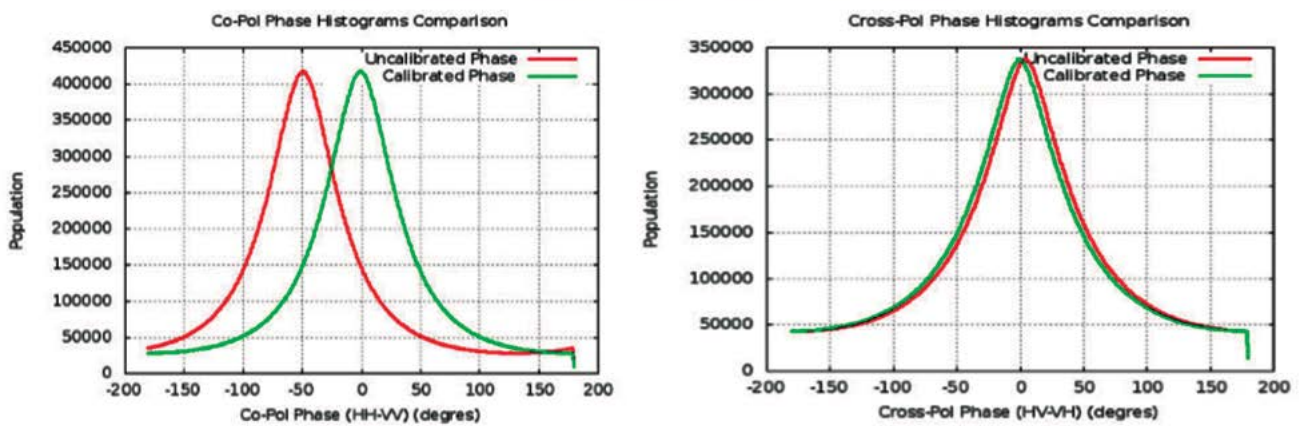


Figure 2.19: Polarimetric calibration illustrated using histograms of Co-pol (HH/VV) and Cross-pol (HV/VH) phase differences.

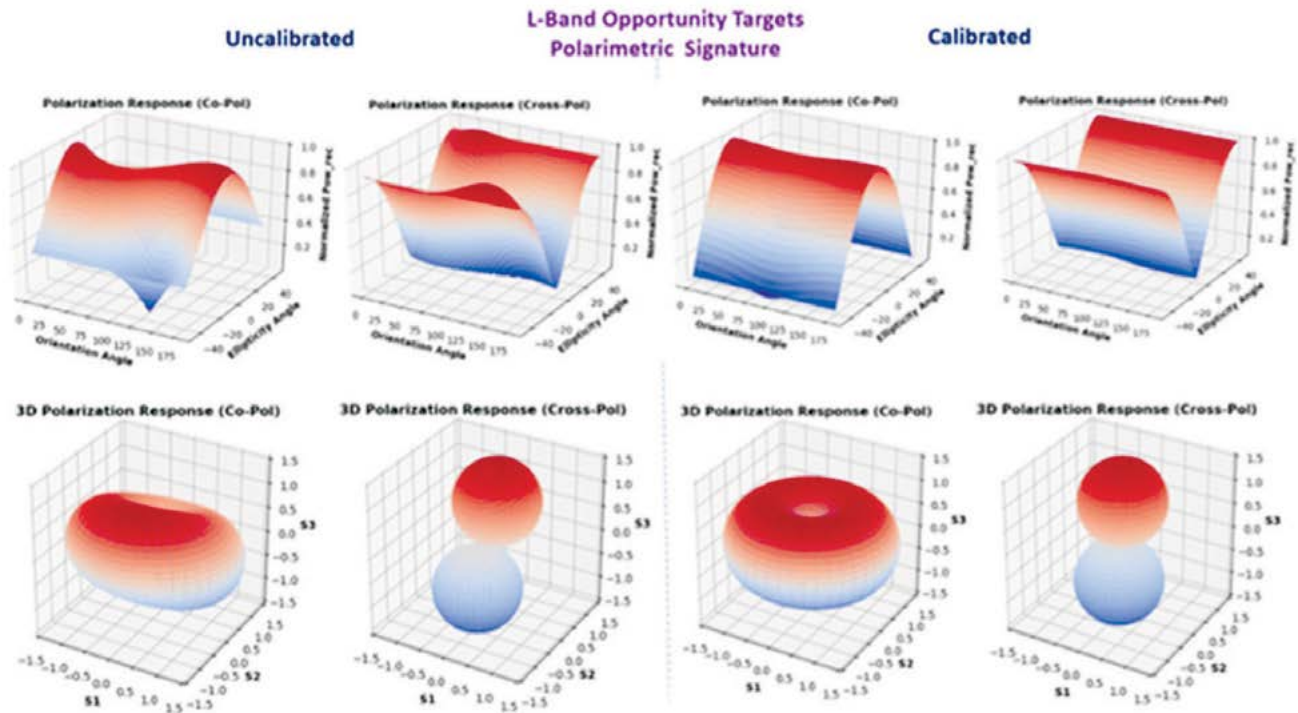
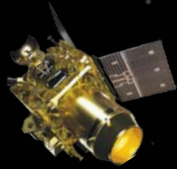


Figure 2.20: Polarimetric signatures corresponding to opportunity point target, to assess the efficacy of polarimetric calibration.



2.5 Imaging Infra-Red Spectrometer (IIRS)

The primary objective of Chandrayaan-2, Imaging Infra-Red Spectrometer (IIRS) is to detect and map the lunar surface composition and volatiles to understand the origin and evolution of the Moon in a geologic context. Even though almost 95% of the lunar surface has been already mapped by Chandrayaan-1 M³, IIRS aboard Chandrayaan-2 having a relatively higher spatial and spectral resolution and an extended spectral range beyond 3.0 μm will reassess the chemical make-up of the lunar crust and will provide a global inventory of the lunar hydration. Below are the major objectives of IIRS instrument.

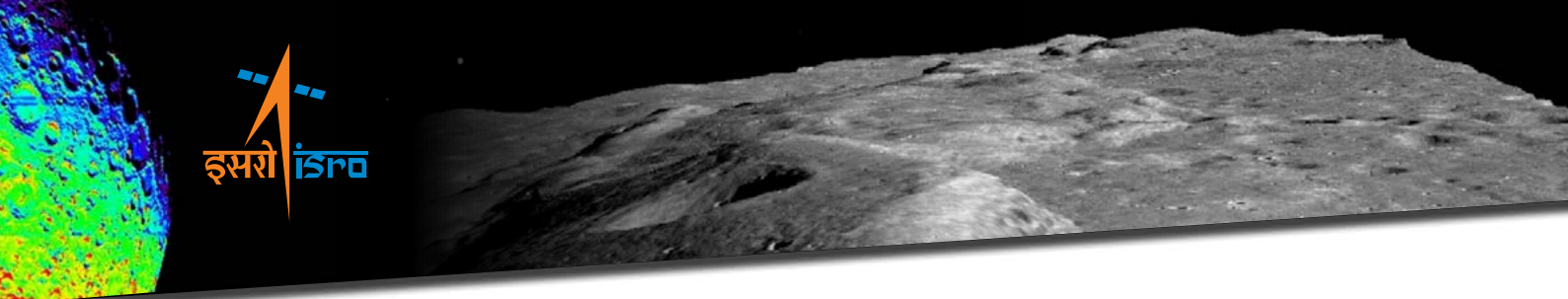
- Global mineralogical and OH/H₂O mapping of the Moon in the spectral range of $\sim 0.8\text{-}5.0 \mu\text{m}$ for the first time at high resolution.
- Complete characterization of OH/H₂O feature near 3.0 μm for the first time at high spatial and spectral resolution.
- To understand the sources and processes (endogenic and/or exogenic) responsible for the presence of OH/H₂O on the Moon.

2.5.1 Instrument Specifications

IIRS measures the reflected solar radiation along with the emissions from the lunar surface at an altitude of 100 km on a polar circular orbit at a spatial resolution of ~ 80 m and spectral resolution of $\sim 20\text{-}25$ nm across the spectral range of $0.8\text{-}5.0 \mu\text{m}$ in ~ 250 spectrally contiguous bands. The diagnostic absorption features of major and minor lunar minerals are found to occur in the spectral domain of $\sim 0.75\text{-}2.5 \mu\text{m}$ that fall well within the spectral range of IIRS thereby making their detection possible by the spectrometer. On the other hand, the spectral range of $\sim 2.5\text{-}3.3 \mu\text{m}$ is being dedicatedly used to detect the presence of lunar OH/H₂O features having fundamental absorptions around 3.0 μm . Table 2.5 highlights the major specifications of IIRS.

Table 2.5: Major specifications of IIRS

Parameter	Values
Platform Altitude (km)	100
GSD (m) at Nadir	80
Swath (km) at Nadir	20
Spectral Range (μm)	0.8 to 5
Spectral Resolution, FWHM (nm)	$\sim 20\text{-}25$
Noise equivalent Differential Radiance, NedR ($\text{mW}/\text{cm}^2/\text{sr}/\mu\text{m}$)	≤ 0.005
No. of spectral bands	~ 250
Quantization (bit)	14



2.5.2 Methodology

The methodology of IIRS data processing is shown in [Figure 2.21](#). Brief description of data processing are provided below.

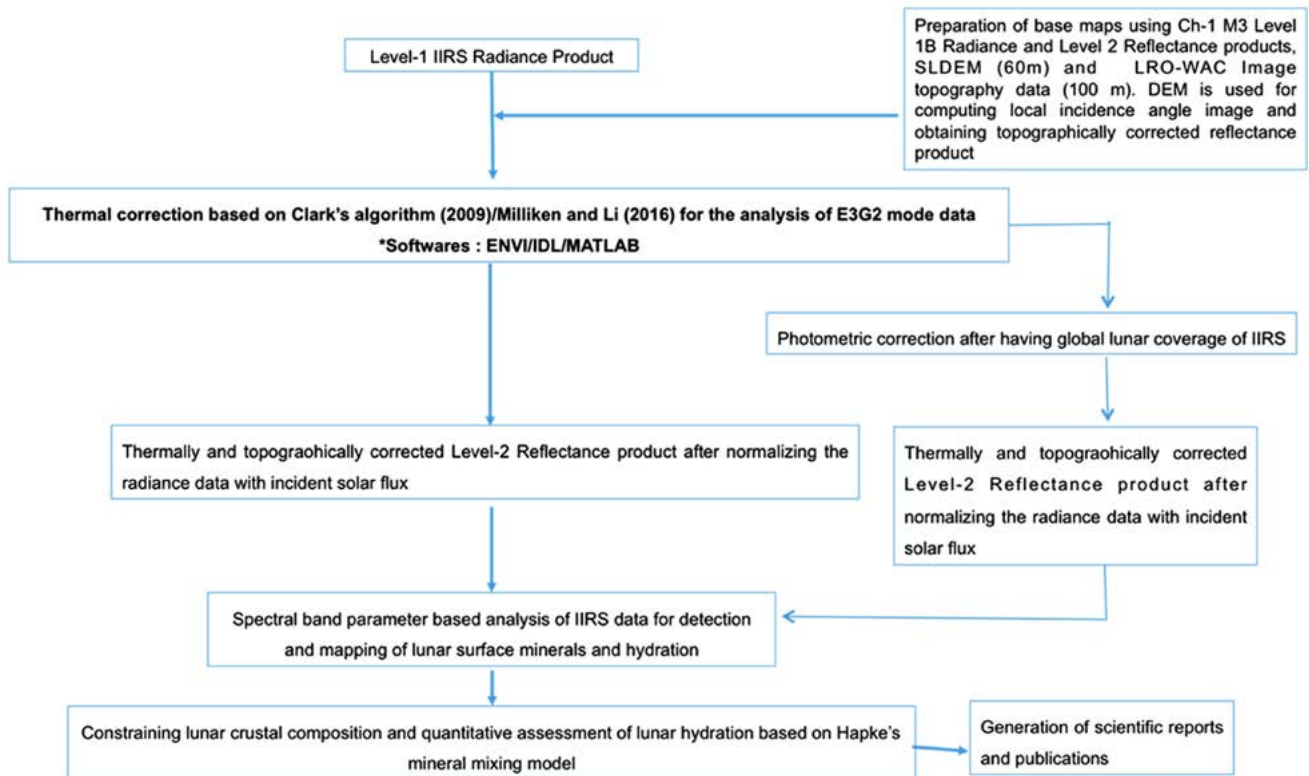
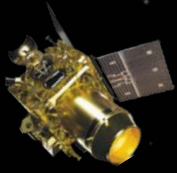


Figure 2.21: Flow chart showing methodology involved in the processing of Ch-2 IIRS data.

Data Processing: The raw data collected from IIRS payload of Chandrayaan-2 is processed to correct different types of distortions present in the data, before it is archived. Data processing is done according to three defined levels (Level-0, 1 and 2). Level-0 data set is consisting of payload raw data (as it is collected from payload), ancillary data (mainly SPICE kernels generated from the mission) and housekeeping data (health of the spacecraft). The data are stored in a specific format in the database without any correction. Level-1 data is radiometrically corrected and geometrically tagged. Level-1 data set includes processed radiance data along with seleno-tagging. Level-2 data include radiometric, photometric, thermal and geometric corrections and are normalized by the incoming solar flux. Polar and regional mosaics are part of special/higher level products. All the products will be disseminated in Planetary Data System (PDS-4) format while special products will be in Geo-Tiff format.

Data Analysis: As already mentioned previously, the instrument specifications of IIRS are well suited to surface mineral and volatile mapping via spectroscopy in the near-infrared



portion of the electromagnetic spectrum (Roy Chowdhury et al., 2020). [Figure 2.22](#) shows the reflectance spectra of particulate lunar soil, rock and minerals measured in Earth-based laboratory (RELAB) in the spectral range $\sim 0.5\text{--}4.0\ \mu\text{m}$ comparable with the IIRS spectral range (Figure source: Supporting online material by Pieters et al., 2009)

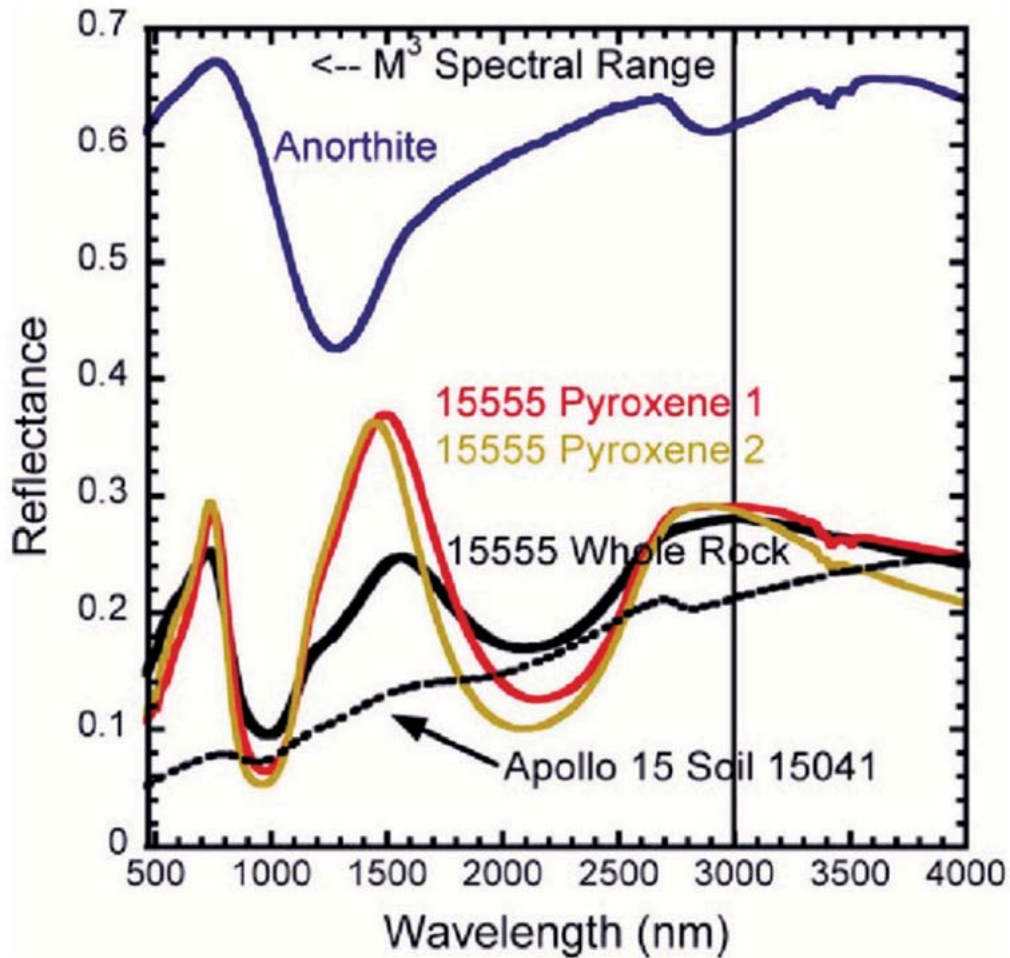
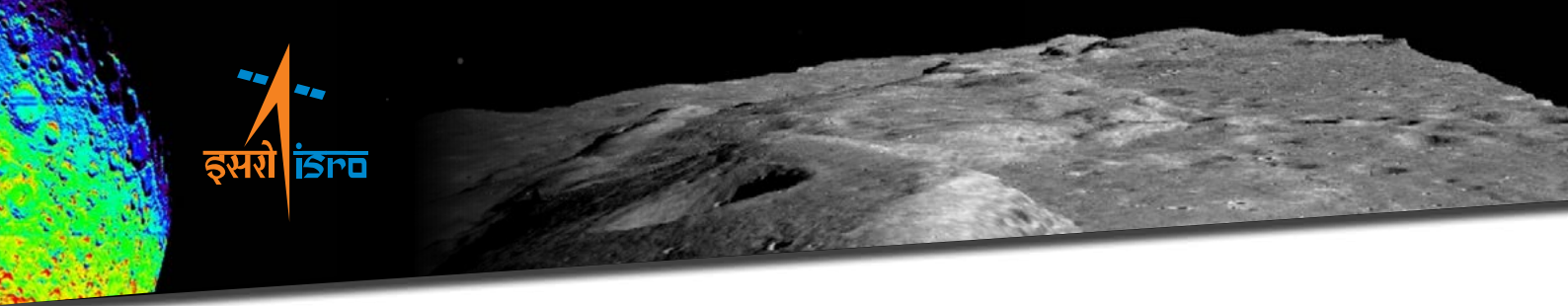


Figure 2.22: Reflectance spectra of particulate lunar soil, rock and minerals measured in Earth-based laboratory (RELAB) in the spectral range $\sim 0.5\text{--}4.0\ \mu\text{m}$ comparable with the IIRS spectral range (Source: supporting on-line material by Pieters et al. (2009) published in Science).

The diagnostic spectral signatures of the lunar rocks and soils in the Infra-Red region of the EM spectrum form the scientific basis for mapping the composition of the lunar surface with an imaging spectrometer. This spectral range is also well suited for carrying out spectroscopic measurements from passive reflected solar radiation at $\sim 1\ \text{AU}$. Additional measurable signal arises at longer wavelengths ($\sim 2.0\text{--}5.0\ \mu\text{m}$) due to the thermal emission from the lunar surface when the surface temperature is 300 K and above. To achieve the science goals and objectives of IIRS, measurement of the full spectral range with contiguous sampling is required. The reflectance spectroscopic measurement approach is best suited



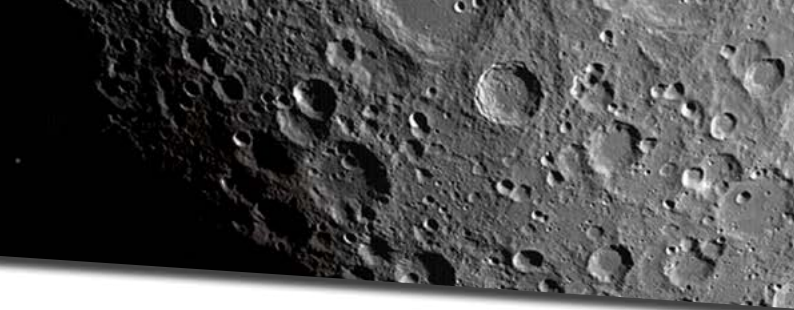
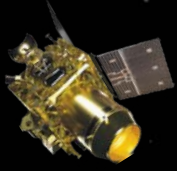
to conditions of small zenith angle solar illumination when the reflected signal is strong and there are few shadows. Measurement of the full spectral shape allows minerals and other components to be unambiguously identified and abundance can be estimated even in the presence of compositional mixtures.

The first step towards analyzing a spectrometer data is to convert the raw counts into spectral radiance and subsequently to spectral reflectance by normalizing the effects of solar irradiance. The IIRS data reduction from raw counts to apparent surface reflectance involves several steps. Briefly, the detector background is subtracted using systematic measurements of the dark current. These dark-corrected data are then converted to radiance using preflight calibration measurements. From these calibrated radiance data an estimate of reflectance is generated by dividing with a solar spectrum and the cosine of the incidence angle.

Thermal Correction: The lunar surface is illuminated by solar radiation which also contains a major portion of thermal radiation. The scattered light observed by the sensor in the visible-near-infrared (VIS-NIR) consists of reflected and emitted radiation. These two parts need to be separated for the right interpretation of the data. An iterative scheme proposed by (Clark et al, 2011) is used for modelling thermal emission and correcting the data for the same. Apart from this, a physics based thermal correction model has been developed for the removal of thermal contributions from the reflectance spectra of IIRS using co-located temperature measurement of lunar surface.

Hydration Estimation: Using Hapke's model [Hapke, 2012], the thermally corrected IIRS reflectance spectra have been converted to single scattering albedo (SSA), as the use of SSA spectra is preferred over the reflectance spectra in quantifying the absorption strength [Li and Milliken, 2017]. Subsequently, a continuum removal technique has been performed on the SSA spectra by considering a linear continuum encompassing 3000-nm hydration feature. From these continuum-removed SSA spectra, the effective single particle absorption thickness (ESPAT) [Hapke, 2012] values have been estimated. The lab-based analyses of various hydrous materials and hydroxyl-bearing lunar materials have confirmed that there is a linear relation between the water absorption strength and the ESPAT values [Milliken and Mustard, 2005; Milliken and Mustard, 2007a; Milliken and Mustard, 2007b].

Spectral Band Parameter Analysis: Spectral band parameters such as Integrated Band Depth (IBD), Band Center, Band Area, Band Depth etc. have been computed from continuum-removed spectra for detailed spectral characterization. In the current continuum removal technique, a straight line continuum was fitted to the shoulders on either sides (the points



of highest reflectance on both sides of the absorption) of the absorption features and the spectra were then divided by the respective continuum

IBD - is computed as the running sum of reflectance values between fixed wavelength ranges. IBD parameters are generally used to characterize the variations in the strengths of the 1000-nm and 2000-nm mafic features that capture the spectral variations related to mafic minerals, soil maturity and space weathering (Mustard et al., 2011). Same methodology is followed to obtain IDB for 1000-, 2000- and 3000-nm spectral absorption features that correspond to the presence of mafic silicates and hydration respectively.

Band Center - is derived as the central wavelengths of the 1000- and 2000-nm pyroxene-olivine absorption features designated as Bands I and II respectively (Cloutis et al., 1986; Gaffey et al., 2002). Similarly, Band Center for 3000-nm hydration feature is also computed. Band center can be calculated by fitting a 3rd order polynomial to the bottom of the continuum-removed absorption feature and the minimum point on the polynomial fit is considered as the band center.

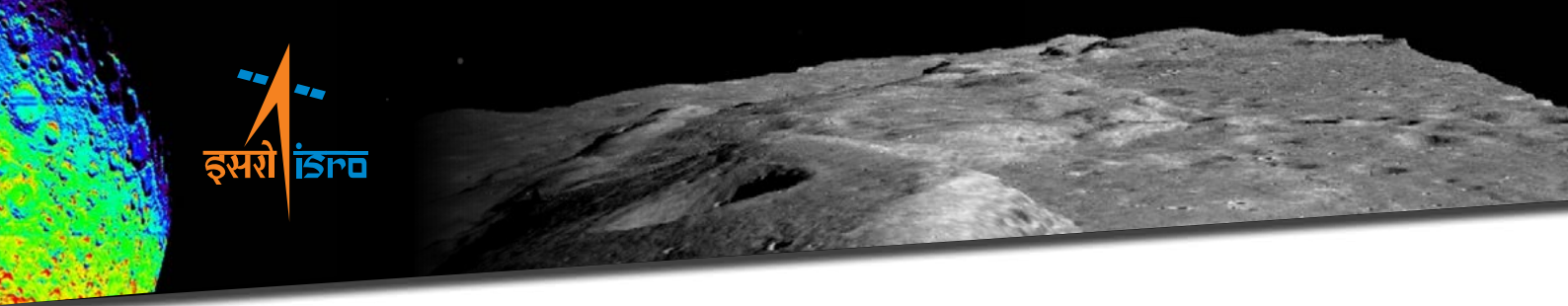
Band area - is calculated as the area between the continuum slopes and the data points. The spectral band parameters, thus computed, allow quantification of the surface mineralogy, relative mafic mineral abundances (olivine/ortho- and/or clinopyroxene) and pyroxene chemistry.

Band depth - of a particular spectral absorption has been estimated by subtracting the relative reflectance value found at a band minimum from the continuum slope in a continuum-removed spectra.

2.6 Terrain Mapping Camera-2 (TMC-2)

Terrain Mapping Camera-2 (TMC-2) on board Chandrayaan-2 mission has similar capabilities as its predecessor TMC-1. TMC-2 provides images with a spatial resolution of 5 m and swath of images of 20 km from the spacecraft altitude of 100 km. This camera enables in preparing global high resolution image mosaic and Digital Elevation Model (DEM). TMC-2 ortho-images and DEM data sets can be collectively used for detailed morphological, morphometric, morpho-structural, rheological analysis and surface age estimation of geological units for understanding the lunar surface processes and origin/evolution of the Moon.

An important aspect of Lunar studies is understanding Lunar volcanism, tectonism, cratering processes, crustal shortening etc. which can be done using TMC-2 DEM and Ortho-images. Similarly, these data sets can also be used for surface age estimation of geological units using Crater Size Frequency Distribution (CSFD) technique in the different



regions of the Moon, which is useful for litho-stratigraphic co-relation between different geological units.

All these finally help in understanding the origin and evolution of Moon since it came into existence.

2.6.1 Science Objectives

The broad objective of TMC-2 is systematic morphological, morphometric, morpho-structural, rheological analysis and surface age estimation of geological units for reconstruction of lunar geological evolutionary history and understanding the past volcanic and tectonic processes. This involves:

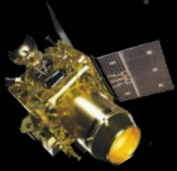
- Understanding of Lunar crustal shortening through morpho- structural analysis of wrinkle ridges distributed in different regions of the Moon.
- Impact Crater Dynamics through analysis of elongated craters.
- Study of Lunar volcanism through systematic mapping of domes/cones in high land and mare regions, estimation of their rheological properties using morphometric parameters and age estimation of those volcanic regions.
- Understanding the evolution of near and farside regions e.g. type and distribution of craters.

2.6.2 Instrument Specifications:

Technical specifications of TMC-2 are given below in Table 2.6.

Table 2.6: Specifications of TMC-2 payload

S.No	Parameter	TMC (Chandrayaan-2)
1	Altitude	100 km
2	Spatial sampling	Along track 5 m Across track 5m
3	Swath	20 km
4	Stereo Mode	3 view along track, $\pm 25^\circ$, B/H=1
5	Spectral range	Panchromatic 0.5-0.85 μm



6	Quantisation	12 bit
7	Data rate	16.2 Mbps/view
8	Gain/Exposure	4-exposures and single gain
9	Square wave response at Nyquist (%)	>28
10	SNR	>75@1.2 mW/cm ² /str/μm >500@14 mW/cm ² /str/μm
11	Raw Power	3.9W
12	Mass (kg)	3.5
13	EOM (mm) (YxPxR)	280x120x440

2.6.3 Principle of Operation:

For stereoscopic imaging, TMC-2 has three telescopes with 4000 one dimensional detectors looking in fore (+25°), nadir (0°) and aft (-25°) directions respectively. [Figure 2.23](#) shows the Isometric view of electro optical module and camera electronics of Terrain Mapping Camera (TMC-2). [Figure 2.24](#) shows the schematic of principle of operations of TMC-2.

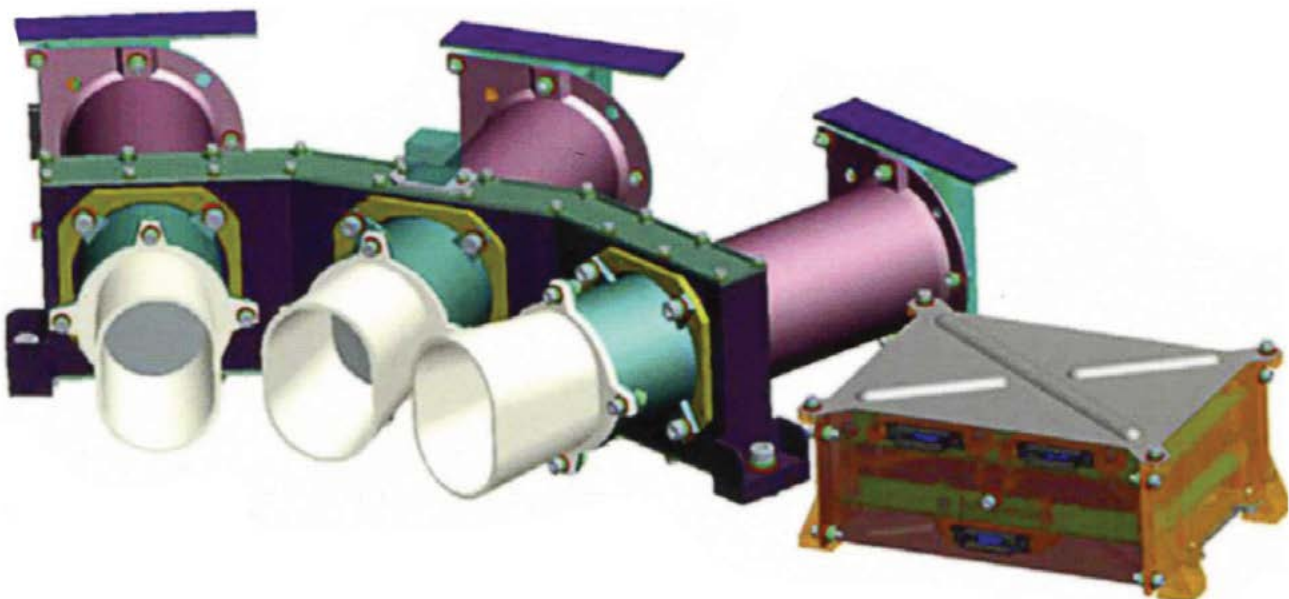


Figure. 2.23: Isometric view of electro optical module and camera electronics of Terrain Mapping Camera (TMC-2).

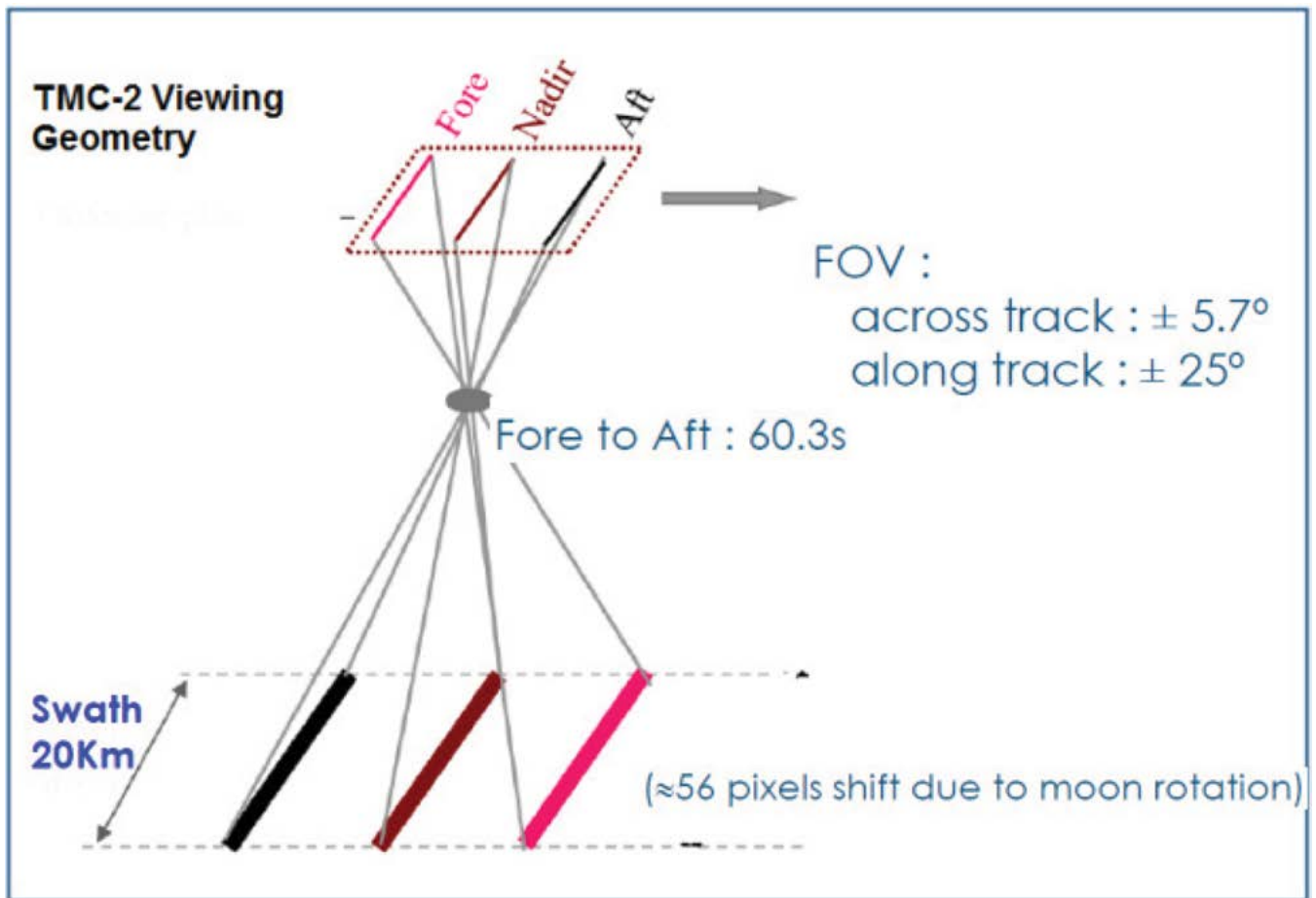
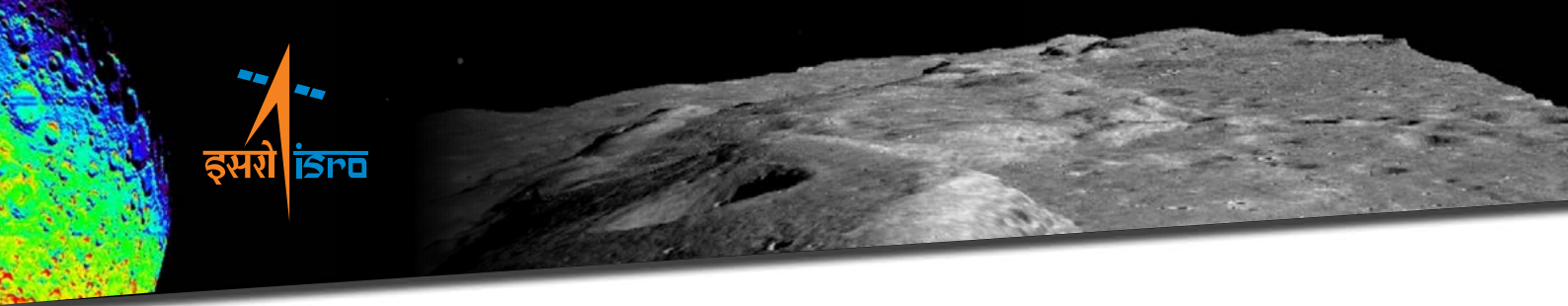
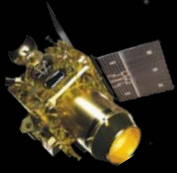


Figure. 2.24: TMC-2 Principle of Operations.

2.6.4 In-orbit Payload Performance:

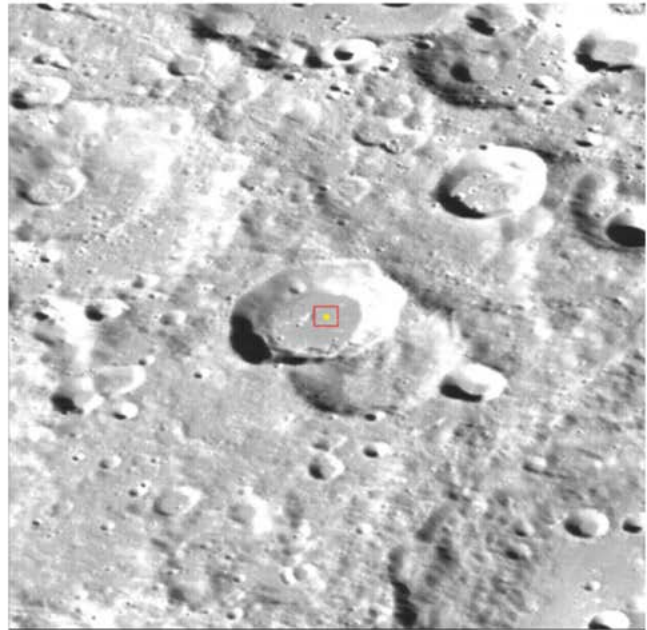
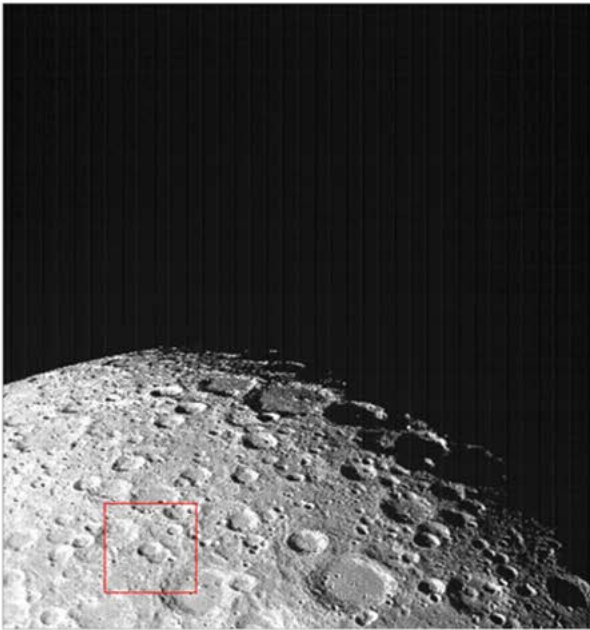
Signal-to-noise Ratio (SNR):

SNR defines the level of desired signal in comparison to the background noise. In an image, it can be measured as the ratio of mean count to the standard deviation for a uniform region. Mean count and standard deviation are provided below for a space view in comparison to laboratory measurement. [Figure 2.25](#) shows uniform region selected in a Nadir image of a Lunar pole taken by TMC-2 and comparison of achieved and expected SNR (according to laboratory measurements). SNR of 108 was achieved in comparison to expected SNR of 110 at the mean count value of 130.



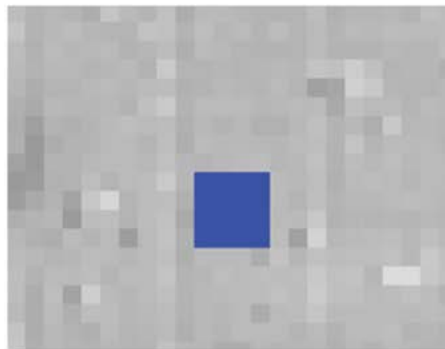
Mean and SD count for space view in comparison to Lab measurement.

Sensor	Lab measured Mean Count	Space View Mean Count	Lab Measured SD Count	Space View SD Count
Fore	42.8	43.7	3.5	3.5
Nadir	43.4	45	3.5	3.6
Aft	46	45.6	3.5	3.5



SNR

- Achieved 108
- Expected ~110

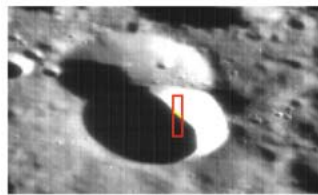


4X4 window
Mean: 130.375
SNR: 108.285

Figure. 2.25: Figure shows uniform region selected in a Nadir image of a Lunar pole taken by TMC-2 and comparison of achieved and expected SNR.

Modulation Transfer Function (MTF):

MTF describes the detector capability in maintaining the contrast of the original object in the image. Quick MTF software was used to calculate the MTF in the nadir image of a lunar pole. Figure 2.26 shows the region of interest (ROI) in a crater having a sharp edge separating the illuminated and shadow region of the crater. MTF achieved was 28 % (at Nyquist) with respect to expected MTF of 30 percent (from laboratory measurements).



- MTF :**
- Achieved : 28 % (At Nq)
 - Expected : 30 %

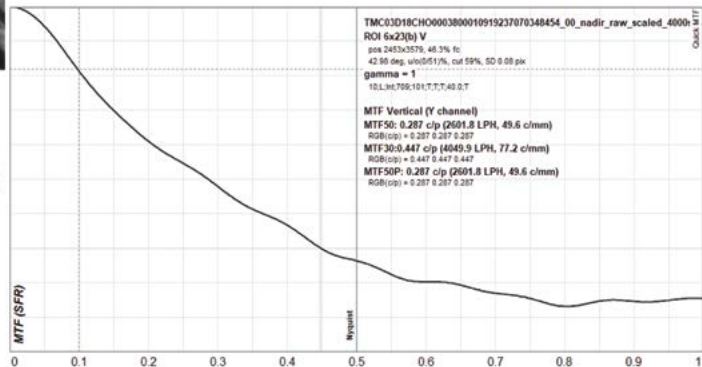


Figure. 2.26: Figure shows the ROI in a crater having a sharp edge separating the illuminated and shadow region of the crater and MTF generated.

2.6.5 Methodology

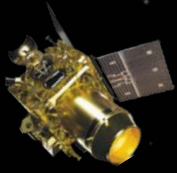
Data Products:

TMC-2 Data Products Generation System (DPGS) produces the following level of products for all the three sensors (Fore, Nadir and Aft).

Table 2.7: Table showing the details of TMC data products.

Data Products Levels	Level-0	Level-1	Level-2
Data Products Definition	Raw data along with system level corner coordinates	Radiometrically corrected, refined corner coordinates and grid data	Higher Level data products, Special Products (Image Mosaics, Anaglyph etc.)
Data Products	Fore/Aft/Nadir raw count image and browse chips Product Context	Fore/Aft/Nadir rad count image and browse chips Product Context Fore/Aft/Nadir grid data (csv)	DEM (10m) Ortho image (5m)
Data Formats	Generic Binary image, Geo Tiff, PNG, XML	Geo Tiff, PNG, XML	Geo Tiff, PNG, XML
PDS4 Data Archive	Raw data sets	Calibrated data sets	Derived data sets

TMC ortho images and DEM data sets of spatial resolution 5m, 10m respectively are useful for detailed stratigraphic mapping, surface age estimation of geological units and estimation of morphometric parameters of features with width greater than 10s of meter and lengths of more than few 100s of m.



Methodology Flow:

The TMC-2 level-2 (L-2) data sets comprising Ortho-images and DEM are evaluated for its application worth. Data gaps / jumps, Registration accuracy, DEM etc. are evaluated by comparing to validated contemporary data sets from other missions (LRO, Kaguya etc.). Visual interpretation of the Ortho-images are used for identifying and mapping of morphological features like impact craters, volcanic domes, rilles, wrinkle ridges etc. DEM is used to measure the morphometric parameters (depth, height, length, width, diameter etc.) for various Lunar features like Craters, Volcanic Domes, Wrinkle Ridges etc. These parameters are useful in deriving secondary information like viscosity and rate of effusion of Lava, Stress/strain in Lunar wrinkle ridges etc. An important aspect of geological interpretation is stratigraphic correlation through surface age determination of morphostructural entities using Crater Size Frequency Distribution (CSFD) method. TMC-2 ortho-images serve as an excellent source for identifying primary craters and measure their size / frequency distribution in order to estimate ages of different morpho-structural units. All the above help in holistically understanding the Lunar surface processes in time and space as well as how Lunar surface has evolved over the years. Broad methodology is given below as flow chart (Figure 2.27).

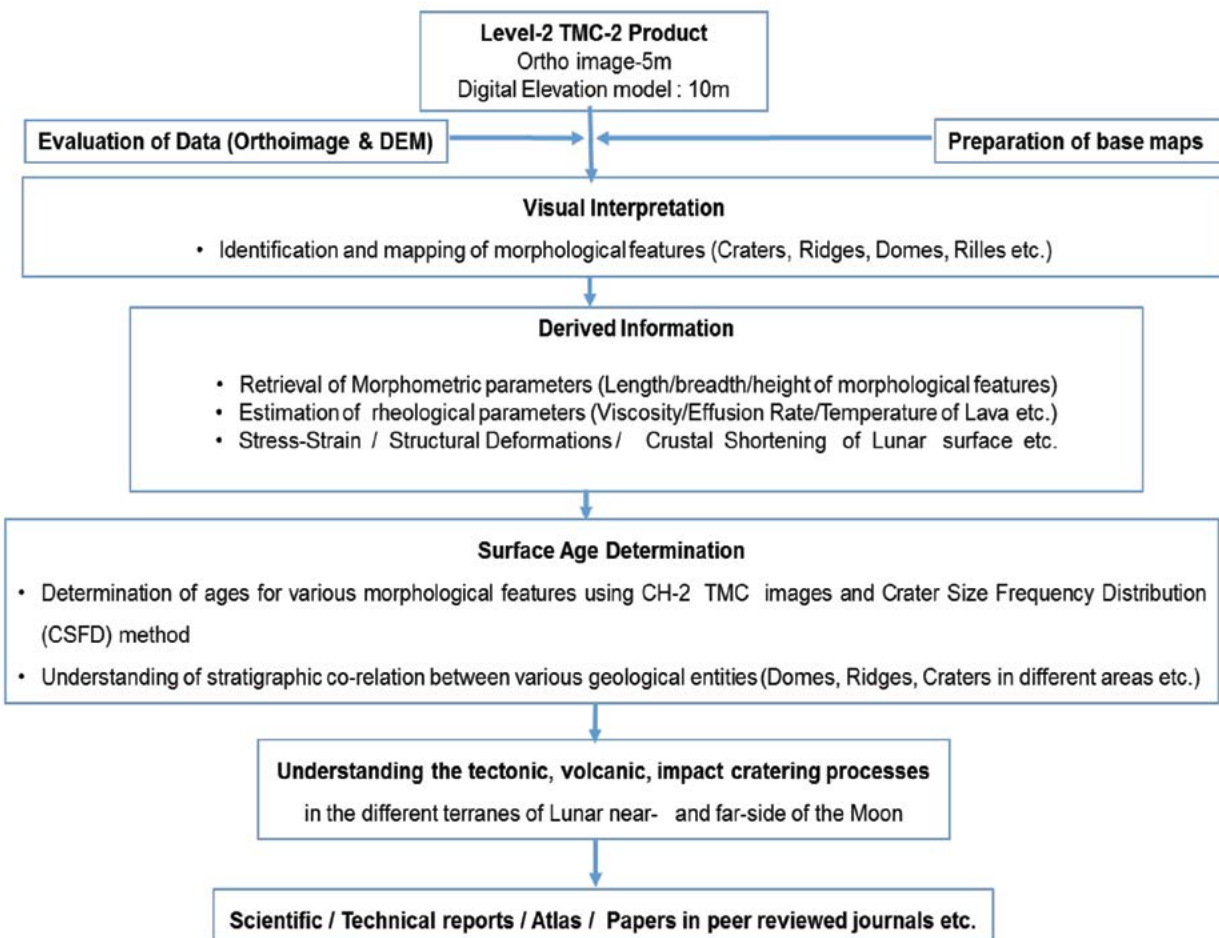


Figure 2.27: Figure showing the flow chart of methodology adopted for TMC-2 data analysis.

2.7 Orbiter High Resolution Camera (OHRC)

Orbiter High Resolution Camera (OHRC) is a panchromatic (0.45-0.70 μm) camera with a very high spatial resolution of 0.25 m (at nadir) onboard Chandrayaan-2 orbiter. OHRC is designed for imaging in very low sun elevation conditions. OHRC was primarily used to image the landing site at two different look angles from consecutive orbits to prepare a DEM and generate the hazard map.

2.7.1 Objectives:

Mission objective: Imaging of Chandrayaan-2 Landing site for preparation of high resolution DEM required for landing. It has also been used for imaging potential landing sites for Chandrayaan-3.

Science Objectives:

High resolution imaging of selected targets of scientific interest for:

- Recent volcanism sites and small features like boulders.
- Central peak of young impact craters.
- Small scale tectonic features, impact craters and mass wasting sites.
- Anthropogenic sites - landing sites (Apollo, Luna etc) of earlier and proposed future missions.

2.7.2 Instrument Specifications

OHRC is an optical camera system based on Time Delay Integration (TDI) imaging sensors with 12000 detectors. It has 4 TDI settings and 7 different integration times. [Figure 2.28](#) shows the OHRC in lab with its primary mirror visible. Technical specifications are given below in Table. 2.8

Table 2.8: OHRC instrument major specifications.

Sr. No.	Parameter	Value
1	Ground sampling distance (m) at nadir	0.25
2	Swath (km) at nadir	3
3	Spectral range (μm)	PAN (0.45-0.70)
4	TDI settings	64, 128, 192 and 256
5	Variable integration time settings (μs)	7 values: 213.84, 209.58, 205.32, 181.74, 178.14, 174.87 and 162.10

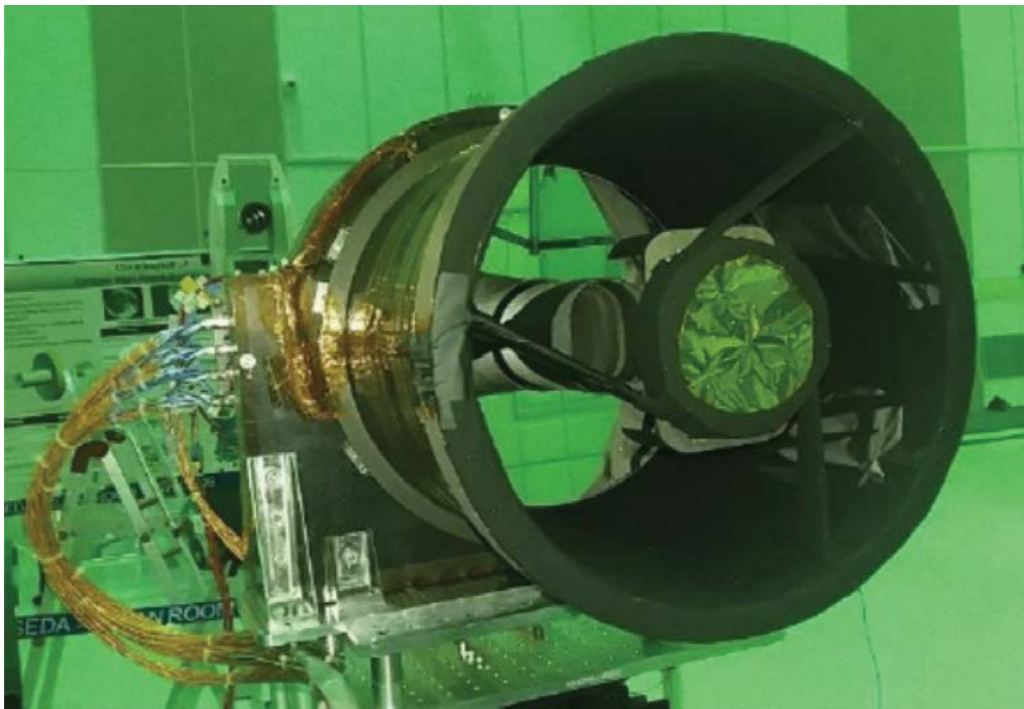
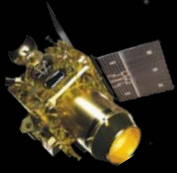


Figure 2.28: This shows the front view of the OHRC in lab.

The details of the instrument design, lab tests and calibration are given in Roy Chowdhary et al., 2020.

2.7.3 Methodology

OHRC images are of high spatial resolution which can be used to identify sub-meter scale features on lunar surface. It measures the reflected solar light and records it as digital numbers (DN) which are then converted to radiance counts through processing.

Data Processing – There are two levels of data that is being generated by data processing team.

Level 0 – This is the original data that is recorded by the instrument and provided without any data processing along with system level coordinates.

Level 1 – This is the calibrated data that has been radiometrically corrected and converted to physical units with refined coordinates.

Data Analysis – OHRC images have been used for manual identification of small features of interest. Boulders have been identified around a fresh simple crater and basic statistics were generated for the boulders distributions. Anthropogenic features have also been identified on OHRC images. A generalized flow chart for the OHRC data analysis and interpretation is given in the flow chart in [Figure 2.29](#).

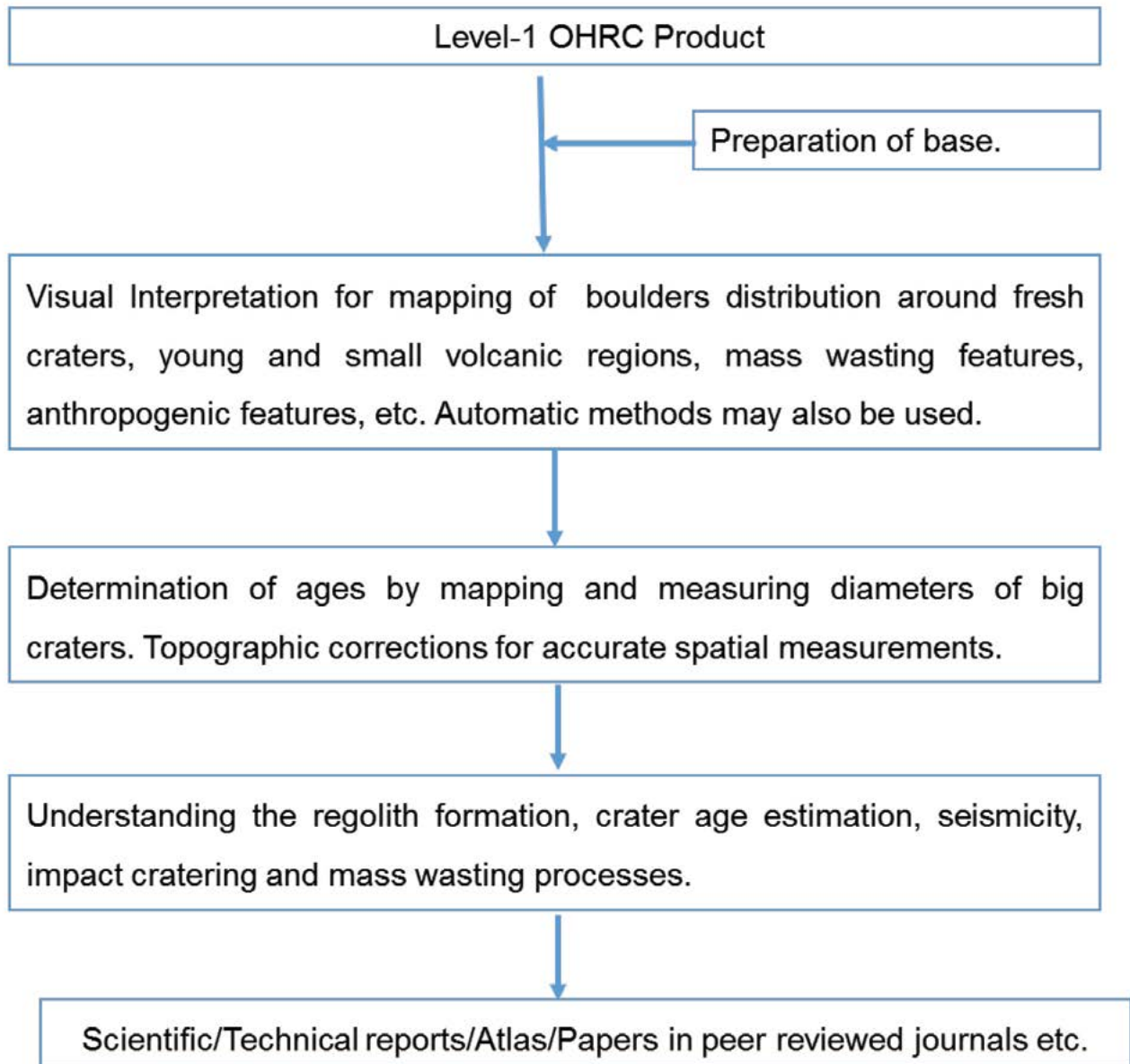
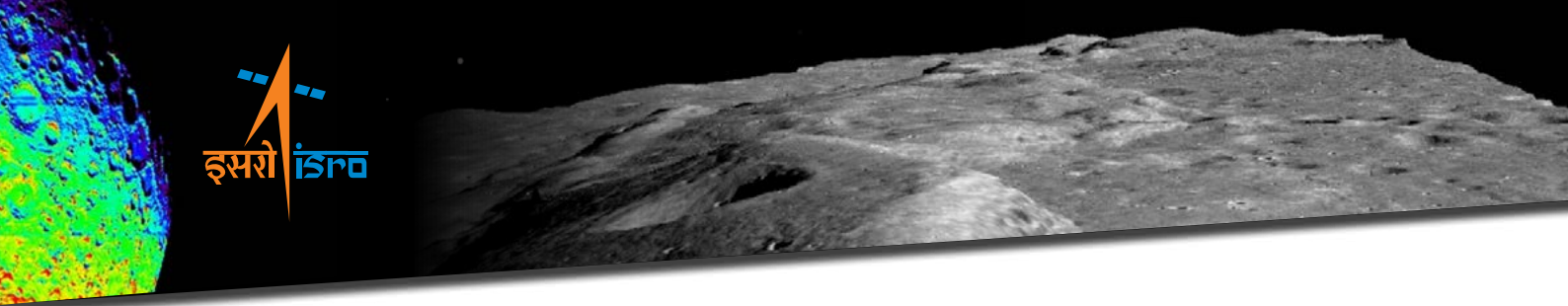


Figure 2.29: The data analysis and interpretation for generalized problems using OHRC data.

2.8 Dual Frequency Radio Science (DFRS)

DFRS is a radio science experiment used to analyze the planetary/lunar atmosphere-ionosphere. It uses two highly correlated radio frequencies in X- and S-bands. Since there is no need for any specific data to be sent for the DFRS experiment, the signals allocated for tele-command and ranging can also be used to carry out the said experiment.

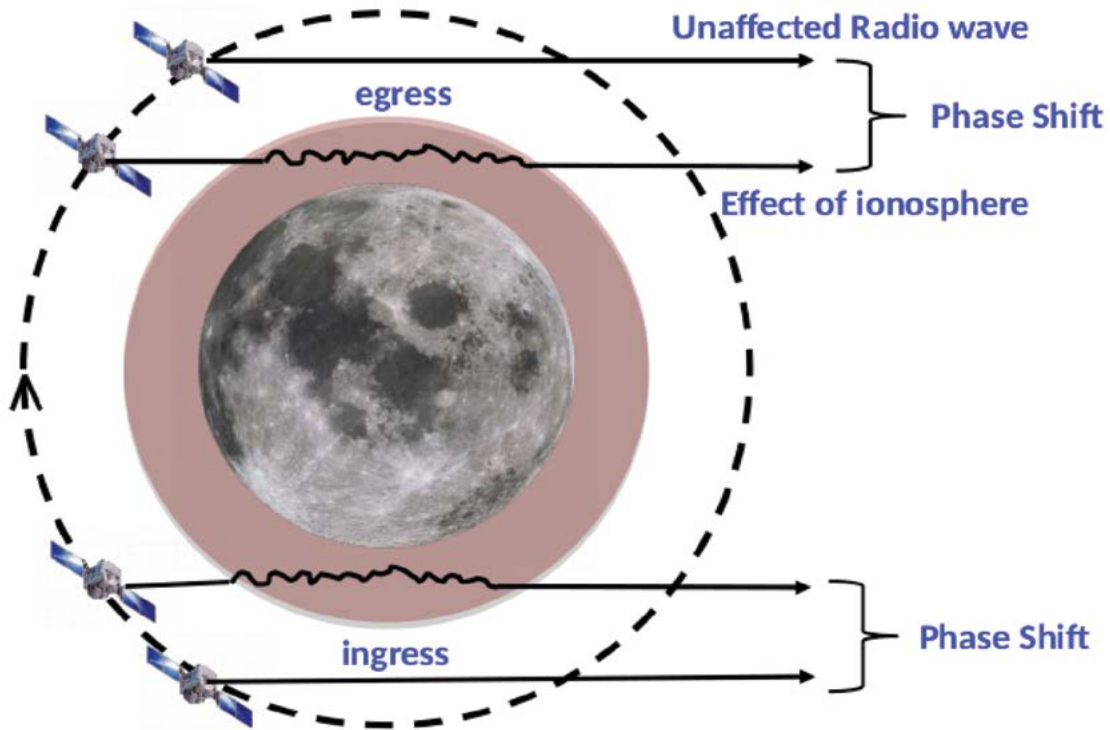
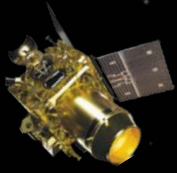


Figure 2.30 : Schematic for Radio Occultation (After Choudhary et al, 2019).

When a radio signal transmitted by a transmitting satellite is obstructed by a celestial object, it is said to be radio occulted. If the body contains an atmosphere - ionosphere then, as the satellite follows its trajectory, before being radio occulted, initial radio signals passes through the ionosphere-atmosphere before reaching the receiver. This period is said to be ingress. The signal is then completely occulted, as a result the receiver will not receive any signal but noises. As the satellite emerges from radio occultation, the signal again passes through the atmosphere-ionosphere of the body before reaching the receiver.

As the signal transverses the atmosphere of the celestial body, the signal undergoes bending due to the differential refractive index of the atmosphere (Figure 2.30). This bending introduces a path difference in the signal which in-turn introduces a phase shift. Extracting this phase shift from the received signal will help us in understanding the atmosphere of the celestial body.

Schematic diagram of Radio occultation experiment is shown in Figure 2.31. In this transmitter on spacecraft is sending radio signal toward receiver. While signal passes through the planetary atmosphere, it deviates from the straight line path.

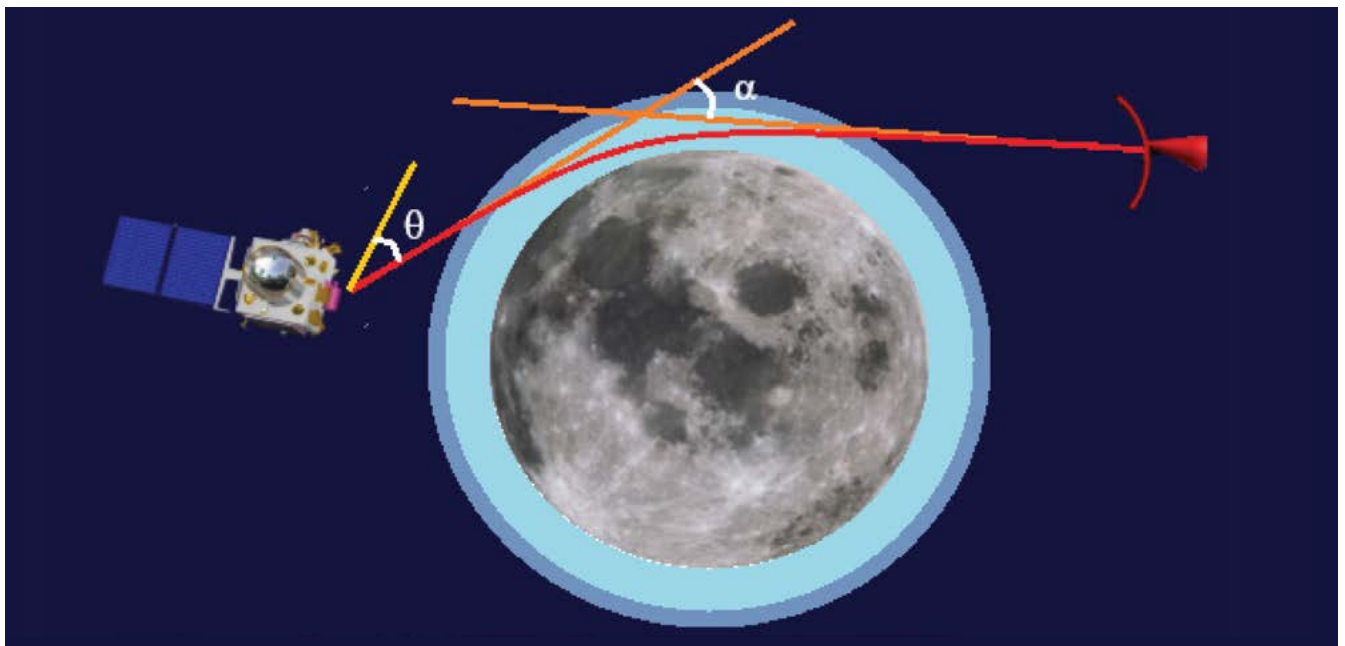
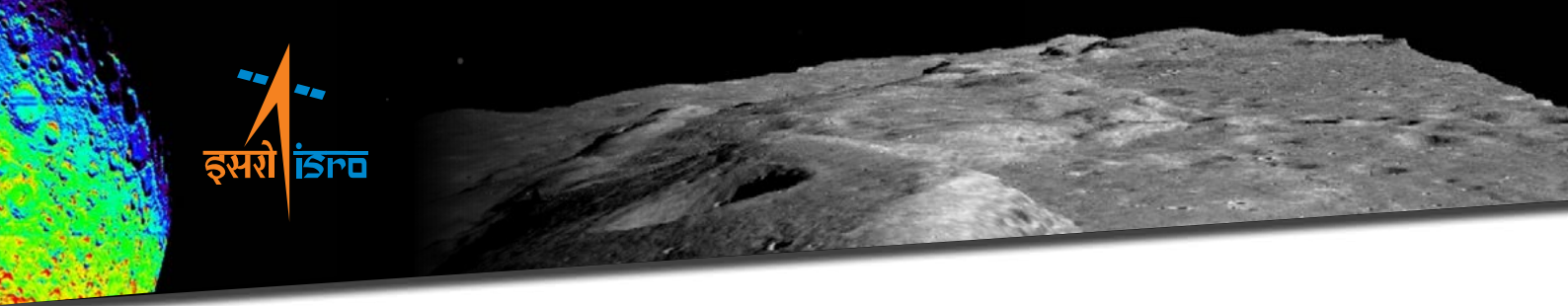


Figure 2.31: Bending of waves due to the atmosphere of the celestial body.

2.8.1 DFRS instrument and Its Scientific Objectives

The payload DFRS aims to study (a) the total electron content (TEC) of the Lunar ionosphere and its morphological changes, (b) quantification of the effect of Earth's magnetosphere and magneto-tail on the production and distribution of plasma in the Lunar Ionosphere, and (c) the altitude profiles of the lunar ionosphere. It uses Orbiter to Ground communication channel in occultation mode for this purpose.

DFRS experiment requires coherent generation of a highly stable carrier in S- and X-Band. To achieve the same, it is required to use a highly stable reference oscillator source for the carrier generation. Thus using Evacuated Miniaturized Crystal Oscillator (EMXO) as a master oscillator to generate radio signal at 20 MHz, which is then further divided to generate coherent dual frequencies at X- and S- band. It provides a short-term stability (Allan Deviation) of better than 10^{-11} in 1 sec with very low power (0.5 W after stabilization) and low mass. To generate the coherent signals, the output of 20 MHz basic EMXO source is fed to a two-way power divider. The two outputs are further fed to the carrier generating circuits using PLL synthesizers, one giving the output at S-band and the other at X-band. Both the carrier generating circuits are similar in function. Carrier is generated directly at the required band using an X-band / S-band VCO and by locking it to the reference EMXO using PLL technique. The carrier at the required frequency is generated by applying appropriate control voltage to VCO from the PLL. The VCO output is passed through a directional coupler whose coupled port output is given to the RF input port of the PLL synthesizer PE97042, the main port output being used as the carrier. A lock status is provided from PLL synthesizer, which is processed to act as the lock indication telemetry. The S-band carrier of frequency 2240MHz is amplified to a level of 26 dBm and is transmitted through a separate S-band

patch antenna having a gain of about 2 dBi. The X-band signal is also amplified to a power level of 20 dBm and then applied to the coupled port of a 10 dB directional coupler. The main port of the directional coupler is fed from the X-band Data Transmitter. The frequency of X-band signal for RAMBHA experiment is selected to be 8496 MHz. The combined signal from directional coupler is transmitted through 0.7 m reflector antenna. Hardware is realized as two packages viz. DFRS 10 which houses the X band and S band carrier generators and DFRS 20 which houses the X band and S band amplifiers. [Figure 2.32](#) shows the block diagram showing different components of DFRS. The flight models of DFRS 10, and DFRS 20 are shown in [Figure 2.33](#).

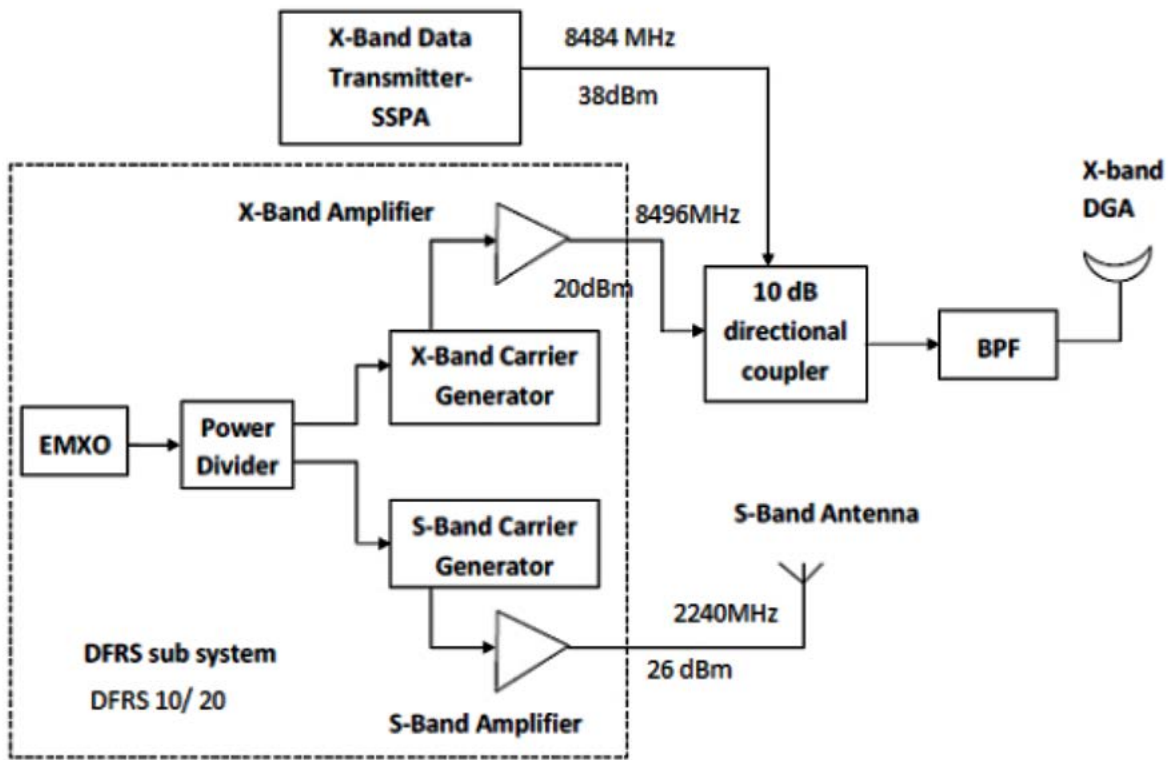


Figure 2.32: Block diagram of different components of DFRS.



DFRS-10

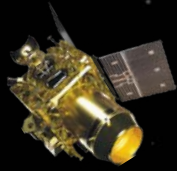


DFRS-20

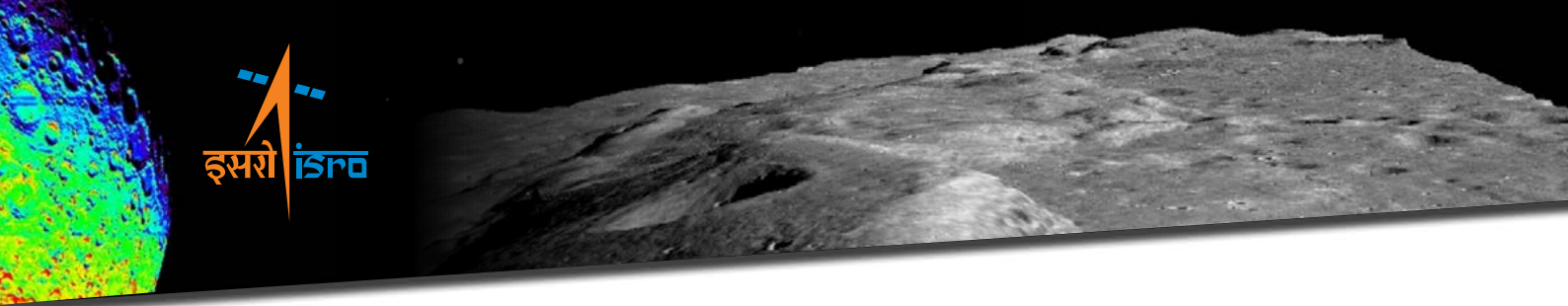
Figure 2.33: Flight model version of DFRS-10 and DFRS-20 at Chandrayaan-2 (After Choudhary et al, 2019).

References

1. Arnaud. XSPEC: The First Ten Years. In George H. Jacoby and Jeannette Barnes, editors, "Astronomical Data Analysis Software and Systems V", volume 101 of Astronomical Society of the Pacific Conference Series, page 17, (1996).
2. Athiray, P.S., Narendranath, S., Sreekumar, P., Dash, S., K., Babu, B.R.S., "Validation of methodology to derive elemental abundances from X-ray observations on Chandrayaan-1", Planet. Space Sci, 75, 188-194, (2013).
24. Athiray, P.S., P. Sreekumar, S. Narendranath and J.P.D.Gow, "Simulating charge transport to understand the spectral response of Swept Charge Devices", Astronomy and Astrophysics, 583, A97 (2015).
3. Athiray, P. S., Sudhakar, M., Tiwari, M. K., S. Narendranath, P. Sreekumar., "Planet. Space Sci"., 89, 183 (2013).
4. C. Houck and L. A. Denicola. "ISIS: An Interactive Spectral Interpretation System for High Resolution X-Ray Spectroscopy", volume 216 of Astronomical Society of the Pacific Conference Series, page 591. (2000).
5. Clark, R.N., Pieters, C.M., Green, R.O., Boardman, J.W. and Petro, N.E. "Thermal removal from near-infrared imaging spectroscopy data of the moon". Journal of Geophysical Research, 116, E00G16, doi: 10.1029/2010JE003751, (2011).
6. Cloutis, E.A., Gaffey, M.J., Jackowski, T.L., Reed, K.L., "Calibrations of phase abundance, composition, and particle size distribution for olivine-orthopyroxene mixtures from reflectance spectra". J. Geophys. Res. Solid Earth 91 (B11), 11641–11653 (1986).
7. Cook, J.C., Stern, S.A., Feldman, P.D. et al., "New upper limits on numerous atmospheric species in the native lunar atmosphere". Icarus 225, 6 81–6 87 (2013).
8. Das, T.P et al., "Chandra's Atmospheric Composition Explorer-2 onboard Chandrayaan-2 to study the lunar neutral exosphere" , Current Science, 118(2):202, DOI: 10.18520/cs/v118/i2/202-209, (2020).
9. Gaffey, M.J., Cloutis, E.A., Kelley, M.S., Reed, K.L., "Mineralogy of asteroids". In: Bottke, W.F., Cellino, A., Paolicchi, P., Tucson, Binzel R.P. (Eds.), Asteroids III. The University of Arizona Press, Arizona, pp. 183–204 (2002).
10. Hapke, B., "Theory of Reflectance and Emittance Spectroscopy". Cambridge University Press. <https://doi.org/10.1017/CB09781139025683> (2012).
11. Li, S., Milliken, R.E., "Water on the surface of the Moon as seen by the Moon Mineralogy Mapper. Distribution, abundance, and origins". Sci. Adv. 3 (9) <https://doi.org/10.1126/sciadv.1701471> e1701471, (2017).

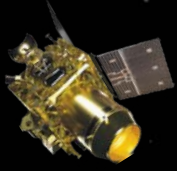


12. Milliken, R.E., Mustard, J.F., “Quantifying absolute water content of minerals using near-infrared reflectance spectroscopy”. *J. Geophys. Res. Planets* 110 (E12) (2005).
13. Milliken, R.E., Mustard, J.F., a. “Estimating the water content of hydrated minerals using reflectance spectroscopy: I. Effects of darkening agents and low-albedo materials”. *Icarus* 189 (2), 550–573 (2007).
14. Milliken, R.E., Mustard, J.F., b. “Estimating the water content of hydrated minerals using reflectance spectroscopy: II. Effects of particle size”. *Icarus* 189 (2), 574–588 (2007).
15. Mohammed Modi, Rajkumar Gupta, S. Kane, et al. “A soft x-ray reflectivity beamline for 100- 1500 eV energy range at indus-2 synchrotron radiation source. In *AIP Conference Proceedings*”, volume 2054, page 060022,. doi: 10.1063/1.5084653 (2019).
16. Morse A.D. , K. Altwegg, D.J. Andrews, H.U. Auster, C.M. Carr, M. Galand, F. Goesmann, S. Gulkis, S. Lee, I. Richter, S. Sheridan, S.A. Stern, M.F. A’Hearn, P. Feldman, J. Parker, K.D. Retherford, H.A. Weaver, I.P. Wright, “The Rosetta campaign to detect an exosphere at Lutetia, *Planetary and Space Science*”, Volume 66, Issue 1, Pages 165-172, (2012) <https://doi.org/10.1016/j.pss.2012.01.003>.
17. M. Tiwari, Pooja Gupta, Anil Sinha, et al. “A micro focus x-ray fluorescence beamline at indus-2 synchrotron radiation facility. *Journal of synchrotron radiation*”, 20:386–9,. doi: 10.1107/S0909049513001337 (2013).
18. Mustard, J. F., Pieters, C. M., Isaacson, P. J., Head, J. W., Besse, S., Clark, R. N., Klima, R. L., Petro, N. E., Staid, M. I., Sunshine, J. M., Runyon, C. J., Tompkins, S., “Compositional diversity and geologic insights of the Aristarchus crater from Moon Mineralogy Mapper data”. *J. Geophys. Res.*, 2011, 116, E00G12 (2011).
19. Netra S. Pillai, Narendranath, S., Vadodariya, K., Tadepalli, S. P., Radhakrishna, V., Tyagi, A., Yadav, R., Singh, B., Sharan, V., Athiray, P. S., Sreekumar, P., Sankarasubramanian, K., Bhatt, M., Basu, S., Amit, Mithun, N. P. S., and Vadawale, S., , ICARUS DOI: 10.1016/j. icarus.2021.114436 “Chandrayaan-2 Large Area Soft X-ray Spectrometer (CLASS): Calibration, In-flight Performance and First results”, (2021).
20. N. P. S. Mithun, Santosh V. Vadawale, Aavek Sarkar et al. “Solar X-Ray Monitor on Board the Chandrayaan-2 Orbiter: In-Flight Performance and Science Prospects. *Sol. Phys.*,” 295(10):139,. doi: 10.1007/ s11207-020-01712-1 (October 2020).
21. N. P. S. Mithun, Santosh V. Vadawale, Arpit R. Patel, et al. “Data processing software for chandrayaan-2 solar x-ray monitor. *Astronomy and Computing*,” 34:100449, a. ISSN 2213-1337. doi: <https://doi.org/10.1016/j.ascom.2021.100449>. URL <https://www.sciencedirect.com/science/article/pii/S2213133721000032> (2021).
22. N. P. S. Mithun, Santosh V. Vadawale, M. Shanmugam et al. “Ground calibration of Solar



X-ray Monitor on board the Chandrayaan-2 orbiter. *Experimental Astronomy*, 51(1):33–60, b. doi: 10.1007/s10686-020-09686-5 (February 2021).

25. Pieters, C.M., Goswami, J.N., Clark, R.N., Annadurai, M., Boardman, J., Buratti, B., Combe, J.P., Dyar, M.D., Green, R., Head, J.W., Hibbitts, C., Hicks, M., Isaacson, P., Klima, R., Kramer, G., Kumar, S., Livo, E., Lundeen, S., Malaret, E., McCord, T., Mustard, J., Nettles, J., Petro, N., Runyon, C., Staid, M., Sunshine, J., Taylor, L.A., Tompkins, S., Varanasi, P., “Character and spatial distribution of OH/H₂O on the surface of the Moon seen by M3 on Chandrayaan-1”. *Science* 326 (5952), 568–572. <https://doi.org/10.1126/science.1178658> (2009).
26. Roy Chowdhury, A., Banerjee, A., Joshi, S. R., Dutta, M., Kumar, A., Bhattacharya, S., Amitabh, Rehman, S., U., Bhati, S., Karelia, J. C., Biswas, A., Saxena, A. R., Sharma, S., Somani, S. R., Bhagat, H. V., Sharma, J., Ghonia, D. N., Bokarwadia, B. B., and Parasar, A.: “Imaging Infra-Red Spectrometer onboard Chandrayaan-2 Orbiter”. *Current Science*; 118(3):368-375 (02/2020).
27. Roy Chowdhury, A., Saxena, M., Kumar, A., Joshi, S. R., Singh, A., Dagar, A. K., Mittal, M., Kirkire, S., Desai, J., Shah, D., Karelia, J. C., Kumar, A., Jha, K., Das, P., Bhagat, H. V., Sharma, J., Ghonia, D. N., Desai, M., Bansal, G., Gupta, A. “Orbiter High Resolution Camera onboard Chandrayaan-2 Orbiter”, *Current Science*, Vol. 118, No. 4, (2020).
28. S. Narendranath, PS Athiray, P Sreekumar, BJ Kellett, L Alha, CJ Howe, KH Joy, M Grande, J Huovelin, IA Crawford, U Unnikrishnan, Lalita S, S Subramaniam, SZ Weider, LR Nittler, O Gasnault, D Rothery, VA Fernandes, N Bhandari, JN Goswami, MA Wieczorek and the C1XS team, “Lunar X-ray fluorescence observations by the Chandrayaan-1 X-ray Spectrometer (C1XS): Results from the nearside southern highlands” , *Icarus*, 214, 53–66 (2011)
29. Schlappi B., et al., “Influence of spacecraft outgassing on the exploration of tenuous atmospheres with in situ mass spectrometry”. *Journal of Geophysical Research Space Physics*, American Geophysical Union/Wiley, 115, pp.A12313.10.1029/2010JA015734, (2010).
30. Sridharan R., S.M.Ahmed, TirthaPratim Das, P.Sreelatha, P. Pradeep Kumar, Neha Naik, Gokulapati Supriya, Corrigendum to “The Sunlitlunar atmosphere: A Comprehensive study by CHACE on the Moon Impact Probe of Chandrayaan-1”, *Planetary and Space Science*, 111167–168, (2015).



CHAPTER 3

Science Results from Chandrayaan-2 Large Area Soft X-ray Spectrometer (CLASS)

In the previous chapter, the payloads details were presented. This chapter provides the scientific details from CLASS payload. The major science outcome from the analysis of CLASS data are discussed below.

3.1 Science Outcomes

The major outcomes from CLASS observations can be summarized as follows,

- Largest coverage in X-rays.
- Highest spatial resolution elemental maps.
- First global distribution of Na.
- First remote detection of minor elements Cr and Mn.
- High time resolution measurements of the particle dynamics in the geotail.
- Clustering of particle enhancements near lunar poles discovered.

3.2 Global Measurements

X-ray spectrometers flown to the Moon in the past 50 years together have covered only less than 20% of the surface ([Figure 3.1a](#)). Chandrayaan-2 Large Area Soft X-ray Spectrometer has made a significant improvement over this with the largest coverage in X-rays ever done. [Figure 3.1 b](#) shows the coverage with CLASS when there is a XRF signal detected. As the strength of the XRF signal depends on solar activity, the spatial resolution achieved is currently different across the map. The red areas on the map are regions with higher spatial resolution than previous elemental maps. The largest coverage is for the elements O, Mg, Al and Si which are excited even at low levels of solar activity.

Oxygen is the most abundant element in the lunar surface with an abundance in a narrow range of ~ 40 – 45 wt %. All of this is locked as oxides into minerals. Studies show that Oxygen can be released from these minerals and thus is a potential source for insitu resource utilization for future missions. CLASS detects the XRF line from Oxygen even at very low solar activity levels.

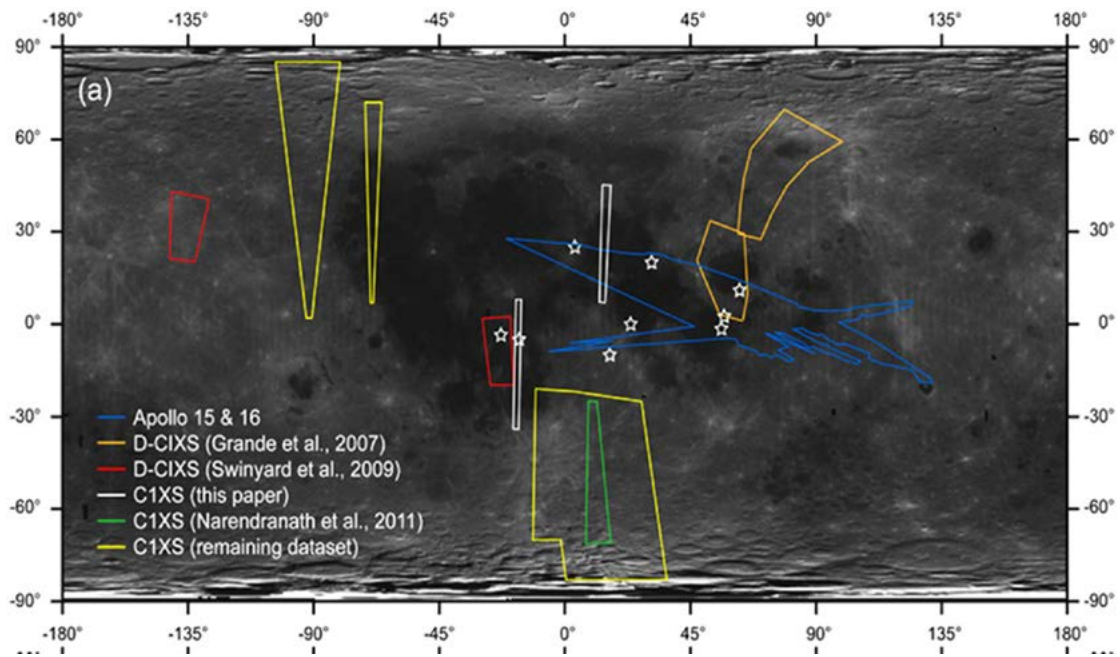


Figure 3.1(a): X-ray coverage of the Moon from pre-Chandrayaan-2 measurements (Ref: Weider et al, 2012).

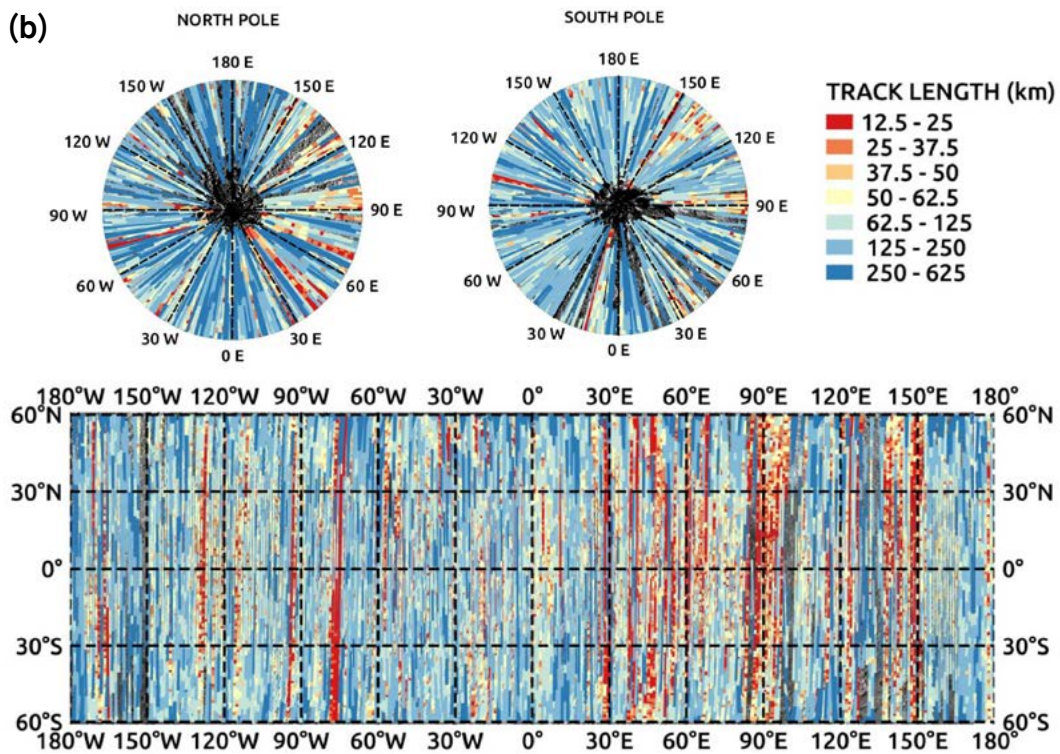
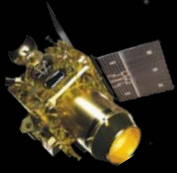


Figure 3.1 (b): X-ray Fluorescence coverage with Chandrayaan-2 Large Area Soft X-ray Spectrometer



3.3 Lunar Surface Chemistry: Regional Studies

It is well established that the mare and highland regions of the Moon are clearly distinct in their compositions. Mare regions contain more of Mg, Fe and Ti while highlands are rich in Al and Ca. However, deriving the elemental weight % at regions from where there are no returned samples enable us to bring out the difference in composition beyond this broad classification. [Figure 3.2](#) shows two regions where such a study was done (Netra et al, 2021) with R1 a region in the far side highlands and R2 a track in Mare Imbrium. The elemental abundances derived show the clear distinction. The far side highland composition show lower Al values than found in the returned samples. Chang'e-3 landed in Mare Imbrium, east of the region R2 sampled by CLASS and the insitu measurements from Chang'e-3 X-ray spectrometer is also plotted in [Figure 3.3](#). Mare Imbrium region is geochemically complex with multiple emplacements of melts over its geological history. CLASS measurements show higher Al compared to Chang'e-3 with similar values for Mg.

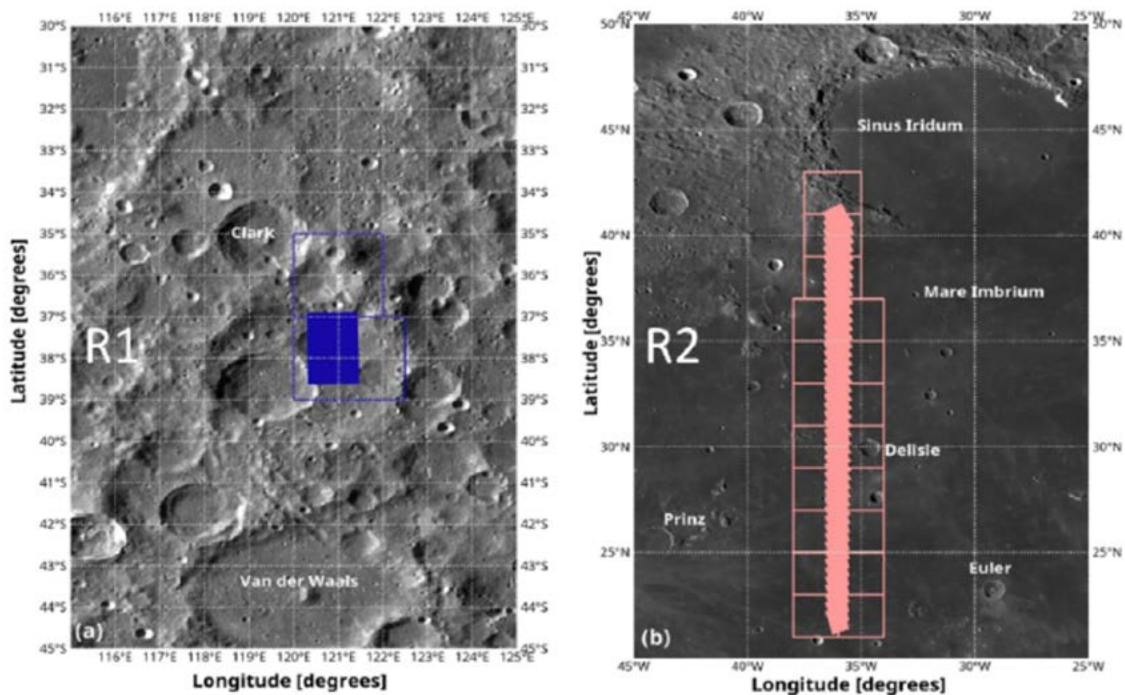


Figure 3.2: CLASS observations in the far side highland (R1) and a region in Mare Imbrium (R2) (Netra et al, 2021).

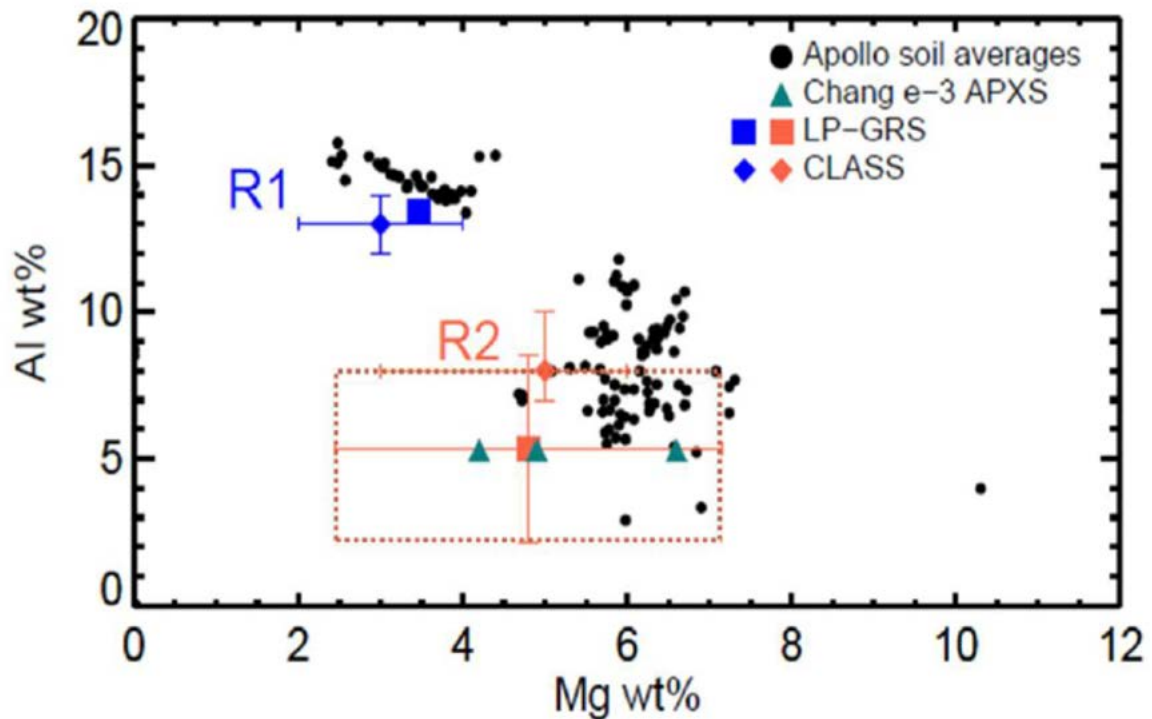


Figure 3.3: Elemental abundances of Mg and Al derived from R1 (Far side highlands) and R2 (In Mare Imbrium) compared to Apollo soil averages and Chang'e-3 insitu measurements (Netra et al, 2021).

Figure 3.4 shows a track through Mare Tranquillitatis and Mare Nectaris during a strong solar flare of M4.4 class enabling mapping of all the major elements proposed with CLASS.

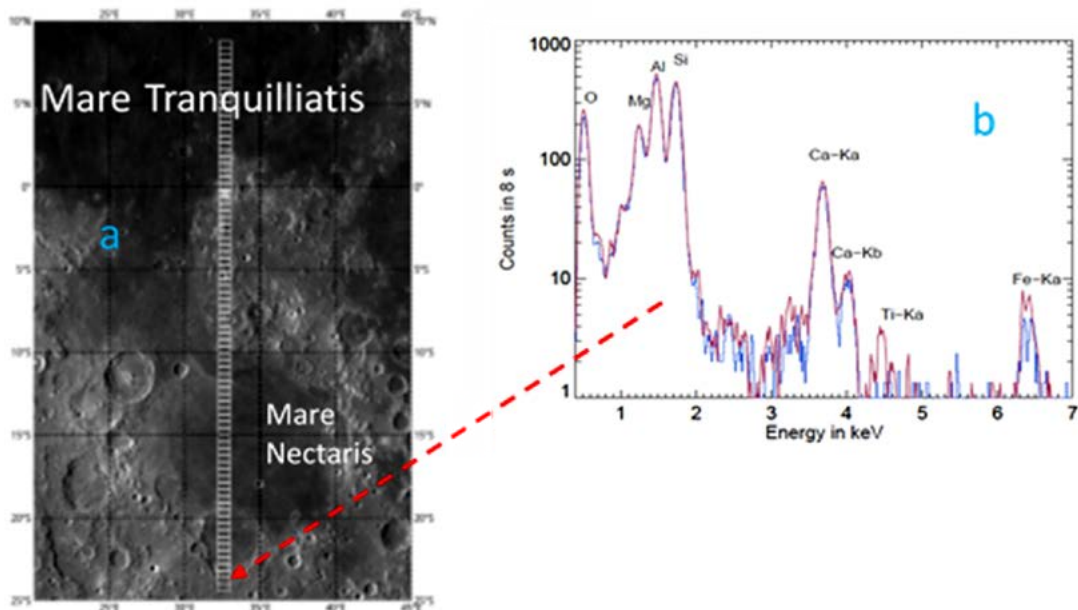


Figure 3.4: (a) A track across the near side Mare at 12.5 Km spatial resolution. (b) Spectra from two adjacent pixels show discernible differences in composition. All major elements present are clearly detected.

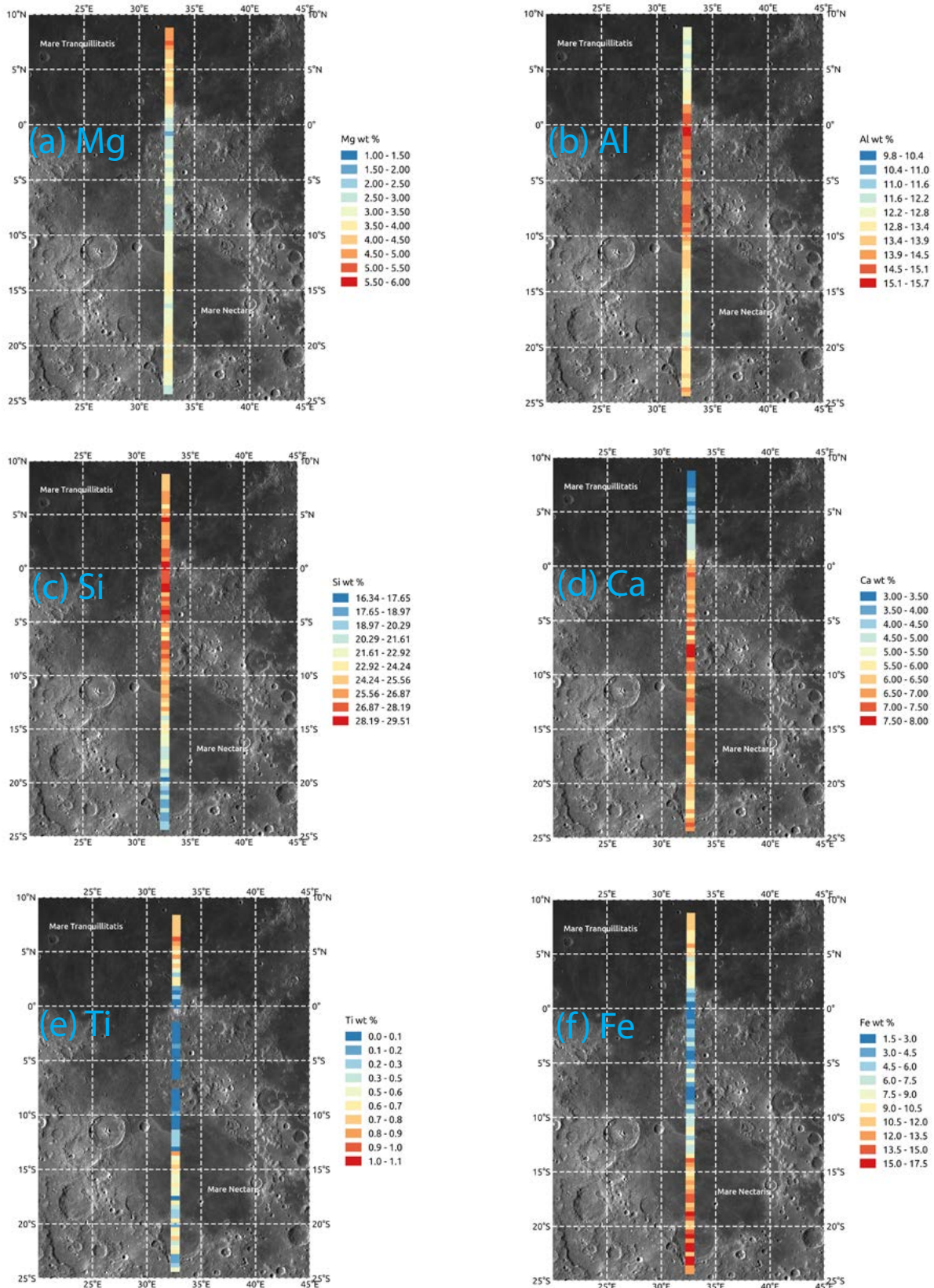
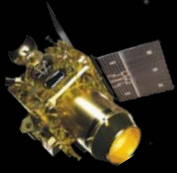


Figure 3.5 : Elemental maps of (a) Mg , (b) Al, (c) Si, (d) Ca (e) Ti and (f) Fe show compositional differences at the spatial resolution of 12.5 km , first of its kind.

The elemental maps show compositional difference at the highest spatial scales ever which allows us to study the geochemistry of the region in detail. [Figure 3.6](#) shows the expected anti correlation between Al and Fe across the track very clearly. Small features such as a fresh crater (marked in [Figure 3.6](#)) is revealed as well.

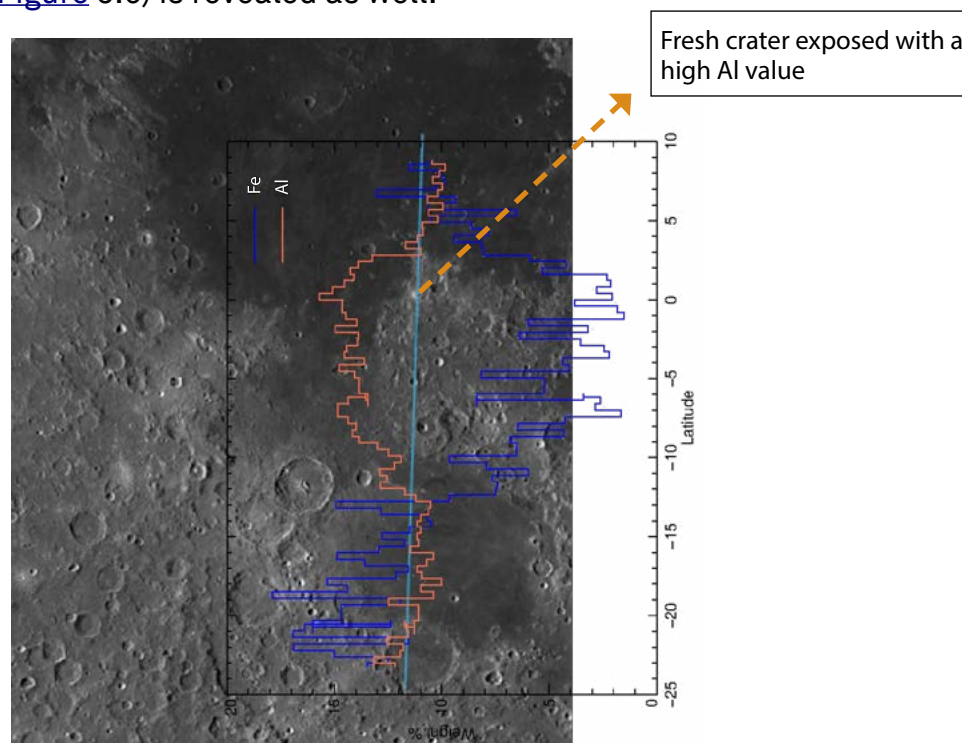


Figure 3.6: Al and Fe abundance (in weight %) shows the expected anti-correlation across the track. Small features such as freshly exposed crater (in the background LRO-WAC image) shows high Al value.

3.4 Detection of Minor Elements

CLASS has detected Na, Cr and Mn all of which occur in small amounts in lunar rocks. Na was first detected by Chandrayaan-1 X-ray Spectrometer (Athiray et al, 2014) in the region of the Tycho crater ejecta. [Figure 3.7](#) shows an example of Na detection from CLASS in a region in the Mare Imbrium. Further, we have mapped 3 sigma detections of Na line with CLASS to generate its global distribution. [Figure 3.8](#) shows a subset of these detections where we have simultaneous measurement of solar spectrum with XSM. This is crucial to model the Na line from Moon accurately (work in progress). Na is a moderately volatile element and occurs as minor to trace element in the Apollo returned soil samples. The detection here shows that the abundance of Na is variable and could possibly suggest new lithologies not found in Apollo samples. Mapping of the exospheric Na from ground has shown that it varies spatially and temporally but correlation to the surface has not been so far possible. With the observations from CLASS, a direct link of exospheric Na to surface can be established (with global data).

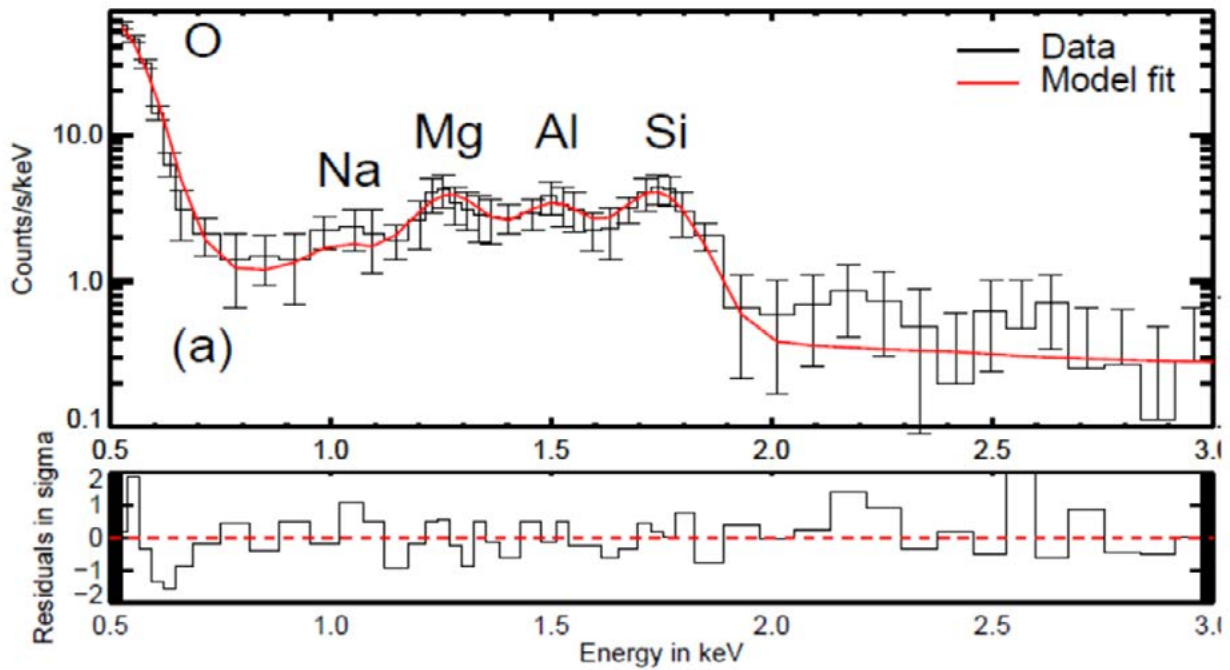
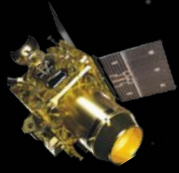


Figure 3.7: Lunar XRF spectrum from a region in Mare Imbrium modelled. There is a clear detection of Na XRF line.

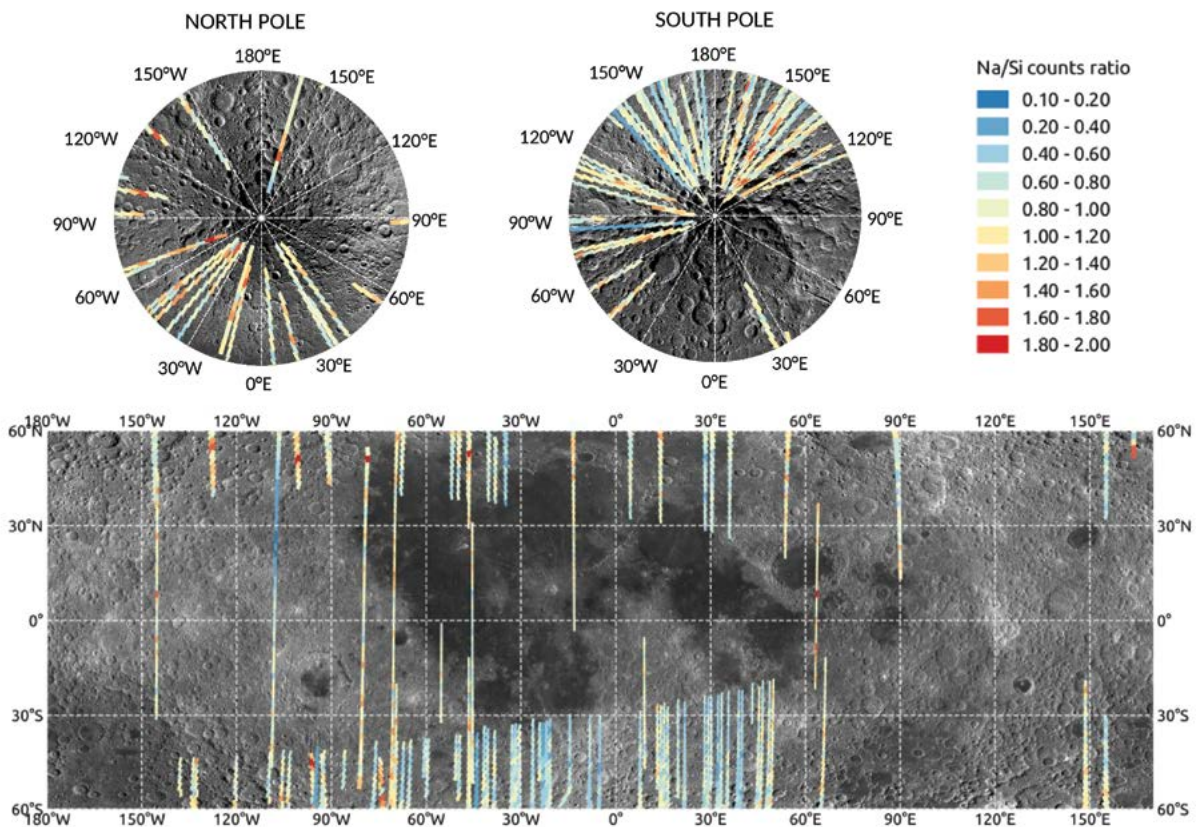
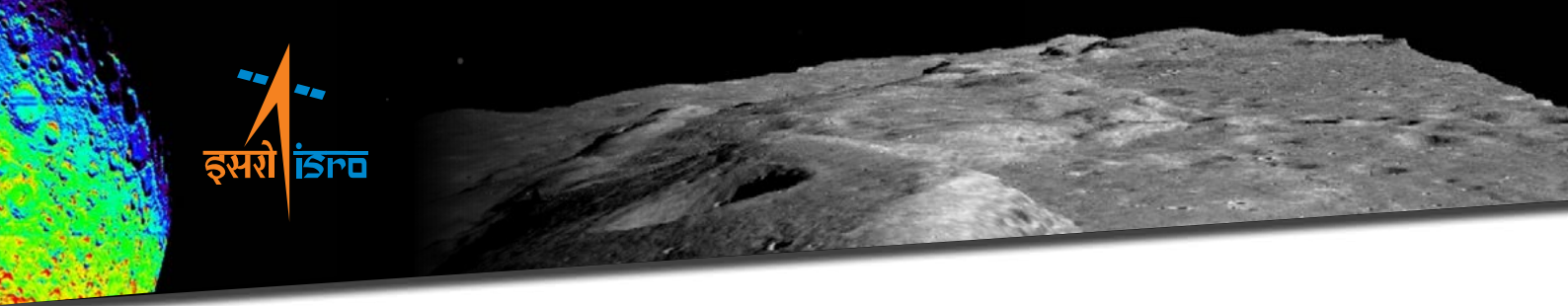


Figure 3.8: Na detections with CLASS (only intervals where XSM spectrum is available is plotted). The weight % of Na in these areas are being derived (work in progress).



CLASS detects for the first time Cr and Mn remotely in the near side Mare during a strong solar flare (Figure 3.9). Cr and Mn on the Moon has been measured only from the returned samples and meteorites. Lunar Cr is mostly contained in the mineral Chromite. The weak signals detected here suggests bulk Cr at < 1 wt % level. Though in minor quantities, these elements are important for deeper insights into the nebular conditions as well as planetary differentiation.

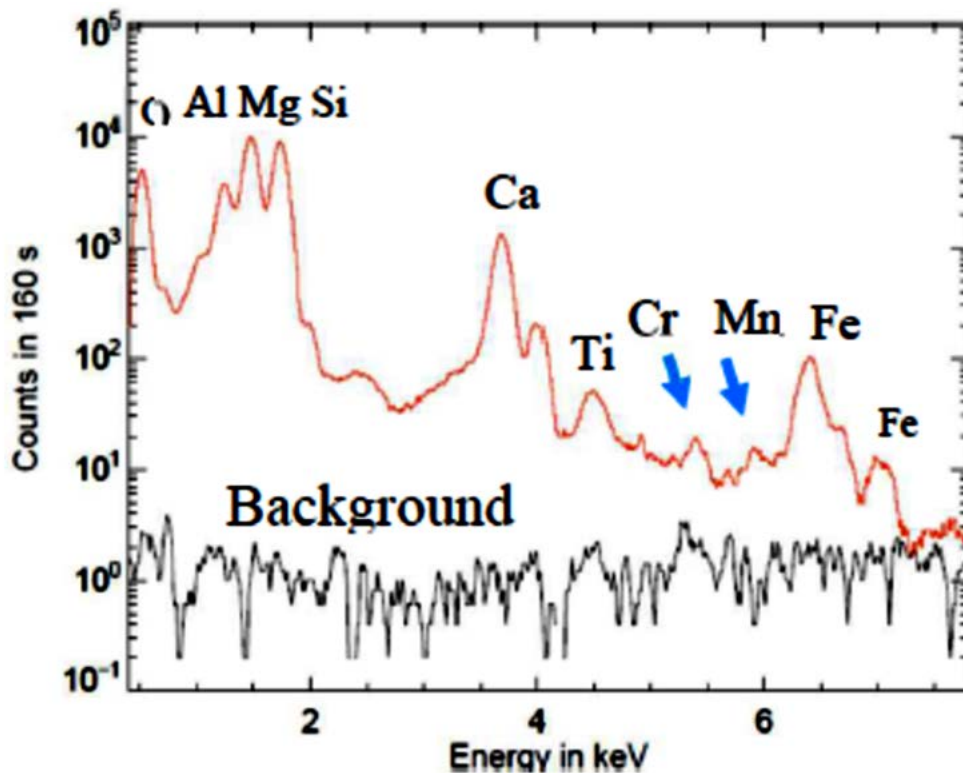


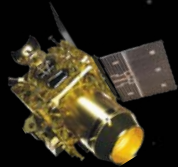
Figure 3.9: First detection of Cr and Mn through remote sensing with CLASS from a 250 km x 12.5 km pixel in Mare Nectaris (Narendranath et al, NASA_SSERVI and ELS 2021 proceedings 2021).

3.7 Summary

CLASS X-ray Fluorescence experiment has mapped ~ 95 % the lunar surface in X-rays for the first time. In addition to the major refractory elements, minor elements Na, Mn and Cr are also detected during strong solar flares. Particle dynamics at lunar distances are also studied with CLASS during the passage through geotail once a month.

Publications

1. Netra S Pillai, S. Narendranath, K. Vadodariya, Srikar P Tadeipalli, Radhakrishna V, Anurag Tyagi, Reena Yadav, Brajpal Singh, Vaishali Sharan, P. S. Athiray, P. Sreekumar, K. Sankarasubramanian, Megha Bhatt, Amit Basu Sarbadhikari, N. P. S. Mithun, Santosh Vadawale, 'Chandrayaan-2 Large Area Soft X-ray Spectrometer (CLASS): Calibration, In-flight performance and first results' Icarus, 363, 15, 114436 (2021)



2. Vatedka, R., Tyagi, A., Narendranath, S., Vadodariya, K., Yadav, R., Singh, B., Balaji, G., Satya, N.K., Shetty, A., Kumar, H., Kumar, Vaishali, S., Pillai, N., Tadepalli, S., Raghavendra, V., Sreekumar, P., Agarwal, A., Valarmathi, N., 'Chandrayaan-2 large area soft x-ray spectrometer', Current science 118, 219, (2020).

References

1. Athiray P. S., S. Narendranath, P.S.M.G., 2014. C1xs results—first measurement of enhanced sodium on the lunar surface. Planetary and Space Science 104, 279 – 287.
2. Narendranath et al, NASA_SSERVI and ELS 2021 proceedings 2021.
3. Remote sensing minor elements on the lunar surface, S. Narendranath, Netra S Pillai, R.Chakrabarti, M. Bhatt, D. Dhingra, P.Sreekumar, Joint NASA Exploration Science Forum and European Lunar Symposium 2021.
4. Weider, S., Kellett, B., Swinyard, B., Crawford, I., Joy, K., Grande, M., Howe, C., Huovelin, J., Narendranath, S., Alha, L., Anand, M., Athiray, P., Bhandari, N., Carter, J., Cook, A., d'Uston, L., Fernandes, V., Gasnault, O., Goswami, J., Gow, J., Holland, A., Koschny, D., Lawrence, D., Maddison, B., Maurice, S., McKay, D., Okada, T., Pieters, C., Rothery, D., Russell, S., Shrivastava, A., Smith, D., Wieczorek, M., 2012. The chandrayaan-1 x-ray spectrometer: First results. Planetary and Space Science 60, 217 – 228.



Contact detail: Dr. Shyama Narendranath K.C. (kcshyama@ursc.gov.in)

Science Results from Solar X-ray Monitor (XSM)

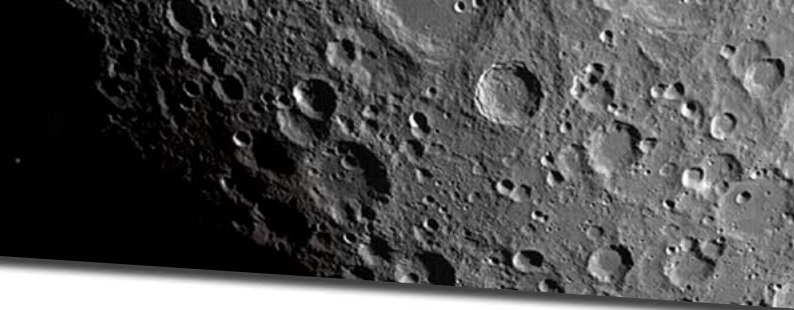
In this chapter, the results obtained from XSM payload are presented.

The solar minimum at the end of cycle 24 was the deepest minimum in the recent history, with the year 2019 having the largest number of sunspot-less days in the past hundred years. This provided a unique opportunity to study the quiet Sun corona, which was well exploited by the Solar X-ray Monitor (XSM) [Vadawale et al., 2014, Shanmugam et al., 2020] on board the second Indian lunar mission, Chandrayaan-2. The XSM was the only soft X-ray spectrometer monitoring the Sun during this period, and had sufficient sensitivity to measure, possibly the lowest level of solar X-ray intensity, with a very high (~ 35) signal to background ratio [Mithun et al., 2020]. This has yielded very interesting observations of the microflares occurring outside active region as well as elemental abundances in the quiet Sun corona. XSM has also observed number of B-class flares and their analysis has yielded unprecedented observations of variation of the elemental abundances during such flares. These results, as well as the ongoing analysis of the XSM observation are described in the following sections.

4.1 Sub-A Class Microflares and Elemental Abundances in Quiet Sun

[Figure 4.1](#) shows the solar X-ray flux measured by the XSM in the energy range of 1 to 15 keV during the first two observing seasons (referred to as DD1 lasting from September 12, 2019 to November 20, 2019 and DD2 lasting from February 14, 2020 to May 20, 2020). The solar X-ray light curve for the entire period exhibits rich variability including multiple small flares.

Seven B-class solar flares, several fainter A-class and a large number of sub-A class flares (in the conventional scale defined by the 1 – 8 Å band of GOES/XRS, the de-facto monitor for solar X-ray flux) were observed by the XSM during this period. The lowest flux level in the 1 – 8 Å range during these periods is about $6 \times 10^{-10} \text{ W m}^{-2}$ corresponding to A0.06 class of solar activity, which is well below the detection limit of the GOES/XRS. The light curve for the selected period shows a large number of flare-like events, lasting for a few minutes and having their peak flux well below A-class, even though there are no active regions present on the Sun. A total of 98 sub-A class microflares are identified during this period, each marked in the figure. While a small number of such microflares occurring outside ARs have been reported earlier with Yokoh (4 microflares [Krucker et al., 1997]), SphinX (16 microflares [Sylwester et al., 2019]), as well as recently with NuSTAR (3 microflares [Kuhar



et al., 2018]), this is the first observation of such a large number of microflares occurring outside Active Regions.

Most of the microflares are impulsive in nature and in all cases where the microflare location could be identified from the EUV images, they are associated with magnetic bipolar regions. By fitting the observed X-ray spectra of microflares with a two-temperature isothermal emission model, we obtained the temperature and emission measure associated with the flaring plasma, which are shown in [Figure 4.2a](#). Further, by using these spectroscopic results with the volume estimates from analysis of EUV images from SOD/AIA, the thermal energies of these microflares are estimated to range from $\sim 3 \times 10^{26} - 6 \times 10^{27}$ erg and the flare frequency distribution follows a power law as shown in [Figure 4.2b](#). These observations provide the first comprehensive analysis of a large sample of quiet Sun microflares, demonstrating that microflares are not confined only to the active regions and supports the hypothesis on presence of small scale impulsive events everywhere on the solar corona.

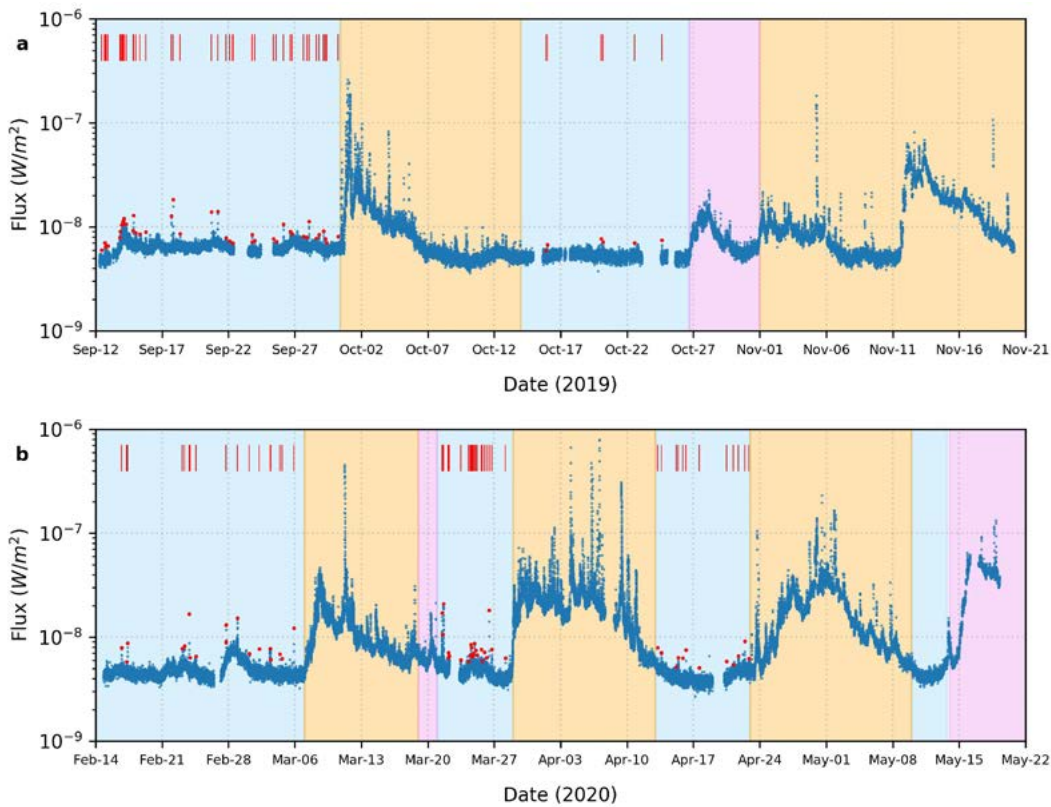
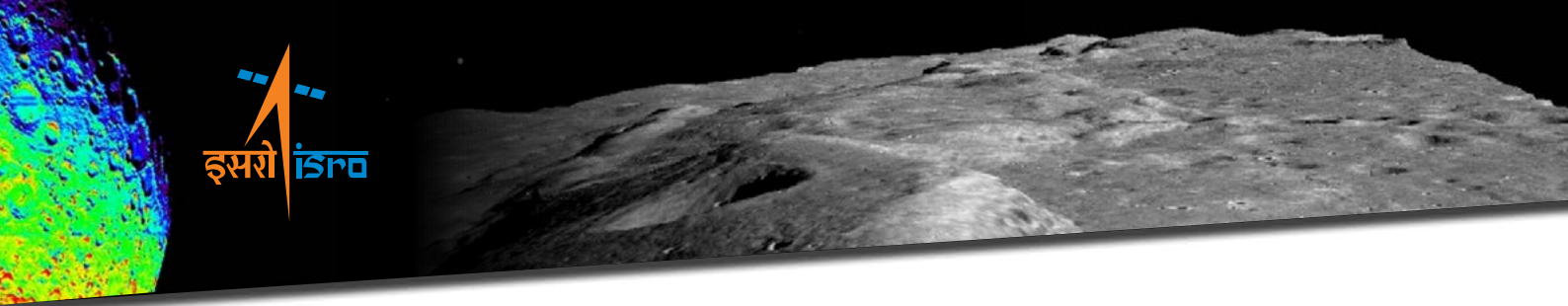


Figure 4.1: Panels a and b show the X-ray flux in the 1 – 15 keV energy range with a time cadence of 120 s, as measured by the XSM during two observing seasons. Different background shades represent activity levels on the Sun, with orange representing periods when NOAA active regions are present; pink representing periods of enhanced activity visible in both the XSM light curve as well as EUV/X-ray images but not classified as AR; and blue representing periods selected for the present study when no major activity was observed on the Sun. The microflares detected during the quiet periods are marked with red points, representing their peaks; and red vertical bars, representing their time. Vadawale et al. [2021a].



Further, [Figure 4.2b](#) shows with certainty that the observed flare energy histogram is significantly different from the power law derived from previous observations of quiet-Sun EUV (Extreme Ultra-Violet) nanoflares (Krucker & Benz 1998; Aschwanden et al. 2000b; Parnell & Jupp 2000) extrapolated to higher energies. This suggests that the difference may be either due to a change in power-law index over the typical nanoflare to microflare energies or the EUV and X-ray events are from two different populations. Since the EUV events are not hot enough to produce X-rays, this further suggests that it is important to consider the nano/micro-flares at the X-ray energies only, for addressing the problem of coronal heating. Thus, the XSM observations, being the first statistical survey of X-ray microflares outside active regions, are likely to provide crucial inputs to understand the role of smallscale impulsive events in coronal heating.

The durations marked by blue background in [Figure 4.1](#) are considered in this work, corresponding to a total of 76 days (32 in DD1 and 44 in DD2 season) when there are no active regions (ARs) present on the solar disk. [Figure 4.3](#) is the representative spectrum of Quiet Sun. The high energy resolution of XSM makes the line complexes of Mg, Al, and Si clearly visible in the spectrum. Thus, our spectroscopic analysis of the quiet corona X-ray spectra is also capable of constraining the elemental abundances apart from temperature and EM. It should be noted that elemental abundances obtained by the X-ray spectral fitting are the absolute abundances i.e. relative to H, unlike the UV/EUV spectroscopy, where the abundances of minor elements are usually quoted relative to other minor element, typically O or Fe.

One day integrated spectra for each day of the selected quiet Sun periods are analysed and obtained temperature, EM, and abundances of Mg, Al, and Si as shown in [Figure 4.4](#). Typically, temperature and EM of the quiet period corona are found to be constant around ~ 2.1 MK and $\sim 1.5 \times 10^{47} \text{ cm}^{-3}$, respectively, except when there are clear enhancements seen in the X-ray emission. The estimated abundances for the low FIP (First Ionization Potential) elements Mg, Al, and Si are most of the time higher than the photospheric values. However, compared to different coronal abundance values reported in the literature [Feldman, 1992, Fludra and Schmelz, 1999, Schmelz et al., 2012], our average values are 20 – 60 % lower for Mg and Si. Whereas, for Al, the present derived values are ~ 30 % lower than the Feldman et al. (1992) [Feldman, 1992] value, but comparable with the remaining.

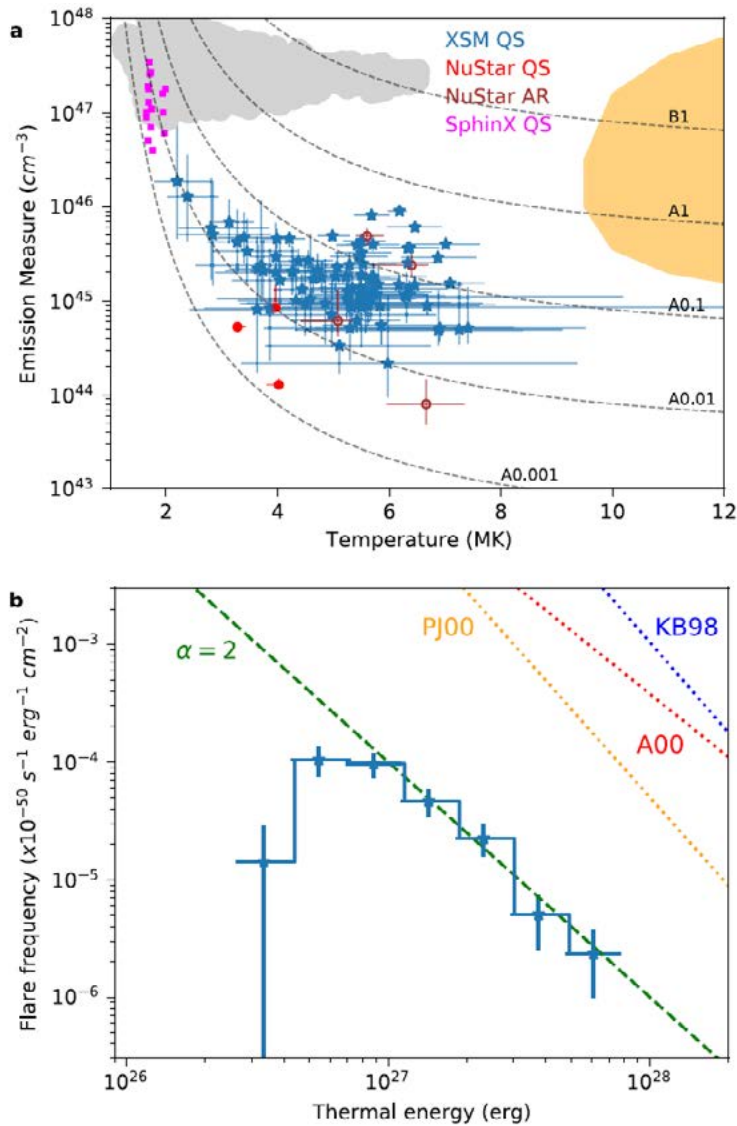


Figure 4.2: Panel **a** shows temperature and EM for 86 of the 98 quiet Sun (QS) microflares observed by the XSM with blue star symbols. The error bars represent 1σ uncertainties. Magenta squares and red filled circles correspond to QS microflares observed by SphinX [Sylwester et al., 2019] and NuSTAR [Kuhar et al., 2018], respectively. Parameter space of active region (AR) events observed by RHESSI [Hannah et al., 2008] and SphinX [Gryciuk et al., 2017] are shown with orange and gray shades, respectively. The brown open circles represent the four AR microflares reported by NuSTAR [Wright et al., 2017, Glesener et al., 2017, Hannah et al., 2019, Cooper et al., 2020]. Dashed lines represent the isoflux curves corresponding to GOES/XRS 1 – 8 Å X-ray flux levels from A0.001 (10^{-11} Wm⁻²) to B1 (10^{-7} Wm⁻²). Panel **b** shows the frequency distribution of thermal energies of 63 microflares for which the measurements are available. The green dashed line corresponds to a power law index (α) of two shown for comparison. The dotted lines correspond to power laws reported from quiet Sun EUV observations by Krucker and Benz [1998][KB98], Aschwanden et al. [2000] [A00], and Parnell and Jupp [2000] [PJ00] as shown in Figure 10 of Aschwanden et al. [2000]. Vadawale et al. [2021a].

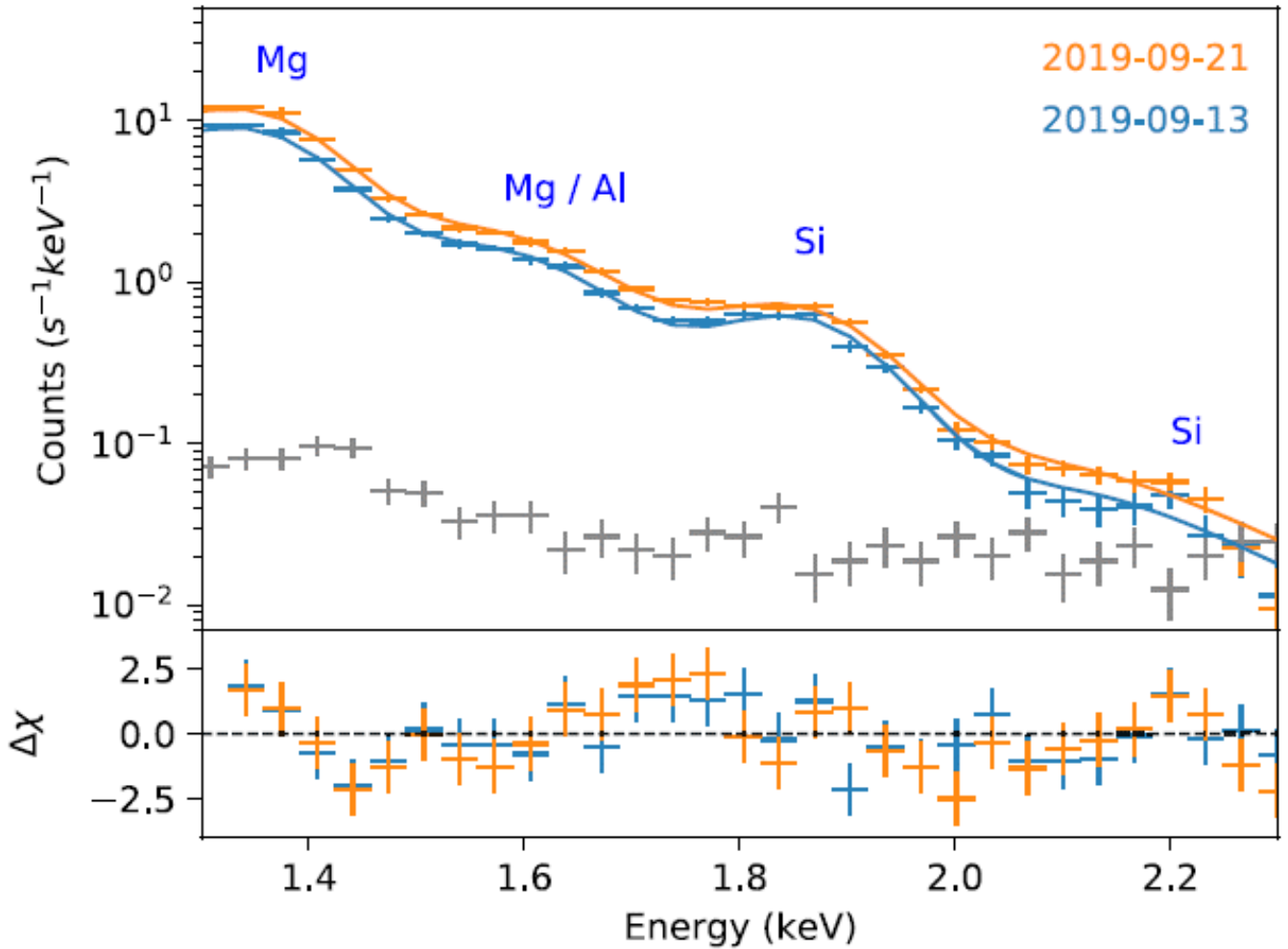
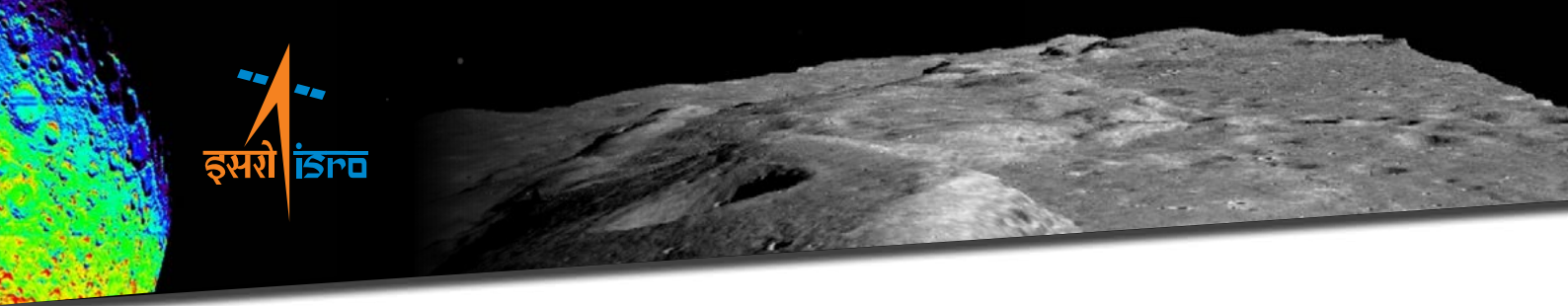


Figure 4.3: Soft X-ray spectra measured by the XSM for two representative days of quiet Sun observations are shown. Solid lines represent the best fit isothermal model and the residuals are shown in the bottom panel. Gray points correspond to non-solar background spectrum. Vadawale et al. [2021b].

To verify the consistency of our elemental abundance estimates, a similar analysis is carried out with the spectra integrated over multiple days as well the whole duration of respective quiet period, as shown in the [Figure 4.4](#). To the best of our knowledge, this is the first report of the elemental abundances for XBPs having plasma of ~ 2 MK temperature.

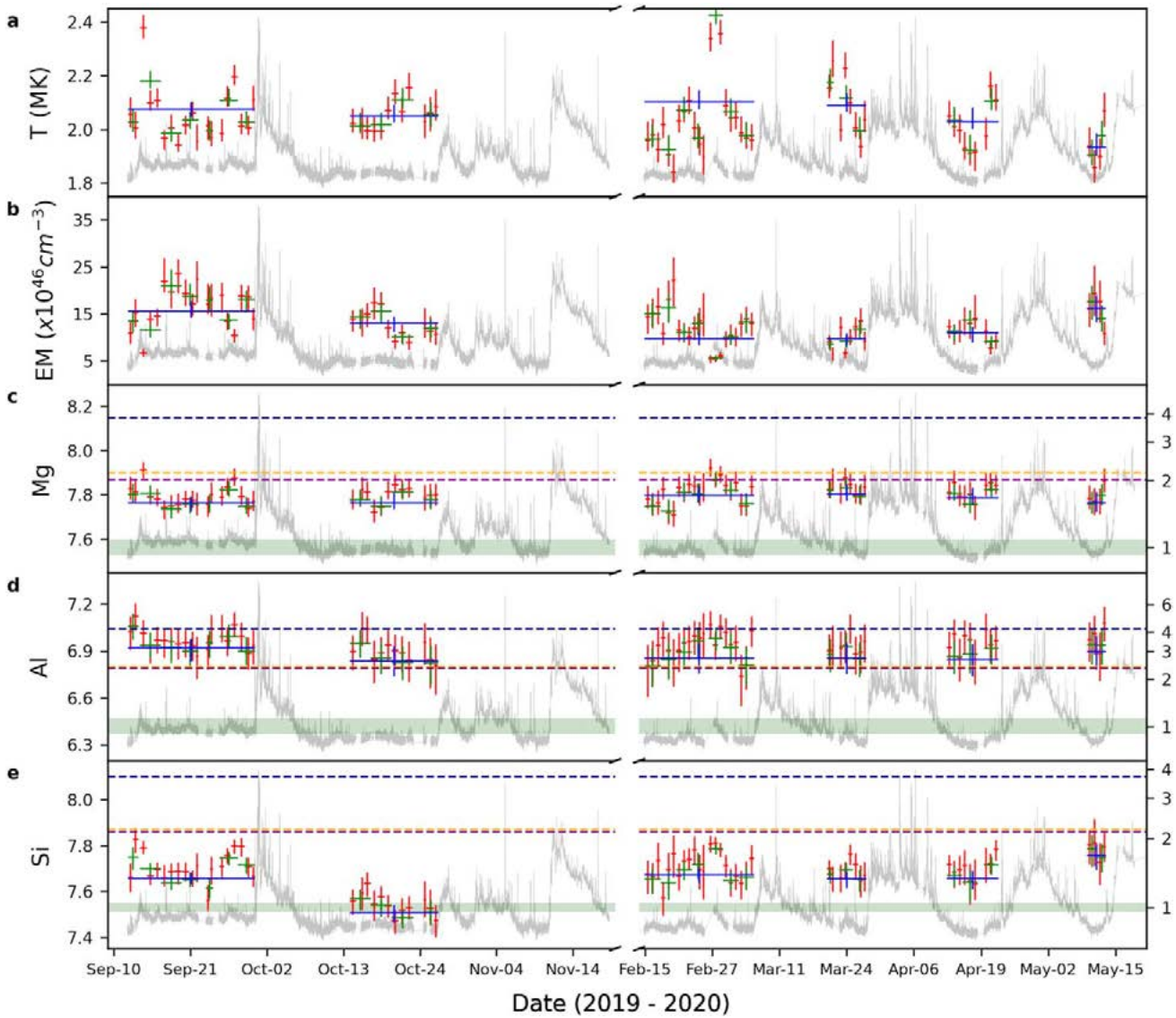
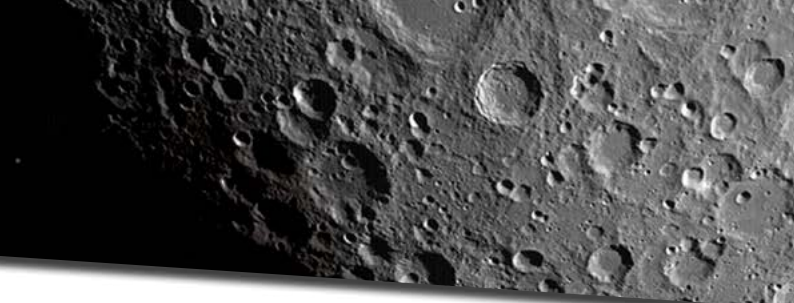
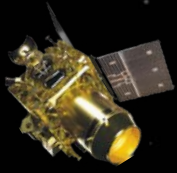
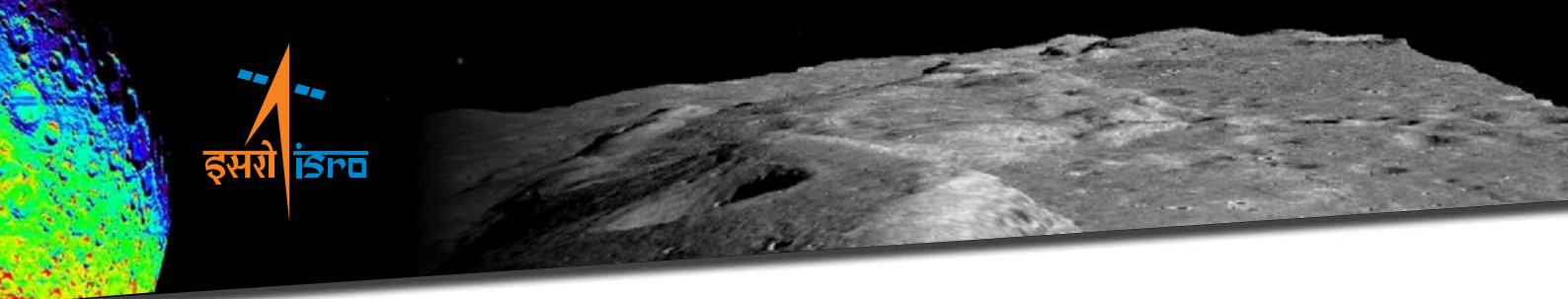


Figure 4.4: The five panels show the results of the spectral fitting, viz. Temperature (a), EM (b), as well as the absolute abundances of Mg (c), Al (d), and Si (e) in logarithmic scale with $A(H)=12$. The red, green and blue points represent the best fit parameters obtained from the spectra integrated over one day, multiple days (2–4 days), and each quiet period, respectively. The y-error bars represents 1σ uncertainty for each parameter, whereas the x-error bars represent the duration over which a given spectrum is integrated. XSM light curves for the entire duration are shown in gray in the background. For a quick comparison with the reported values of abundances for these elements, the corresponding panels (c-e) also show lines representing active region values reported by [Feldman, 1992] (navy blue), [Fludra and Schmelz, 1999] (orange), and [Schmelz et al., 2012] (purple). The range of photospheric abundances from various authors compiled in the CHIANTI database are shown as green bands. The right y- axis in panels c-e show the FIP bias values for the respective elements with respect to average photospheric abundances. Vadawale et al. [2021b].



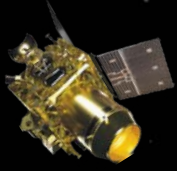
4.2 Evolution of Elemental Abundances During Solar Flares

During the period from September 2019 to May 2020, covering the minimum of Solar Cycle 24, XSM observed nine B-class flares ranging from B1.3 to B4.5. Using time-resolved spectroscopic analysis during these flares, the evolution of temperature, emission measure, and absolute elemental abundances of four elements Mg, Al, Si, and S are examined. These are the first measurements of absolute abundances during such small flares and this study offers a unique insight into the evolution of absolute abundances as the flares evolve. The results demonstrate that the abundances of these four elements decrease towards their photospheric values during the peak phase of the flares. During the decay phase, the abundances are observed to quickly return to their pre-flare coronal values.

The depletion of elemental abundances during the flares is consistent with the standard flare model, suggesting the injection of fresh material into coronal loops as a result of chromospheric evaporation. This indicates that during the flares, the coronal loops are quickly filled with plasma originating from the lower parts of the solar atmosphere without having sufficient time for the usually observed fractionation in non-flaring loops to take place. The observation of quick recovery to the coronal values show that any process giving rise to such fraction must be occurring on a time scale of few tens of minutes. To explain the quick recovery of the so-called coronal First Ionization Potential (FIP) bias, two scenarios are proposed based on the Ponder motive force model. One of the scenario suggests the presence of the long sought after, alfvén waves induced by magnetic reconnection, in the flaring loops. This is the first observation hint of such alfvén waves.

4.3 Summary

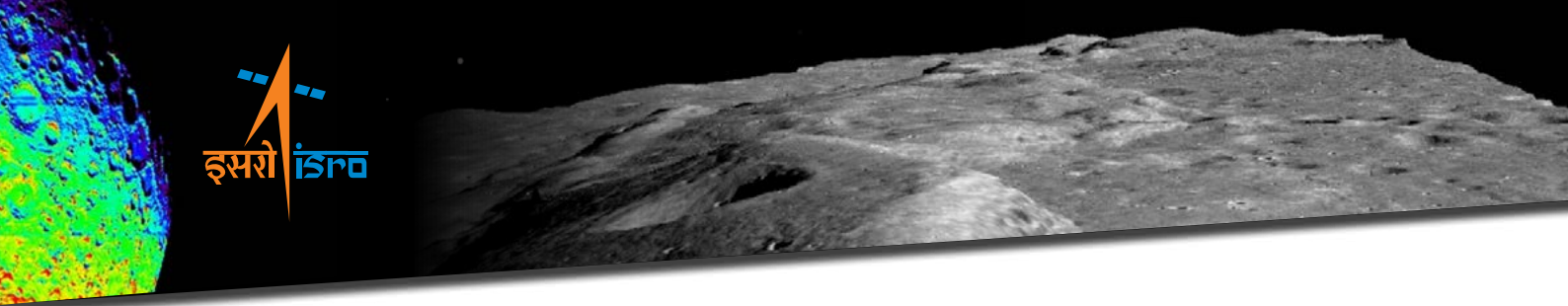
XSM started observations of the Sun during the minimum of solar cycle 24. Due to the high sensitivity and high energy resolution of the XSM, the observations during the period of the lowest solar activity have also yielded very interesting and novel scientific results. It has observed large number of microflares occurring outside the active region. This is the first such observation and has great implication on the understanding the mechanism behind heating of the solar corona, which is open problem for many decades. Another completely new observation by XSM during the quiet Sun period, is that the abundances of the low FIP elements in the X-ray bright points are enhanced compared to the photospheric abundances. However, the enhancement is not as high as that observed in the active regions. Since the X-ray bright points are known to have magnetic fields compared to the active region, the XSM observations indicate the important role played by the magnetic field in determining the FIP bias, and thus provide crucial insights in understanding the origin of the FIP bias. XSM has also enabled, for the first time, the time resolved spectroscopic analysis of the solar flares as small as B-class, which was possible so far only for very large flare of M and X-class. A key result from such analysis is that FIP bias that reduces during the onset of the



flare quickly recovers to its original value over the time scale of few tens of minutes. While the reduction of the FIP bias during large flares have been reported earlier, the rapid recovery of the FIP bias is first time revealed by XSM observations. This points to the illusive alfvén waves induced by magnetic reconnect, and has a strong implication for understanding both the origin of the FIP bias as well as the coronal heating. The Sun was largely quiet during the first year of XSM operation, and the solar activity has been increasing over the second year. Thus it is expected that the continued XSM observations as the solar cycle 25 reaches to its maximum, will provide many more interesting results.

Publications

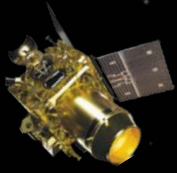
1. Mondal, Biswajit ; Sarkar, Aveek ; Vadawale, Santosh V. ; Mithun, N. P. S. ; Janardhan, P. ; Del Zanna, Giulio ; Mason, Helen E. ; Mitra-Kraev, Urmila ; Narendranath, S., "Evolution of Elemental Abundances During B-Class Solar Flares: Soft X-ray Spectral Measurements with Chandrayaan-2 XSM", ApJ (accepted), 2021.
2. Vadawale, Santosh V.; Mithun, N. P. S.; Mondal, Biswajit; Sarkar, Aveek; Janardhan, P.; Joshi, Bhuwan; Bhardwaj, Anil; Shanmugam, M.; Patel, Arpit R.; Adalja, Hitesh Kumar L.; Goyal, Shiv Kumar; Ladiya, Tinkal; Tiwari, Neeraj Kumar; Singh, Nishant; Kumar, Sushil, "Observations of the Quiet Sun During the Deepest Solar Minimum of the Past Century with Chandrayaan-2 XSM – Sub-A Class Microflares Outside Active Regions", ApJL, 912:L13, 2021.
3. Vadawale, Santosh V.; Mondal, Biswajit; Mithun, N. P. S.; Sarkar, Aveek; Janardhan, P.; Joshi, Bhuwan; Bhardwaj, Anil; Shanmugam, M.; Patel, Arpit R.; Adalja, Hitesh Kumar L.; Goyal, Shiv Kumar; Ladiya, Tinkal; Tiwari, Neeraj Kumar; Singh, Nishant; Kumar, Sushil, "Observations of the Quiet Sun During the Deepest Solar Minimum of the Past Century with Chandrayaan-2 XSM – Elemental Abundances in the Quiescent Corona", ApJL, 912:L12, 2021.
4. Mithun, N. P. S.; Vadawale, S. V.; Patel, A. R.; Shanmugam, M.; Chakrabarty, D.; Konar, P.; Sarvaiya, T. N.; Padia, G. D.; Sarkar, A.; Kumar, P.; Jangid, P.; Sarda, A.; Shah, M. S.; Bhardwaj, A., "Data Processing Software for Chandrayaan-2 Solar X-ray Monitor", Astronomy & Computing, 34:100449, 2021.
5. Mithun, N. P. S.; Vadawale, Santosh V.; Shanmugam, M.; Patel, Arpit R.; Tiwari, Neeraj Kumar; Adalja, Hiteshkumar L.; Goyal, Shiv Kumar; Ladiya, Tinkal; Singh, Nishant; Kumar, Sushil; Tiwari, Manoj K.; Modi, M. H.; Mondal, Biswajit; Sarkar, Aveek; Joshi, Bhuwan; Janardhan, P.; Bhardwaj, Anil, "Ground Calibration of Solar X-ray Monitor on board the Chandrayaan-2 Orbiter", Experimental Astronomy, 51:1, 2021.
6. Mithun, N. P. S.; Vadawale, Santosh V.; Sarkar, Aveek; Shanmugam, M.; Patel, Arpit R.; Mondal, Biswajit; Joshi, Bhuwan; Janardhan, P.; Adalja, Hiteshkumar L.; Goyal, Shiv Kumar; Ladiya, Tinkal; Tiwari, Neeraj Kumar; Singh, Nishant; Kumar, Sushil; Tiwari, Manoj K.; Modi, M. H.; Bhardwaj, Anil, "Solar X-ray Monitor On board the Chandrayaan-2 Orbiter: In-flight Performance and Science Prospects", Solar Physics , 295:139, 2020.



7. Shanmugam, M.; Vadawale, Santosh V.; Patel, Arpit R.; Adalaja, Hitesh Kumar; Mithun, N. P. S.; Ladiya, Tinkal; Goyal, Shiv Kumar; Tiwari, Neeraj K.; Singh, Nishant; Kumar, Sushil; Painkra, Deepak Kumar; Acharya, Y. B.; Bhardwaj, Anil; Hait, A. K.; Patinge, A.; Kapoor, Abinandhan; Kumar, H. N. Suresh; Satya, Neeraj; Saxena, Gau- rav; Arvind, Kalpana, "Solar X-ray Monitor Onboard Chandrayaan-2 Orbiter", *Current Science*, 118(1):45, 2020.
8. Netra S Pillai, S Narendranath, K Vadodariya, Srikar P Tadepalli, V Radhakrishna, Anurag Tyagi, Reena Yadav, Brajpal Singh, Vaishali Sharan, PS Athiray, P Sreekumar, K Sankarasubramanian, Megha Bhatt, Amit Basu Sarbadhikari, NPS Mithun, Santosh Vadawale, "Chandrayaan-2 Large Area Soft X-ray Spectrometer (CLASS): Calibration, In-flight performance and first results", *Icarus*, 2021.

References

1. Markus J. Aschwanden, Ted D. Tarbell, Richard W. Nightingale, et al. Time Variability of the "Quiet" Sun Observed with TRACE. II. Physical Parameters, Temperature Evolution, and Energetics of Extreme-Ultraviolet Nanoflares. *ApJ*, 535(2):1047–1065, June 2000. doi: 10.1086/308867.
2. Kristopher Cooper, Iain G. Hannah, et al. Unstart Observation of a Minuscule Microflare in a Solar Active Region. *ApJ*, 893(2):L40, April 2020. doi: 10.3847/2041-8213/ab873e.
3. Feldman. Elemental abundances in the upper solar atmosphere. *Phys. Scr*, 46(3):202–220, September 1992. doi: 10.1088/0031-8949/46/3/002.
4. Fludra and J. T. Schmelz. The absolute coronal abundances of sulfur, calcium, and iron from Yohkoh-BCS flare spectra. *A&A*, 348:286–294, August 1999.
5. Lindsay Glesener, S'am Krucker, et al. NuSTAR Hard X-Ray Observation of a Sub-A Class Solar Flare. *ApJ*, 845(2):122, August 2017. doi: 10.3847/1538-4357/aa80e9.
6. M. Gryciuk, M. Siarkowski, J. Sylwester, et al. Flare Characteristics from X-ray Light Curves. *Sol. Phys.*, 292(6):77, June 2017. doi: 10.1007/s11207-017-1101-8.
7. G. Hannah, S. Christe, S. Krucker, et al. RHESSI Microflare Statistics. II. X-Ray Imaging, Spectroscopy, and Energy Distributions. *ApJ*, 677 (1):704–718, April 2008. doi: 10.1086/529012.
8. Iain G. Hannah, Lucia Kleint, S'am Krucker, et al. Joint X-Ray, EUV, and UV Observations of a Small Microflare. *ApJ*, 881(2):109, August 2019. doi: 10.3847/1538-4357/ab2dfa.
9. S'am Krucker and Arnold O. Benz. Energy Distribution of Heating Processes in the Quiet Solar Corona. *ApJ*, 501(2):L213–L216, July 1998. doi: 10.1086/311474.
10. S'am Krucker, Arnold O. Benz, T. S. Bastian, and Loren W. Acton. X-Ray Network Flares of the Quiet Sun. *ApJ*, 488(1):499–505, October 1997. doi: 10.1086/304686.



11. Matej Kuhar, Sam Krucker, Lindsay Glesener, et al. NuSTAR Detection of X-Ray Heating Events in the Quiet Sun. *ApJ*, 856(2):L32, April 2018. doi: 10.3847/2041-8213/aab889.
12. N. P. S. Mithun, Santosh V. Vadawale, Aveek Sarkar et al. Solar X-Ray Monitor on Board the Chandrayaan-2 Orbiter: In-Flight Performance and Science Prospects. *Sol. Phys.*, 295(10):139, October 2020. doi: 10.1007/s11207-020-01712-1.
13. C. E. Parnell and P. E. Jupp. Statistical Analysis of the Energy Distribution of Nanoflares in the Quiet Sun. *ApJ*, 529(1):554–569, January 2000. doi: 10.1086/308271.
14. J. T. Schmelz, D. V. Reames, et al. Composition of the Solar Corona, Solar Wind, and Solar Energetic Particles. *ApJ*, 755(1):33, August 2012. doi: 10.1088/0004-637X/755/1/33.
15. M. Shanmugam, S. V. Vadawale, Arpit R. Patel, et al. Solar X-ray Monitor Onboard Chandrayaan-2 Orbiter. *Current Science*, 118(1):45–52, January 2020. doi: 10.18520/cs/v118/i1/45-52.
16. B. Sylwester, J. Sylwester, et al. Analysis of Quiescent Corona X-ray Spectra from SphinX During the 2009 Solar Minimum. *Sol. Phys.*, 294(12):176, December 2019. doi: 10.1007/s11207-019-1565-9.
17. S. V. Vadawale, M. Shanmugam, et al. Solar X-ray Monitor (XSM) on-board Chandrayaan-2 orbiter. *Advances in Space Research*, 54(10):2021–2028, November 2014. doi: 10.1016/j.asr.2013.06.002.
18. Santosh V. Vadawale, N. P. S. Mithun, et al. Observations of the Quiet Sun during the Deepest Solar Minimum of the Past Century with Chandrayaan-2 XSM: Sub-A-class Microflares outside Active Regions. *ApJ*, 912(1):L13, May 2021a. doi: 10.3847/2041-8213/abf0b0.
19. Santosh V. Vadawale, Biswajit Mondal, et al. Observations of the Quiet Sun during the Deepest Solar Minimum of the Past Century with Chandrayaan-2 XSM: Elemental Abundances in the Quiescent Corona. *ApJ*, 912(1):L12, May 2021b. doi: 10.3847/2041-8213/abf35d.
20. Paul J. Wright, Iain G. Hannah, Brian W. Grefenstette, et al. Microflare Heating of a Solar Active Region Observed with NuSTAR, Hinode/XRT, and SDO/AIA. *ApJ*, 844(2):132, August 2017. doi: 10.3847/1538-4357/aa7a59.



Contact detail: Dr. Santosh Vadawale (xsmpoc@prl.res.in)

Science Results from CHandra's Atmospheric Composition Explorer-2 (CHACE-2)

In the previous chapter, the scientific results from XSM payload were discussed. In this chapter, the key findings from CHACE-2 payload are presented.

5.1 Science Outcome

5.1.1 Variability of Lunar Exospheric Argon

Argon-40 (Ar-40) is a noble gas, in the lunar exosphere, understood to be originated from the radiogenic potassium-40 and it had been detected by several previous missions. The observations by Lunar Atmospheric Composition Experiment (LACE) on Apollo-17 detected Ar-40 at the landing site near 20°N latitude for nine lunations [Hoffman et al 1973, Hodges et al 1974]. However, the LACE observations were confined to the Lunar night side due to the detector saturation effects on the dayside. The observations showed that the number density of Ar-40 peaks near the sunrise and sunset terminators. Later, CHACE/MIP of Chandrayaan-1 also detected Ar-40 during its descent to lunar surface [Sridharan et al 2013, Thampi et al., 2015]. These observations indicated significant spatial heterogeneity in Ar-40, but were limited in spatial and temporal coverage. Recently, the neutral mass spectrometer (NMS) on LADEE orbiter mission also confirmed the sunrise and sunset enhancements in the number density of Ar-40 over different longitudes in the near equatorial plane of Moon, and showed a localised enhancement in Ar-40 over the KREEP region in the western maria [Benna et al., 2015].

In summary, our understanding about the variability of Ar-40 are also mostly confined to the processes operated in the low-latitude regions of Moon. From September 2019, CHACE-2 could observe the distribution of Ar-40 in the lunar exosphere for both the low and mid latitude regions. [Figure 5.1](#) shows a typical variation of the amu 40 signal in the dawn-dusk Lunar orbit, along with variation in the context parameters.

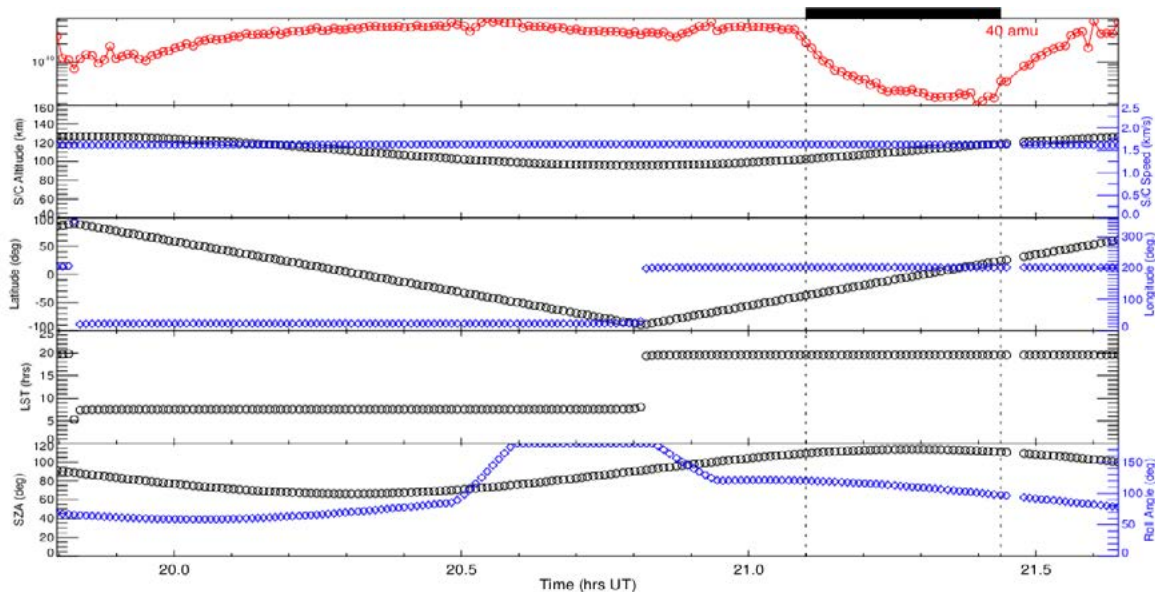


Figure 5.1 : Typical variation of the amu 40 signal (Ar-40) in the Lunar dawn-dusk orbit, along with variation in the context parameters, including selenographic latitude, longitude, spacecraft speed, altitude, Roll angle as well as Solar Zenith Angle (SZA).

The surface densities of Ar-40 from CHACE-2 observations over the low-latitude regions are compared with Apollo observations. These are found to be consistent. The CHACE-2 observations not only covered the low-latitude regions, but also covered the other latitude regions as well, for the first time, in-situ from a polar orbit. Figure 5.2 shows the map of argon, showing both low- and mid-latitude variations.

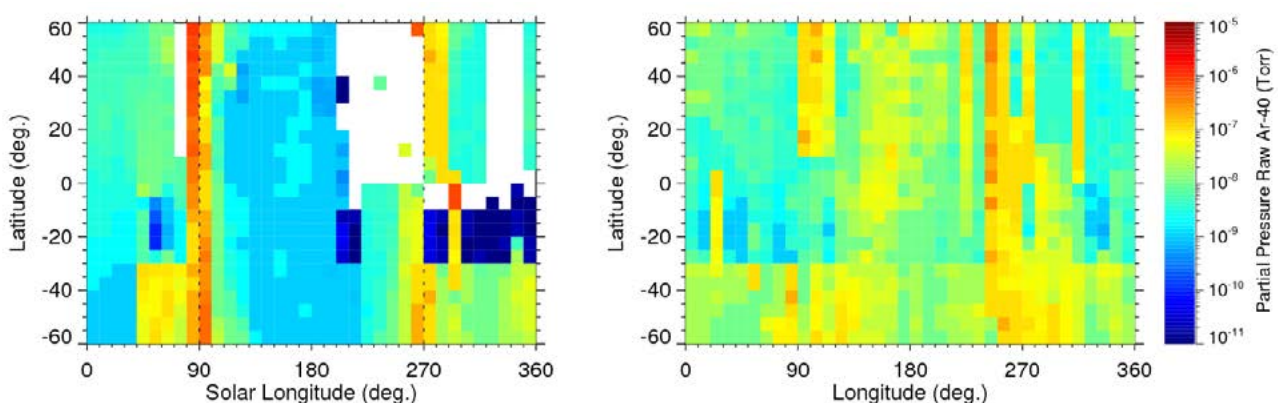
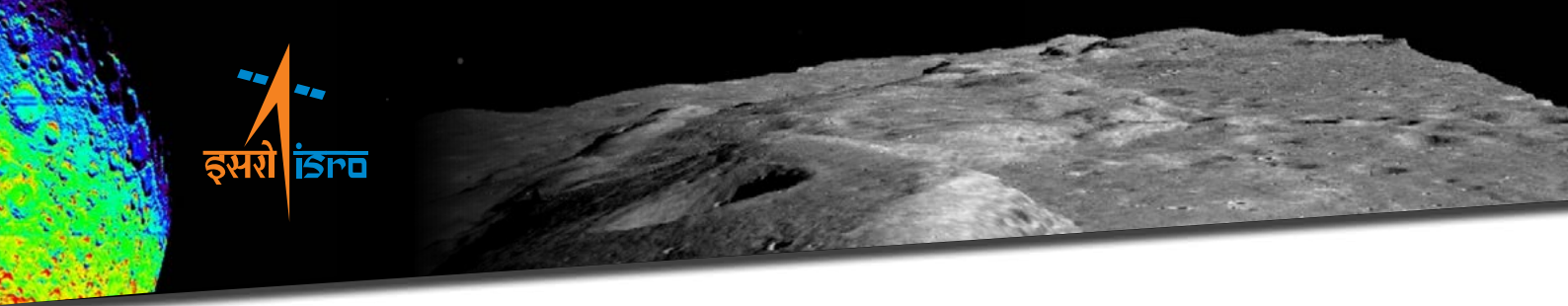


Figure 5.2: Argon-40 global distribution from CHACE-2 observations, showing both low- and mid-latitude variations.

The observations showed that the diurnal trend agrees with LACE/Apollo observations in the low latitude region in the lunar surface. In addition, CHACE-2 observations show for the first time that these features extend to the mid-latitude regions. Further, the number density of argon also shows significant spatial heterogeneity. For instance, when we compare different



longitudes, enhanced Ar-40 concentration was observed over the selenographic longitudes of 280-320°. These could be partly attributed to the KREEP (Potassium, Rear Earth Elements and Phosphorus) region on the Moon, because they are basically potassium-rich regions.

5.1.2 Lunar Exospheric CO₂

CHACE-2 has detected CO₂ (amu 44) signals in the lunar exosphere. The significant amount of CO₂ detected by CHACE/MIP aboard Chandrayaan-1 was actually the first direct (in-situ) experimental confirmation of the prediction that CO₂ could be present in the Lunar exosphere [Sridharan et al., 2010, 2015]. However, CHACE was only a one-time measurement and could not provide the variability. CHACE-2 data have shown the presence of CO₂ in both low and mid-latitude regions, and has also shown its temporal variation for the first time. [Figure 5.3](#) shows the map of CO₂, in terms of raw partial pressures, as observed by CHACE-2. The observations show a clear cut difference from the pattern observed in Ar-40, both spatially and temporally. This points towards the differences in the process of the absorption, desorption and volatility of these on the ultra-high vacuum lunar exosphere. Detailed analysis is in progress.

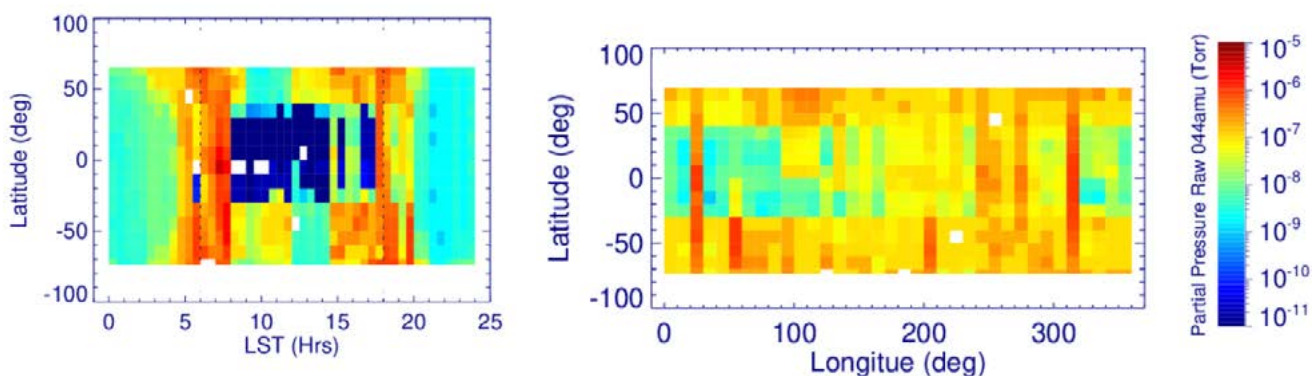
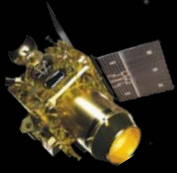


Figure 5.3: Map of amu-44 partial pressures observed by CHACE-2 observations, showing both low- and mid-latitude variations.

5.1.3 Lunar Exospheric Neon

The Neon-20 signature in the Lunar exosphere was first observed by LACE, but it was believed to be contaminated by the signal of H₂O (Hodges et al., 1973). The estimated surface abundance of Neon at the terminator crossing was $\sim 10^5 \text{ cm}^{-3}$. Though there was no reliable observation from LACE on Neon, model calculations (Hodges et al., 1973) suggested that the concentration of Neon during the lunar day could be near $4-7 \times 10^3 \text{ cm}^{-3}$. Recently, the Neutral Mass Spectrometer (NMS) instrument aboard the LADEE has reported the longitudinal variation of Neon at lower latitudes (Benna et al., 2015). The CHACE-2 also could detect Ne-20 signal in the Lunar exosphere. There are some noticeable changes in the



Neon signal on some occasions, when the upstream and magnetotail region observations are compared. [Figure 5.4](#) shows such a comparison, along with the location of observation, with respect to Sun.

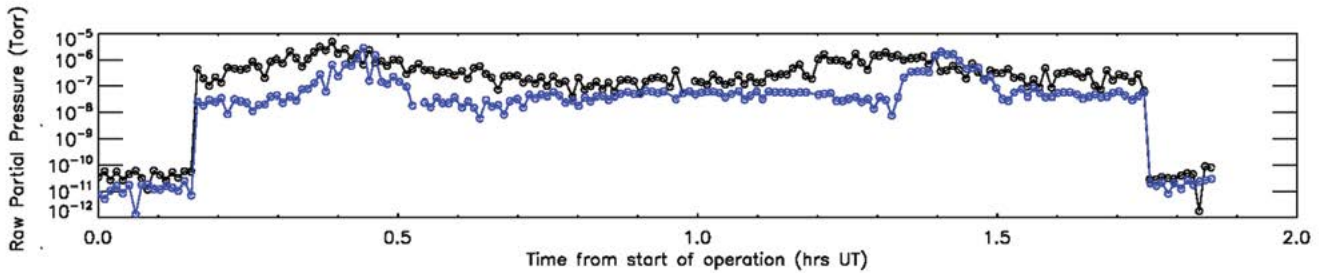


Figure 5.4: Comparison of Neon signal observed when Moon is in the upstream region and the magnetotail regions. The black and blue lines correspond to observations in the upstream and within the magnetotail respectively.

The observations clearly show that the densities of Neon could be low when the Moon is inside the terrestrial magnetotail. However, we do not observe such a clear signature on all occasions. Detailed analysis is in progress.

5.2 Importance of These Findings on Lunar Science

The observations of exospheric composition and variability has the potential to help us understand about the solar wind, the lunar interior and outgassing, the efficiency of volatile sequestration, and the kinetics of adsorption and desorption in low-pressure environments. The new observations from mid-latitudes indicate significant spatial heterogeneity. For example, the enhancement observed in Argon-40 could only be partly attributed due to the KREEP region, and we also have indications of the influence of the South Pole Aitken (SPA) terrain, for the first time. These will provide new insights into the variability in radiogenic activity of the lunar interior.

As mentioned earlier, the CO_2 observations from CHACE-2 are first of their kind, which is expected to provide new constraints to the exospheric composition, especially in the context that there are model calculations which suggest that the lunar ionosphere is dominated by molecular ions including CO_2^+ , with near-surface electron density 250 cm^{-3} [Choudhary et al., 2016]. The new observations on spatial and temporal variation of CO_2 can provide realistic inputs on exospheric neutral densities for such models. Similarly, the observations on Neon is expected to provide new insights into the solar wind interaction with Lunar exosphere.

5.3 Summary

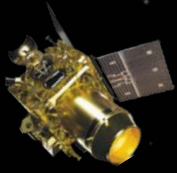
CHandra's Atmospheric Composition Explorer-2 (CHACE-2) onboard Chandrayaan-2 orbiter is a quadrupole based neutral mass spectrometer aimed at observing the tenuous Lunar exospheric composition from spacecraft altitude. CHACE-2 is being regularly operated at Lunar orbit since September 2019, and completed both noon-midnight and dawn-dusk orbit geometries. The major science results obtained so far from these observations include first in-situ observations of Argon-40 from the mid-latitude regions of Moon, first observations of the spatio-temporal variation of CO₂ in the Lunar exosphere etc. These observations has the potential to help us to understand about the solar wind, the lunar interior and outgassing, and volatiles in the ultra high vacuum environments.

Publications

1. Chandra's Atmospheric Composition Explorer-2 onboard Chandrayaan-2 to study the lunar neutral exosphere, Das et al, Current Science, 118(2):202, DOI: 10.18520/cs/v118/i2/202-209, 2020.
2. Argon-40 in Lunar Exosphere: Observations from CHACE-2 on Chandrayaan-2 Orbiter, Dhanya et al., Manuscript submitted; under review (2021).

References

1. Benna, M., Mahaffy, P.R., Halekas, J.S., et al., 2015. Variability of helium, neon, and argon in the lunar exosphere as observed by the LADEE NMS instrument. Geophys. Res. Lett. 42, 3723–3729.
2. Choudhary, R. K., Ambili, K. M., Choudhury, S., Dhanya, M. B., and Bhardwaj, A. (2016), On the origin of the ionosphere at the Moon using results from Chandrayaan-1 S band radio occultation experiment and a photochemical model, Geophys. Res. Lett., 43, 10,025– 10,033, doi:10.1002/2016GL070612.
3. Hodges, R.R., Hoffman, J.H., Johnson, F.S., 1974. The lunar atmosphere. Icarus 21, 415–426.
4. Hodges, R.R., Hoffman, J.H., Johnson, F.S., et al., 1973. Composition and dynamics of the lunar atmosphere. In: Proceedings of Lunar Science Conference, vol. 4, pp. 2864–2865.
5. Hoffman, J.H., Hodges Jr., R.R., Johnson, F.S., et al, 1973. Lunar atmospheric composition results from Apollo 17. In: Lunar and Planetary Science Conference Proceedings, vol. 4, pp. 2865–2875.



6. Sridharan R., S.M.Ahmed, Tirtha Pratim Das, P.Sreelatha, P. Pradeep Kumar, Neha Naik, Gokulapati Supriya, Corrigendum to “The Sunlitlunar atmosphere: A Comprehensive study by CHACE on the Moon Impact Probe of Chandrayaan-1”[Planet. SpaceSci.58(2010)1567–1577], Planetary andSpaceScience,111167–168, 2015.
7. Sridharan, R., S. M. Ahmed, T.P. Das, P. Sreelatha, P. Pradeepkumar, N. Naik, and G. Supriya, The sunlit lunar atmosphere: A comprehensive study by CHACE on the Moon Impact Probe of Chandrayaan-1, Planetary and Space Science, 58, 1567–1577, 2010.
8. Sridharan, R., T. P. Das, S. M. Ahmed, G. Supriya, A. Bhardwaj, and J. A. Kamalakar, Spatial heterogeneity in the radiogenic activity of the lunar interior: Inferences from CHACE and LLRI on Chandrayaan-1, Advances in Space Research, 51, 168–178, 2013.
9. Thampi, S.V., R. Sridharan, T.P. Das, S.M. Ahmed, J.A. Kamalakar, and A. Bhardwaj, The spatial distribution of molecular Hydrogen in the lunar atmosphere – New results, Planetary and Space Science, 106, 142–147, 2015.



Contact detail: Dr Smitha V Thampi (smitha_vt@vssc.gov.in)
Dr Dhanya M B (mb_dhanya@vssc.gov.in)

Science Results from Dual Frequency Synthetic Aperture Radar (DFSAR)

This chapter presents some of the salient science results from DFSAR payload onboard Chandrayaan-2 Orbiter.

6.1 Comparative Analysis of DFSAR and LRO-MiniRF Data:

This study exhibits the results obtained from compact-pol (CP) data acquired by DFSAR instrument in both L and S-band. Circular Polarization Ratio (CPR), a parameter indicative of radar wavelength scale roughness on lunar surface, is derived from DFSAR CP data. Further, CPR value over same study region obtained from S-band LRO-MiniRF CP data is computed for comparative analysis.

6.1.1 Comparative Analysis of S-band DFSAR and S-band LRO-MiniRF CP Data:

Both CH-2 DFSAR and LRO-MiniRF have the capability to image the lunar surface using S-band radar in CP mode. In this, a comparative analysis of the same has been done to understand the variability between these two datasets over same study region. Hence, study has been conducted over fresh and partially degraded craters imaged by both the sensors in S-band due to their variable roughness properties. [Figure 6.1a](#) and [6.1b](#) show the Raney decomposed images of S-band DFSAR and S-band Mini-RF instruments, respectively. The DFSAR image due to higher spatial resolution shows better clarity in deciphering small surface features, which are not so apparent in LRO Mini-RF data. [Figure 6.1c](#) shows the distribution of CPR values obtained from S-band data of both MiniRF and DFSAR. The plot reveals that, both the sensors show almost similar average CPR values of the sample craters. DFSAR data shows lesser variability (standard deviation) compared to MiniRF data which may be attributed to difference in the spatial resolution between these two sensors.

6.1.2 Comparative Analysis of L-band DFSAR and S-band LRO-MiniRF CP Data:

To understand the sensitivity of the L-band DFSAR data over various lunar impact craters with different degradation stage, CPRs have been derived over sample craters ranging from fresh to highly degraded stage. [Figure 6.2a](#) and [6.2b](#) show the Raney decomposed images acquired over the study regions in L-band and S-band by DFSAR and MiniRF instruments, respectively. The DFSAR image due to higher spatial resolution (4m/pixel) shows numerous small craters which are not clearly decipherable in MiniRF data. High resolution (0.5m pixel size) optical image from LRO Narrow Angle Camera of the same region is shown in [Figure 6.3c](#). The boundary of highly degraded crater in the region is identifiable in DFSAR data, whereas, in the optical image the crater is barely visible. Similar is the case for the



ejecta distributions, seen as bright yellowish tone around the craters in SAR images, possibly due to its presence below the surface.

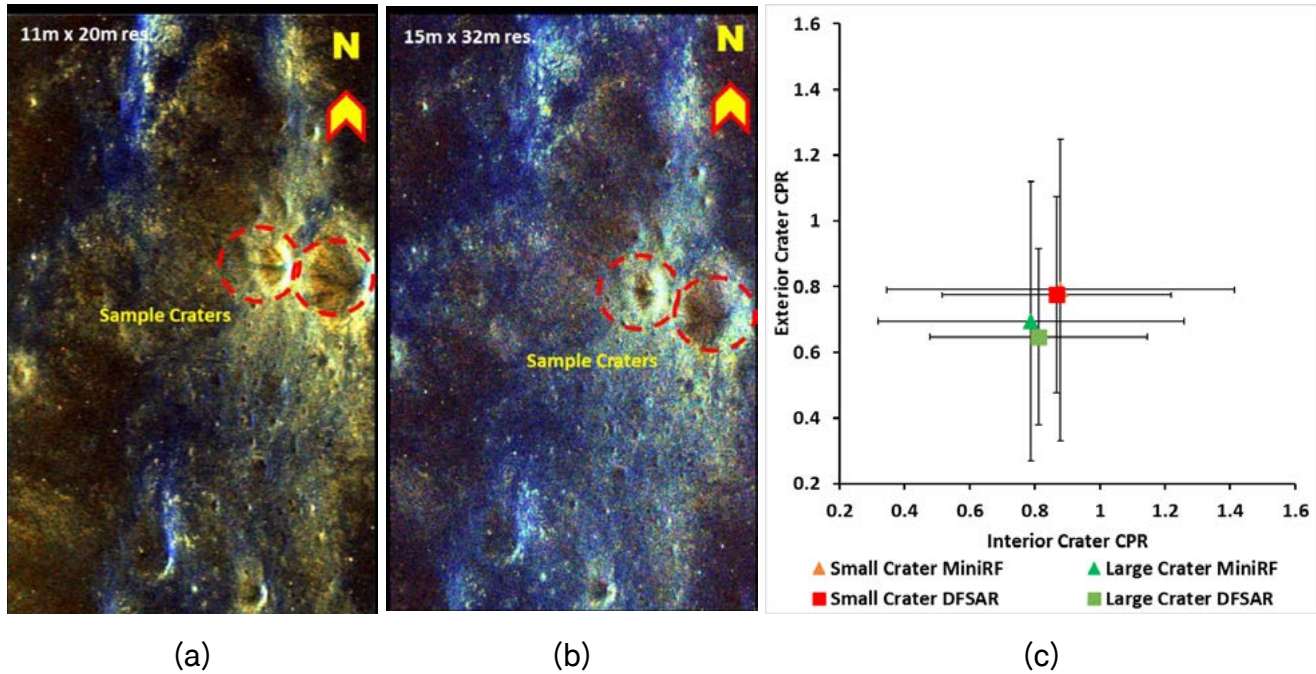


Figure 6.1: Raney ($m-\chi$) decomposed image of study area acquired by (a) CH-2 DFSAR S-band; (b) LRO Mini-RF S-band; (c) Average CPR values in the interior and exterior parts of various craters (one small and one large crater marked by red dotted circle) imaged by LRO-MiniRF (S-band) and CH-2 DFSAR (S-band). The triangle data points correspond to Mini-RF data and square data points correspond to DFSAR data.

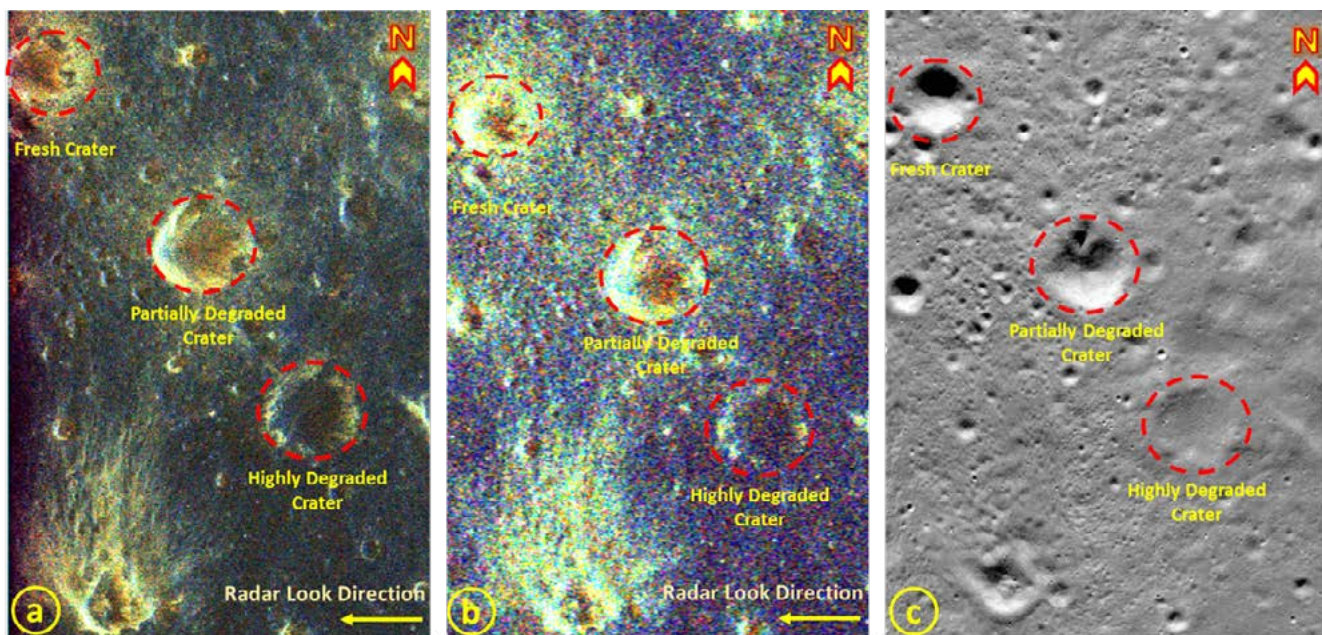
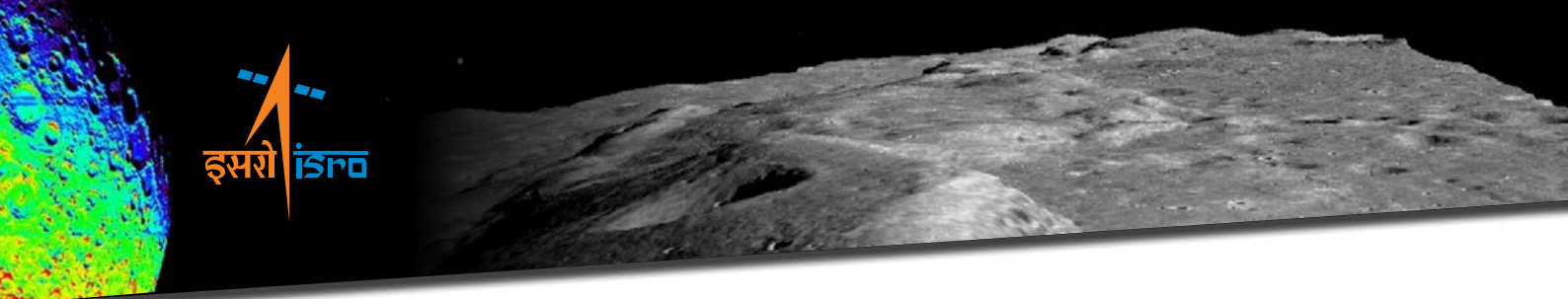


Figure 6.2: Raney ($m-\chi$) decomposed image of study area acquired by (a) CH-2 DFSAR L band; (b) LRO-MiniRF S band; (c) corresponding optical image acquired by LRO Narrow Angle Camera image.



The distribution of CPR determined in MiniRF (S-band) and DFSAR (L-band) data over interior and exterior part of the craters is presented in [Figure 6.3](#). The plot shows that, CPR values in the exterior and interior part of the fresh crater are similar and highest among all the three craters. In the partially degraded crater the interior part has higher CPR values than the exterior part of the crater. In case of highly degraded crater, the exterior and interior CPR values are similar and lower compared to other types of craters. The average CPR values corresponding to the craters reveal facts about the stages of evolution of these craters. Freshness of the crater indicates that it is not exposed enough to space weathering. Due to this reason, the ejecta material is blocky and larger in size in both the interior and exterior part of the crater. However, with time the exterior part of the crater experiences higher weathering in comparison to interior part. Hence, the ejecta present outside the crater are more fragmented and reduced in size. So, for partially degraded stage, the CPR value of interior part is higher than that of the exterior. For highly degraded crater, with relatively more time, both interior and exterior parts of the crater are exposed to more space weathering leading to fining of ejecta present in both the parts. Hence, the CPR values in degraded crater are the lowest and alike in both their interior and exterior parts.

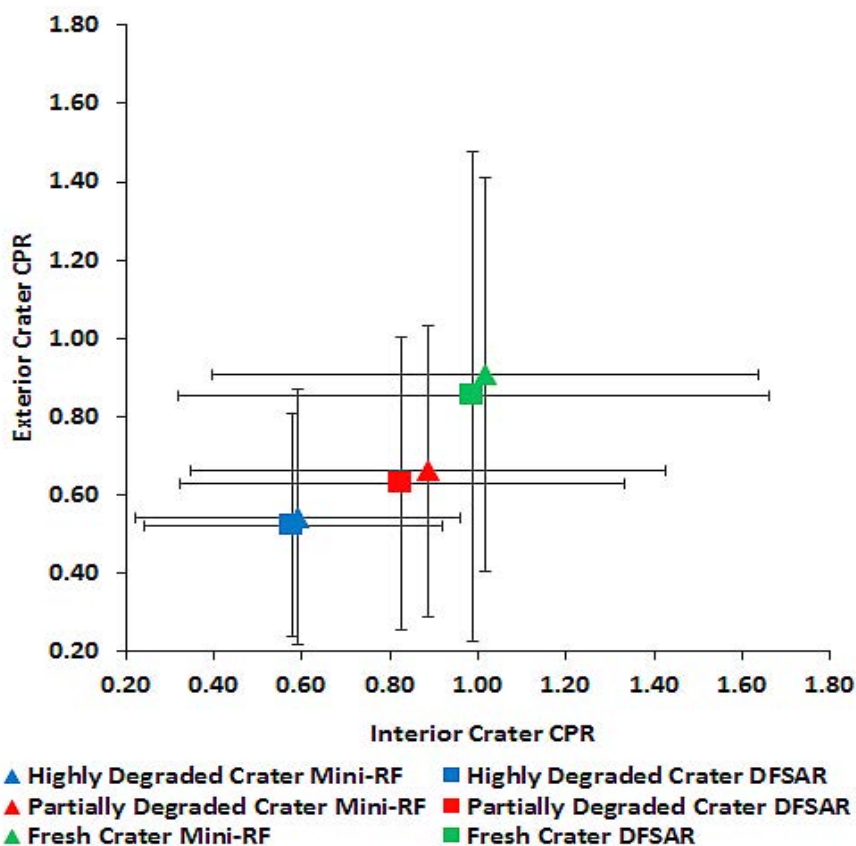


Figure 6.3: Average CPR values in the interior and exterior parts of various craters imaged by LRO-MiniRF (S-band) and CH-2 DFSAR (L-band). The triangle data points correspond to MiniRF data and square data points correspond to DFSAR data.

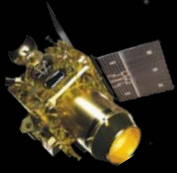
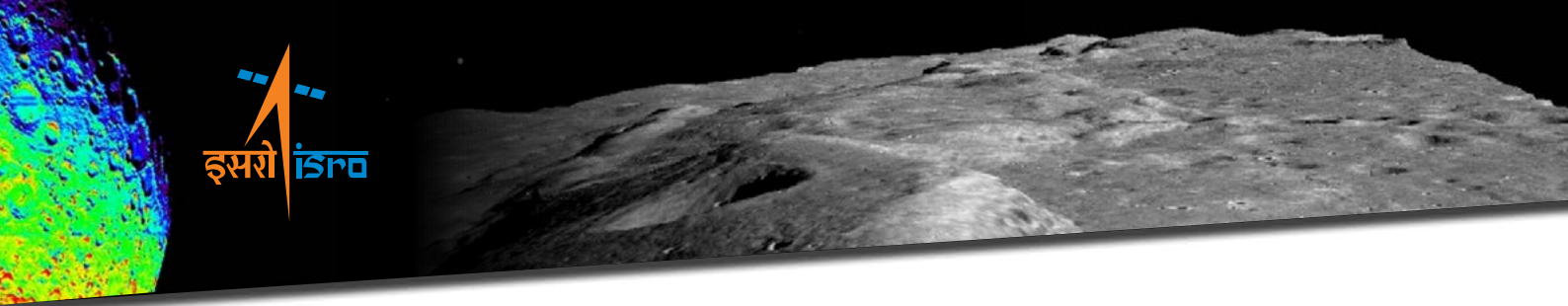


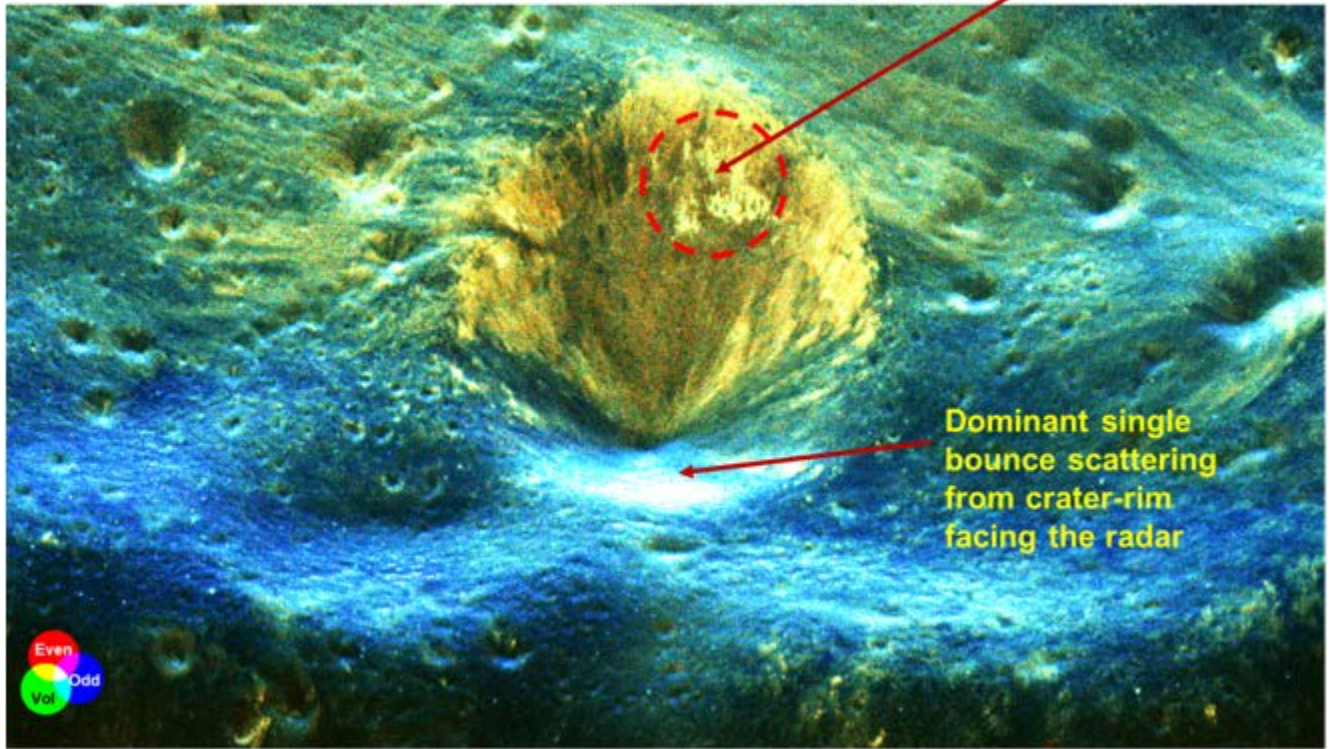
Table 6.1: Average CPR values in the interior and exterior parts of various craters imaged by LRO-MiniRF (S-band) and CH-2 DFSAR (L-band).

Sl. No.	Feature		CPR LRO-MiniRF (S-band)	CPR CH-2 DFSAR (L-band)
1	Highly Degraded Crater	Exterior	0.54 ± 0.33	0.52 ± 0.28
2		Interior	0.59 ± 0.37	0.58 ± 0.34
3	Partially Degraded Crater	Exterior	0.66 ± 0.37	0.63 ± 0.37
4		Interior	0.89 ± 0.54	0.83 ± 0.50
5	Fresh Crater	Exterior	0.91 ± 0.50	0.85 ± 0.62
6		Interior	1.02 ± 0.62	0.99 ± 0.67

Table 6.1 reveals that the CPR values for the same craters is slightly higher in S-band (MiniRF) compared to L-band (DFSAR). This is due to the fact that, some of the rock boulders of the scale of S-band wavelength appear as prominent scatterers in MiniRF data but not so with L-band (which has longer wavelength than S-band). Moreover, for fresh crater the average CPR value difference between L and S-band is more in exterior part (0.06) compared to interior part (0.03). This indicates that, the internal part of the fresh crater is dominated by bigger size rock blocks which are equally sensitive to both L and S-band. On the contrary, for partially degraded crater the average CPR difference in L and S-band is higher in interior part (0.06) relative to exterior part (0.03). This relation may be tracked to the reduction in the blocky nature of the interior part leading to variable sensitivity to different frequencies. Additionally, the exterior part is dominated by fine fragmented particles so giving rise to almost matching CPR values in both frequencies. Finally, for highly degraded crater, both interior and exterior part is dominated by fine fragmented particles, so, giving rise to identical CPR values in both L and S- band frequencies. An illustration of results from boulder distribution studies using high-resolution mode is given in [Figure 6.4](#).



Enhanced Radar Scattering due to presence of meter scale boulders on the inner crater wall



Slant range resolution: 2m

Figure 6.4: Boulder distribution studies using high-resolution data. Presence of large (cm to m scale) boulders on the inner wall of the secondary crater (on the floor of Manzinus crater) is identified from high resolution polarimetric decomposed image.

6.2 Physical Model Based Estimation of Lunar Dielectric Constant and Surface Roughness - First Time Retrievals

The dielectric constant and surface roughness over the lunar surface is important to study the lunar regolith features, distribution of lunar-resources, and origin of the Moon. Further, it plays a very important role in the surface and sub-surface scattering, and regolith penetration, which is crucial in determining potential landing sites for the future lunar missions and reducing the ambiguities on existence of water-ice in the lunar South Polar Region.

Previous studies using hybrid-pol data (Ch1 MiniSAR & LRO-MiniRF) used either empirical models or semi-empirical models, which do not account for physical behavior and have limited applicability over large area; moreover, direct estimation of surface roughness



is also not possible using the previous data. These lacunae have been addressed using Chandrayaan-2 Dual Frequency SAR (DFSAR) full-polarimetric data. For this, a parameterized multilayer model based on Advanced Integral Equation Method (AIEM) for rough surface scattering has been developed which establishes quantitative relationship between radar backscatter and the physical properties of the regolith layer for different lunar scenario. This in-house developed model is used for retrievals of lunar dielectric constant and surface roughness using the DFSAR data.

Methodology:

Full Polarimetric DFSAR data is used for estimation of lunar dielectric constant and roughness. The in-house developed lunar forward radar backscatter model is physics based model and depends on multiple input lunar parameters with non-linear relations amongst them. An iterative inversion framework is adopted and implemented using global minimization techniques which is mainly driven by cost function, involving the model simulated values and DFSAR backscatter measurements (in HH, VV and HV-polarizations), as non-linear constrained problems. Due to the dependence of SAR backscatter on topography of region of interest, the model is designed to take into account the changes due to local incidence angle. Using this methodology, dielectric constant, surface roughness (rms height) and correlation length are estimated pixel-wise over the image.

Inversion Results and Validation:

Retrievals of lunar dielectric constant and surface roughness have been done over multiple DFSAR L-band Full-pol datasets acquired over polar and non-polar regions of the Moon. The inversion results have been validated over Apollo-17 and Apollo-11 landing sites, which were specifically imaged for this purpose, as shown in [Figure 6.5](#). Dielectric properties reported from lab based characterization of these Apollo landing sites have been used as reference.

Due to limited samples available from Apollo-11 and lack of precise location of in-situ samples, the validation was corresponding to an averaged area instead of point based matching ([Figure 6.6](#)). Ranges of retrieved dielectric constant are found to be matching well with those of the reported lab values.

The dielectric constant and surface roughness retrievals have been carried out over various regions of the Moon using Full-pol DFSAR data; specimen results over the non-polar anomalous Gardner Crater is as given in [Figure 6.7](#).

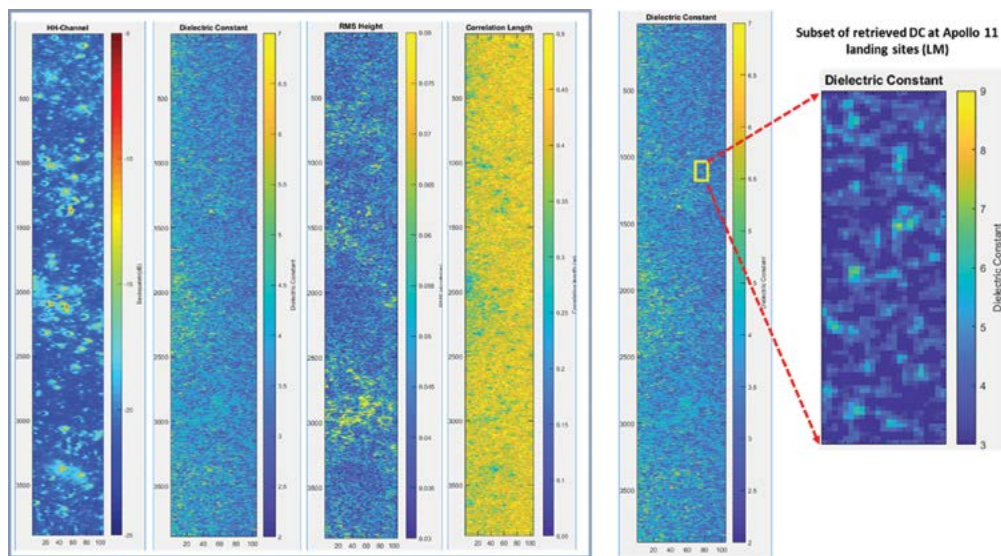


Figure 6.5: Inversion for Lunar Dielectric Constant and RMS height over Apollo-11 landing site.

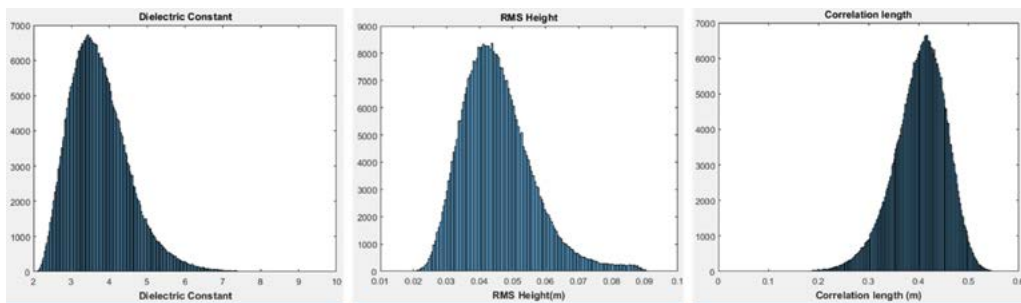


Figure 6.6: Histogram showing distribution of Lunar Dielectric Constant and surface roughness parameters over Apollo-11 landing site

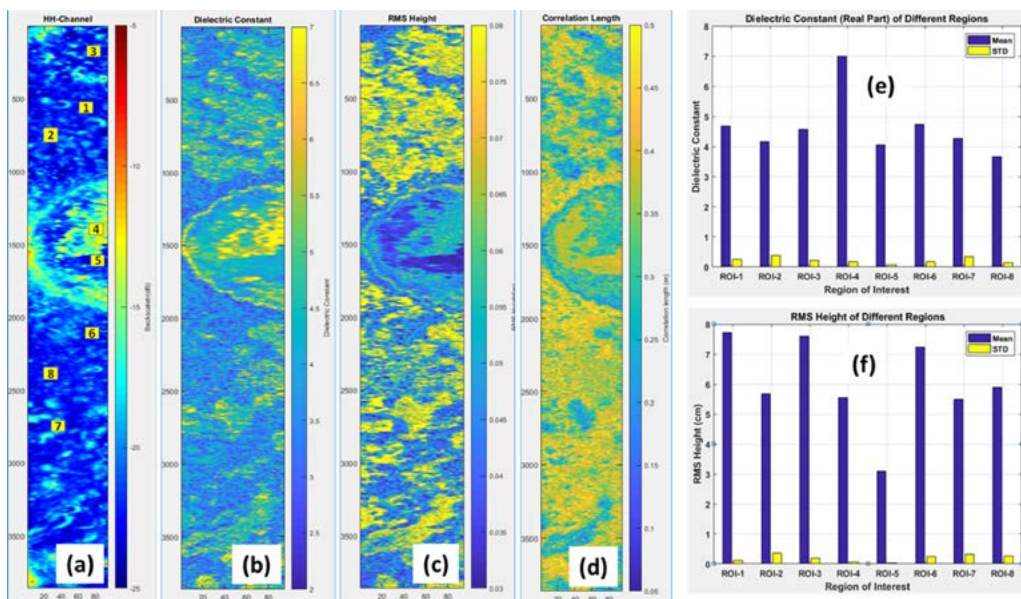
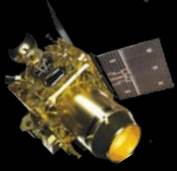


Figure 6.7: Inversion results (a) HH-pol backscatter image with multiple ROIs (b) Dielectric Constant (c) RMS Height (d) Correlation length (e) Statistics of DC (f) RMS Height over multiple ROIs over Non-polar anomalous Gardner Crater.



6.3 Unambiguous Detection of Potential Water Ice Regions:

Earlier radar based studies of lunar polar region for presence of water-ice were ambiguous (disputed) as they were based on CPR enhancement, which can be attributed to both water-ice presence as well as surface roughness. The separability of these two factors could not be achieved due to hybrid-polarimetric radar observations, leading to the above ambiguity. DFSAR instrument on Chandrayaan-2 is the first ever fully polarimetric dual-frequency imaging radar system in lunar orbit and is capable of probing these regions up to few meters depth with full scattering matrix information, unlike its predecessors like CH-1 MiniSAR and LRO-MiniRF. In the present study L-band full-polarimetric SAR data over a section of Peary crater in lunar North Pole is analysed with radar parameters necessary for unambiguous detection of water ice.

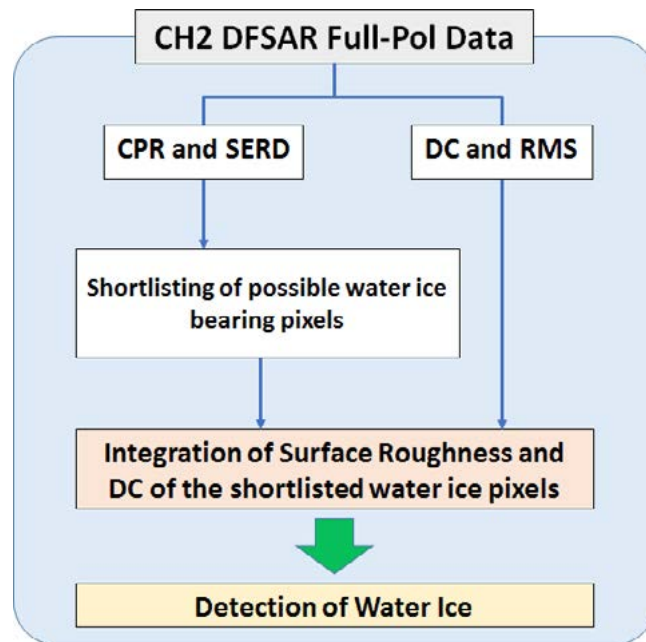
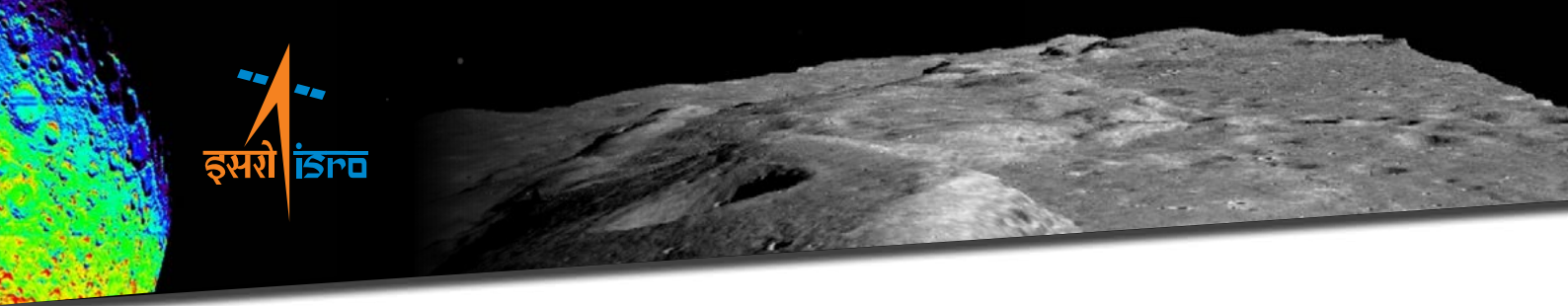


Figure 6.8: The novel integrated approach to unambiguously detect water ice, combining polarimetric parameters and model based Dielectric Constant and surface roughness properties derived from Full-Pol Chandrayaan-2 DFSAR data.

Enhancement of CPR could be either due to surface roughness or presence of water ice. However, decoupling these two factors is essential to detect water ice in PSRs on the Moon. Hence, additional factors to derive the regions with water ice with better confidence are required. Novel polarimetric parameters derived from full-pol (FP) SAR data, like Single Bounce Eigenvalue Relative Difference (SERD), T-Ratio etc. are found efficient over conventional parameters to address the surface features like roughness and dielectric constant. Hence, to decouple the effect of surface roughness and presence of water ice, we used SERD along with CPR observations. The permanently shadowed regions (PSRs) in Lunar poles are reported to contain water-ice of various concentrations mixed with



the lunar regolith. Hence, first, polar CPR anomalous craters, situated in the Permanently Shadowed Regions (PSR) with Peary crater in lunar pole are delineated. Then, SERD and CPR parameters are derived from full-pol DFSAR data. Further the pixels with enhanced CPR compared to SERD are tagged as best possible locations for water ice. The SAR data are ortho-rectified and radiometrically calibrated using LOLA DEM to result final pixel resolution of 25m/pix. Regolith dielectric constant and roughness are estimated through two-layer, multi-parametric inversion models using L-band full-polarimetric data. The water ice regions/pixels are validated using model derived dielectric constant and surface roughness values. The entire methodology is as illustrated in [Figure 6.8](#).

[Figure 6.9](#) exhibits the distribution of most possible locations for existence of water-ice mixed with lunar regolith within the permanently shadowed regions of Peary crater in the Lunar North Pole. The locations of water ice mixed regolith meet the criteria of very low dielectric constant, very low roughness, volume scattering and high circular polarization ratio ([Figure 6.10](#)), the parameters vital for lunar water-ice detection.

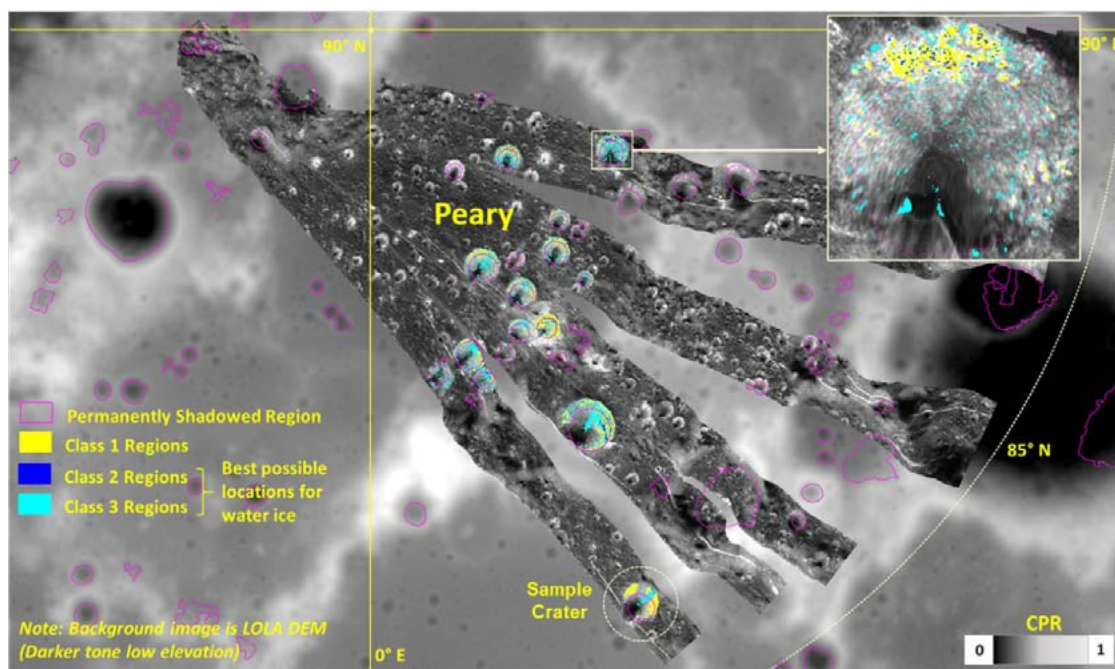


Figure 6.9: Map showing most probable locations (in cyan and blue colours) of regolith mixed water ice overlaid on CH-2 L-band CPR image within the interiors of secondary craters (mostly permanently shadowed regions) on the floor of Peary crater in Lunar North Pole. The SAR images are ortho-rectified and radiometrically terrain corrected using lunar DEM. The background image is a grey-scale DEM derived from NASA's LRO-LOLA data.

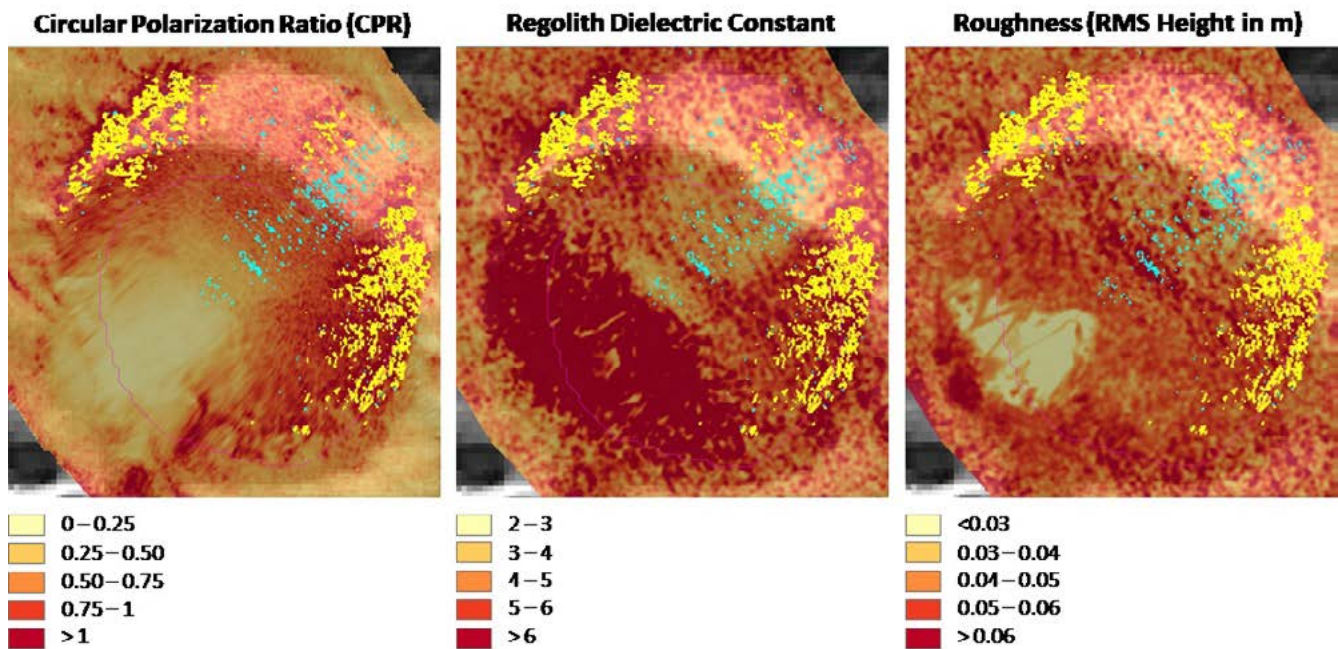
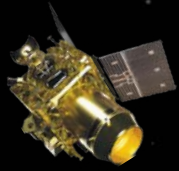


Figure 6.10: Distribution of probable water-ice bearing regions (in yellow and cyan colour) within a sampled crater (as shown in a box in Figure 6.9) overlaid on CPR, regolith dielectric constant and regolith roughness, derived from L-band full-polarimetric data. The cyan coloured regions are associated with low dielectric constant, low roughness and high CPR values and meet the criteria of water-ice bearing regolith, whereas yellow regions do not meet similar criteria and are categorised as no water ice.

Cabeus crater, located near the South Pole of the Moon, is the impact site of Lunar Crater Observation and Sensing Satellite (LCROSS) experiment in 2009. Spectral measurements of the LCROSS ejecta plume detected the presence of water and hydroxyl along with the presence of a number of other volatile species, including CO₂, light hydrocarbons, ammonia, and sulfur-bearing species. Using DFSAR L-band acquisitions of a part of Cabeus crater region, at 25 and 45 m resolution in fully and hybrid (compact-) polarimetric modes respectively, combined with S band radar data from LRO-MiniRF, the initial results indicated no presence of thick, pure water ice deposits within the top ~2-3 meters of the surface in either the permanently shadowed or the sunlit portion of the Cabeus interior analyzed in this work. Also, the results suggest that the form and quantity of water ice detected in the LCROSS impact ejecta plume is not detectable at L- and S-band radar wavelengths. However, using model-based estimates of RMS roughness and dielectric constant using DFSAR data, a few potential “dirty ice” patches within the Cabeus’s crater floor have been identified, as shown in Figure 6.11. Further characterization of these icy patches using dielectric mixing models is in progress.

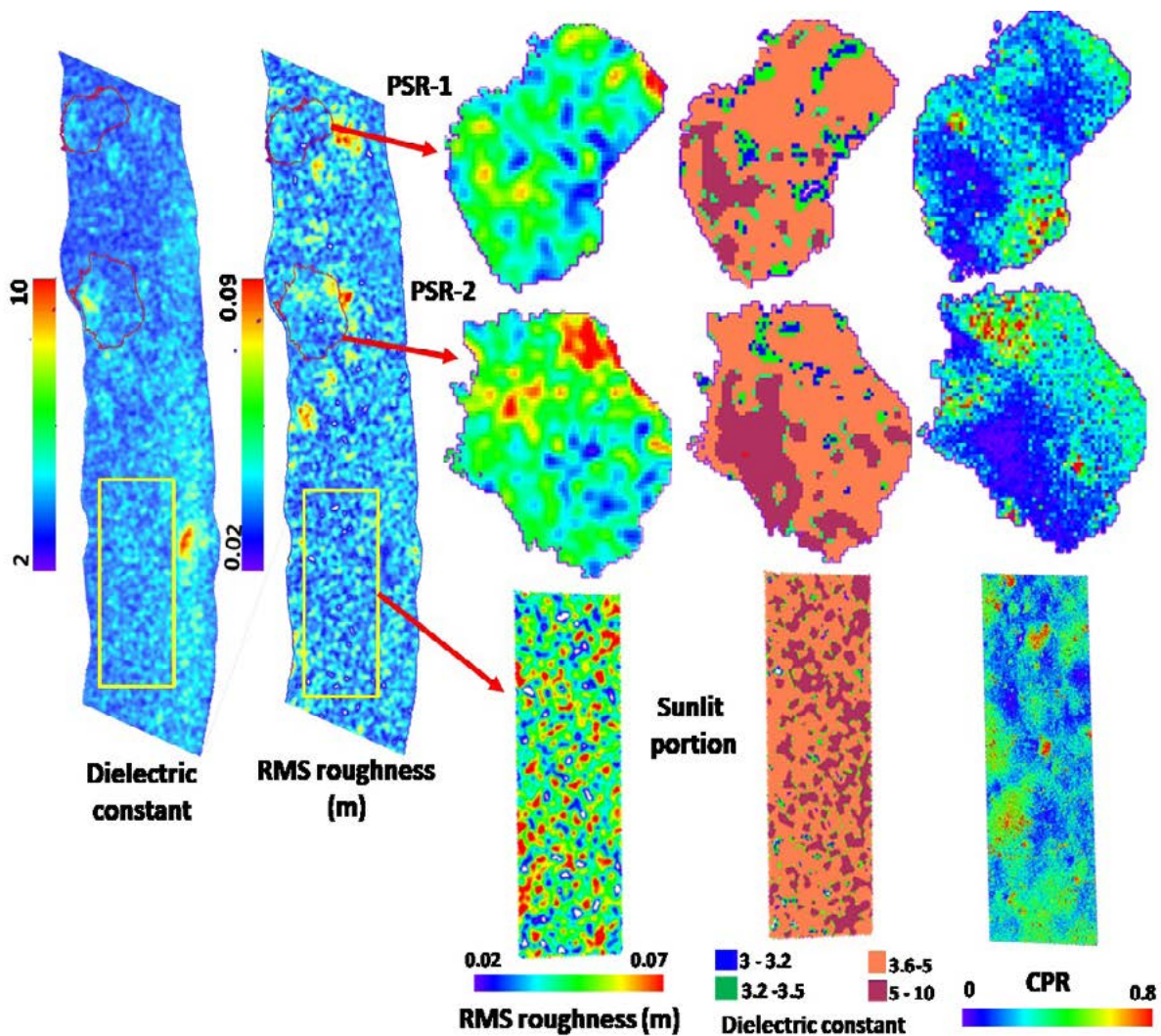
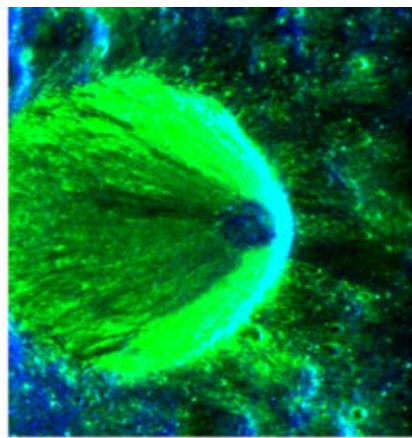
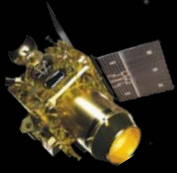


Figure 6.11: RMS Roughness and surface dielectric constant of two permanently shadowed regions (denoted as PSR-1 and PSR-2) and a sunlit portion within the Cabeus's crater floor. Regions with low roughness, low to intermediate circular polarization ratio (CPR), and dielectric constant values within the ice-silicate mixture zone (3.15 to ~6) could possibly contain water ice patches mixed into the regolith.

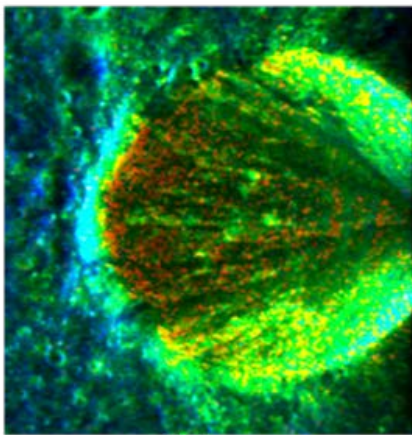
6.4 Polarimetric Characterization of Geomorphological features

6.4.1 Characterization of Impact Craters

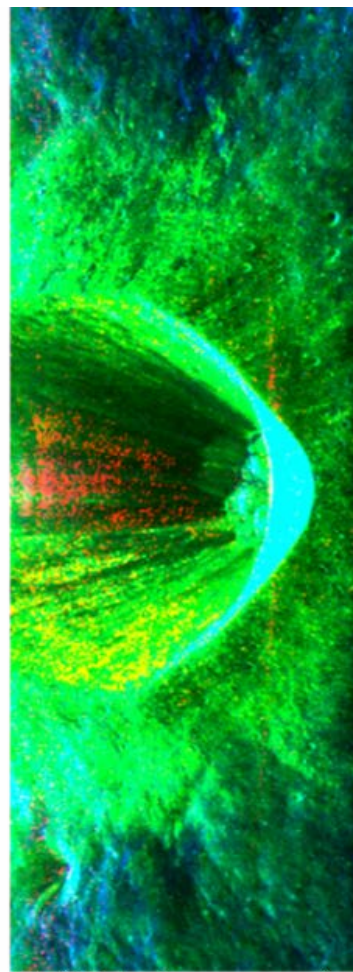
Polarimetric characterization of various types of craters (polar and non-polar, anomalous and non-anomalous/fresh) has been carried out using CPR and other polarimetric indices derived using full-pol data, as shown in [Figure 6.12](#). The studies have been extended to include sensitivity analysis of these indices in order to select the most potential set of parameters for volatile detection.



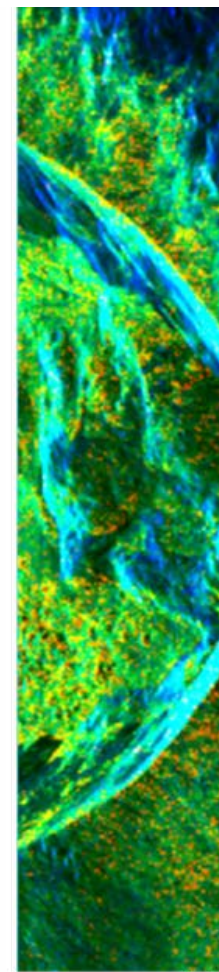
(a) Polar Anomalous Crater of Hermite



(b) Non-Polar Anomalous Byrgius C Crater



(c) Polar Fresh Crater of Rozhdestvenskiy



(d) Non-Polar Fresh Giordano Bruno Crater



Figure 6.12: Polarimetric characterization of various impact craters.

6.4.2 Characterization of Impact Melts of Tycho

Large, complex Copernican craters are some of the best locations on the Moon to study morphologies and settings of well-preserved impact melt units and mineralogy of central peaks, as shown in [Figure 6.13](#). The impact melts and floor deposits associated with Tycho are observed to have high L-band circular polarization ratio values implying that they are very rough at the centimetre to decimetre scale. Combined with IIRS data, studies are planned for compositional and physical properties of impact melt units and non-melt units on the floor and central peak, as well as ejecta blanket of Tycho crater, with the goal of gaining further insight into the regolith development, emplacement dynamics, and space weathering of impact melts.

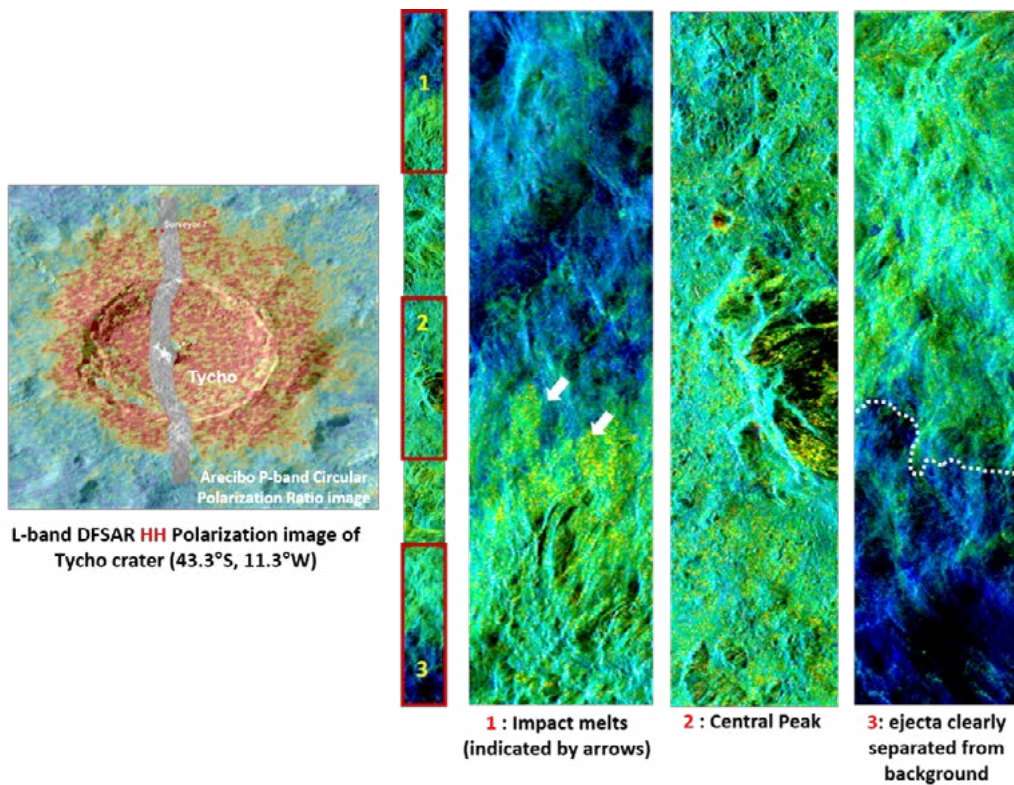
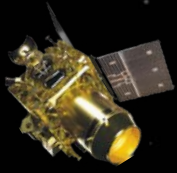


Figure 6.13: Left: L-band DFSAR HH polarization image of Tycho crater overlaid on an Arecibo P-band circular polarization ratio image for context. Right: Decomposition image of Tycho crater region followed by different geologic units shown in zoomed-in subsets. It can be observed from these images that impact melts, floor and ejecta associated with Tycho crater appear 'rough' at L-band wavelength and are clearly separated from the background highlands region.

6.5 Summary

Subsequent to the initial commissioning phase activities of DFSAR during September 2019, the instrument has been tasked for systematic coverage of the lunar poles (85° and polewards) and has been collecting high quality data to cater to various scientific studies. For the first time ever, data from DFSAR support calculation of the 2x2 complex scattering matrix for each resolution cell, which enables lunar near surface characterization in terms of radar polarization properties at different wavelengths and incidence angles. Our initial analysis on polarimetric characterization of a set of impact craters, estimation of surface physical parameters such as dielectric constant RMS roughness, and new techniques to detect the presence of potential water ice zones within the PSRs of the Moon, using dual-wavelength DFSAR data showed promising results and several other studies are in progress. After this initial observation campaign, DFSAR would map the residual polar regions (i.e., ±70° to ±85°) at L-band along with selected non-polar targets at L- and/or S-bands. Based on this coverage, selected regions (e.g., where anomalous CPR values exist) will be observed



with L- and S-band simultaneous, hybrid- and full-polarization imaging. Over the course of the mission, it would be planned to acquire global L-band FP data of the lunar surface to integrate with other global lunar data sets.

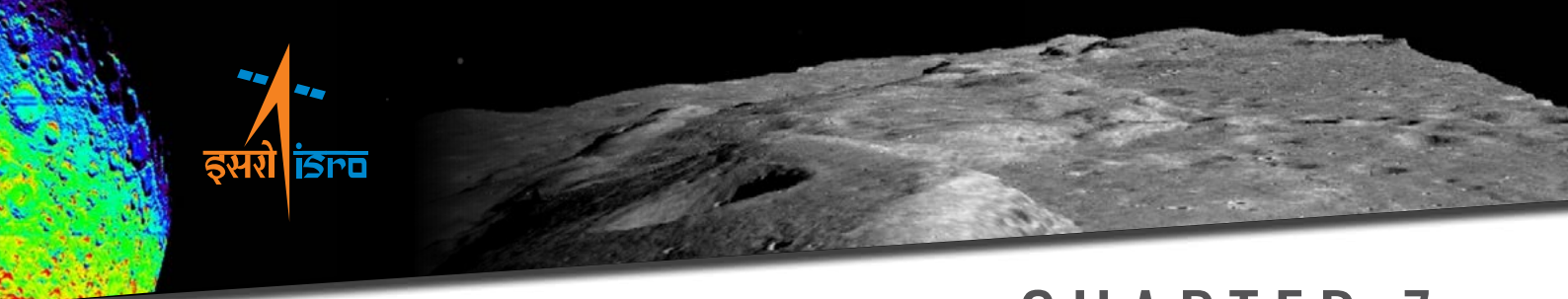
Publications

1. Sriram S. Bhiravarasu, Tathagatha Chakraborty, Deepak Putrevu, Dharmendra Pandey, Anup Das, V. M. Ramanujam, Raghav Mehra, Parikshit Parasher, Krishna M. Agrawal, Shubham Gupta, Gaurav S. Seth, Amit Shukla, Nikhil Y. Pandya, Sanjay Trivedi, Arundhati Misra, Rajeev Jyoti, and Raj Kumar, 2021. Chandrayaan-2 Dual-Frequency SAR (DFSAR): Performance Characterization and Initial Results, The Planetary Science Journal (published: 23 July 2021).
2. Ajeet Kumar, Inderkumar Madanmohan Kochar, Dharmendra Kumar Pandey, Anup Das, Deepak Putrevu, Raj Kumar, and Rajib Kumar Panigrahi (2021), "Dielectric Constant Estimation of Lunar Surface Using MiniRF and Chandrayaan-2 SAR Data", IEEE Transactions on Geoscience Remote Sensing Letters (Accepted).



Contact detail: Dr. Raj Kumar (rksharma@sac.isro.gov.in)

Sri V Manavala Ramanujam (vmanavalan@sac.isro.gov.in)



CHAPTER 7

Science Results from Imaging Infra-Red Spectrometer (IIRS)

The previous chapter has presented the scientific results obtained from DFSAR payload onboard Chandrayaan-2 Orbiter. In this chapter, the scientific results from IIRS payload are presented.

7.1. Unambiguous Characterization of Hydration Feature in the North Polar Region on the far side of the Moon

Spectrometer instruments on-board Chandrayaan-1 (Ch-1) and other recent lunar missions have mapped the surface mineralogy and hydration features of both exogenic and magmatic origin on the Moon. However, due to the limited spectral range of Ch-1 Moon Mineralogy Mapper (M^3) up to $3.0 \mu\text{m}$, the nature of the hydration signatures cannot be ascertained. Thus, in order to properly characterize the lunar hydration feature, Imaging Infra-Red Spectrometer (IIRS) aboard Chandrayaan-2 (Ch-2) is designed with an extended spectral range up to $5.0 \mu\text{m}$ that is presently mapping the lunar surface at a Ground Sampling Distance (GSD) of $\sim 80 \text{ m}$ in ~ 250 spectrally narrow and contiguous channels. Ch-2 was launched on July 22, 2019 from Sriharikota and entered into the lunar orbit on August 20, 2019. The preliminary observations of lunar surface by Ch-2 IIRS from $\sim 4375 \text{ km}$ altitude during the en-route phase are presented here.

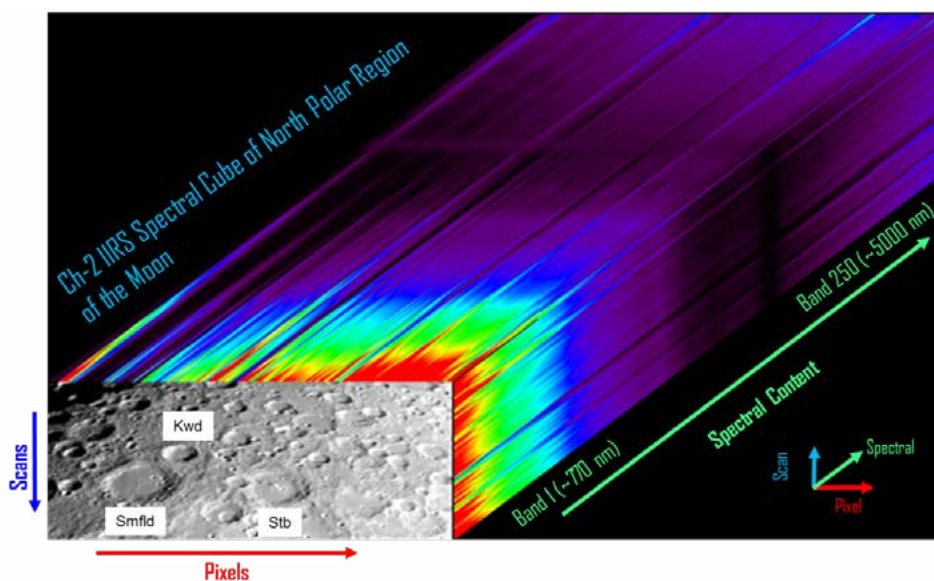


Figure 7.1: IIRS spectral data cube of a subset image acquired on August 23, 2019. The subset of the image has 169 cross-track samples, 73 lines and 251 spectral channels measuring from 810 to 5026 nm.

The first light image (Figure 7.1) of the lunar surface was acquired on August 23, 2019 from an altitude of ~4300 km. It covers part of the lunar far side in the northern hemisphere that include craters Sommerfield, Stebbins and Kirkwood. Preliminary analysis suggests that IIRS could successfully measure the variations in the reflected and emitted solar radiation from the lunar surface from different kinds of surface types, namely, crater central peaks (e.g., Stebbins), crater floors (e.g., Stebbins and Sommerfield), very fresh reworked ejecta associated with small craterlets within the crater floor of a large crater (e.g., Sommerfield) and the sun-illuminated inner rims of craters (e.g., Kirkwood).

Level 1 radiance data has been converted to reflectance by normalizing the measured spectral radiance by the incoming solar flux. Notable differences in the spectral shapes are observed as a function of surface types, degree of optical maturity and the mineralogy/litho-types attributable to the inherent compositional heterogeneity that exist in the lunar crust. A broad absorption near 3000 nm is seen in the mean spectra of Regions of Interest (ROIs) obtained from the image shown in Figure 7.2. This could be attributed to the presence of surface hydroxyl and/or water adsorbed in the lunar regolith. The shape and intensity of the 3000-nm feature is found to vary as a function of surface composition and degree of space weathering (Figure 7.3).

For the first time, OH and H₂O have been separately identified. Band Center value of the 3000-nm feature is found to vary from ~2.82 to 3.16 μm having two modes with mean Band Center locations near ~2.86 and 2.95 μm respectively (Figure 7.4) suggesting the presence of both OH and H₂O in the north polar region on the far side of the Moon (Bhattacharya et al., LPSC-2020, Abstract #1516).

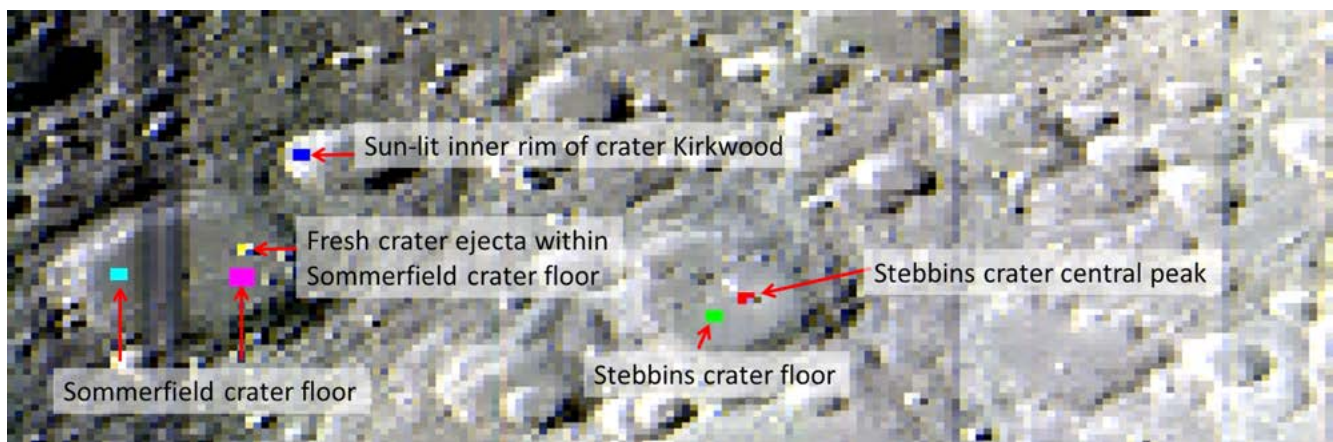


Figure 7.2: Coloured rectangular boxes represent the Regions of Interest (ROIs) from where representative IIRS spectra have been obtained.

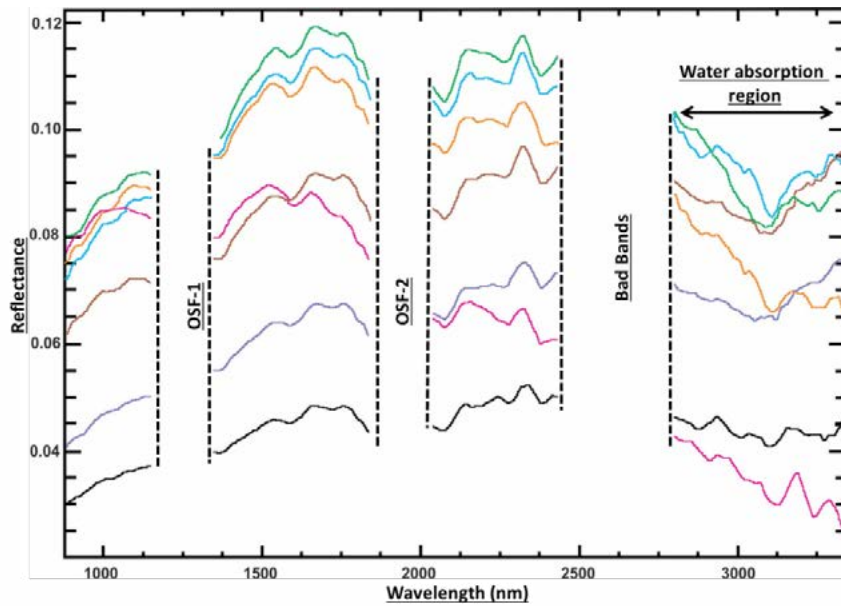


Figure 7.3: Mean spectra of the ROIs shown in Figure 7.2 highlighting the presence of prominent 3000-nm hydration feature (black double-headed arrow). First ever detection of hydration in the spectral range of 2.7-3.2 μm at spatial resolution of ~ 80 m.

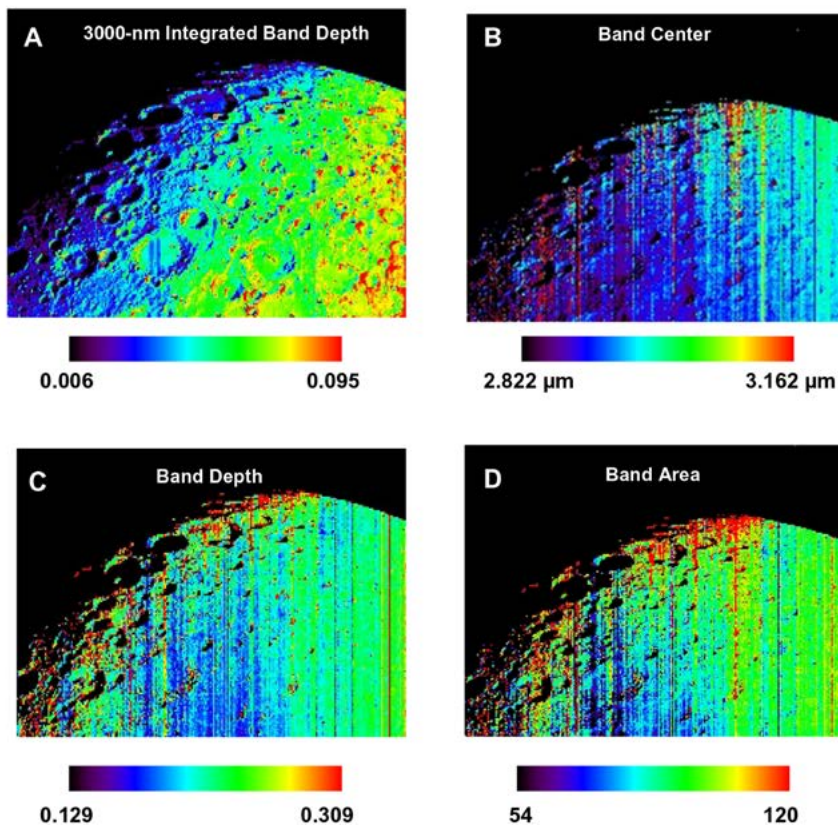
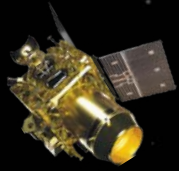


Figure 7.4: **A.** 3000-nm Integrated Band Depth (IBD) map to highlight the variations in the strength of the hydration ($\text{OH}/\text{H}_2\text{O}$) feature as captured by Ch-2 IIRS data over the north polar region on the far side of the Moon; **B.** Band Center; **C.** Band Depth and **D.** Band Area map.



7.2. Detection and Quantification of Hydroxyl at Crater Aristarchus

One of the major objectives of Chandrayaan-2 (Ch-2) Imaging Infra-Red Spectrometer (IIRS) is to detect and map the lunar surface minerals and to understand the mineralogical make-up of the lunar crust vis-à-vis understanding the nature of lunar surface hydration [Bhattacharya et al., 2020; Roy Chowdhury et al., 2020], wherever present. Here, the mineralogical diversity and enhanced hydration feature associated with crater Aristarchus (23.6°N, 47.5°W) is seen (Figures 7.5A and 7.5B). Prominent doublet as well as asymmetric absorption feature is seen near 3000 nm (Figure 7.5 C) having shorter wavelength band/absorption minima around 2810 nm and longer wavelength at ~3030 nm owing to the presence of adsorbed OH/H₂O in the impact melts, ejecta, bedrock exposures and the pyroclastic deposits. The doublet and asymmetric nature of the hydration feature suggests it to be more of adsorbed OH than H₂O. The shape of the hydration features and its strength varies from pyroclasts to impact melts to coarse ejecta and/or bedrock exposures, and it ranges from ~5-20%. Observed water concentration has been quantified using ESPAT parameter that is linearly related with the amount of water present at a given location (pixel) (Milliken and Li, 2017). The water concentration is found to vary from ~15-170 ppm with an average value of ~80 ppm in the studied site (Figure 7.5D and E). For the first time, complete characterization of the 3000-nm hydration feature is carried out using Ch-2 IIRS data at highest ever spatial resolution of ~80 m (Bhattacharya et al., LPSC-2021, Abstract #1848). The nature of the hydration feature strongly suggests it to be hydroxyl (OH) and the water content is found to vary from ~15-170 ppm. The IIRS spectral range beyond 3 μm has helped in complete characterization of the lunar hydration feature for the first time.

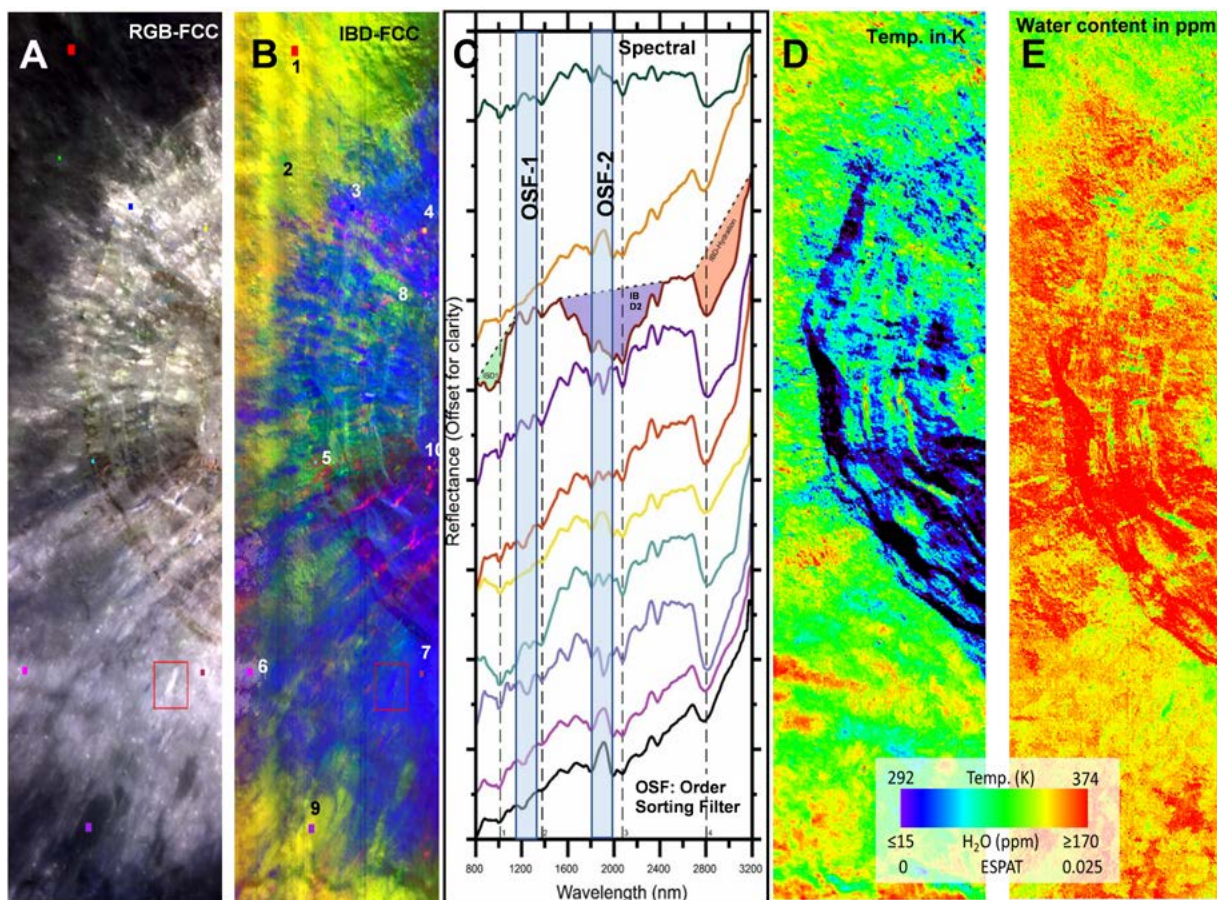
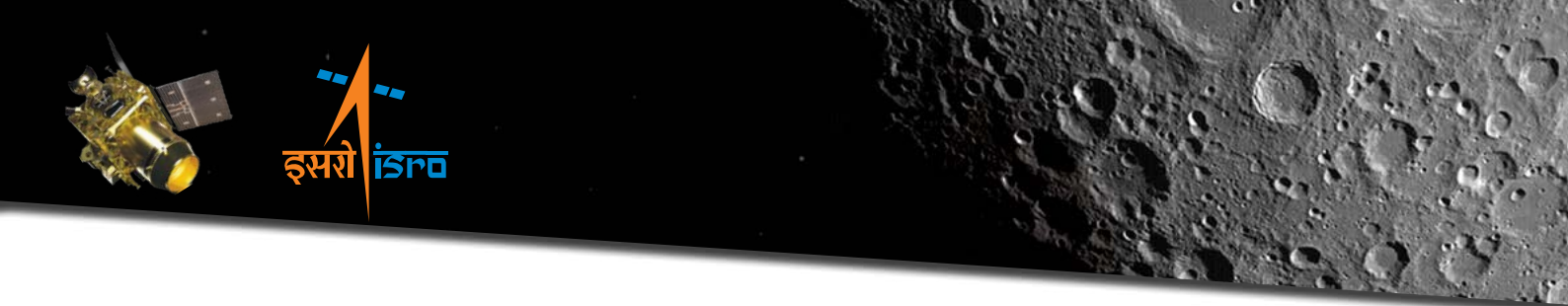


Figure 7.5: A. Ch-2 IIRS RGB-FCC. Coloured boxes indicate Regions of Interest (ROIs); B. IBD-Albedo-based FCC. ROIs are marked as 1-10; C. Mean spectral plot corresponding to the ROIs; D. Temperature map; E. ESPAT vis-à-vis H₂O content map of crater Aristarchus.

7.3. Unambiguous Detection of OH & H₂O on the Moon

IIRS is designed to measure the reflected and emitted solar radiations from the lunar surface in spectral range of 0.8 to 5.0 μm. Its high-spatial (~80m) resolution and extended spectral range is most suitable to completely characterize the lunar hydration in the 2.8 to 3.5 μm region of electromagnetic spectrum (“often called 3 μm absorption band”). The 3.0 μm lunar hydration absorption is attributed to presence of hydroxyl (OH) attached to a metal cation or molecular water (H₂O) or their combination. This remote detection of water and/or hydroxyl signature on the lunar surface was also suggested by several laboratory studies and has acquired significant importance as it provides important clues to understand the hydration sources and formation mechanisms on the Moon. IIRS spectral reflectance data was analysed to detect and quantify 3-μm absorption on the Moon using orbital data with an extended spectral range up to 5.0 μm. Ch-2 IIRS spectral radiance data cubes were subjected to various pre-processing and data reduction techniques such as thermal correction, conversion to apparent reflectance and empirical line correction to



obtain the lunar reflectance spectra between 0.8 to 5.0 μm (Figure 7.6). A physics based thermal correction into analysis of reflectance spectra of IIRS has been developed using co-located temperature measurement of lunar surface. Lunar hydration absorption at 3 μm has been observed to be present at all latitudes and surface types with varying degree for all pixels in study area between 29° to 62° N (Figure 7.6). The spectral absorption depth shows distinct variability associated with lunar mineralogy, surface temperature and latitudinal dependence. It has been observed that lunar plagioclase dominated lithologies show higher degree of hydration, when compared to mare regions related to its crystal structure and thermodynamic properties (Figure 7.7). It is suggested that OH retention is more associated with space-weathered mare surfaces at higher surface temperature (>320K), while coarse grained bright plagioclase-rich fresh surfaces are relatively H₂O dominated due to solar wind implantation of H⁺ at crystal defect sites and their higher binding energy for water (Chauhan et al., Curr. Sci., 2021, *in Press*).

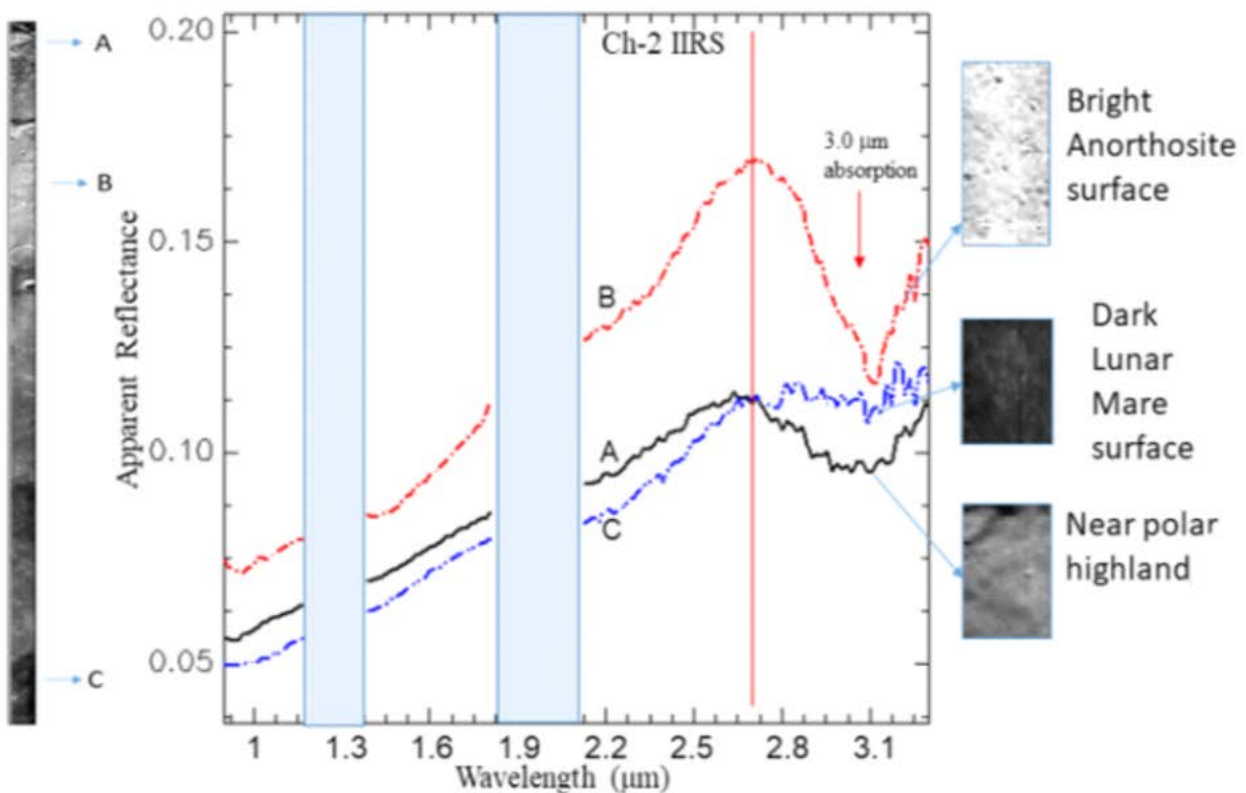


Figure 7.6: Thermally corrected lunar spectra for IIRS data strip-2 for bright anorthositic, mare and near polar highland surface. It shows significant lunar hydration feature varying with different surface composition types.

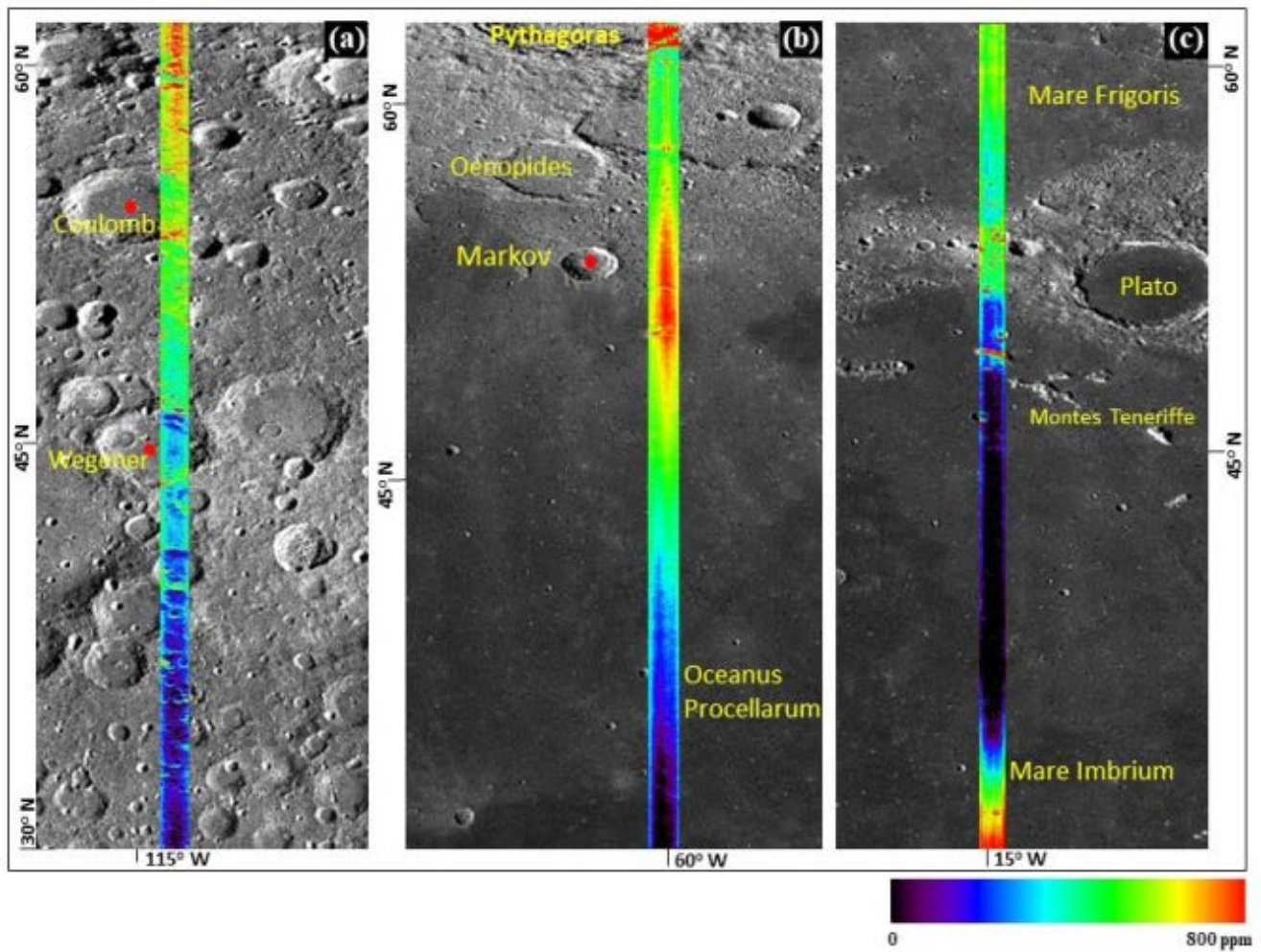
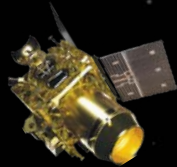


Figure 7.7: Total hydration maps for the thermally corrected Chandrayaan-2 IIRS strips analysed in the present study. The observed total water concentration is varying between near 0 to 800 ppm having strong control on mineralogy and latitudes.

7.4 Summary

First ever full characterization of 3000-nm hydration feature on the Moon at an unprecedented spatial resolution of ~80 m and unambiguous identification of OH and H₂O separately near the north polar region (far side of the Moon) has been carried out by Ch-2 Imaging Infra-Red Spectrometer (IIRS). First time reporting of hydroxyl (OH) within the crater Aristarchus and adjoining regions. This will help in better classification and mapping of the lunar hydration regimen.

Lunar hydration absorption at 3 μm has been observed to be present at all latitudes and surface types with varying degree for all pixels in study area between 29° to 62° N. The spectral absorption depth shows distinct variability associated with lunar mineralogy,



surface temperature and latitudinal dependence. It has been observed that lunar plagioclase dominated lithologies show higher degree of hydration, when compared to mare regions related to its crystal structure and thermodynamic properties.

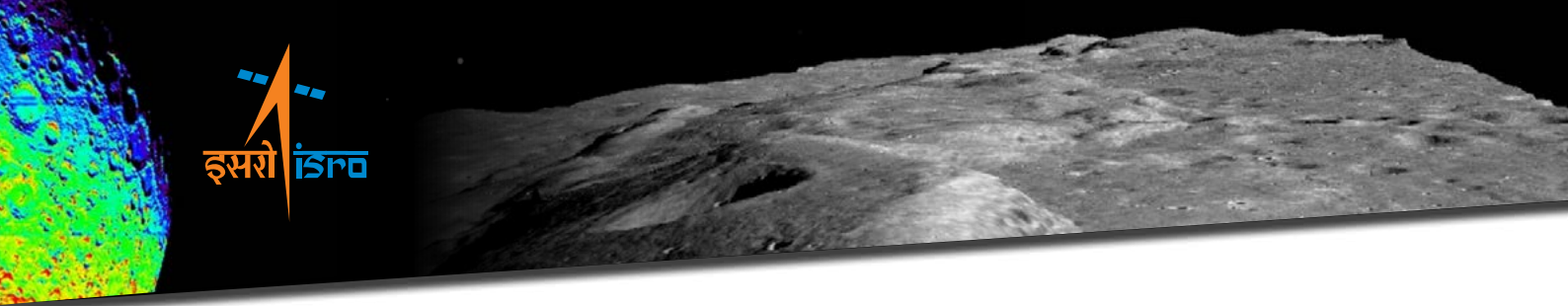
Presently on-orbit calibration and validation of IIRS data is being carried out with more and more acquisition of data over the lunar surface that includes Apollo landing sites and lunar poles. Data sets having common illumination and observation geometries with Ch-1 M³ are also being compared for the qualitative assessment of the IIRS data. In near future, Earth-imaging will be planned for spectral validation of IIRS by comparing spectral features of the atmosphere.

Publication

Chauhan, P., Chauhan, M., Verma, P. A., Sharma, S., Bhattacharya, S., Dagar, A. K., Amitabh, Patil, A. N., Parashar, A. K., Kumar, A., Desai, N. M., Karidhal, R., and Kiran Kumar, A. S., 2021. Unambiguous detection of OH & H₂O on the Moon from Chandrayaan-2 imaging Infra-Red spectrometer (IIRS) reflectance data using 3.0 μm hydration feature. Current Science (in Press).

References

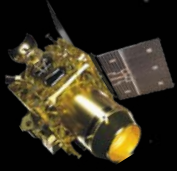
1. Bhattacharya, S., Dagar, A. K., Banerjee, A., Kumar, A., Amitabh, Suresh, K., Prashar, A., Patil, A., Roy Chowdhury, A., Saxena, A. R., Gomathi, S., Vijaysree, V., Chauhan, P., Chauhan, M., Pathak, S., Dhingra, D., Chatteraj, S. L., Moitra, H., Gupta, S, 2020. Preliminary Observations of Lunar Surface by Chandrayaan-2 Imaging Infra-Red Spectrometer (IIRS). 51st Lunar and Planetary Science Conference (2020), Abstract #1516.
2. Bhattacharya, S., Dagar, A. K., Kumar, A., Patil, A., Banerjee, A., Amitabh, A., Suresh, K., Prashar, A., Pathak, S., Chauhan, P., Gomathi, S., Karmakar, P., Karidhal, R., Desai, N. M., Kiran Kumar, A. S. 2021. Mineralogical Diversity and Hydration Feature at Crater Aristarchus as Revealed by Chandrayaan-2 Imaging Infra-Red Spectrometer (IIRS). 52nd Lunar and Planetary Science Conference (2021), Abstract #1848.
3. Chauhan, P., Chauhan, M., Verma, P. A., Sharma, S., Bhattacharya, S., Dagar, A. K., Amitabh, Patil, A. N., Parashar, A. K., Kumar, A., Desai, N. M., Karidhal, R., and Kiran Kumar, A. S., 2021. Unambiguous detection of OH & H₂O on the Moon from Chandrayaan-2 imaging Infra-Red spectrometer (IIRS) reflectance data using 3.0 μm hydration feature. Current Science (in Press).



- 4 Milliken, R.E., Li, S., 2017. Remote detection of widespread indigenous water in lunar pyroclastic deposits. Nat. Geosci. 10 (8), 561–565. <https://doi.org/10.1038/ngeo2993>.
- 5 Roy Chowdhury, A., Banerjee, A., Joshi, S. R., Dutta, M., Kumar, A., Bhattacharya, S., Amitabh, Rehman, S., U., Bhati, S., Karelia, J. C., Biswas, A., Saxena, A. R., Sharma, S., Somani, S. R., Bhagat, H. V., Sharma, J., Ghonia, D. N., Bokarwadia, B. B., and Parasar, A.: Imaging Infra-Red Spectrometer onboard Chandrayaan-2 Orbiter. Current Science 02/2020; 118(3):368-375.



Contact detail: Sri Satadru Bhattacharya (satadru@sac.isro.gov.in)
Sri Aditya Dagar (adagar@sac.isro.gov.in)
Sri Amitabh (amitabh@sac.isro.gov.in)



CHAPTER 8

Science Results from Terrain Mapping Camera-2 (TMC-2)

The results from TMC-2 are categorised into two main categories viz. 1) Glimpses of some spectacular lunar morpho-structural features & 2) Science results.

8.1 Glimpses of Lunar Morphological Features Mapped using TMC-2 Ortho Image and Digital Elevation Model (DEM) Data Sets

Lunar surface is dominated by impact craters of various sizes and other morphological features like rilles, scarps, wrinkle ridges and volcanic landforms like domes and cones. Study of these features through morphological mapping, surface age estimation, stratigraphic relationship between adjoining geological features is very much useful for understanding Lunar surface processes i.e. volcanic, tectonic and impact cratering processes. TMC-2 images acquired over different morphological features are shown and briefly discussed in this section.

8.1.1 Impact Craters:

Lunar surface is dominated by impact craters of various sizes ranging from few m to thousands of km (simple crater to huge basins like South Pole Aitken (SPA) basin).

8.1.2. Oblique Impact Crater:

Oblique impact craters are generally believed to be created by high speed angular impacts. Example of an oblique impact crater is shown in [Figure 8.1](#). This crater (23.2799° W, 18.7235° N) lies near Draper A crater in the southern part of Mare Imbrium region. Study of such craters reveal the past impact dynamics of the incoming projectiles hitting the Moon viz. speed, direction and angle of the impactor.

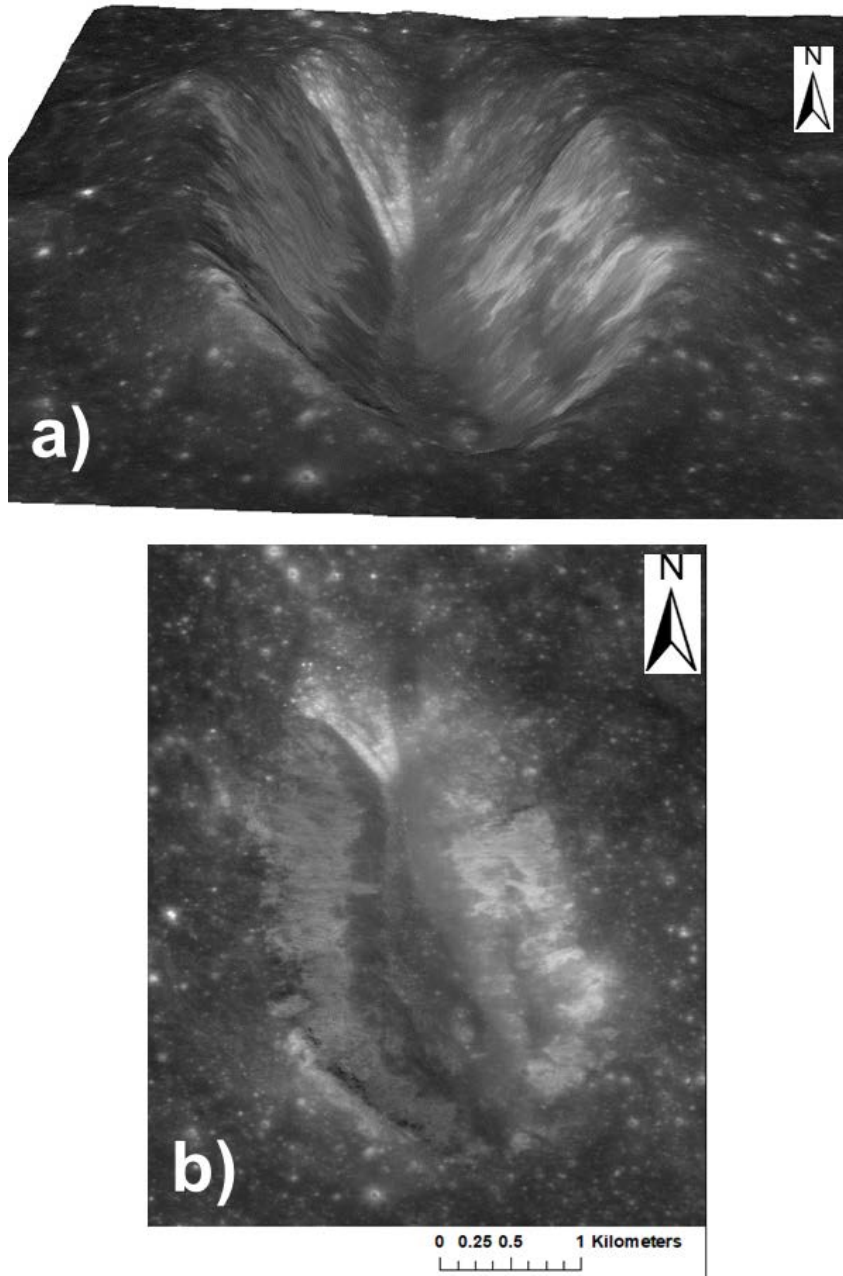
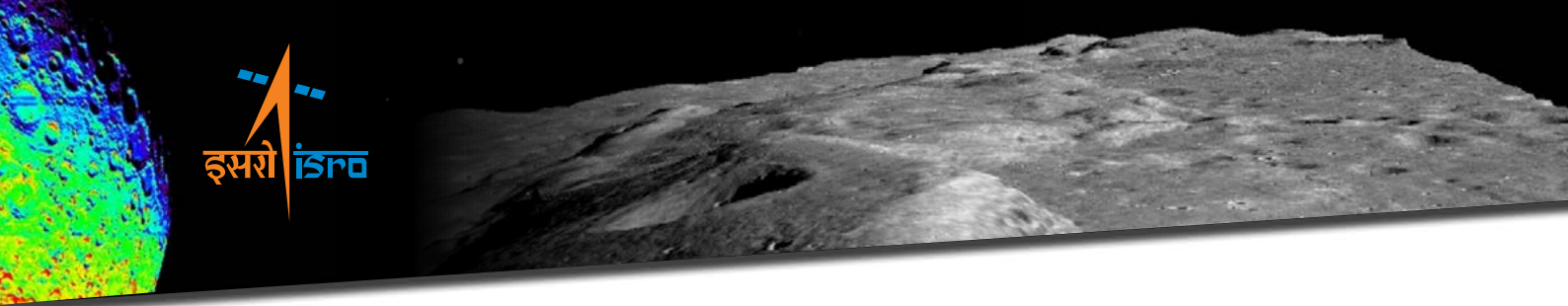


Figure 8.1: (a) 3D perspective view of an oblique crater prepared by draping the TMC-2 orthoimage on DEM (b) Orthoimage.

8.1.3 Mass Wasting in Crater:

Mass wasting in a crater refers to the slumping of loosely held rock debris and/or soil downslope along the wall of crater under the effect of gravity. [Figure 8.2](#) shows Tralles A crater (46.7952° E, 27.3926° N). The signs of mass wasting are seen on the inner wall of crater ([Figure 8.2](#) (a, orange arrows)). Debris accumulated at the floor of the crater are also observed.

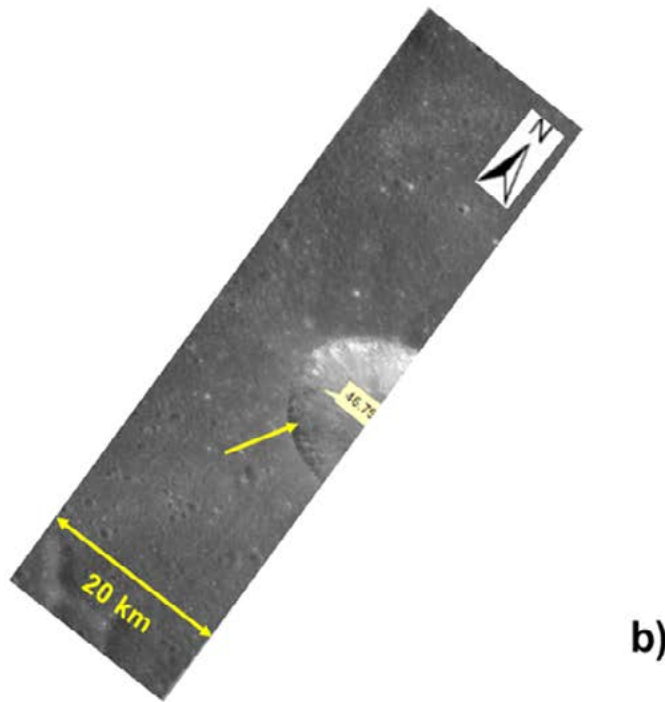
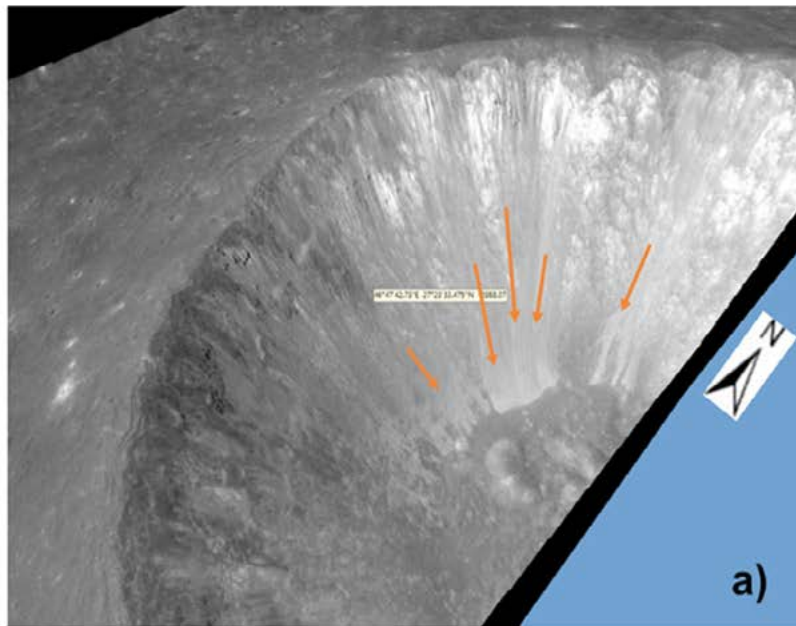
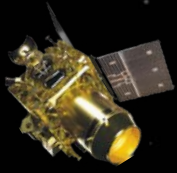


Figure 8.2: (a) 3D perspective view of mass wasting in a crater prepared by draping the TMC-2 orthoimage on DEM (b) Orthoimage.

8.1.4 Lava Filled Crater and an Effusive Dome:

Example of a Lava filled Crater and an effusive dome is shown in [Figure 8.3](#). Image shows partially exposed rims of a crater (Yellow Arrow; 3.2696° E, 16.4446° N) lying in Mare Vaporum region near Yangel' crater. The crater has been filled with Lava, probably supplied by an effusive dome adjacent to the crater.

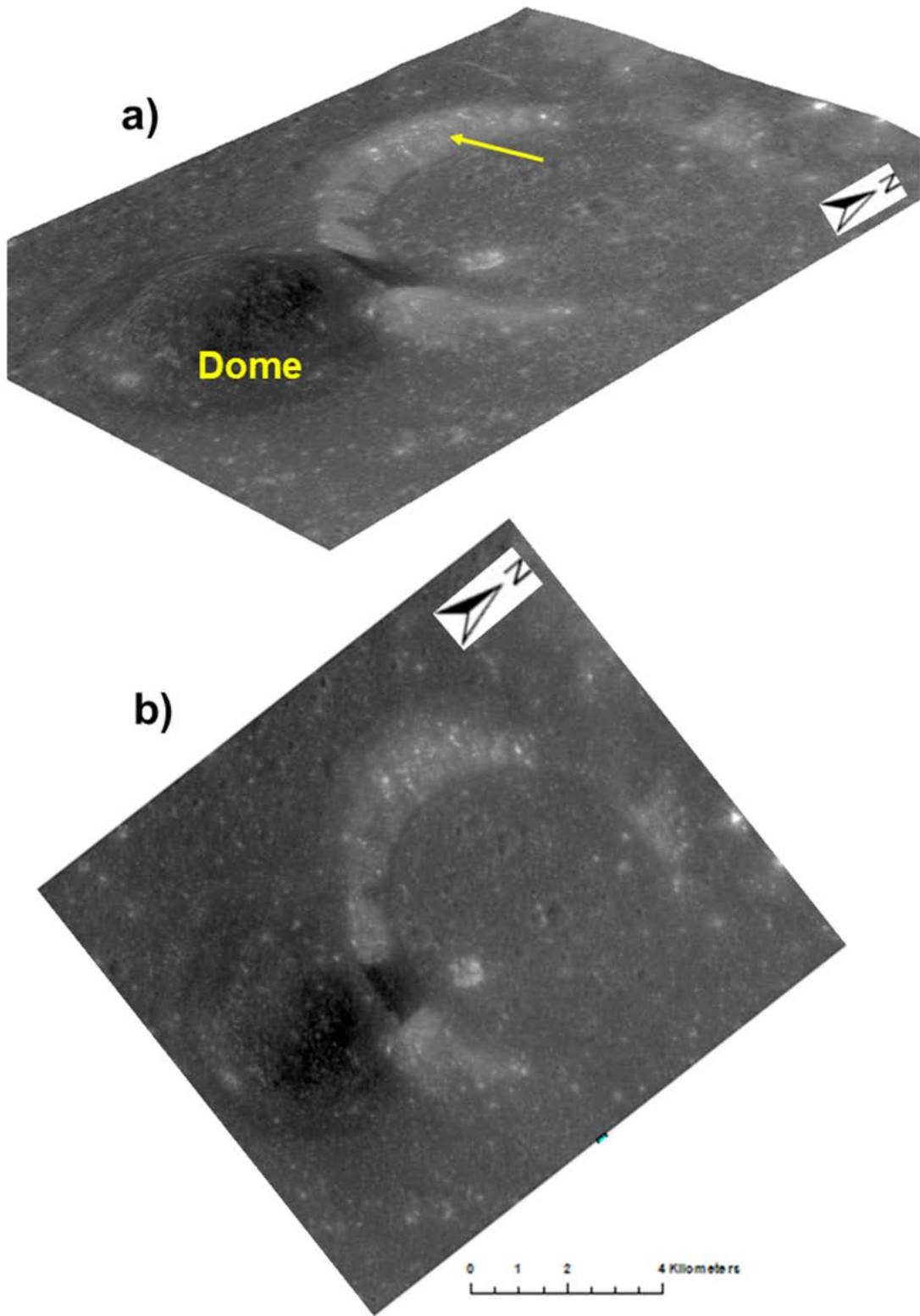
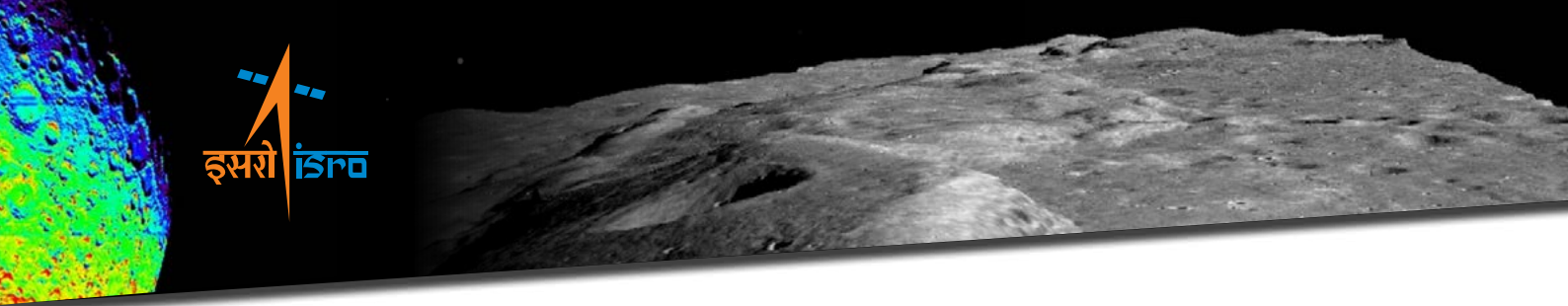
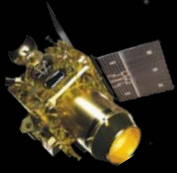


Figure 8.3: (a) 3D perspective view of lava-filled crater (arrow) and an effusive dome prepared by draping the TMC-2 orthoimage on DEM (b) Orthoimage.



8.1.5 Fresh Young Crater:

The fresh young craters are identified by bright rays radially and uniformly distributed around them. TMC-2 Image shows star shaped bright ejecta material spread around a fresh young crater (64.1461° W, 14.5529° N) in western Oceanus Procellarum region near Galilaei S crater. The ejecta material (bright) can be seen uniformly spread in all directions for this fresh crater. Example of fresh young impact crater is shown in [Figure 8.4](#).

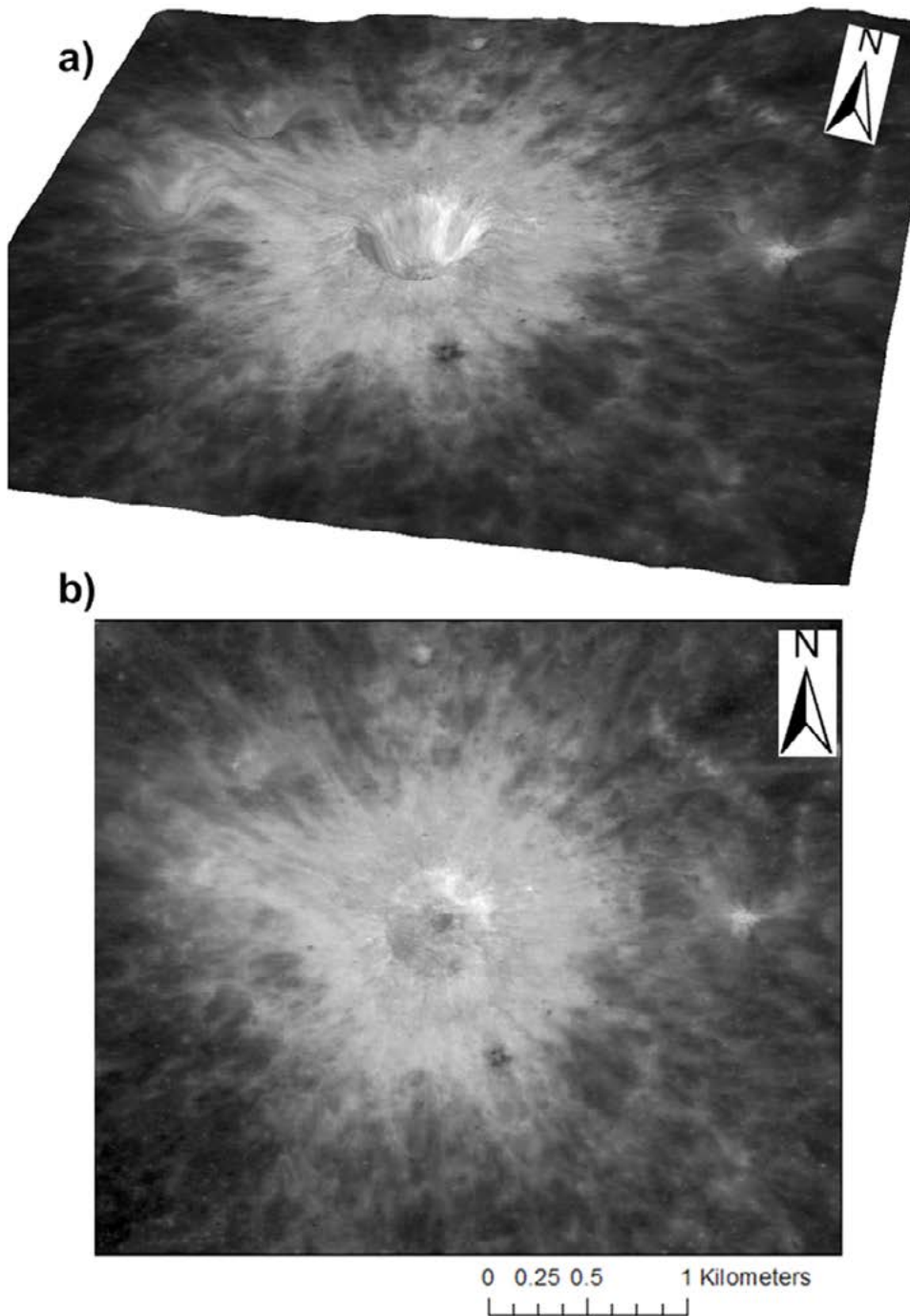
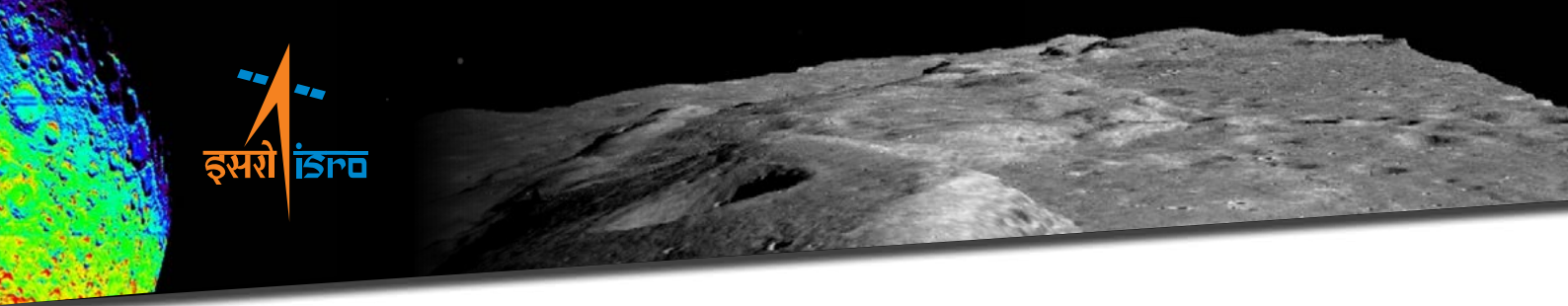


Figure 8.4: (a) 3D perspective view of a fresh young crater prepared by draping the TMC-2 orthoimage on DEM (b) Orthoimage.



8.1.6 Young Crater:

The ray structure of fresh young craters gradually diminishes due to space weathering/maturity of top soil and it becomes non-uniformly spread. [Figure 8.5](#) shows a young crater with bright ejecta non-uniformly spread around the crater (3.3° E, 14.07° N) in Mare Vaporum region of Moon.

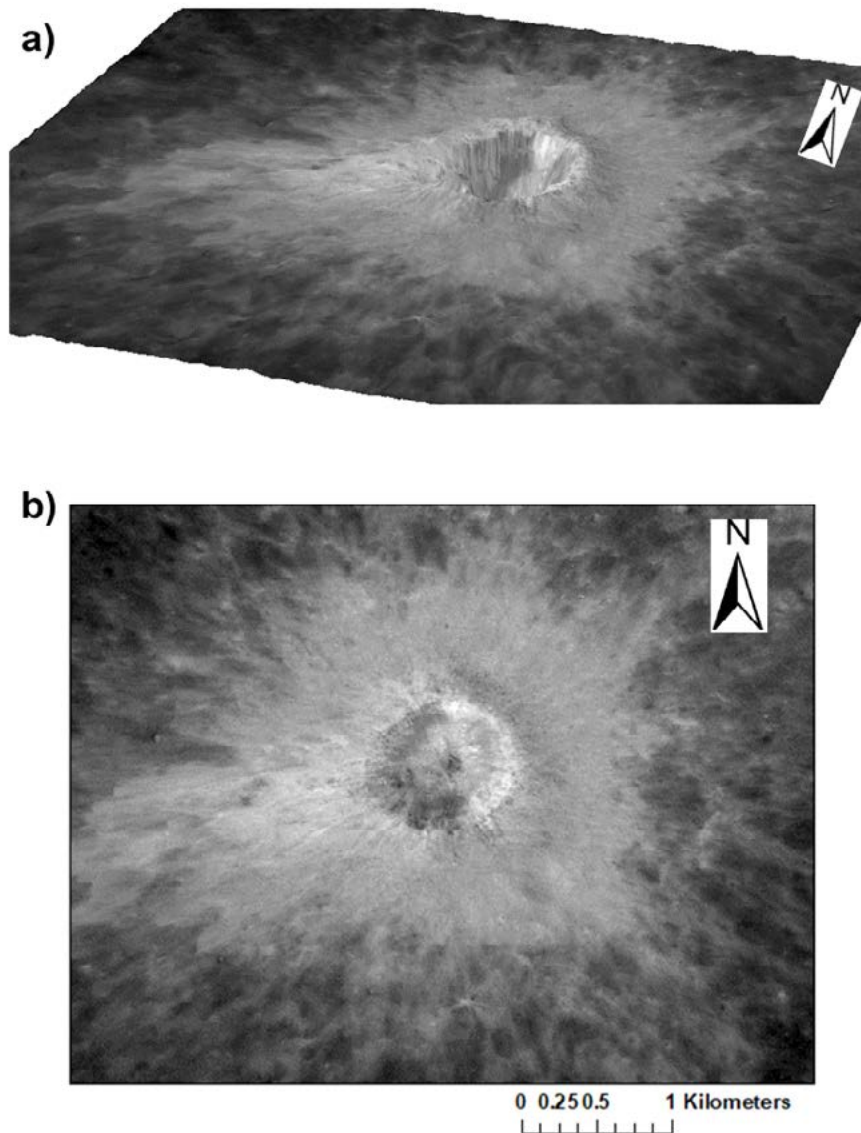
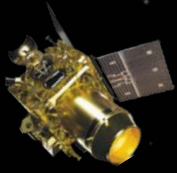


Figure 8.5: (a) 3D perspective view of a young crater prepared by draping the TMC-2 orthoimage on DEM. (b) Orthoimage.

8.1.7 Rilles (Crater Floor):

Rilles are trench shaped features supposed to be formed due to collapse of roof of the lava tubes. Several large complex craters undergo post-emplacment modifications and floor fracturing. This results in secondary volcanic activity within the crater floor resulting



in creation of linear/concentric rille structures. In [Figure 8.6](#), near-linear rille (indicated by yellow arrow) can be seen in the eastern half of Campanus crater (27.90° W, 28.04° S) running north south across the entire crater floor. A crater can be seen superposed over the rille indicating post rille impact activity ([Figure 8.6 \(a\)](#)).

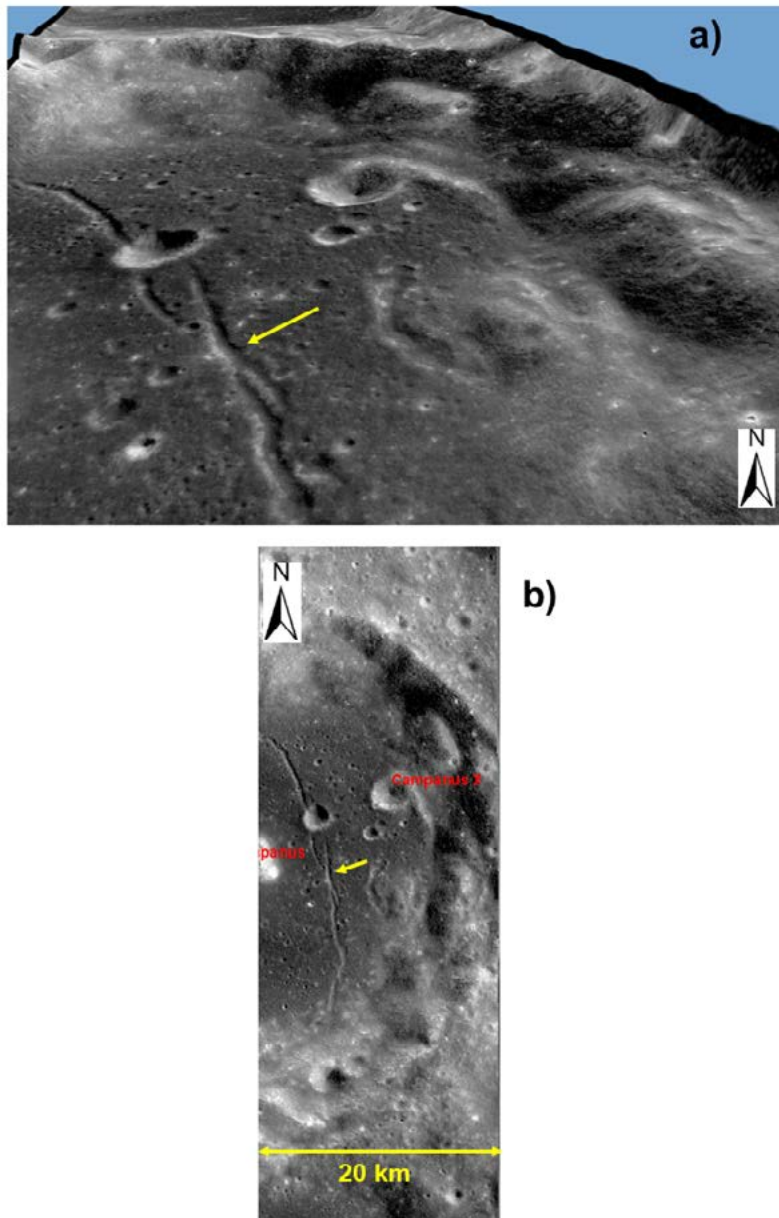


Figure 8.6: (a) 3D perspective view of rilles on a crater floor prepared by draping the TMC-2 orthoimage on DEM (b) Orthoimage.

8.1.8 Rilles (Sinusoidal):

At times, due to tecto-volcanic activities multiple rilles are formed in a crisscross and braided fashion. This image ([Figure 8.7](#)) shows a set of curvilinear rilles lying at 12.49° W, 29.28° S in southern edge of Mare Nubium and extending in a sinusoidal form ([Figure 8.7 b](#)).

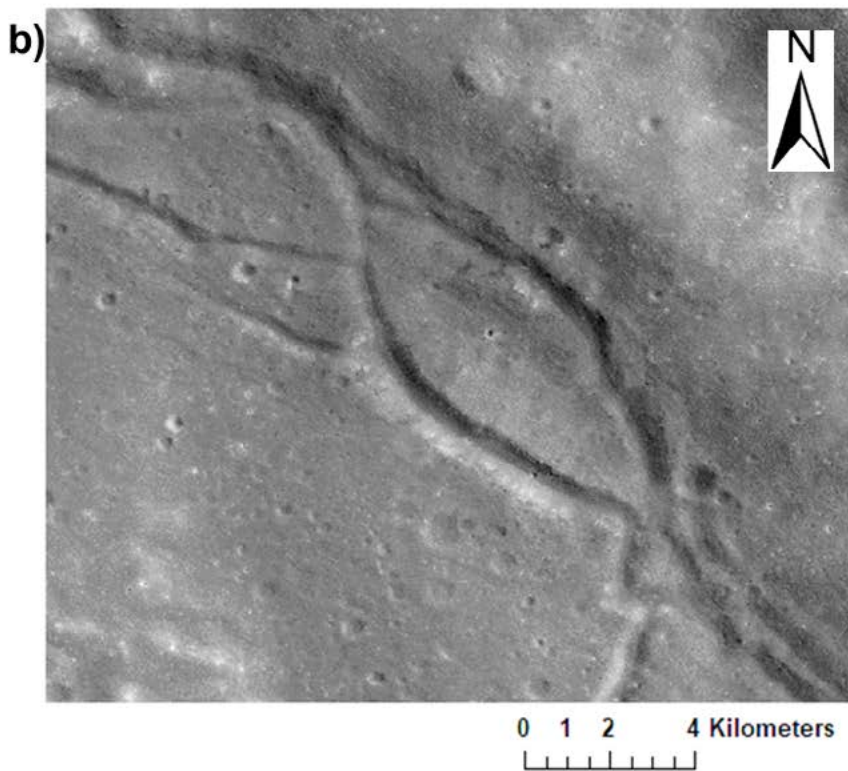
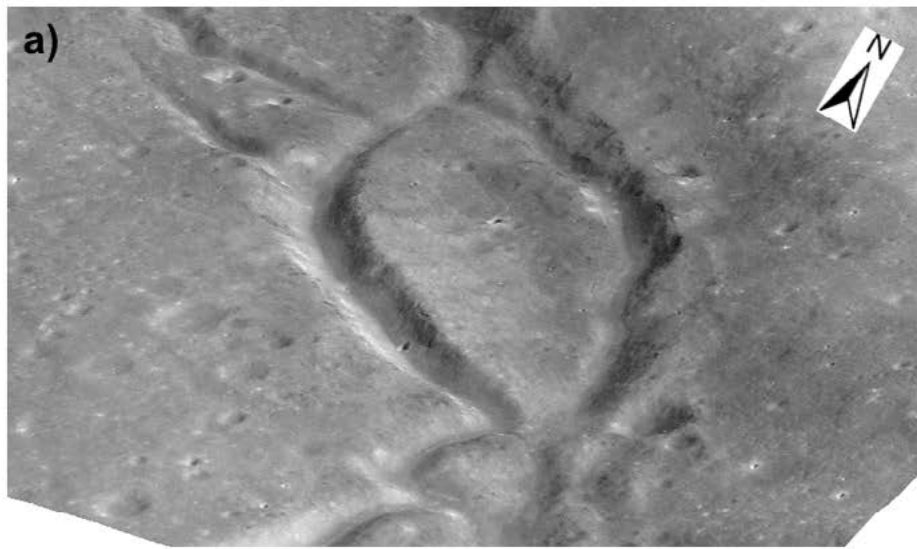
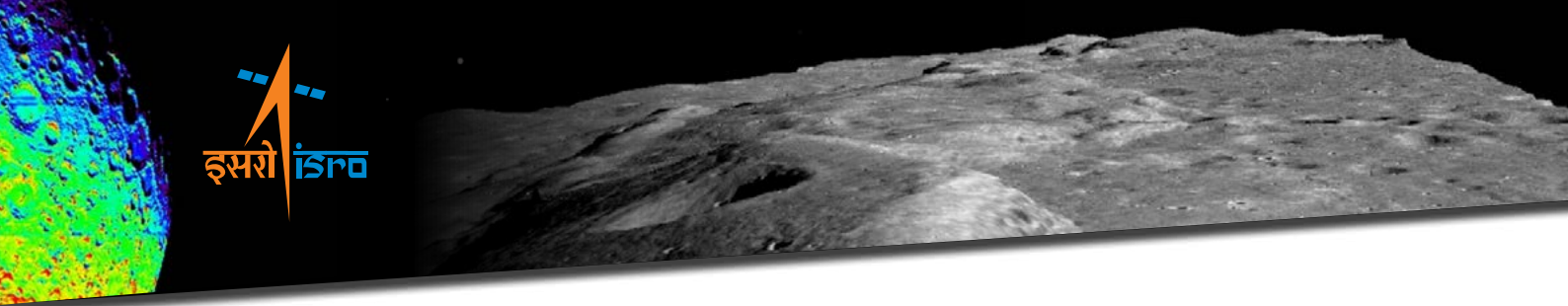


Figure 8.7: (a) 3D perspective view of sinusoidal rilles prepared by draping the TMC-2 orthoimage on DEM (b) Orthoimage.

8.1.9 Lunar Rilles Proximal to Basin Margin:

Many large rilles running for hundreds of kilometers sometimes tend to follow the margins of Mare basins in curvilinear/concentric form. This Rille (Figure 8.8 (b), 329.3° E, 26.4° N) is part of a large concentric rille at the basin margin of Mare Humorum. This might have been emplaced due to tectonic/volcanic processes.

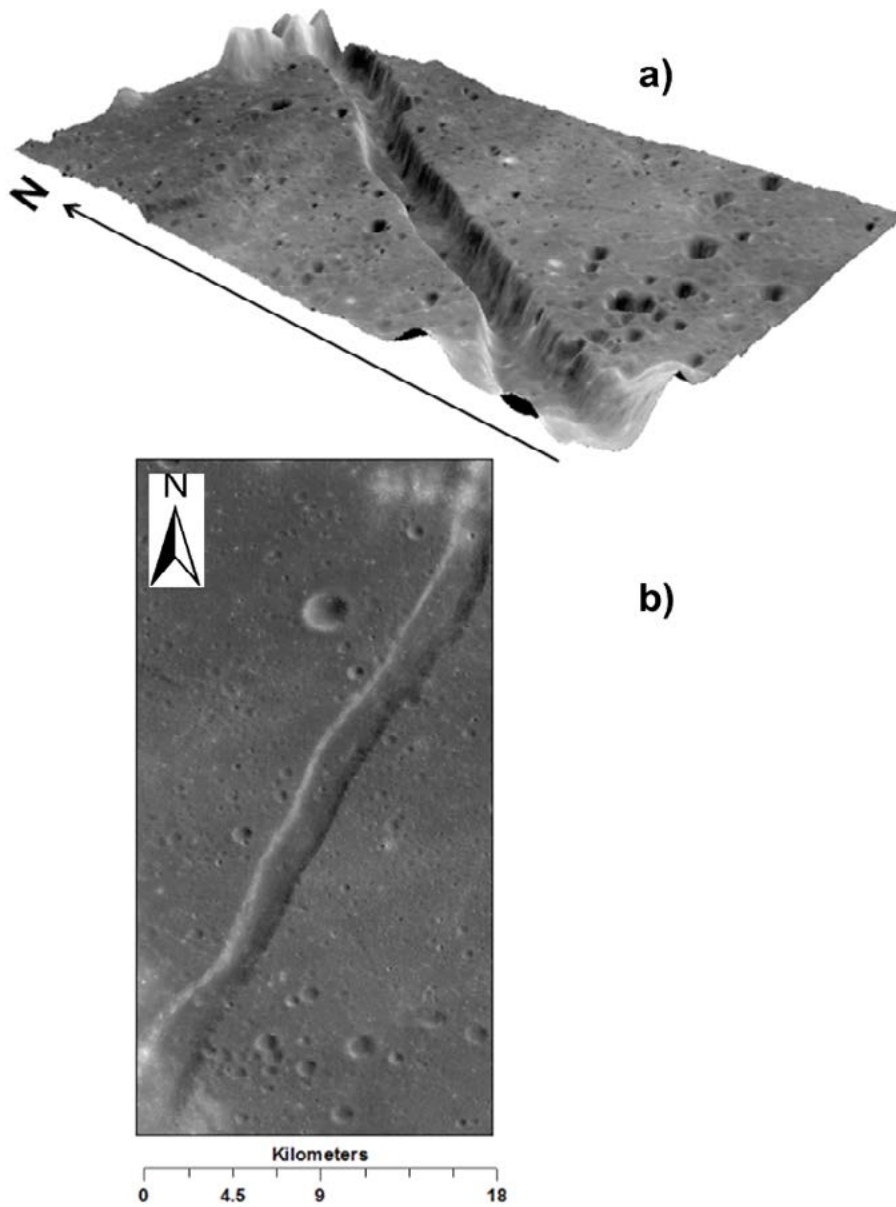
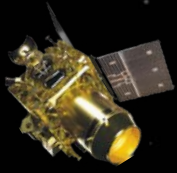


Figure 8.8: (a) 3D perspective view of a Lunar rille proximal to basin margin prepared by draping the TMC-2 orthoimage on DEM (b) Orthoimage.

8.1.10 Lunar Volcanic Dome:

Lunar domes represent past volcanic activity of the Moon and they are important evidences of sites of lava effusion. TMC-2 DEM at spatial resolution of 10 m, enhances topographic variations (Figure 8.9 (c)) and helps in identification/mapping of lunar domes/cones having small relief. Merging of orthoimage (Figure 8.9 (b)) and DEM (Figure 8.9 (c)) helps in creating 3D perspective view (Figure 8.9 (a)). TMC-2 data also helps in surface age determination and estimation of rheological properties (viscosity of lava, effusion rate etc.) based on morphometric parameters (diameter, height).

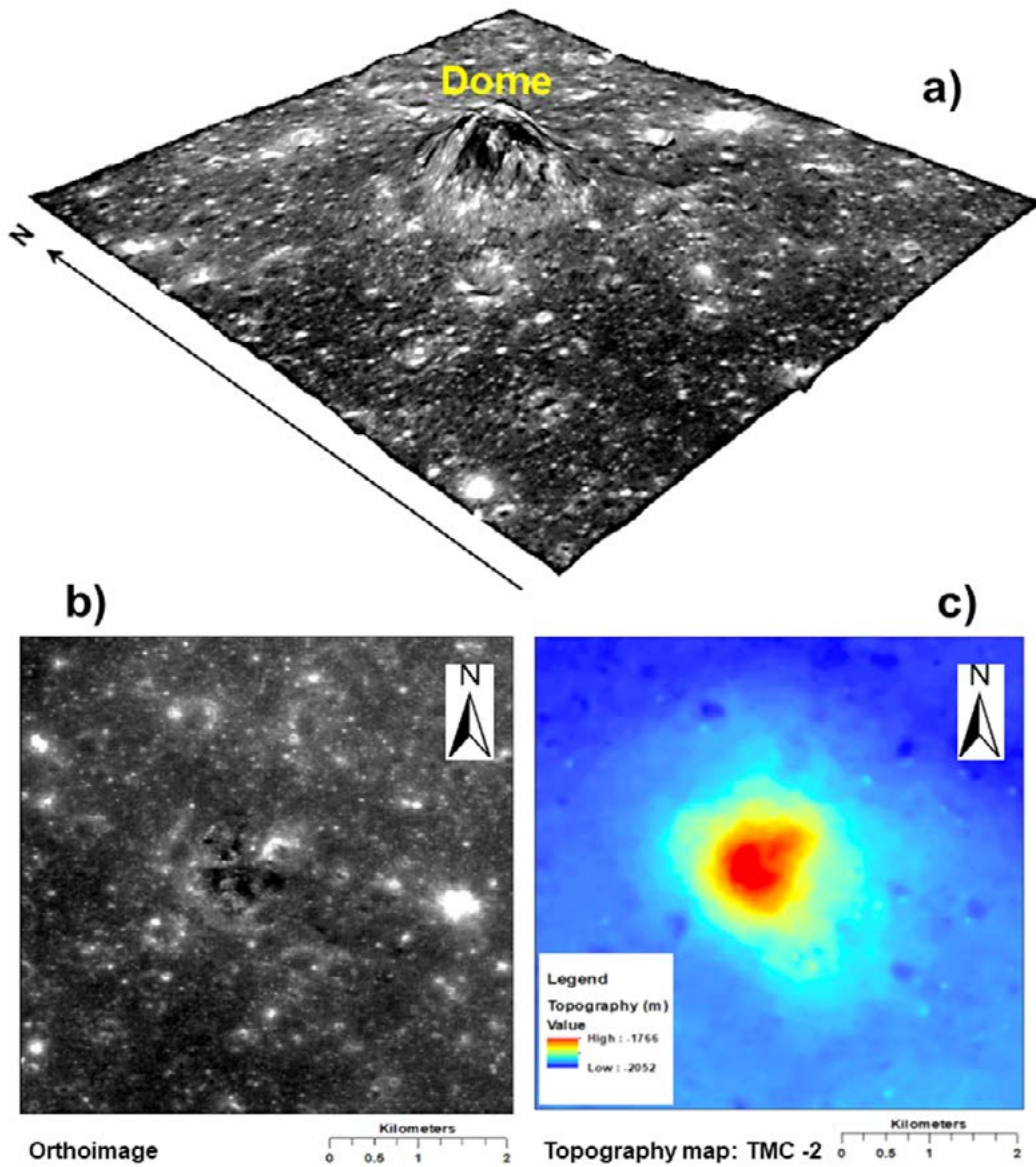
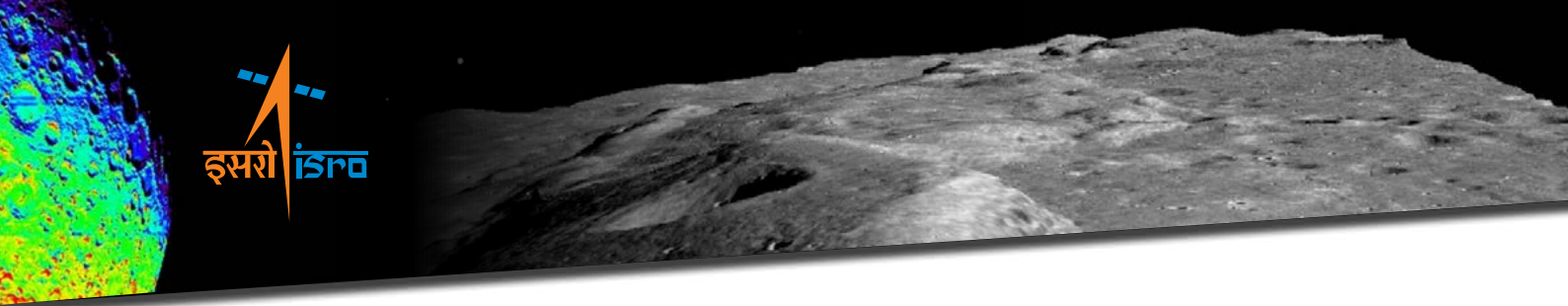


Figure 8.9: (a) 3D perspective view of a Lunar volcanic dome (57.9300 W, 15.3000 N) mapped in the Marius hills region prepared by draping the TMC-2 orthoimage on DEM (b) Orthoimage (c) Topographic Map using DEM.

8.1.11 Lunar Swirls (Albedo Features) - Mare Marginis Region:

The lunar swirls are mysterious high albedo curvilinear surface features. They impart no topography, but rather overlay the existing topography. Lunar swirls are believed to be associated with magnetic anomalies. Ortho image (Figure 8.10 (b)), (83.95° E, 17.12° N) shows part of one of the swirl (bright) in the Mare Marginis region. The derived topographic map (Figure 8.10 (c)) shows no spatial correlation with albedo features in orthoimage (Figure 8.10 (b)).

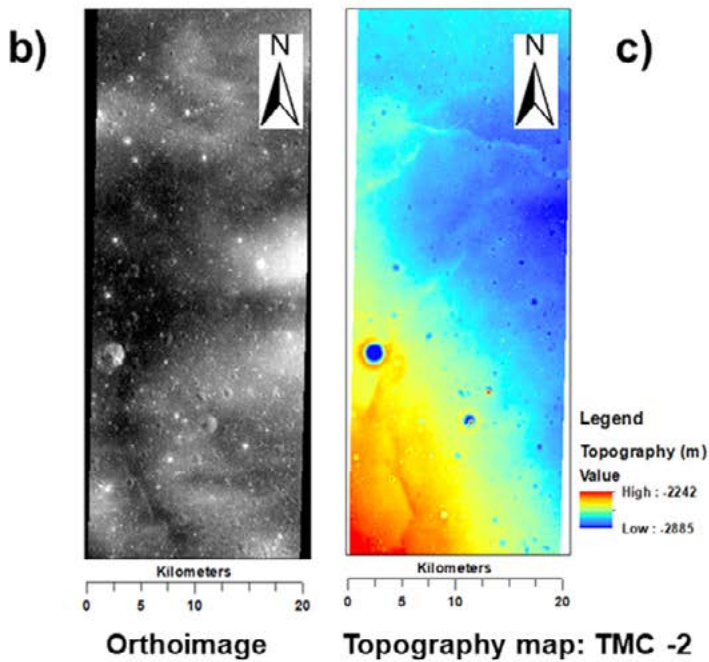
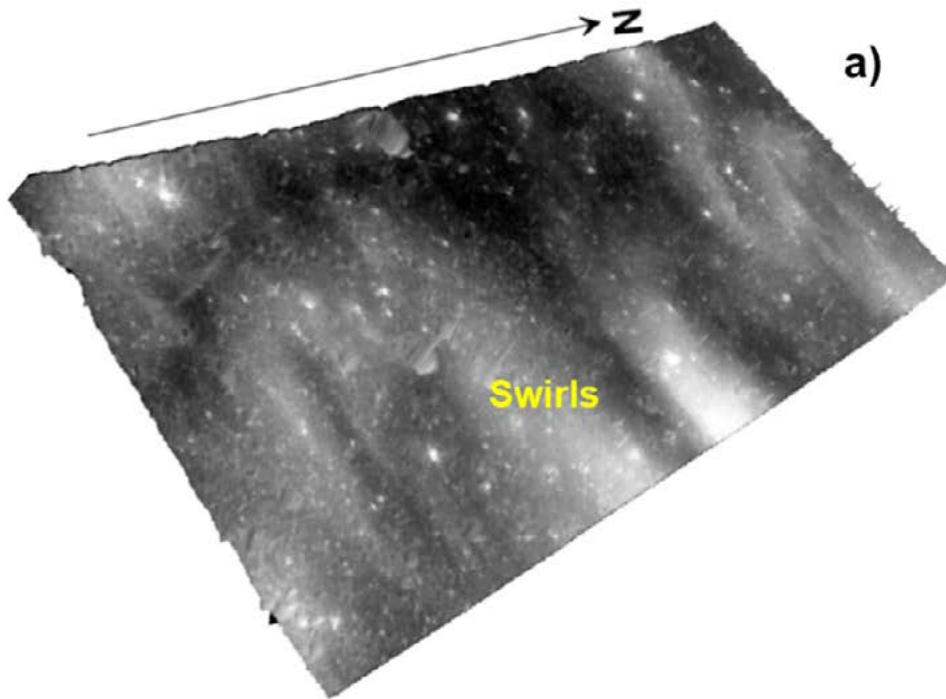
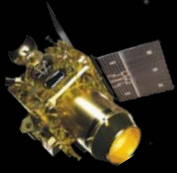
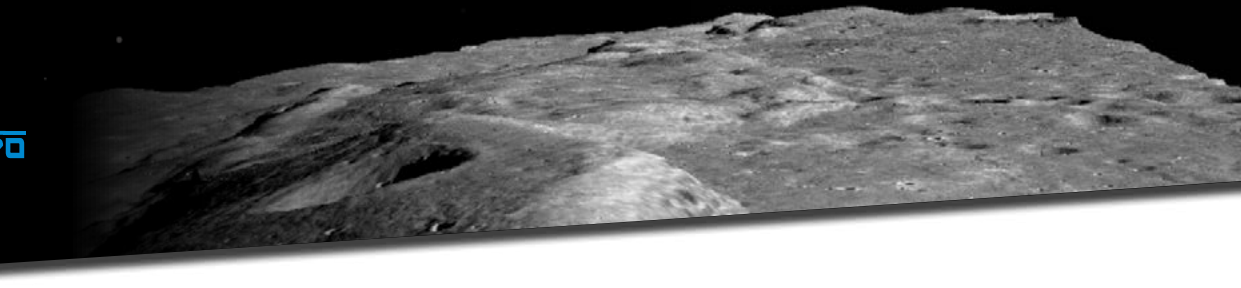


Figure 8.10: (a) 3D perspective view of a Lunar swirls prepared by draping the TMC-2 orthoimage on DEM (b) Orthoimage (c) Topographic Map using DEM.

8.1.12 Wrinkle Ridges:

Wrinkle Ridges are low sinuous ridges found in Lunar Maria regions and involve faulting/folding of the lunar crust and believed to be of tectonic origin. They are evidence of lunar crustal shortening. Wrinkle ridges, a known type of geomorphic features on the terrestrial planets,



form within compressional stress regime. The wrinkle ridges originate due to fault-propagation folding of the surface overlying blind thrust faults and are often envisaged as a superposition of a broad arch and asymmetric ridges. On the Moon these tectonic features are found predominantly within the lunar mare.

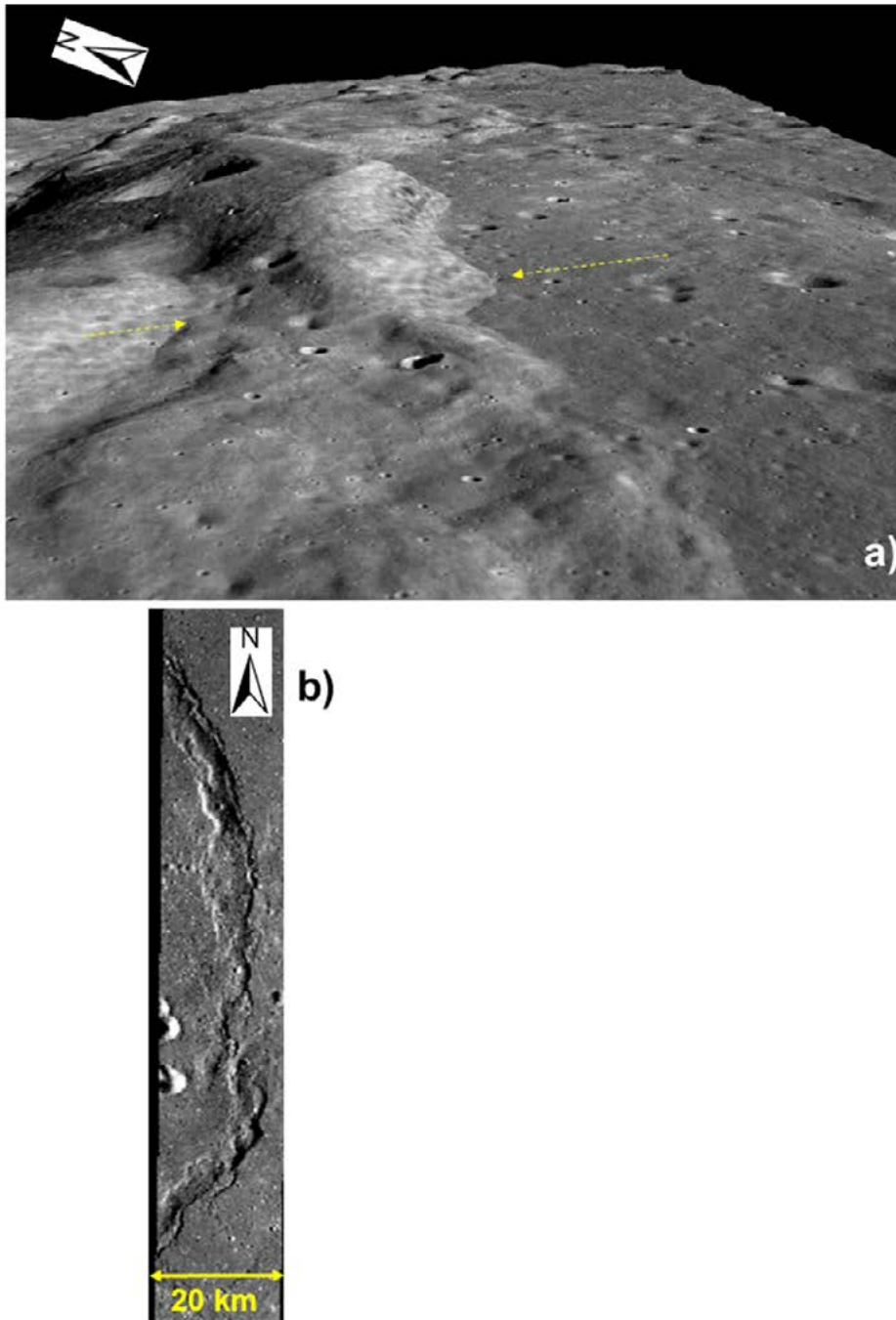
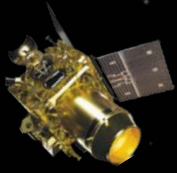


Figure 8.11: (a) 3D perspective view of Dorsa Geikie prepared by draping the TMC-2 orthoimage on DEM. Yellow arrows indicate direction of compressional stress perpendicular to the ridge (b) Orthoimage.



8.1.13 Boulders Outside Crater:

Usually boulders are not so commonly visible on TMC-2 images, however, boulders are seen in an image acquired at low sun elevation angle, on 15th October 2019. This demonstrates that low sun angle imaging helps in detecting boulders (white arrows).

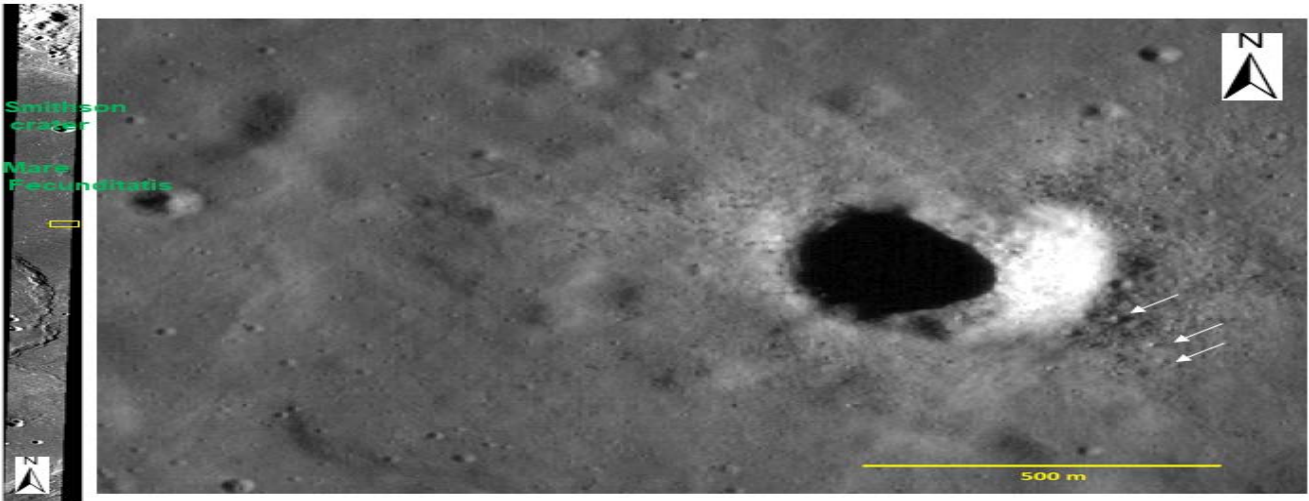


Figure 8.12: Figure showing the boulders (white arrows) in the TMC-2 Image acquired on 15 Oct. 2019

8.1.14 Application Potential of TMC Multi Sun Angle Images:

High and low sun elevation angle images (TMC-1 & 2) show different appearances of the same area as illustrated for two craters (Figure 8.13 (a)/(b) & (c)/(d)). The high sun elevation angle images (TMC-1, Figure 8.13 (a), (c)) give better view of the ejecta spread while low sun elevation angle images (TMC-2, Figure 8.13 (b), (d)) help in detecting subtle relief features like small boulders. A surge in intensity is seen at lower sun-zenith angle images as shown in the plot (Figure 8.14).

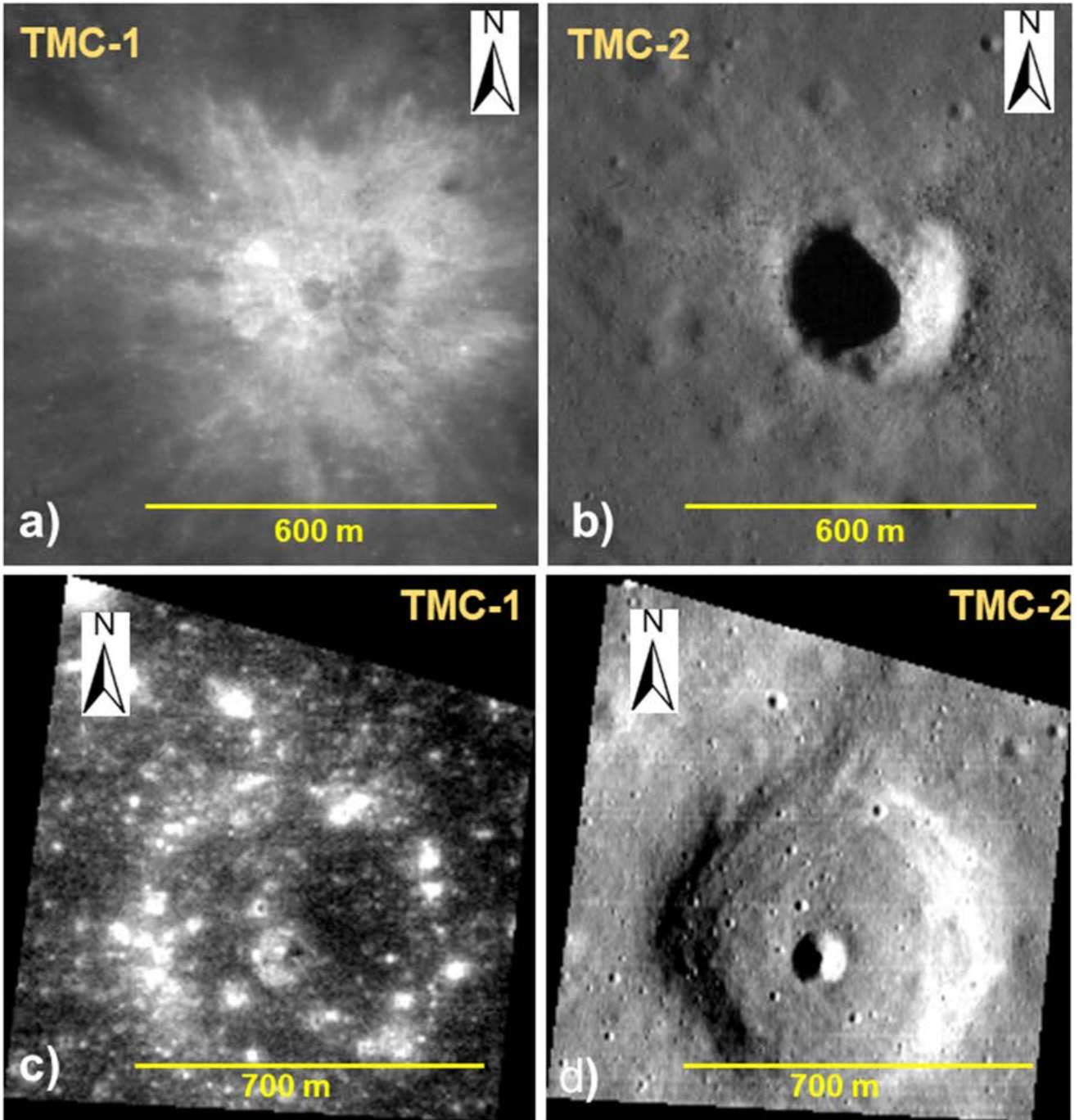
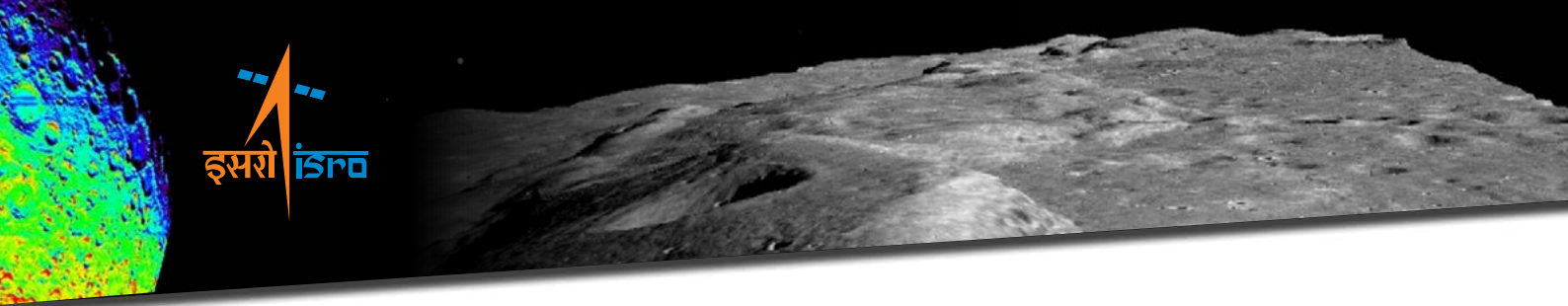


Figure 8.13: (a) and (b) shows a simple crater (0.326° S, 53.69° E) as seen in TMC-1 and TMC-2 images respectively. (c) and (d) show a simple crater (1.40° S, 53.52° E) in TMC-1 and TMC-2 images respectively. TMC-1 image is acquired at high sun elevation angle of 70.46° where as TMC-2 image acquired at low sun elevation angle of 15.03° .

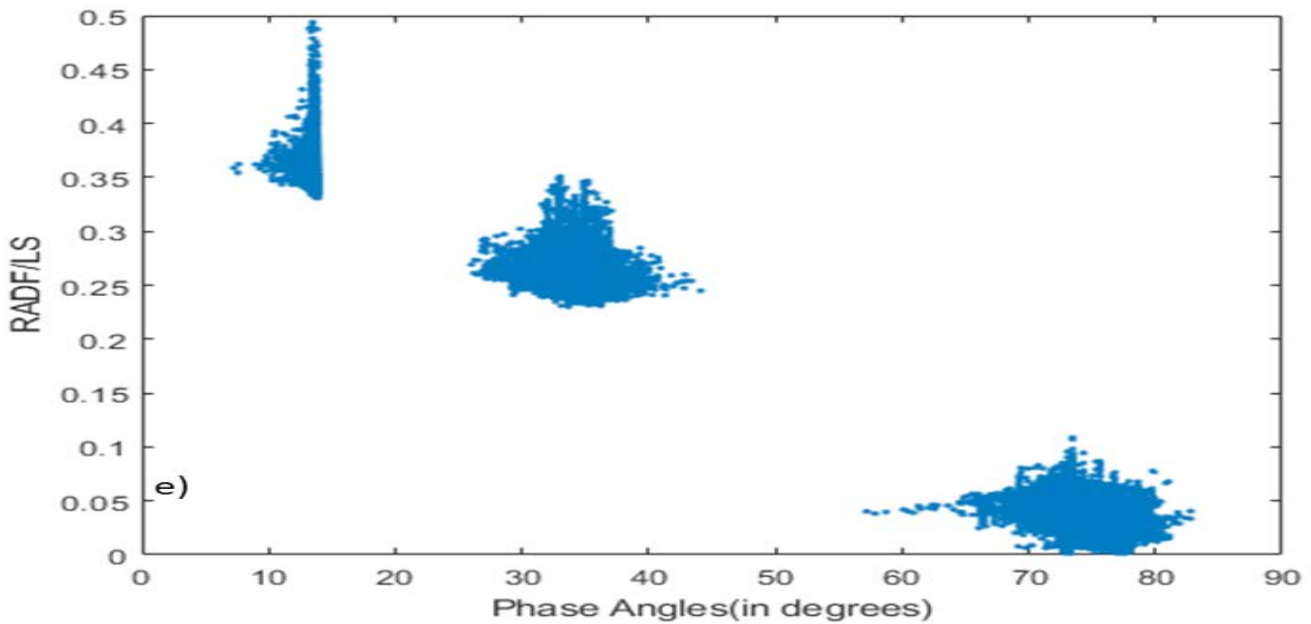
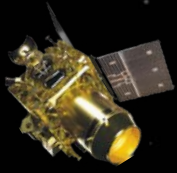


Figure 8.14: Figure showing the plot of Lommel-Seeliger corrected RADF with respect to Phase angles.

8.1.15 Elongated Asymmetric Craters: Impact Cratering Analysis

Elongated asymmetric craters mostly represent an angular impact by the incoming projectile. The shape of the crater and the distal/proximal ejecta spread can be used to determine the projectile dynamic properties like speed and angle of impact. Analysis of TMC-2 (Figure 8.15 (a)) shows the elongated ejecta distribution around an asymmetric crater. This crater has diameter along major, minor axis and ellipticity of 0.51 km, 0.46 km and 1.11 respectively. Two sets of ejecta pattern viz distal and proximal are clearly seen (Figure 8.15 (a)) and are mapped accordingly (Figure 8.15 (b)). The ejecta distribution pattern suggests projectile hit from south at 5 km/sec or less. Shape of crater suggests impact angle of projectile between 30° to 40°. Morphologically confinement of maximum ejecta (asymmetric distribution) in north side suggests it is the downrange side (Melosh, H.J., 1989).

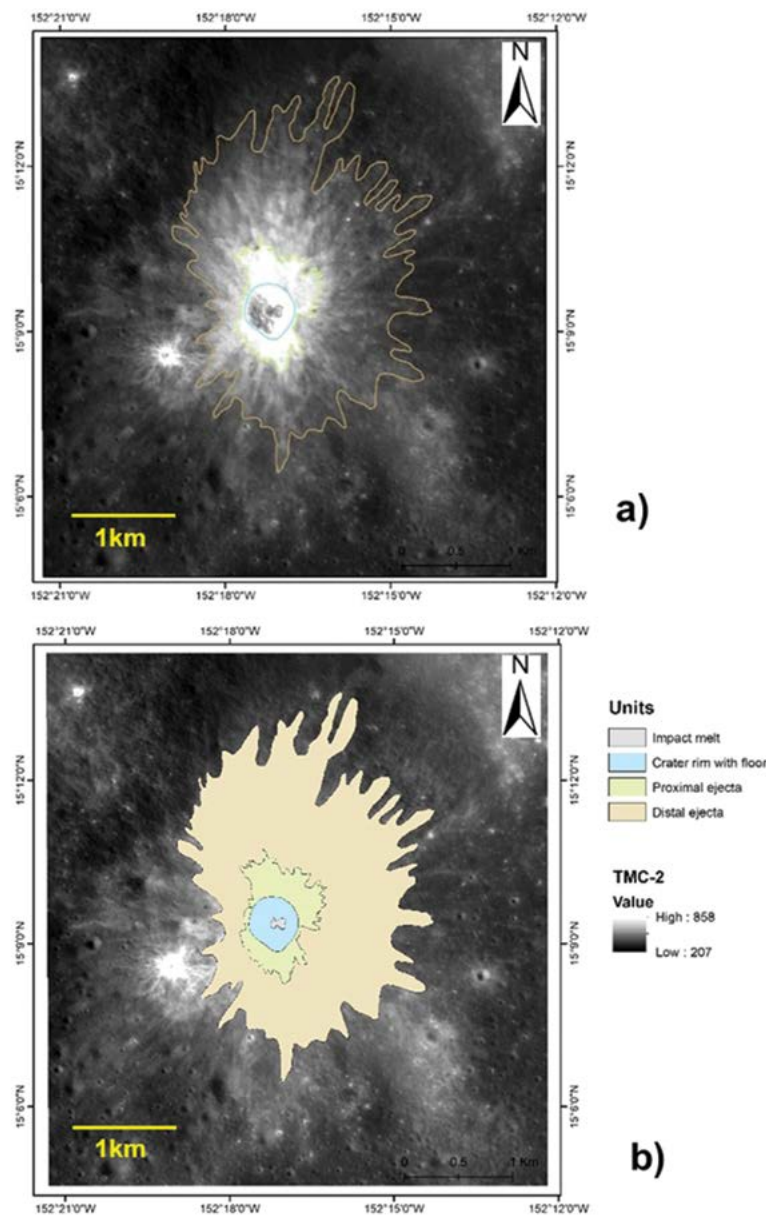


Figure 8.15: (a) An elongated asymmetric crater and (b) Subsequent impact analysis showing distal and proximal ejecta.

8.2 Study of Lunar Crustal Shortening Across Dorsa Geikie, Mare Fecunditatis

On 15th October 2019, TMC-2 imaged the lunar surface at a low sun elevation angle (15.03°) over Mare Fecunditatis from an altitude of ~100 km. This enhanced the subtle lunar topographic variations thus enabling delineation, mapping and morphometry of low elevation landforms of the region. One such important lunar tectonic feature is a wrinkle ridge called Dorsa Geikie, an arcuate wrinkle ridge (~1° S to 4° S and 53.25° E to 53.75° E).

Schematic of a wrinkle ridge is shown in [Figure 8.16](#). Topographic cross-section of a wrinkle ridge Dorsa Geiki using TMC-2 DEM is shown ([Figure 8.17](#)).

Morpho structural analysis of wrinkle ridge Dorsa Geikie using TMC-2 orthoimage ([Figure 8.18 \(a\)](#)) and DEM ([Figure 8.18 \(b\)](#)) has helped in estimating the crustal shrinkage and quantifying it (Arya et.al., 2021)

Summary of observations:

- Average crustal shortening in Dorsa Geiki (DG) is 1.89%, which is commensurable with the Lunar average (0.26 - 3.6%)
- Contractional strain is estimated to be 0.60%. This value is relatively higher for wrinkle ridges in Mare Serenitatis (~0.36%) and Mare Tranquillitatis (~0.14%) (Li et al., 2018).
- Age is estimated to be 3.4-3.1 Ga, which shows that this wrinkle ridge is not older than parent basalt in Mare Fecunditatis (3.8-3.2 Ga)

Systematic morphological/morphometric and stratigraphic mapping, quantitative estimation of the crustal shortening and determining its age will be carried out for wrinkle ridges distributed in the different regions of the Moon.

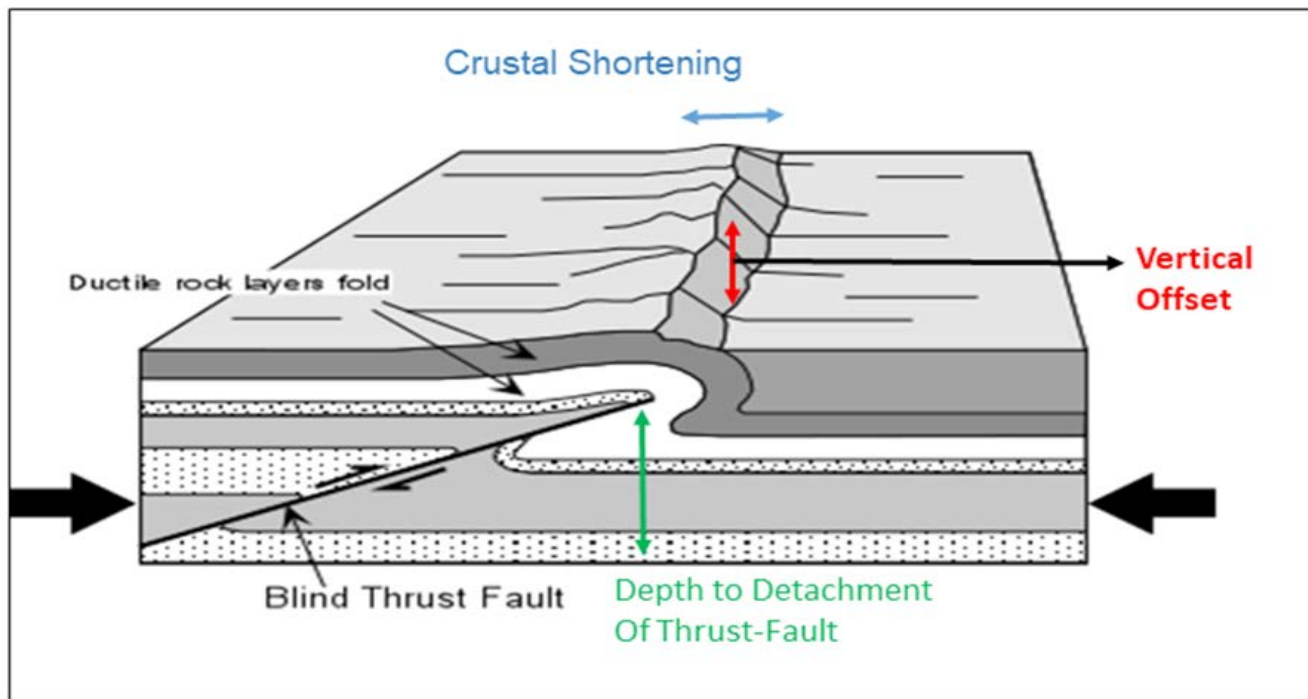


Figure 8.16: Figure showing the schematic of a wrinkle ridge.

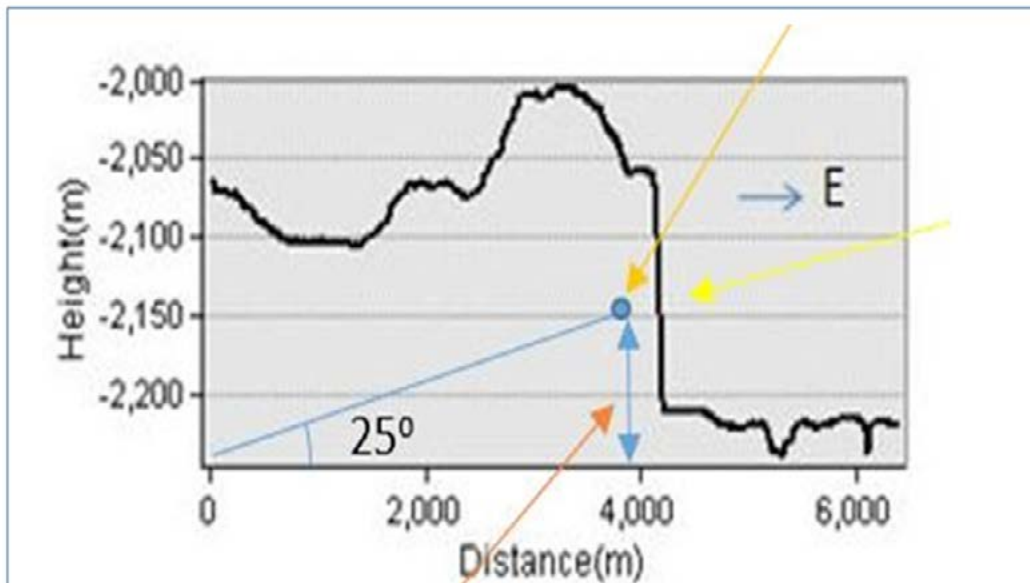
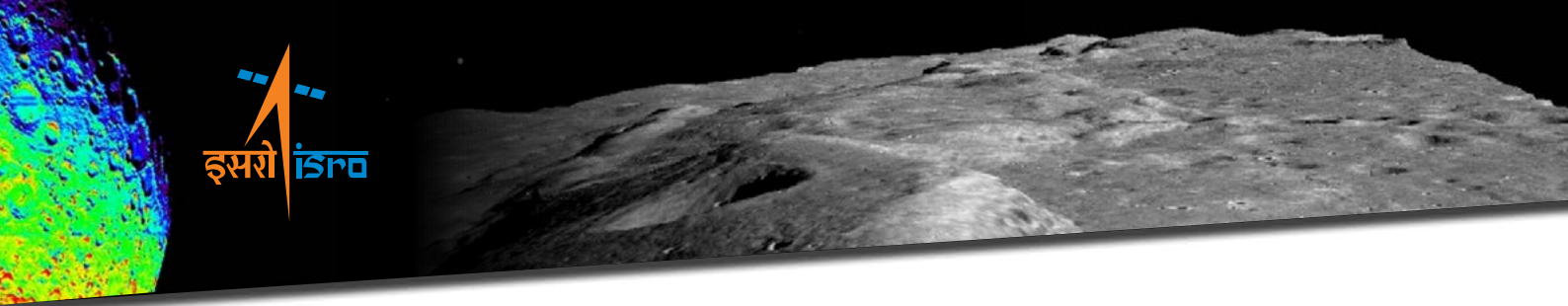


Figure 8.17: Figure showing the topographic cross-section of a wrinkle ridge Dorsa Geiki using TMC-2 DEM.

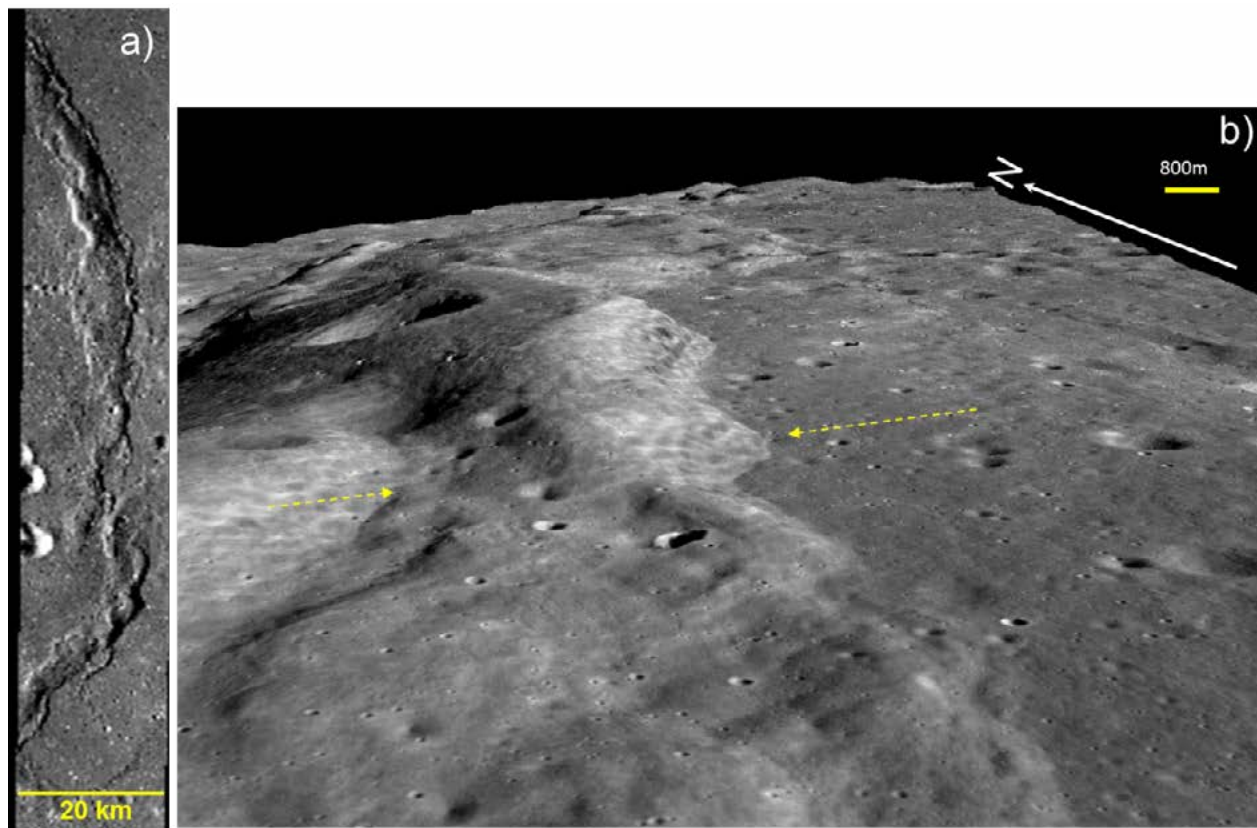
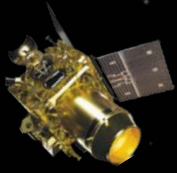


Figure 8.18: (a) Ortho image and (b) 3D perspective view of Dorsa Geikie prepared by draping the TMC-2 orthoimage on DEM. Yellow arrows indicate direction of compressional stress perpendicular to the ridge.



8.3 Summary

- TMC-2 instrument has provided excellent data for planned morpho-structural objectives.
- A detailed characterization of the Dorsa Geikie in Mare Fecunditatis region has been carried out in terms of crustal shortening, accumulated contractional strain, stress regime and its geological age using TMC-2 DEM and images. This kind of study for all wrinkle ridges on Moon can give better and accurate estimate of Moon shrinkage in the past.
- Use of Multi-Sun-elevation angle images is demonstrated for deriving complementary information of a given area.
- Impact dynamics of incoming projectiles is successfully estimated for oblique craters using ortho-image and DEM.

Publication

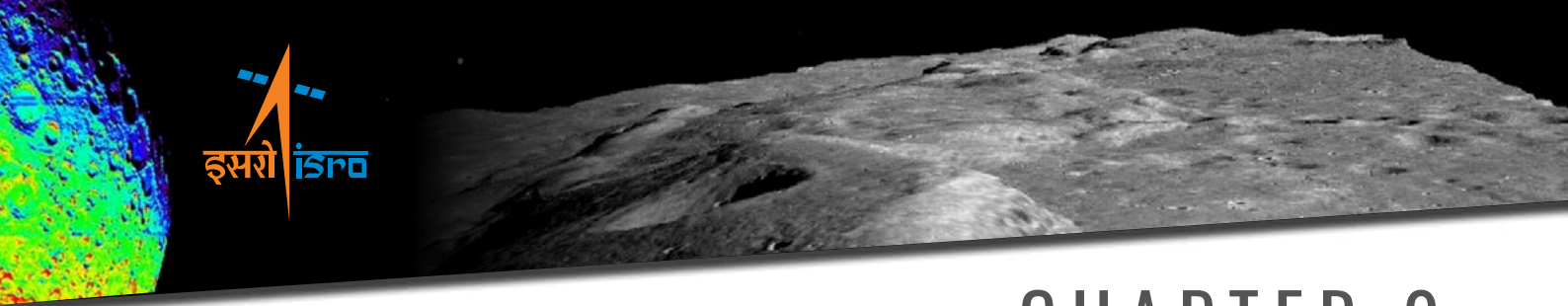
A.S. Arya, Joyita Thapa, Abhik Kundu, Rwiti Basu, Amitabh, Ankush Kumar and Arup Roychowdhury, 2021. Strain /stress evaluation of wrinkle ridge ‘Dorsa Geikie’ and its implication in adjoining region using Terrain Mapping Camera-2 onboard Chandrayaan-2 mission and other data. Current Science, VOL. 121, No. 1, 10 July 2021.

References

1. Li, B., Ling, Z., Zhang, J., Chen, J., Ni, Y. and Liu, C., Displacement-length ratios and contractional strains of lunar wrinkle ridges in mare serenitatis and mare tranquillitatis. J. Struct. Geol., 109, 27–37 (2018).
2. Melosh, H.J., Impact Cratering: A Geologic Process. Oxford University Press, New York, p. 245 (1989).



Contact detail: Dr. A S Arya (arya_as@sac.isro.gov.in)
Sri Amitabh (amitabh@sac.isro.gov.in)



CHAPTER 9

Science Results from Orbiter High Resolution Camera (OHRC)

In this chapter, the results obtained from OHRC payload are presented.

9.1 Analysis of Boulder Population of a Fresh Crater near Boguslawsky E Crater

A relatively small crater of ~340 m diameter situated near Boguslawsky E (74.920° S, 54.520° E) crater was selected for analysis. This is a fresh crater as evident by the presence of substantial population of boulders around the crater. These boulders are distinctly seen in the OHRC image because of the high spatial resolution and low sun elevation (which results in long shadows).

The spatial and statistical distribution of boulders were studied systematically. Boulders were manually mapped as circular entities (marked by red circle in [Figure 9.1](#)) and the shadows of boulders were marked from the center of the mapped boulder to the tip of the dark region (marked as red lines in [Figure 9.1](#)).

Steps followed/ approach adopted for boulders identification, mapping and size estimation are explained below-

1. The OHRC image was georeferenced and topographically corrected.
2. Potential boulders were identified in the image as combination of darker and brighter regions side by side with darker side opposite to direction of Sun.
3. In order to identify any features in the image, multiple pixels are required. Moreover, detection of boulders in the image is limited by topography, contrast, pixel saturation, etc. Only those candidate boulders were marked which can be identified clearly without any ambiguity.
4. Candidate boulders were mapped with a circle of lowest diameter circumscribing the bright region of the candidate boulder.
5. Shadow is marked from the centre of the boulder to the extent upto which it can be clearly distinguished from the background. The height of the boulder is then calculated from the length of the boulder shadow and the topographically corrected Sun elevation angle.
6. Statistics of the distribution were generated from boulders diameter, height and distance from crater centre.

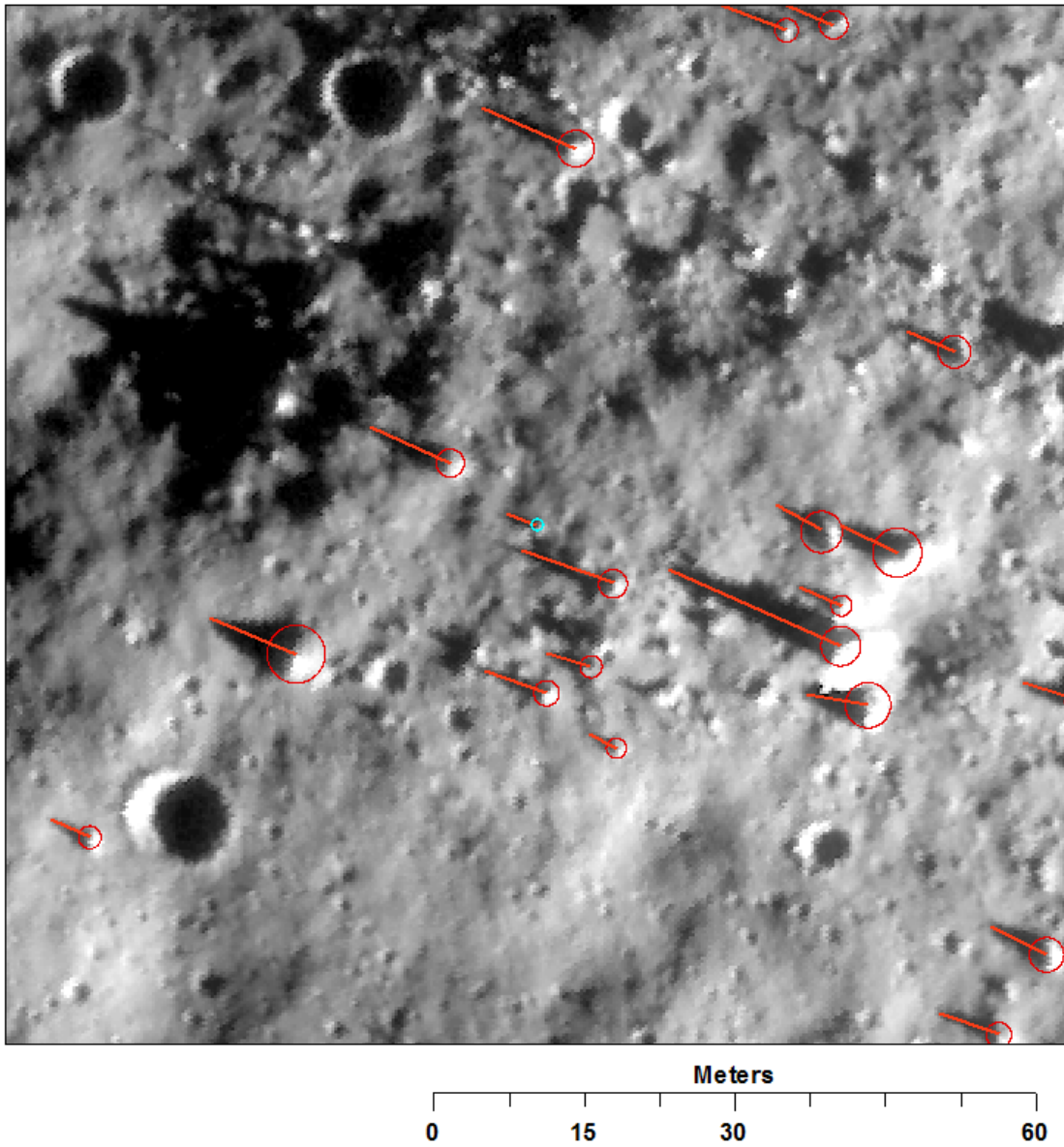
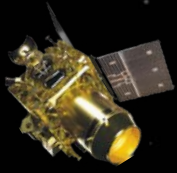


Figure 9.1: OHRC image of boulder field around a fresh crater near Boguslawsky E crater. The red circles represent the boulders bases and the lines represent the shadow length.

A total of 1969 boulders above 1.12 m diameter were identified and measured from the region. The range of estimated diameters is from 1.12 m to 6.64 m. The range of calculated heights is from 0.2 m to 4.34 m. [Figure 9.2](#) is the map indicating the spatial distribution of boulders (yellow circles) around the crater. The radial distribution can also be inferred from the red circles which have a radius as the multiple of the crater radii. This figure also shows that the spatial density of boulders decreases with increase in the distance from the crater centre.

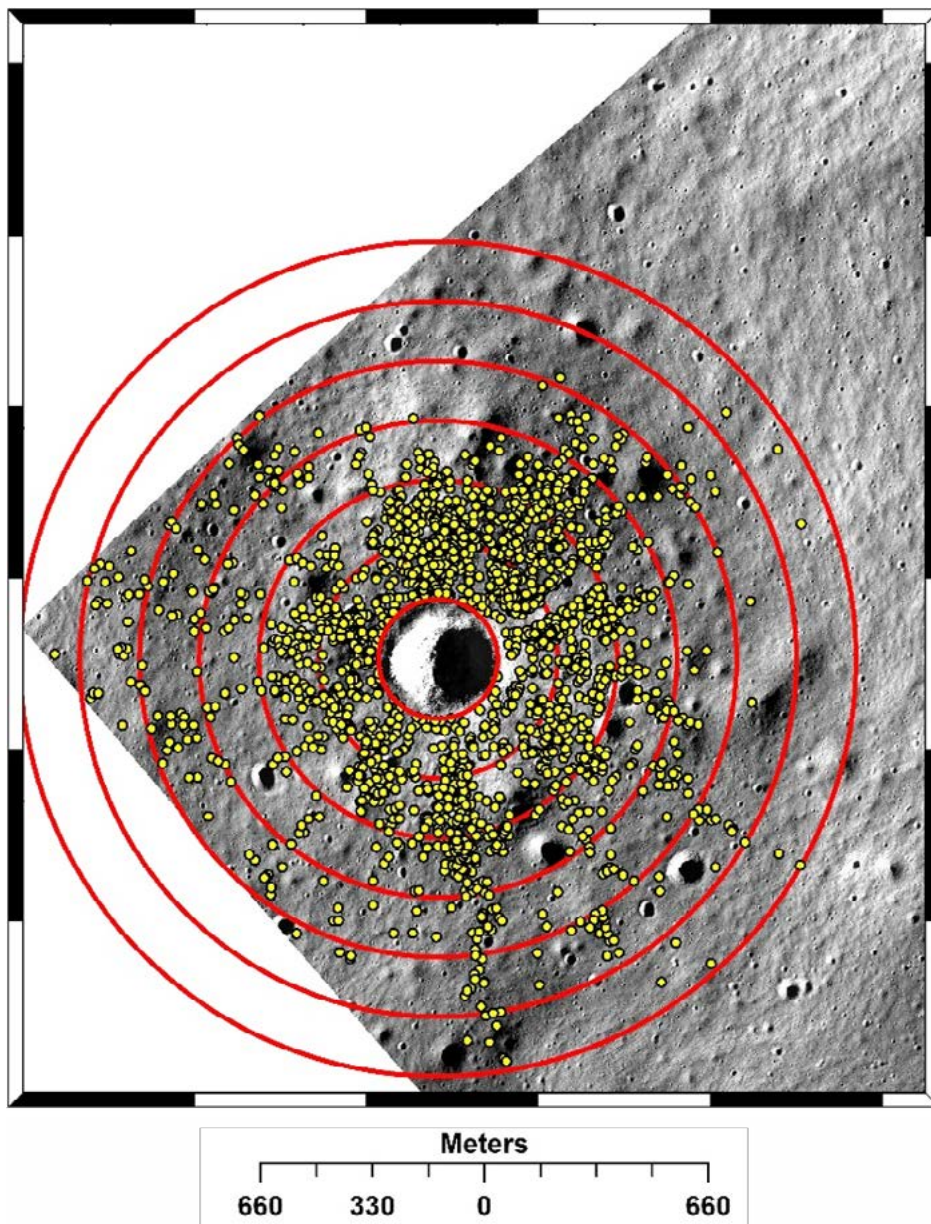
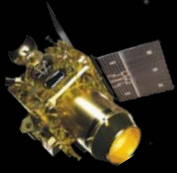


Figure 9.2: Map indicating the spatial distribution of boulders (yellow circles) around the crater.

A rose diagram of the boulder distribution (Figure 9.3) was prepared with crater at its centre. The rose diagram is helpful in understanding the directional distribution of the boulders around the crater. The plot was divided into 12 sectors of 30° each. The blue color numbers in each sector denotes the number of boulders in that direction. The distribution appears to be quite uniform and there is no particular directional dependence of distribution, which indicates that the crater was formed as a result of normal impact.



Angular distribution of Boulders

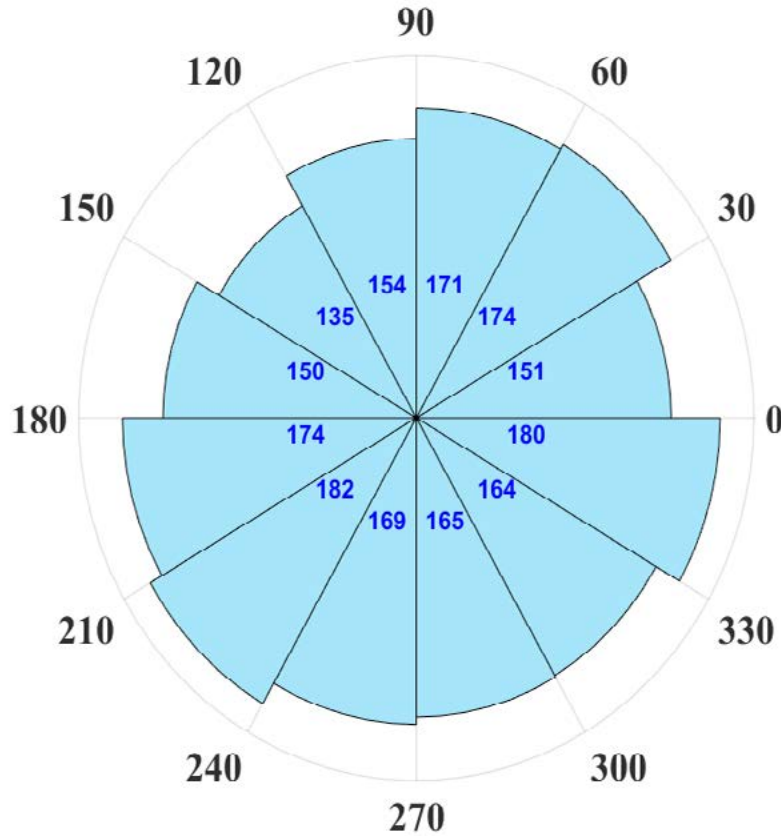


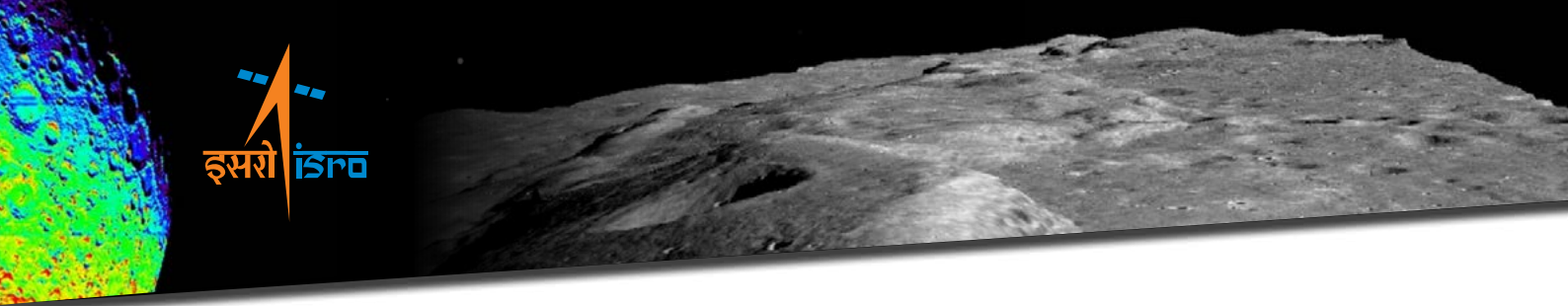
Figure 9.3: Rose diagram showing the spatial distribution of boulders around the crater.

The boulders distribution was taken as a proxy to the age of the crater which was estimated to be around 65-87 Ma based on empirical relations between boulder distance from center of the crater and the crater age.

9.2 Summary

OHRC data is used to understand the boulder distributions around a fresh crater and identified 1969 boulders bigger than 1.12 m. It is found that the smaller boulders are more numerous at all the distances from the crater. However, bigger boulders are distributed closer to the crater and as the distance increases, the average size of the boulders decrease, which is as expected. The distribution of heights also follows the similar trend. The range-frequency distribution showed that the areal density of boulders decreases with distance from the crater centre.

The boulder distance and crater age relations are used to estimate the age of the crater. The age was found to be between 65 Ma and 87 Ma.



Publication

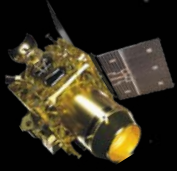
Arup Roy Chowdhury, Manish Saxena, Ankush Kumar, S. R. Joshi, Amitabh, Aditya Dagar, Manish Mittal, Shweta Kirkire, Jalshri Desai, Dhruv Shah, J. C. Karelia, Anand Kumar, Kailash Jha, Prasanta Das, H. V. Bhagat, Jitendra Sharma, D. N. Ghonia, Meghal Desai, Gaurav Bansal and Ashutosh Gupta (2020) Orbiter High Resolution Camera onboard Chandrayaan-2 Orbiter, Current Science, Vol. 118, No. 4, 560-565.

References

1. Dagar, A. K. , Rajasekhar, R.P, R. Nagori, M. Saxena, Amitabh, A. Prashar, A. Gupta, A. Kumar, A. S. Arya, V. D. Patel, A. R. Chowdhury, S. Gomathi, Vijayasree, (2020). Preliminary Observations and Analysis of Orbiter High Resolution Camera (OHRC) Image, On-Board Chandrayaan-2. 51st Lunar and Planetary Science Conference (LPSC), Abstract #2412.
2. Pajola, M., Pozzobon, R., Lucchetti, A., Rossato, S., Baratti, E., Galluzzi, V., & Cremonese, G. (2019) Abundance and size-frequency distribution of boulders in Linne crater's ejecta (Moon), Planetary & Space Science, 165, 99-109, <https://doi.org/10.1016/j.pss.2018.11.008>.
3. Roy Chowdhury, A., Saxena, M., Kumar, A., Joshi, S. R., Singh, A., Dagar, A. K., Mittal, M., Kirkire, S., Desai, J., Shah, D., Karelia, J. C., Kumar, A., Jha, K., Das, P., Bhagat, H. V., Sharma, J., Ghonia, D. N., Desai, M., Bansal, G., Gupta, A. (2020) Orbiter High Resolution Camera onboard Chandrayaan-2 Orbiter, Current Science, Vol. 118, No. 4, 560-565.
4. Watkins, R. N., Jolliff, B. L., Lawrence, S. J., Hayne, P. O., & Ghent, R. R. (2017). Boulder distributions at legacy landing sites: Assessing regolith production rates and landing site hazards. 48th Lunar and Planetary Science Conference, The Woodlands, TX, Abstract #1245.



Contact detail: Sri Aditya Dagar ([adagar\[at\]sac.isro.gov.in](mailto:adagar[at]sac.isro.gov.in))
Sri Amitabh ([amitabh\[at\]sac.isro.gov.in](mailto:amitabh[at]sac.isro.gov.in))



CHAPTER 10

Science Results from Dual Frequency Radio Science (DFRS) Experiment

This chapter presents the scientific findings from DFRS experiment. In total, there are about seven orbits where DFRS payload was operated. First successful experiment using both X- (8496 MHz) and S-band (2240 MHz) frequency signal were conducted on 04 October 2019. Onboard oscillator was turned on at 8:46:00 UT and turned off at 8:56:00 UT.

Using SPICE Kernels for orbital information, theoretical/Newtonian Doppler were estimated (described in previous section) subtracted from the observed Doppler to obtain the frequency residual. The frequency residuals serve as the input data for further analysis. Along with Lunar atmosphere, observed frequency residuals have the effect of interplanetary medium and terrestrial atmosphere as well. Base line correction was carried out to remove this effect. The calibrated residuals for both X and S band radio signals on 04 October 2019 are shown in the [Figure 10.1](#). A uniformity in the phase fluctuations for both the X and S band of radio signals is noted. Plot corresponding to X-band is normalized for the frequency of S-band signal. An important feature in this figure is the deviation of residual in last 2-3 seconds (before signals getting occulted by the Lunar surface). The negative change in residual during ingress event implies a phase loss in signal. Basic understanding is that the radio signal loses their phase while passing through the neutral medium due to their bending which is affected by changes in the refractive index. The known abundant of neutral molecules (reported by previous study) cannot produce such a huge bending in radio signals. So it is an open question whether a layer of neutral particles is present in the near surface is due to Lunar atmosphere. This requires further observations to arrive at a conclusion.

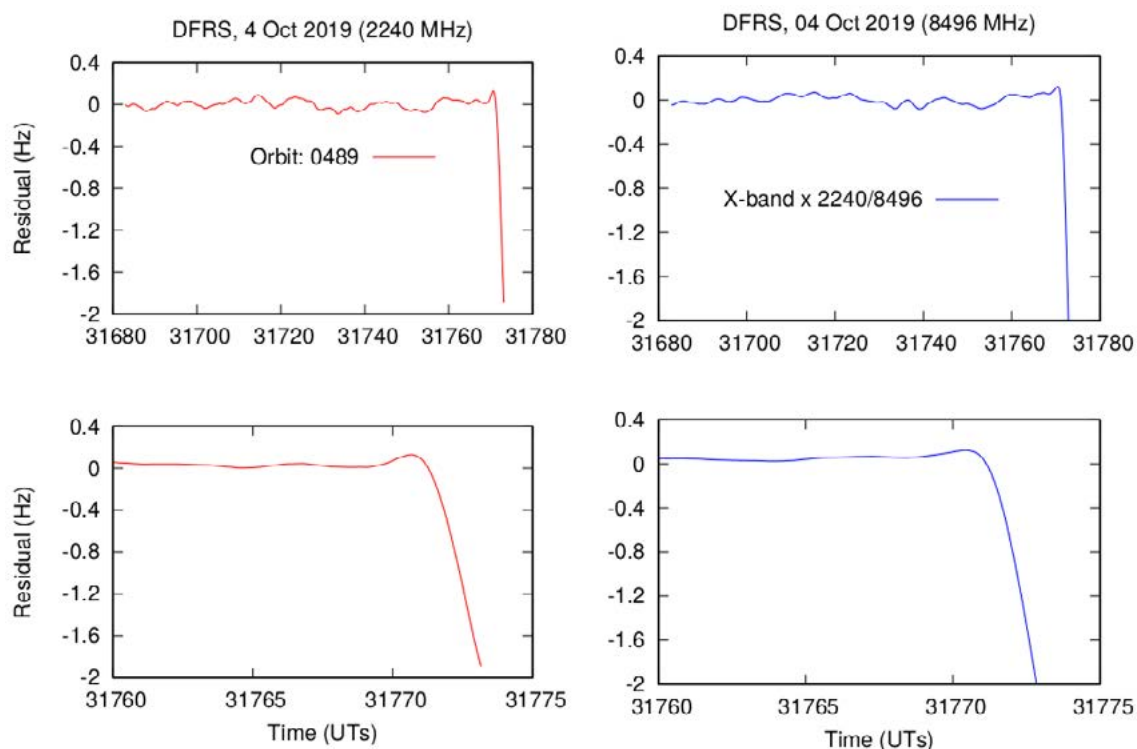


Figure 10.1: Time variation in calibrated frequency residual due to Lunar atmosphere on 04 October 2019 (orbit No. 0489). Left panel is showing variation in S-band signal (red curve) and Right panel is showing variations in X-band (multiplied with frequency ratio of S and X band).

Assuming that Lunar atmosphere is spherically symmetric about center, atmosphere is divided in concentric spherical shells. Second assumption is the medium inside each shell is homogeneous and isotropic in nature. Utilizing the concept of geometrical optics and information about position of spacecraft, Moon and Earth, the time variation is converted to the altitude variation of residual (Figure 10.2). Sudden decrease in frequency residual below 5 km altitude could be noticed in bottom panel of Figure 10.2.

Similar analysis has been done for rest of the five ingress experiments and the time evolution is plotted in Figures 10.3 to 10.7. In all the cases, sharp decrease in the frequency residuals is noted by the same magnitude in both the frequencies. Detailed analysis of the data has been completed and further observations are required to conclude the results.

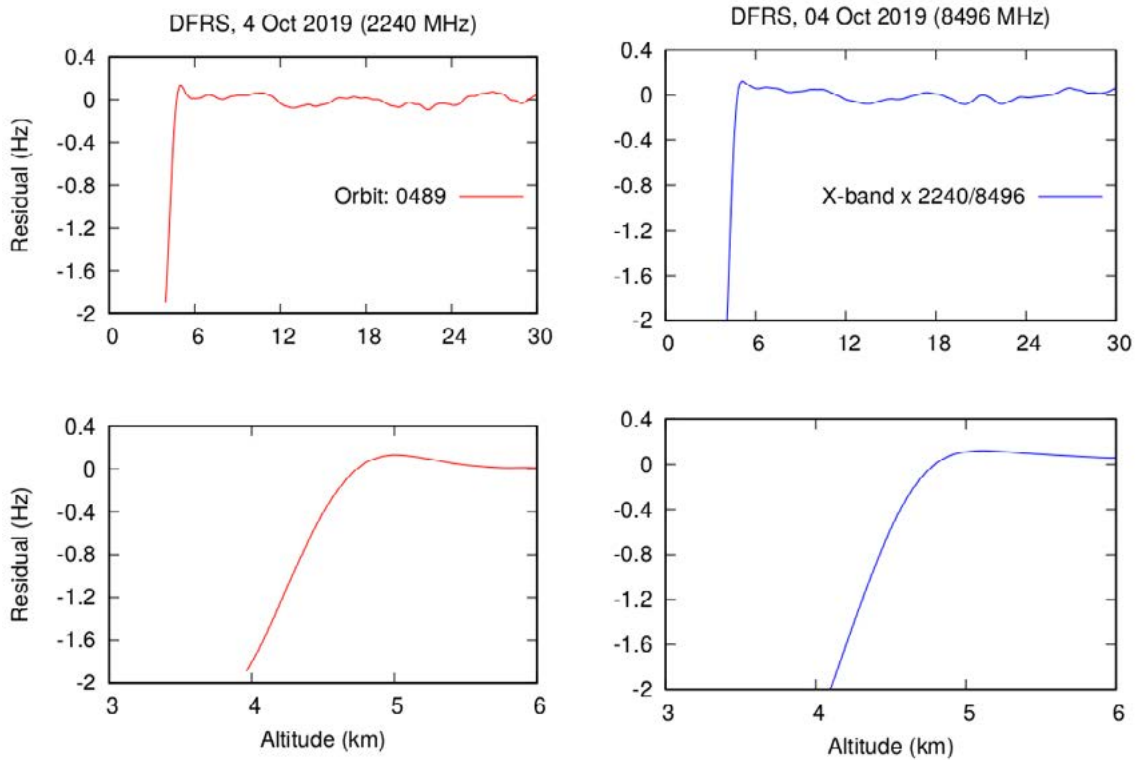
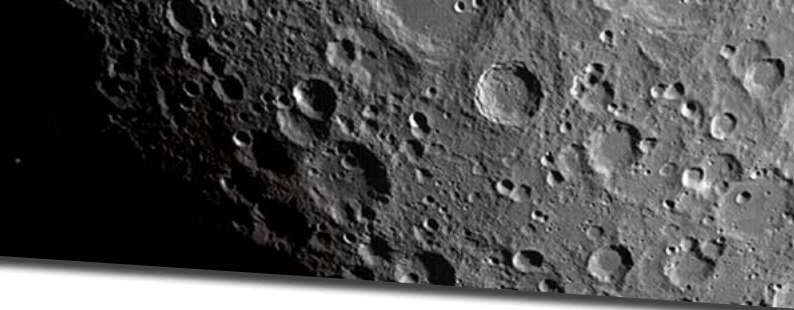
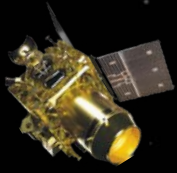


Figure 10.2: Altitude variation in calibrated frequency residual due to Lunar atmosphere. Left panel is showing variation in S-band signal (red curve) and Right panel is showing variations in X-band (multiplied with frequency ratio of S and X band).

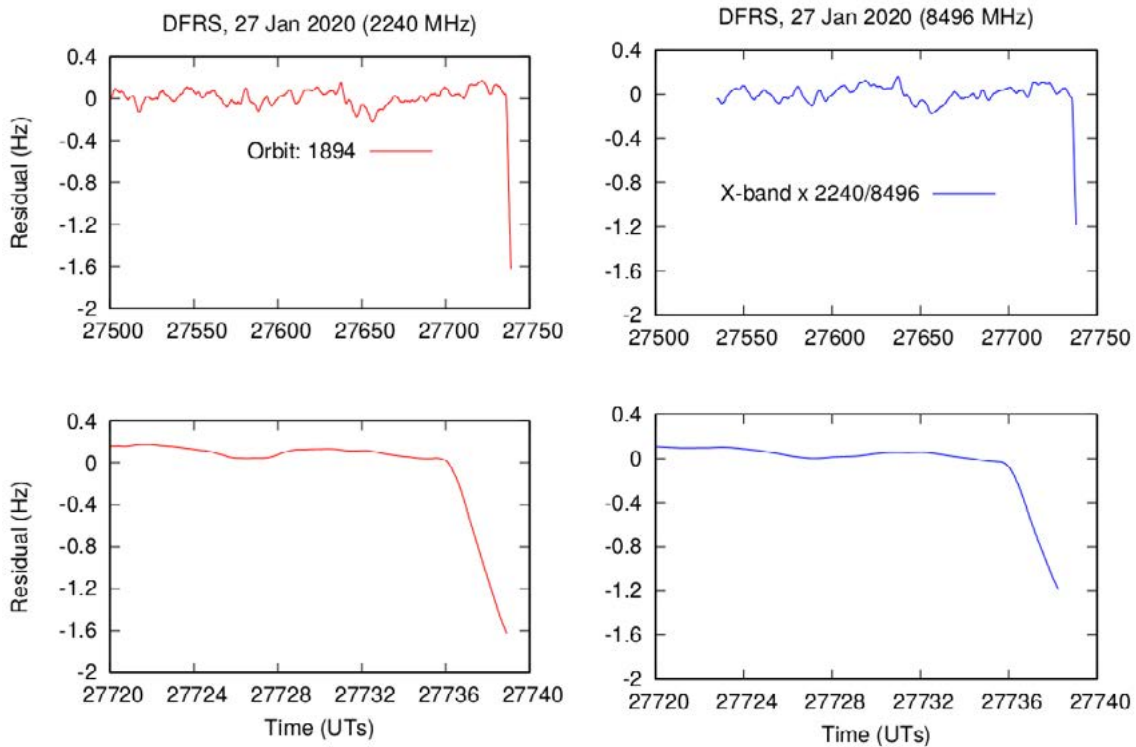


Figure 10.3: Time variation in calibrated frequency residual due to Lunar atmosphere on 27th January 2020 (orbit No. 1894).

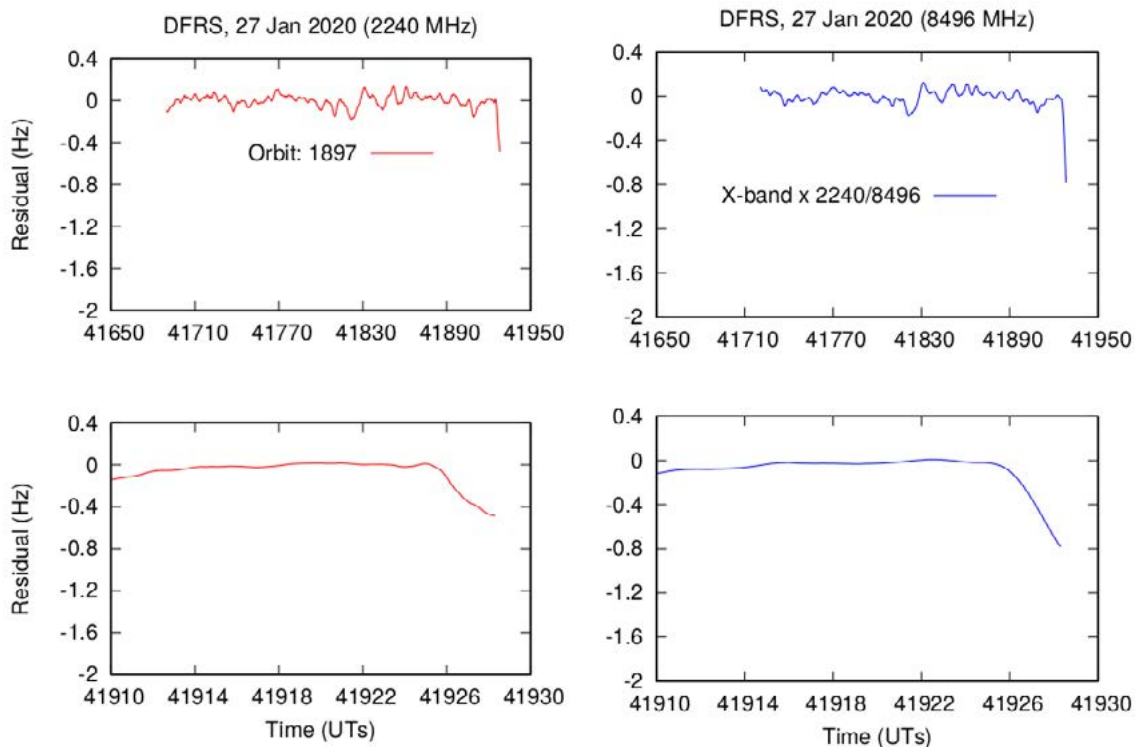


Figure 10.4: Time variation in calibrated frequency residual due to Lunar atmosphere on 27th January 2020 (orbit No. 1897).

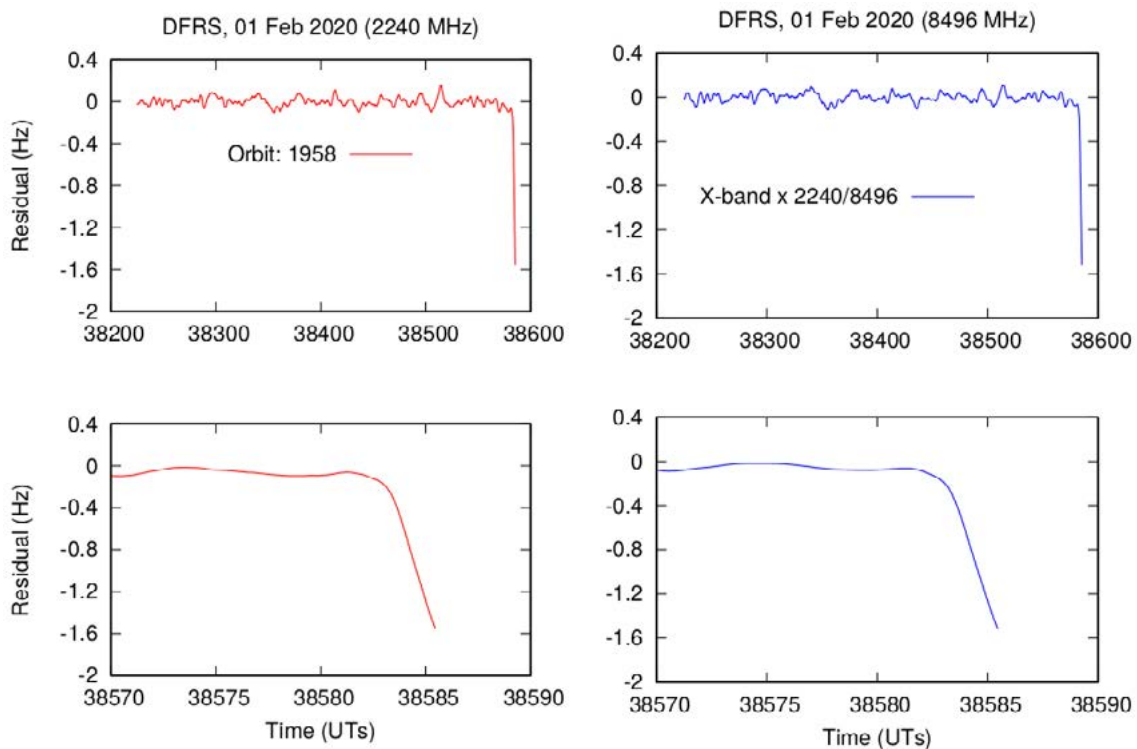


Figure 10.5: Time variation in calibrated frequency residual due to Lunar atmosphere on 01st February 2020 (orbit No. 1958).

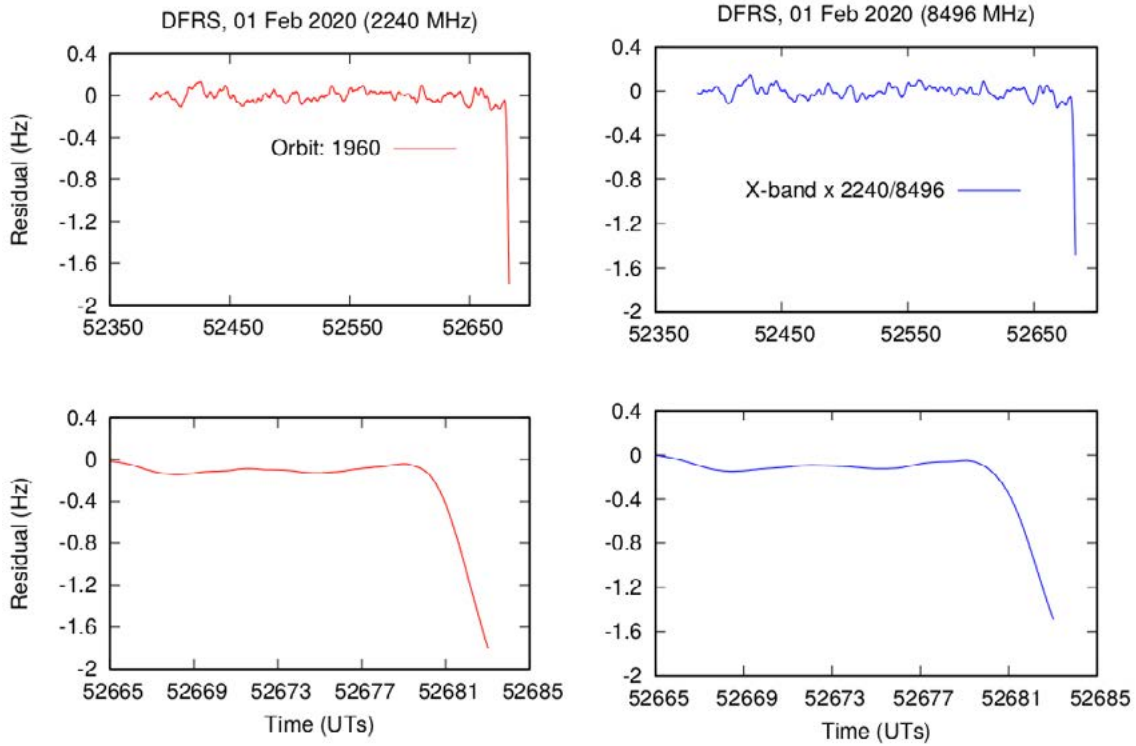
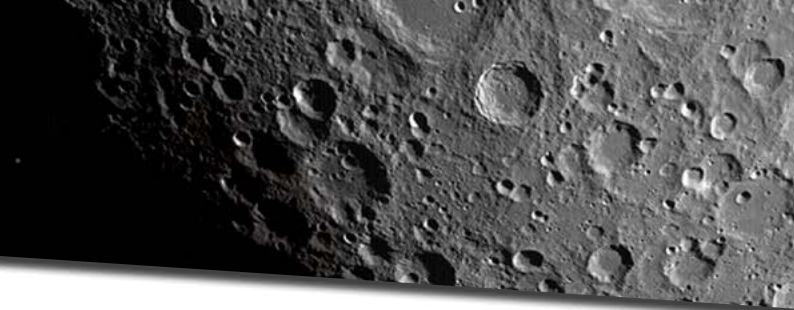
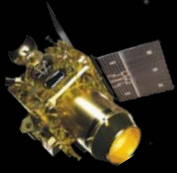


Figure 10.6: Time variation in calibrated frequency residual due to Lunar atmosphere on 01st February 2020 (orbit No. 1960).

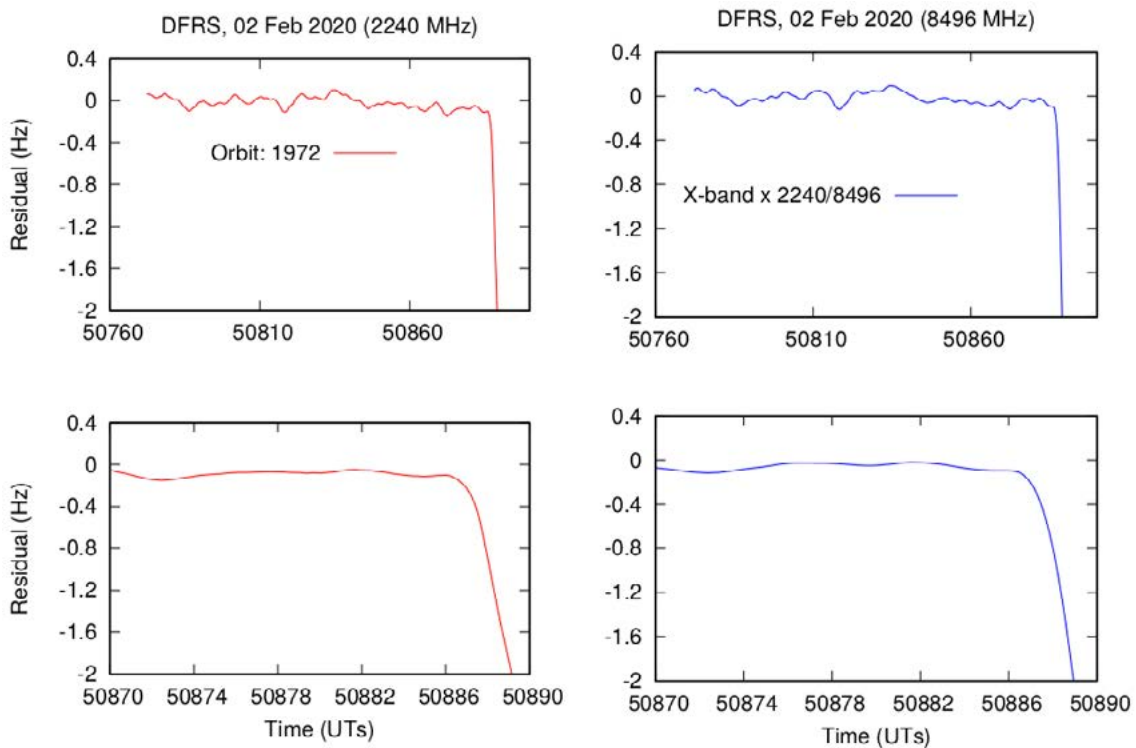
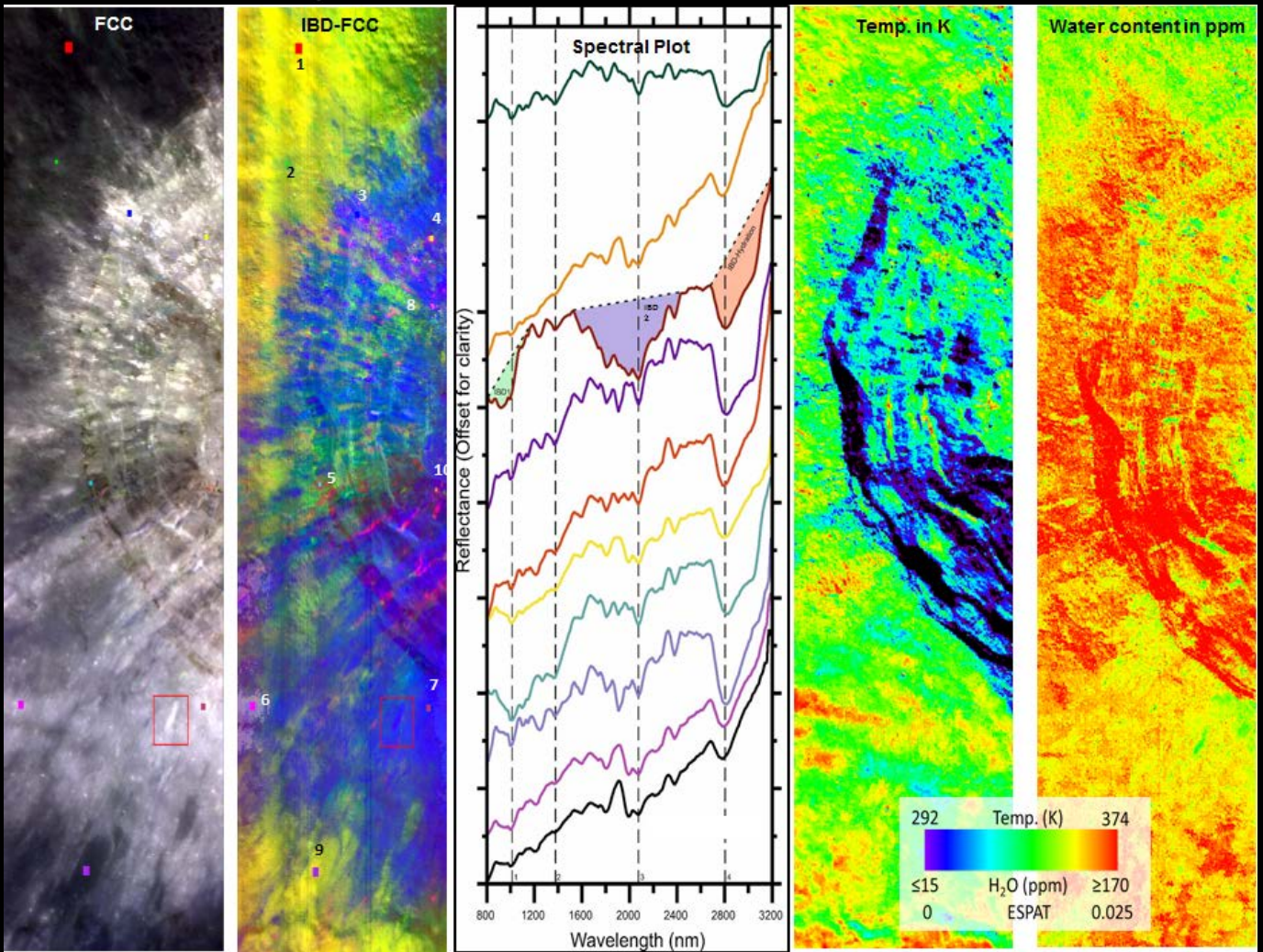


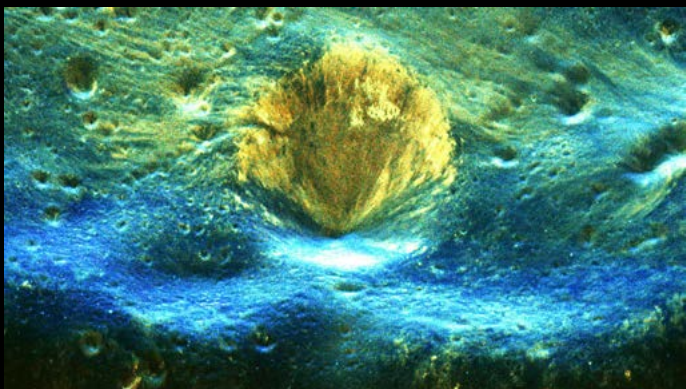
Figure 10.7: Time variation in calibrated frequency residual due to Lunar atmosphere on 02nd February 2020 (orbit No. 1972).



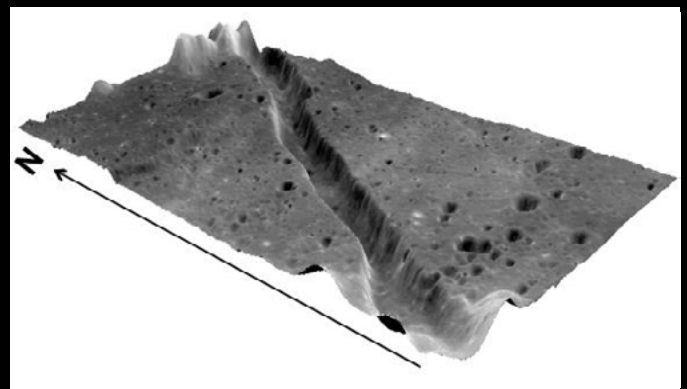
Contact detail: Dr. Raj Kumar Choudhary (rajkumar_choudhary@vssc.gov.in)



Imaging Infra-Red Spectrometer (IIRS) on-board Chandrayaan-2 is the most advanced hyperspectral imager of ISRO. It measures the reflected solar radiation in the spectral range of 0.8–5 μm to identify and map the mineralogical diversity & also to quantify water concentration on the lunar surface.



Chandrayaan-2 L-band High Resolution Synthetic Aperture Radar revealed hidden features of lunar craters



3D View of a Lunar rille proximal to basin margin as viewed by Terrain Mapping Camera-2 onboard Chandrayaan-2

